#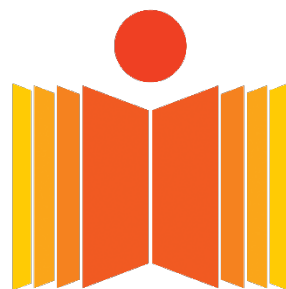 DEVELOPMENT OF MICROSTRUCTURE AND CRYSTALLOGRAPHIC TEXTURE DURING THERMO-MECHANICAL PROCESSING OF EQUIATOMIC CoCrFeMnNi HIGH ENTROPY ALLOY

## G DAN SATHIARAJ

A dissertation submitted to
Indian Institute of Technology Hyderabad
in partial fulfillment of the requirements for the degree of
DOCTOR OF PHILOSOPHY

भारतीय प्रौद्योगिकी संस्थान हैदराबाद
Indian Institute of Technology Hyderabad

**Department of Materials Science and Metallurgical Engineering**

**November, 2015**

# Certificate

I hereby certify that the matter embodied in this thesis entitled **"Development of microstructure and crystallographic texture during thermo-mechanical processing of equiatomic CoCrFeMnNi high entropy alloy "** has been carried out by **G Dan Sathiaraj** at the Department of Materials Science and Metallurgical Engineering, Indian Institute of Technology Hyderabad, India under my supervision and that it has not been submitted elsewhere for the award of any degree or diploma.

Dr. Pinaki Prasad Bhattacharjee

Materials Science and Metallurgical

Engineering Department

Indian Institute of Technology

Hyderabad

502285

INDIA

# Declaration

I declare that this written submission represents my ideas in my own words, and where others' ideas or words have been included, I have adequately cited and referenced the original sources. I also declare that I have adhered to all principles of academic honesty and integrity and have not misrepresented or fabricated or falsified any idea/data/fact/source in my submission. I understand that any violation of the above will be a cause for disciplinary action by the institute and can also evoke penal action from the sources that have thus not been properly cited, or from whom proper permission has not been taken when needed.
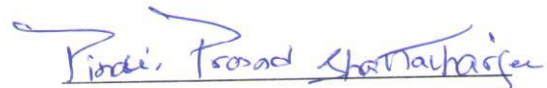
(G Dan Sathiaraj)

(MS12P0003)

# Approval Sheet

This thesis entitled "DEVELOPMENT OF MICROSTRUCTURE AND CRYSTALLOGRAPHIC TEXTURE DURING THERMO-MECHANICAL PROCESSING OF EQUIATOMIC CoCrFeMnNi HIGH ENTROPY ALLOY" by – G DAN SATHIARAJ – is approved for the degree of Doctor of Philosophy from IIT Hyderabad.

-Name and affiliation-

Examiner

SUBHRADEEP CHATTERJEE, AsstProf. IITH

-Name and affiliation-

Examiner

-Name and affiliation-

Adviser

-Name and affiliation-

Co-Adviser

-Name and affiliation-

Chairman

# Acknowledgements

# • Contents

●  List of Figures

## -: Chapter 3:-

# -: Chapter 4:-

-: Chapter 5: -

## -: Chapter 6: -

## -: Chapter 7:-

## -: Chapter 8: -

# • List of Tables

# -: Chapter 6 :-

# -: Chapter 7 :-

# -: Chapter 8 :-

# • List of Abbreviations

| | | |
|---|---|---|
| BCC | – | Body Centred Cubic |
| CGSM | – | Coarse grained starting material |
| CR | – | Conventional Cold-Rolling |
| EBSD | – | Electron Back Scattered Diffraction |
| EDS | – | Energy Dispersive Spectroscopy |
| FCC | – | Face Centred Cubic |
| FEG | – | Field Emission Gun |
| FGSM | – | Fine grained starting material |
| GB | – | Grain boundary |
| HAGB | – | High Angle Grain Boundary |
| HEA | – | High Entropy Alloy |
| IQ | – | Image quality |
| LAGB | – | Low Angle Grain Boundary |
| ND | – | Normal Direction |
| ODF | – | Orientation Distribution Function |
| PFs | – | Pole Figures |
| RD | – | Rolling Direction |
| SEM | – | Scanning Electron Microscope |
| SFE | – | Stacking Fault Energy |
| TBs | – | Twin Boundaries |
| TD | – | Transverse Direction |
| TWIP | – | Twin Induced Plasticity |
| UTS | – | Ultimate Tensile Strength |
| XRD | – | X-Ray Diffraction |

# • Synopsis

High entropy alloys (HEAs) are multicomponent alloys based on the novel alloy design concept of mixing a sufficiently large number of elements (more than five) in equiatomic or near equiatomic proportion. Remarkably, despite having the presence of a large number of components, the HEAs often show rather simple crystal structures, such as FCC (e.g. equiatomic CoCrFeMnNi), BCC or FCC+BCC. This rather surprising behavior is explained on the basis of large configurational entropy of mixing, which increases with increasing number of the alloying elements according to the relationship $\Delta S = -R \sum n \ln n$ (where n is the number of elements and R is the universal gas constant). It has been argued that large increase in the configurational entropy can sufficiently lower the free energy, thereby stabilizing the HEAs into solid solution phases with simple crystal structures. HEAs have attracted considerable research interest which have resulted in the discovery of many interesting and unique properties of these materials. The origin of these unique properties in HEAs is attributed to the core effects of multicomponent solid solution formation, including distorted lattice structure, cocktail effect, sluggish diffusion and extensive formation of deformation nano-twins.

In order to accelerate the engineering applications of HEAs, it is important to further enhance their properties through appropriate thermo-mechanical processing (TMP) routes. TMP of materials combining heavy deformation and annealing affects the development of microstructure and crystallographic texture. These in turn affect the properties of the processed materials. As a consequence, development of microstructure and texture during TMP has been intensely investigated in a wide range of materials including single phase metals and alloys, two phase alloys and intermetallic alloys. However, the effect of TMP on HEAs, particularly on the development of texture, has not been investigated so far. This essentially constitutes the prime novelty of the present research.

In the present work, the effect of TMP on the evolution of microstructure and texture is investigated in equiatomic CoCrFeMnNi alloy. The effect of key processing parameters, such as strain, starting grain size and temperature on the microstructure and texture evolution is systematically investigated. In order to highlight the differences with regard to the microstructure and texture formation, the TMP processing behavior of the HEA is critically compared with model low stacking fault energy (SFE) FCC materials.

The equiatomic HEA used in the present research work is prepared by vacuum arc melting. The as-cast alloy is homogenized at 1100°C to enhance the chemical homogeneity. The as-cast and homogenized alloy shows rather coarse microstructure. In order to achieve a wrought recrystallized microstructure suitable for the present research, the homogenized alloy is initially cold-rolled and subjected to suitable annealing treatments. These fully recrystallized materials are used as the starting materials for further TMP processing.

In order to understand the evolution microstructure and texture during TMP, the fully recrystallized alloy having average grain size ~7 μm is 90% cold-rolled at room temperature and then isochronally annealed (for 1 hour) at temperatures ranging from 700°C-1000°C. The microstructure of the heavily cold-rolled material appears rather fragmented. Bulk and micro texture analyses reveal a systematic transition from pure metal to brass (or alloy type) texture with increasing deformation, confirming the low stacking fault energy (SFE) of the HEA. Annealing of the 90% cold-rolled material leads to the development of an ultrafine microstructure (grain size ~ 1.0 μm). The alloy shows remarkable resistance to grain growth up to annealing temperature of 1000°C. The recrystallization texture shows the presence of α-fiber (ND//<110>) and retention of deformation texture components, such as S ({123}<634>). However, the brass recrystallization texture component (BR) {236}<385>, which is typically reported as a dominant recrystallization texture component in low SFE

brass, is not found to be particularly strong in the HEA. The texture evolution in the HEA appears consistent with discontinuous recrystallization without preferential orientation selection. Remarkably, the volume fractions of different texture components show only marginal variation with annealing temperature.

In order to further elucidate the unique behavior of the HEA, the evolution of recrystallization texture in HEA is compared and contrasted with that of low SFE Ni-60wt.%Co alloy. While the two alloys have similar SFE, they differ considerably with regard to multicomponent solid solution formation behavior. Despite the fact that the two alloys develop uniform brass type texture after cold-rolling, the microstructure and texture after annealing is found to be striking dissimilar. The Ni-Co alloys reveals preferential growth of the G ({110}<001>) and G/B ({110}<115>) oriented grains. In sharp contrast, more homogenous grain growth and negligible variation of volume fraction of texture components with annealing temperature is observed in the HEA. The preferential growth of G and G/B in Ni-Co alloy is explained on the basis of orientation pinning effect. The preferential growth of texture components necessitates rapid boundary movement or easy diffusion across boundaries. The sluggish diffusion behavior of the multicomponent HEA essentially restricts preferential growth of recrystallized grains and texture components.

It is felt necessary to investigate the effect of different processing parameters on the development of microstructure and texture. In order to investigate the effect of strain, the HEA is cold-rolled to three different strain levels, namely 60%, 80% and 95% reduction in thickness corresponding to pure metal, transition and brass type textures. The cold-rolled materials are annealed at different temperatures. It is observed that the average grain size after different annealing treatments decreases consistently with increasing prior strain. This is consistent with microstructural refinement and increase in the number of potential nucleation sites with increasing prior strain. Despite the fact that the cold-

rolling texture at the three deformation levels are different, the recrystallization texture is found to consist of very similar components. BR and {113}<332> components do not reveal strong presence in the recrystallization texture. The volume fractions of different texture components are not significantly affected by annealing temperature.

The effect of grain size on microstructure and texture formation is revealed by comparing two starting materials with widely different average grain size ~ 7 μm and 200 μm. Irrespective of the starting grain size, development of a strong brass type texture is observed during cold-rolling. The recrystallized grain size decreases systematically with decreasing prior grain size. However, the recrystallization texture is not significantly affected by the prior grain size or annealing temperature. Absence of preferential nucleation and growth restrict the development of strong BR and {113}<332> components.

The effect of deformation temperature is investigated by comparing the deformation and recrystallization behavior of cold and cryo-rolled HEA deformed to 90% reduction in thickness. Cryo-rolling leads to significant fragmentation of microstructure but the deformation texture can still be classified as brass type. Upon recrystallization, cryo-rolled material consistently shows finer recrystallized grains size as compared to the cold-rolled material. The finer recrystallized microstructure in the cryo-rolled material is found consistent with the fragmented microstructure offering significantly greater number of potential nucleation sites in the deformed state. However, the recrystallization texture is not affected by cryo-rolling.

In summary, the present work systematically analyzes the development of microstructure and texture during TMP of equiatomic CoCrFeMnNi HEA. It is clearly demonstrated that the development of microstructure during deformation and recrystallization is strongly affected by the processing parameters. The recrystallized microstructure shows more uniform growth and the recrystallization texture is not significantly affected by the processing parameters. The recrystallization texture of the HEA does not

show strong presence of the typical recrystallization texture components of low SFE materials, namely $\{236\}<385>$ and $\{113\}<332>$. The development of recrystallization texture in the HEA could be adequately explained on the basis absence of strong preferential nucleation and growth.

# -: CHAPTER 1 :-

## *Introduction*

The majority of the conventional engineering alloys is based on one principal element to which other alloying elements are added in suitable quantities to achieve desired properties. As a major departure from this conventional alloy design approach, the high entropy alloys (HEAs) have recently been developed based on the novel alloy design concept of mixing a sufficient large number of elements (≥5) in equiatomic or near equiatomic proportions. Surprisingly, despite having the presence of a large number of components, the HEAs often show rather simple crystal structures such as, FCC (e.g. equiatomic CoCrFeMnNi), BCC and FCC+BCC. This rather interesting behavior is explained on the basis of large configurational entropy of mixing of elements in equiatomic proportions, which increases with the increasing number of the alloying elements according to the relationship $\Delta S = -R \sum X_i \ln X_i$ (where $X_i$ is the mole fraction of the $i^{th}$ element and $R$ is the universal gas constant). It has been postulated that large increase in the configurational entropy can lower the free energy sufficiently, thus stabilizing the HEAs into simple solid solution phases. Depending on the entropy of mixing, HEAs are defined as those having at least five elements, while alloys containing three to four elements in equiatomic proportion may be classified as medium entropy alloys. Intensive investigations on HEAs are presently being carried out which have led to the discovery of many interesting and attractive properties.

A major area of research in widening the potential applications of HEAs is to understand the thermo-mechanical processing (TMP) behavior of HEAs. Appropriate understanding of the TMP response of HEAs can significantly affect the microstructure and mechanical properties of HEAs. TMP routes usually involve heavy deformation and annealing, which leads to the refinement of microstructure and development of crystallographic texture. Consequently, microstructure and texture of TMP processed materials are crucial aspects which have been intensely researched in different materials, but much less

investigated and understood in the HEAs. These essentially remain the major focus and constitute the prime novelties of this research.

A brief but critical literature review has been presented in Chapter 1 which clearly shows that considerable attention has been directed toward alloy design, phase stability and mechanical properties of HEAs processed through melting or other routes. In comparison, systematic investigation of different processing parameters on the microstructure and particularly texture evolution during TMP of HEAs has not been carried out.

In the present work an attempt has been made to understand the evolution of microstructure and texture during TMP of single phase HEAs using the equiatomic FCC CoCrFeMnNi as a model system. The experimental details are provided in Chapter 3. In Chapter 4, the evolution of microstructure and texture after heavy cold-rolling and annealing is presented. In order to highlight the differences with other low SFE alloys, a comparative study with low SFE Ni-60wt.%Co is presented in Chapter 5. Further, the effect of different processing parameters, namely cold-rolling strain (Chapter 6), starting grain size (Chapter 7) and cryo-rolling (Chapter 8) on the evolution of microstructure and texture has been critically analyzed. Finally, the key observations and explanations are summarized in Chapter 9.

# -: CHAPTER 2 :-

## *Literature review*

## 2.1 High entropy alloys

The vast majority of the conventional alloys are based on one major element to which other alloying elements are added purposefully to achieve or enhance the desired properties. For example, steels, aluminum alloys, Ni/Co/Fe based superalloys, various intermetallic alloys and metal matrix composites. As a fundamental departure from the conventional alloy design approach, multicomponent high entropy alloys (HEAs) have been recently developed using the novel alloy design concept of mixing a large number of elements in equiatomic or near equi-atomic proportions [1, 2]. Therefore, in sharp contrast to conventional alloys, the HEAs do not have any clearly defined solutes or solvents. The HEAs can thus be conceived to be alloys with whole solute matrix. Surprisingly, despite having the presence of a large number components, the HEAs may possess simple crystal structures e.g. FCC, BCC or FCC+BCC. The possibility of formation of simple crystal structures in these alloys makes them attractive for a wide range of engineering applications. As a result, HEAs in their present state of development, constitute a novel class of advanced materials which have attracted unprecedented attention in recent times [3-16].

The formation of simple solid solution phases in HEAs is attributed to the increased configurational entropy ($\Delta S_{conf}$) which reduces the free energy of the system and renders stability. The configurational entropy per mole can be calculated as shown below for an equiatomic alloy at its liquid state or regular solid solution state [2].

$$\Delta S_{conf} = -k \ln w = -R \left( \frac{1}{n} \ln \frac{1}{n} + \frac{1}{n} \ln \frac{1}{n} + \cdots \frac{1}{n} \ln \frac{1}{n} \right) = -R \ln \frac{1}{n} = R \ln n \qquad (2.1)$$

Where, R is the gas constant (= 8.314 J/K mol).

From Richard's rule [17] it may be written that,

$$\frac{\Delta H_f}{T_m} = \Delta S_f \sim R \qquad (2.2)$$

Where, $\Delta H_f$ and $\Delta S_f$ are enthalpy and entropy change per mole, respectively. During solid to liquid transformation (i.e. during melting) $\Delta S_f$ is ~ R, and

the enthalpy change or latent heat per mole ($\Delta H_f$) can be estimated as $RT_m$, where $T_m$ is the melting point. Therefore, mixing entropy of R per mole in random solid solution is quite large to lower its mixing free energy ($\Delta G_{mix}$) [2].

Fig.2.1 shows the configurational entropy as a function of number of elements for equiatomic alloys [3]. For example, the configurational entropy of ternary equiatomic alloy is already slightly higher than R and that of equiatomic quinary alloy is even higher (1.61R) than ternary alloy (by ~61%). Thus, it is conceived that solid solution phases are preferred as stable phase in HEAs at high temperatures. Accordingly, depending on the configurational entropy, Yeh et al [18] have classified the HEAs as high ($\geq 1.5R$), medium ($1 \leq \Delta S_{conf} \geq 1.5R$) and low ($<1R$) entropy alloys (Fig.2.2).

Table 2.1 shows the configurational entropy values for conventional alloys in their liquid state or random state. It can be clearly seen that many conventional alloys possess low entropy (smaller than R), whereas some concentrated alloys (Ni-base, Co-base super alloys and bulk metallic glasses (BMGs)) have medium entropy ranging from R to 1.5R [18]. This indicates that none of the conventional alloys have high mixing entropy $\geq$ 1.5R which is expected for HEAs. Yeh et al [2] have emphasized that the high mixing entropy significantly affects the thermodynamics and kinetics of phase formation which in turn affect the microstructure and properties of HEAs.
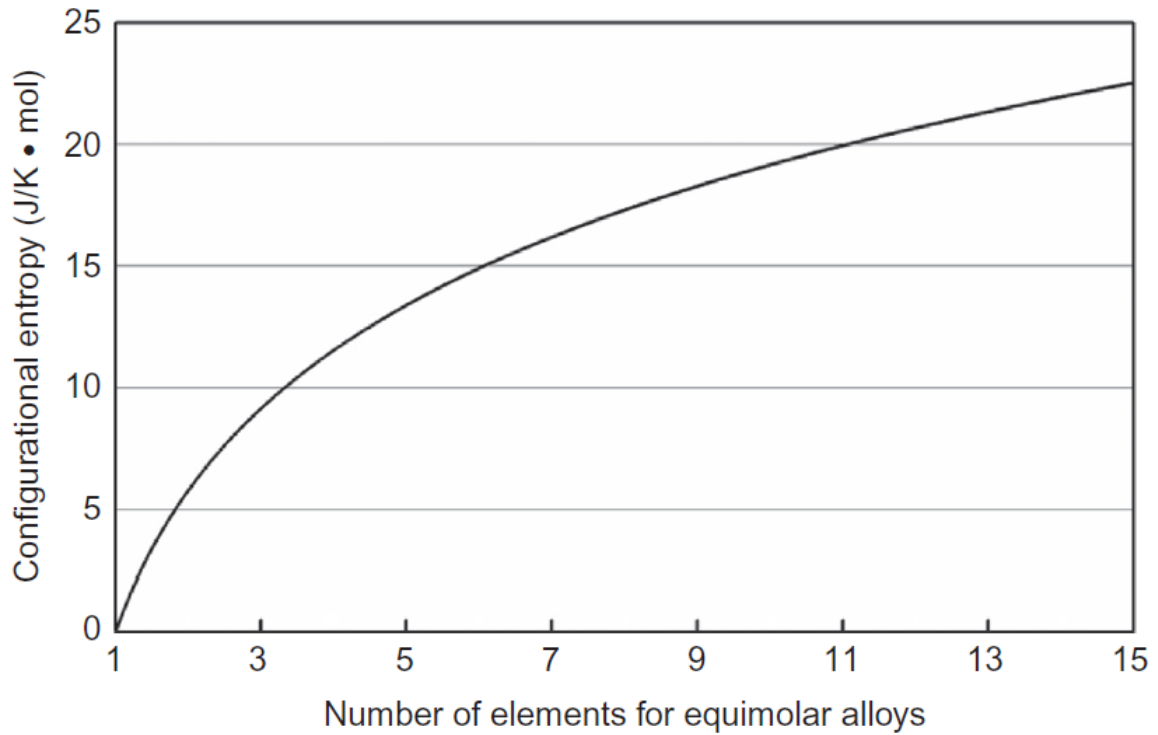
Fig.2.1: Entropy of mixing as a function of the number of elements for equiatomic alloys in the random solution state [3].
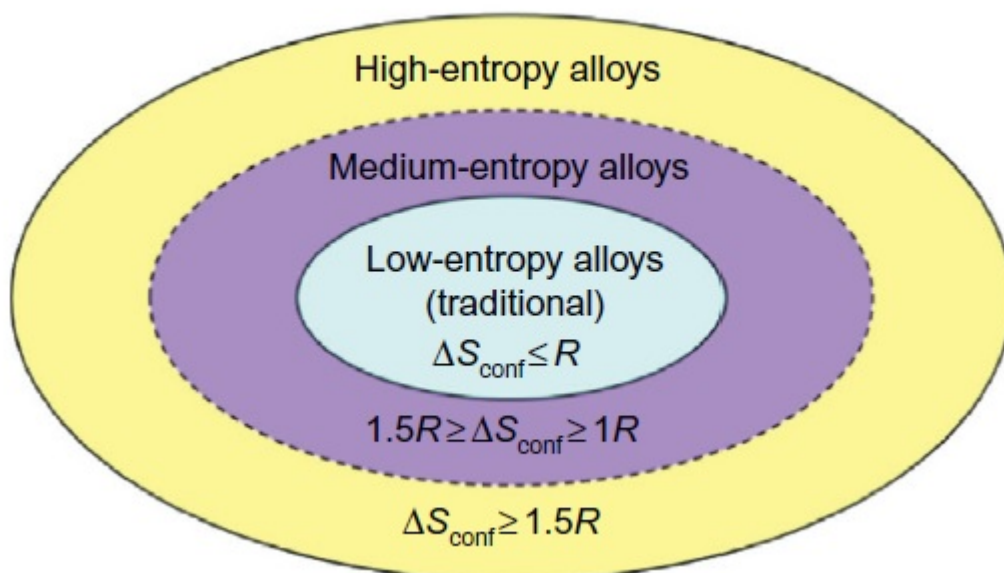


Fig.2.2: Classification HE alloys based on configurational entropy [18].

Table.2.1: Configurational entropy calculated for conventional alloys at their liquid state or random state [18].

| Systems | Alloy designation or composition | $\Delta S_{conf}$ at liquid State | Entropic categorization |
|---|---|---|---|
| Low-alloy steel | 4340 | $0.22R$ | low |
| Stainless steel | 304 | $0.96R$ | low |
|  | 316 | $1.15R$ | medium |
| High-speed steel | M2 | $0.73R$ | low |
| Mg alloy | AZ91D | $0.35R$ | low |
| Al alloy | 2024 | $0.29R$ | low |
|  | 7075 | $0.43R$ | low |
| Cu alloy | 723 brass | $0.61R$ | low |
| Ni-base superalloy | Inconel 718 | $1.31R$ | medium |
|  | Hastelloy X | $1.37R$ | medium |
| Co-base superalloy | Stellite 6 | $1.13R$ | medium |
| BMG | $Cu_{47}Zr_{11}Ti_{34}Ni_8$ | $1.17R$ | medium |
|  | $Zr_{53}Ti_5Cu_{16}Ni_{10}Al_{16}$ | $1.30R$ | medium |

The present work attempts to study the thermo-mechanical processing (TMP) behavior of HEAs. TMP can significantly enhance properties which has been shown for conventional materials and thus should be investigated in-depth in HEAs [19]. However, this also necessitates understanding the fundamental properties distinguishing HEAs with conventional alloys. The brief but critical literature review presented here attempts to provide the present state of understanding on the key aspects of HEAs and their influence on the TMP processing behavior in order to place the current research in the most appropriate context.

## 2.2 Four core effects of HEAs

There are four key/core effects which are less dominant in conventional alloys but greatly affect the development of microstructure and properties of the HEAs. These core effects are (1) Thermodynamics: high-entropy effects; (2) Kinetics: sluggish diffusion; (3) Structures: severe lattice distortion; and (4) Properties: cocktail effects [9].

### 2.2.1 High-entropy effect

The high-entropy effect which tends to stabilize the solid-solution phases has been explained by Yeh et al [9] and already mentioned before. Based on the traditional physical metallurgy concepts, it may be expected that the large number of elements in the HEAs have different interactions and should form many different types of intermetallic compounds or phases with complex crystal structures [3]. As already pointed out, high entropy effect renders the stabilization of solid solution phases with simple crystal structures.

A key issue in the HEA research is whether or not the simple solid solution phases frequently observed are stable equilibrium phases. It is now increasingly supported by new evidences that high entropy can extend the solid solubility limit [5]. Lucas et al [19] have recently reported absence of long range ordering in equiatomic CoCrFeNi alloy, thus confirming the formation of true disordered solid solution. In contrast, equiatomic AlCoCrCuFeNi contain several phases of different compositions [20].

Recently single phase non-equiatomic HEAs have also been reported [21]. Therefore, not all equimolar multi-component systems show simple solid solution phases and at the same time non-equiatomic systems may also show the formation of single phase [22]. Therefore, the understanding of solid solution formation criteria is yet to be understood fully and remains a critical issue (which would be further discussed).

### 2.2.2 Severe Lattice Distortion Effect

Unlike conventional alloys, HEAs have a whole-solute matrix, in which every atom is bounded by different types of atoms, thereby subjected to lattice strain and stress due to the atomic size difference (Fig.2.3) [3]. In addition, different bonding energy and crystal structure amongst constituent elements may contribute significantly to lattice distortion. Thus, most lattice sites and overall lattice distortion would be more severe in HEAs than that in the conventional alloys in which the dominant constituent (or solvent atoms) have almost identical surroundings.

Severe lattice distortion can significantly affect the properties of the HEAs. Anomalous decrease in the x-ray intensity in HEAs has been explained by the roughness of the crystal planes originating from the severe lattice distortion effect [23]. Hardness of BCC HEAs can be particularly enhanced due to significant lattice distortion [24, 25]. The extent of lattice distortion on hardness of refractory BCC equiatomic alloys, such as, MoNbTaVW may be considered as a good example [26, 27]. Senkov et al [27] have reported that hardness value of the refractory HEA is 5250 MPa which is three times that obtained by the mixture rule.
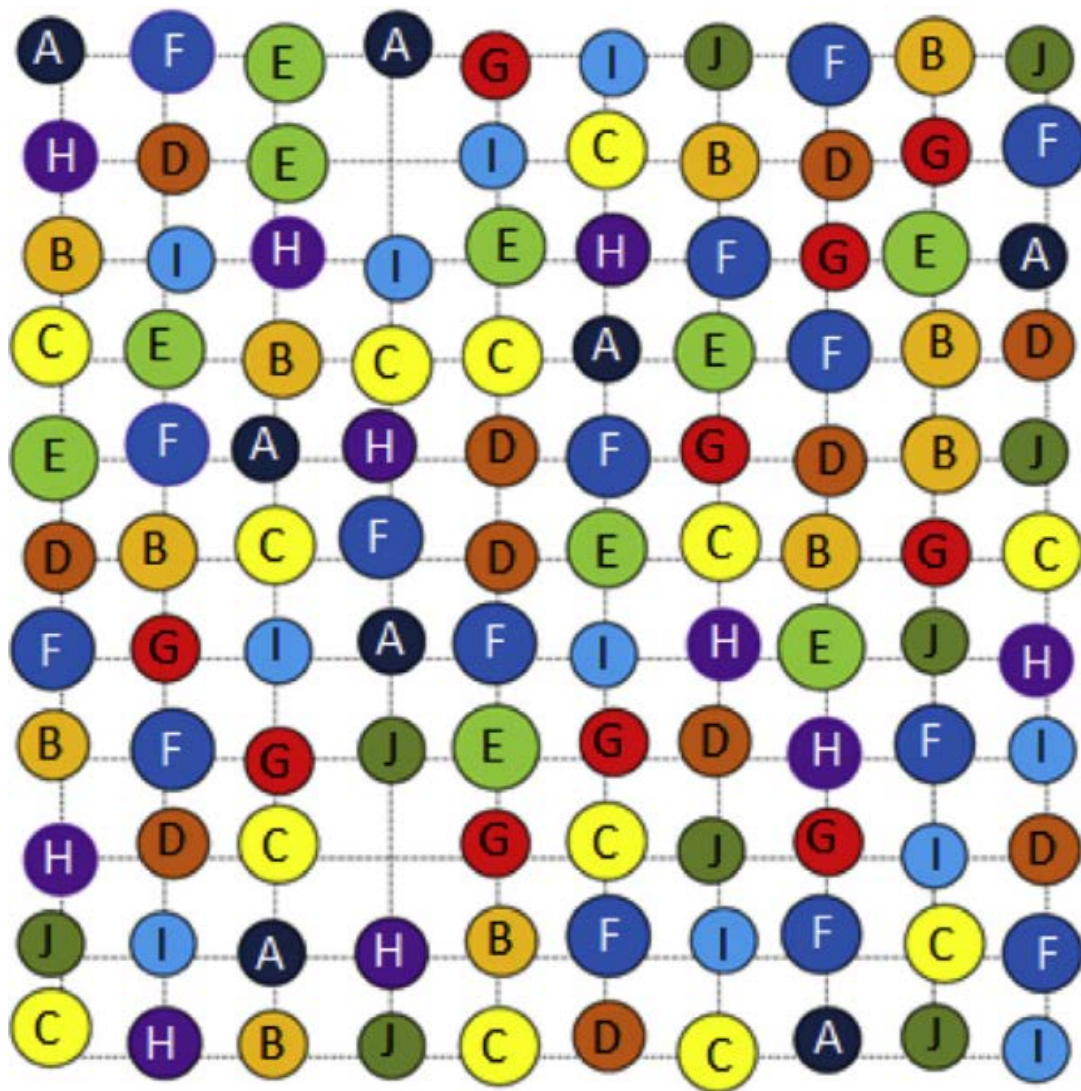
Fig.2.3: Two-dimensional matrix of a solid solution HEA with 10 different components. Two vacancies are also shown. Average lattice is shown by the dotted lines [3].

## 2.2.3 Sluggish diffusion effect

The diffusion of an atom in the whole-solute matrix of HEAs would be considerably more difficult as compared to that in the matrix of conventional alloys. Tsai et al [28] have carried out careful investigations on near-ideal solution system of CoCrFeMnNi to analyze the diffusion of each element in the matrix. The results show that the diffusion rate is decreasing in the order of Mn, Cr, Fe, Co, and Ni. The diffusion coefficients of different elements at the same homologous temperature ($T/T_m$) in the CoCrFeMnNi alloy system are much lower as compared to the corresponding figures in different FCC alloys. It is thus apparent that greater the diffusion rate is slowed down with increasing number of constituent elements. Fig.2.4 shows the normalized activation energies ($Q/T_m$) of the constituent elements in the CoCrFeMnNi HEA. The sluggish diffusion effect in the HEA is indicated by the much higher value of $Q/T_m$ of the constituent elements in the HEA as compared to those in the elemental state and other alloys systems. Slower diffusion and higher activation energy would occur in HEAs due to larger fluctuation of lattice potential energy (LPE) between lattice sites. The ample low-LPE sites can serve as traps and hinder the diffusion of atoms. This finally gives rise to the sluggish diffusion effect [28].

Liu et al [29] also found a significantly high value of activation energy ($\sim$321 kJ mol$^{-1}$) and slow grain growth kinetics of the CoCrFeMnNi HEA following cold-rolling and annealing, which is in excellent agreement with the sluggish diffusion effect. It is understood that sluggish diffusion plays an important role on the development of microstructure and properties of the HEAs. Sluggish diffusion assisted fine precipitation and microstructure development can improve the combination of strength and toughness of HEAs [30-32].
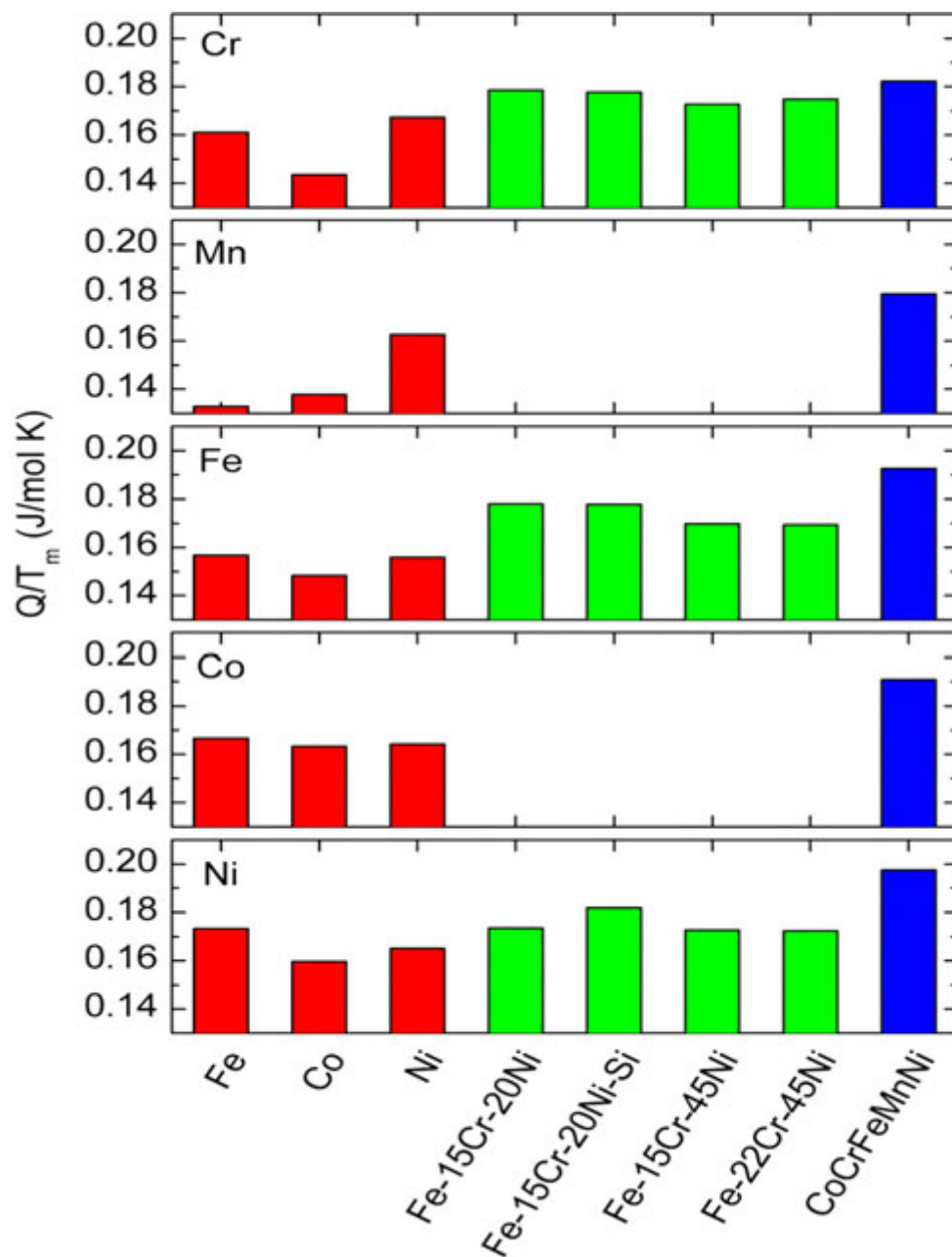
Fig.2.4: Melting-point normalized activation energy of diffusion for Cr, Fe, Mn, Co and Ni in different matrices [28].

## 2.2.4 Cocktail Effect

The concept of ''multimetallic cocktails'' has been introduced by Ranganathan [33]. For metallic alloys, the cocktail effect indicates that the unusual properties can be obtained after mixing many elements, which could not be obtained from any individual element. Similarly, in HEAs this cocktail effect is significant as all the constituent elements may be conceived as a principle elements (i.e. whole solute matrix). Subsequently, the end properties of the HEAs are determined by the overall contribution of the constituent elements including phase morphologies, phase distribution, phase boundaries, and properties of each phase. For example, interaction of constituent elements in the $Al_xCoCrCuFeAl$ alloy leads to a phase transformation from an FCC structure to a BCC when the Al content is increased beyond certain critical value (Fig.2.5) [3, 34].
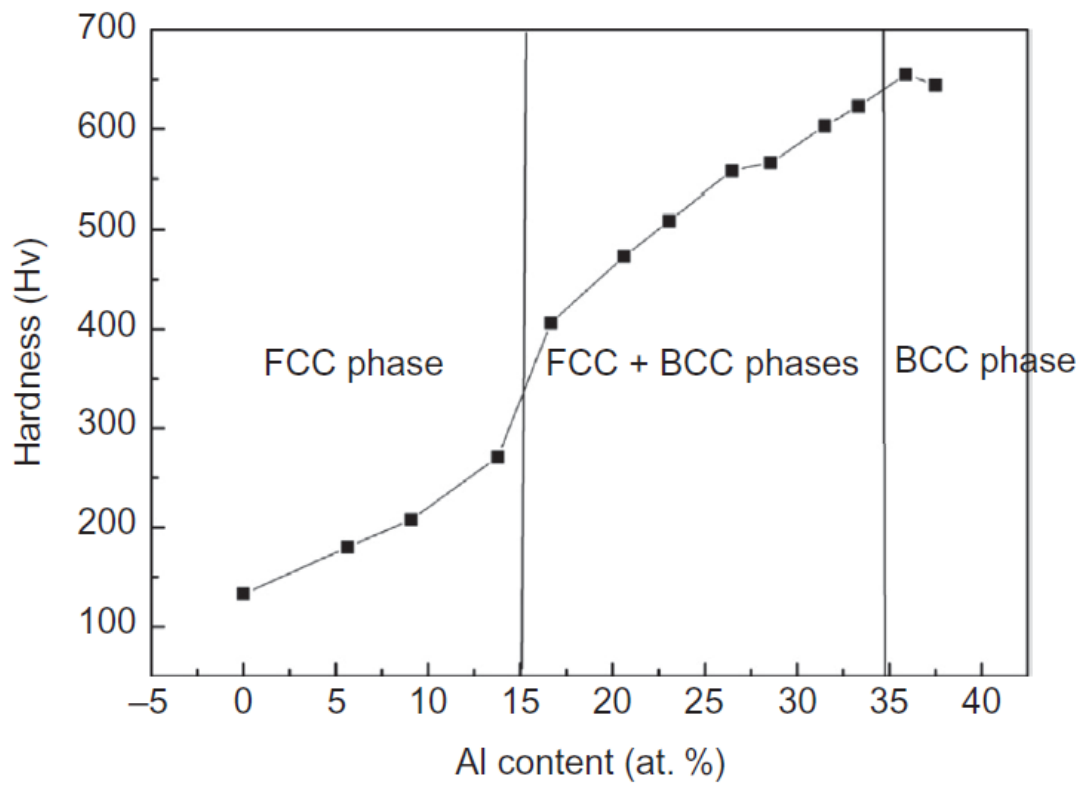
Fig.2.5: Cocktail effect introduced by the interaction of constituent elements in the $Al_xCoCrCuFeNi$ system [3].

## 2.3 Phase stability and phase selection criteria in HEAs

An important direction in the HEA research is to develop robust thermodynamic guiding principles for predicting the phase stability as a function of temperature and composition. From the classical Hume-Rothery rule two important parameters, namely atomic size difference (δ) and enthalpy of mixing (ΔH$_{mix}$) may be considered [35, 36]:

$$\delta = \sqrt{\Sigma_{i=1}^{N}(c_i(1 - r_i/(\Sigma_{i=1}^{n} c_i r_i))^2} \qquad (2.3)$$

$$\Delta H_{mix} = \Sigma_{i=1,i\neq j}^{N} 4\Delta H_{AB}^{mix} c_i c_j \qquad (2.4)$$

Where, $r_i$ is the atomic radius and $\Delta H_{AB}^{mix}$ is the enthalpy of mixing for the binary A and B elements. Fig.2.6 shows $\Delta H_{mix}$ plotted against δ [37]. It is clearly observed that $\Delta H_{mix}$ is decreased to more negative values with increasing δ. For the formation of random solid solution the $\Delta H_{mix}$ should be in the range -15 to 5 kJ mol$^{-1}$, while δ should be varying from 1% to 5%. This approach has been used by other authors which results in very similar observations (Fig.2.7) [38].

Zhang and Fu [39] has also developed quantitative phase formation rules based on the fundamental thermodynamic parameters. These authors have explored several HEA systems and the results are summarized in Fig.2.8. It may be noted that CoCrFeNiCu, CoCrFeNiMn, and CoCrFeNiV HEAs can form simple solid-solution phases as the $\Delta H_{mix}$ and δ values of these alloys approach zero. However, other alloys not following these conditions (i.e. not located at the upper left corner of Fig.2.8) may form random solid solution as well as other intermetallic compounds. The criteria for the formation of random solid solution alloys in HEAs should be that $\Delta H_{mix}$ and δ are located at the upper left corner satisfying the high entropy of mixing criteria. These may be summarized as follows:

$\Delta S_{mix}$ > 13.38 J/K mol, -10 < $\Delta H_{mix}$< 5 kJ mol$^{-1}$, and δ < 4%

It may recalled from the ΔG expression ($\Delta G = \Delta H - T\Delta S$) that $\Delta H_{mix}$ originate from interaction amongst the elements, so that for binary system A-B, $\Delta H_{AB}$ is -ve if A-B is attractive and +ve if they are repulsive. For a

multicomponent systems the $\Delta H_{mix}$ may be considered the average value. On the other hand the $-T\Delta S_{mix}$ term should decrease the total free energy free energy. Therefore, to realize the net effect a term $\Omega$ may be introduced such that:

$$\Omega = \frac{T_m \Delta S_{mix}}{|\Delta H_{mix}|} \qquad (2.5)$$

where $T_m$ is the average melting point.

$\Omega > 1$ implies that the entropy term dominates over the enthalpy at the melting temperature $(T_m)$, so that the high entropy phase formation is preferred. Fig.2.9 shows the $\Omega$-$\delta$ plot which indicates that high entropy solid solution phase formation is preferred when $\Omega \geq 1.1$ and $\delta \leq 6.6\%$. It is further observed that $\Omega$ and $\delta$ follow a hyperbolic relationship given by [40]

$$\delta \times Ln\Omega = \text{constant} \qquad (2.6)$$
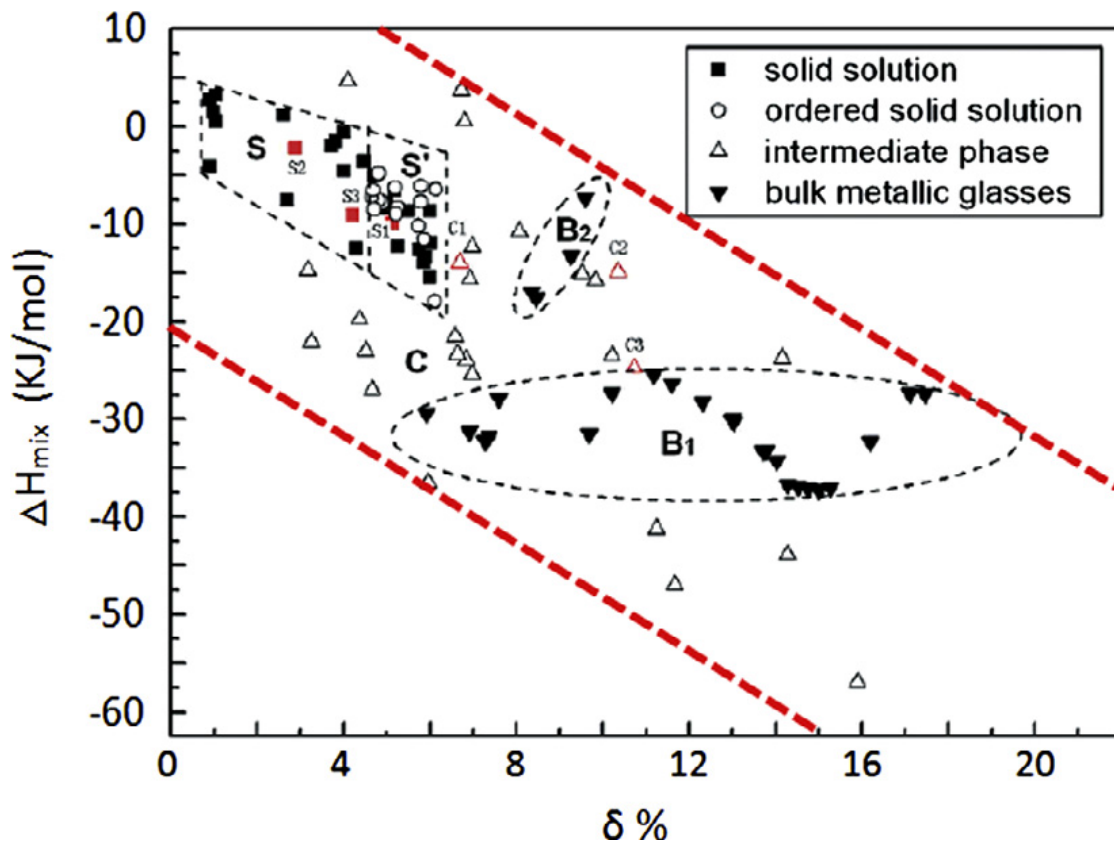
Fig.2.6: Phase stability map based on enthalpy of mixing ($\Delta H_{mix}$) and the atomic size difference (δ). The criteria for the formation of random solid solid solution are given by: -15 < $\Delta H_{mix}$ < 5 kJ mol$^{-1}$ and δ<5%. B1 and B2 are glass forming zones [37].
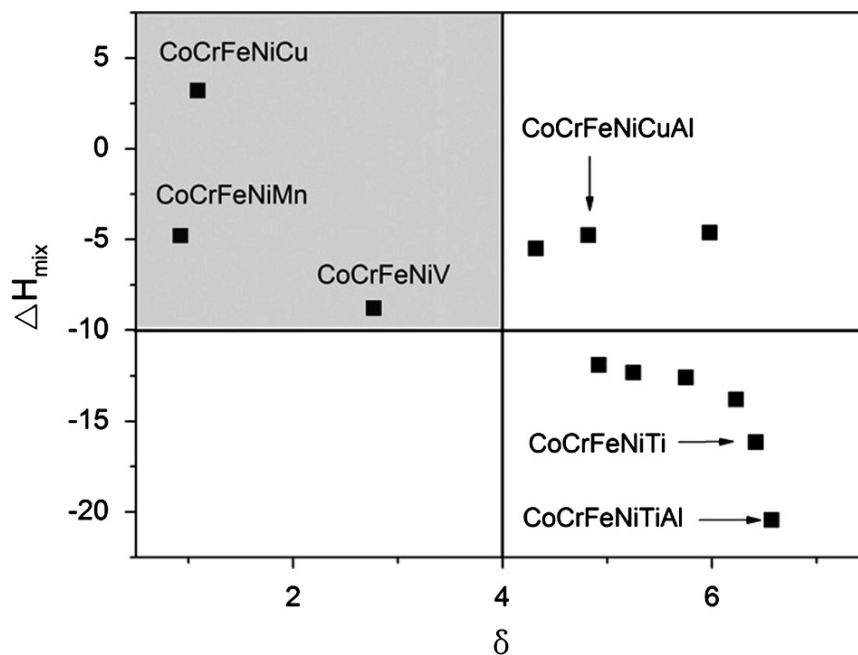
Fig.2.7: Relationship between $\Delta H_{mix}$ and δ values of some HEA systems [39]
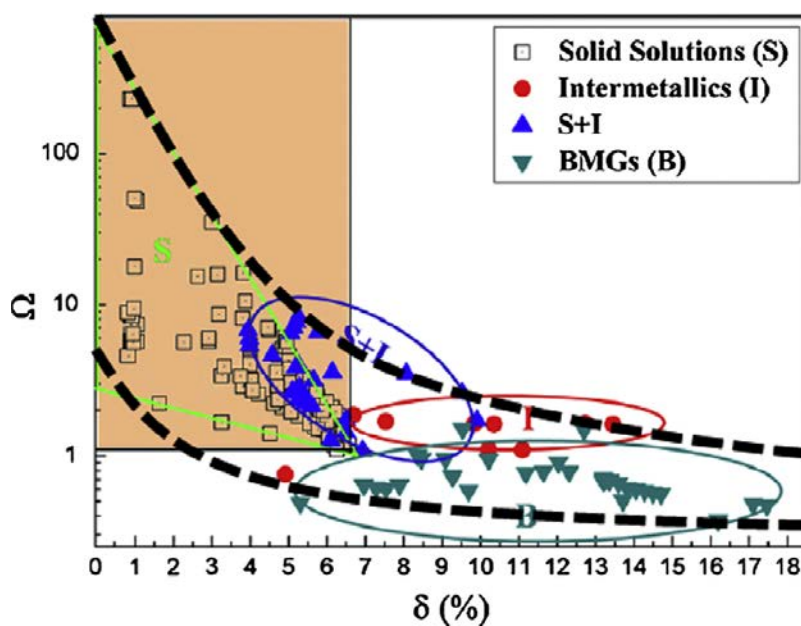


Fig.2.8: Phase-formation map based on the Ω and δ for the multi-component alloys. For the formation of solid-solutions, Ω > 1.1 and δ < 6.6%. The zone marked B and I indicate preference for the formation of BMGs and intermetallic compounds. A transition zone is noted where both the random solid solution and the intermetallic compound formation is preferred [40].

## 2.4 Thermo-mechanical processing of HEAs

Thermo-mechanical processing (TMP) of materials combining heavy deformation and thermal treatments can greatly enhance the properties of engineering materials. An area of prime interest in the HEA research is designing appropriate TMP routes for developing HEAs with enhanced properties. TMP can affect the development of microstructure and properties which in turn influence the properties of the processed materials. Therefore, understanding the microstructure and texture evolution during TMP is critical. Since the evolution of crystallographic texture during TMP is a key aspect and also a major focus of the present research, the following section would give a brief introduction to the fundamental principles of texture analysis of materials. This will be followed by a critical review of the present state of knowledge on the TMP processing of HEAs in order to place the objective of the present research in the most appropriate context.

### *2.4.1 Representation and development of texture*

TMP of polycrystalline materials usually leads to the development of preferred orientations or crystallographic texture. The crystallographic texture is described with respect to a fixed reference frame. In case of rolling deformation the three principal directions defined by the normal direction (ND), transverse direction (TD) and rolling direction (RD) constitute the reference frame. Therefore, for rolled sheets, the crystallographic texture components may be described as ideal orientation {hkl} <uvw>, where the {hkl} set of planes are parallel to the rolling plane (or the <hkl> directions are parallel to the ND for cubic systems) and <uvw> set of directions are parallel to the RD.

Amongst several methods of representing texture, pole figure (PF) and orientation distribution function (ODFs) are particularly popular. PFs are basically 2D stereographic projections which show the distribution of poles (or plane normal) with respect to the sample reference system. The basic principles of projection is shown in the Fig.2.9 where the {100} poles of a cubic crystal are projected with respect to the sample reference system (for

rolling deformation geometry). Fig.2.9(a) shows the crystal in the unit sphere whose {100} poles are projected onto the equatorial plane (Fig. 2.9(b)). Fig.2.9(c) shows the {100} PF and definition of the radial and azimuthal angles $\alpha$ and $\beta$, respectively for the {100} poles.

Although, PFs are simple ways of representing texture, they suffer from inherently qualitative or semi-quantitative nature [41]. Thus, analysis of PFs may be quite difficult for complex textures. In these cases, analysis of ODFs yields more detailed and satisfactory results. ODFs are basically 3-D representation of texture and provides the frequency of appearance of any given orientation or texture component in the Euler space. The Euler space is represented by three mutually orthogonal axes defined by a set of three Euler angles $\varphi_1$, $\Phi$, $\varphi_2$. These set of Euler angles constitute a scheme of three consecutive rotations for coinciding the sample frame (S) into crystal frame (C) as shown in Fig.2.10. Thus, each orientation given by {hkl}<uvw> notation would correspond to a set of Euler angles $\varphi_1$, $\Phi$, $\varphi_2$ and should occupy a point in the 3-D Euler space. Depending on the crystal and sample symmetries, the Euler space can be reduced. For example the Euler space is reduced to $0° \leq \varphi_1 \leq 90°$, $0° \leq \Phi \leq 90°$ and $0° \leq \varphi_2 \leq 90°$ for cubic crystal structure and orthorhombic sample symmetry (Fig.2.11). As it is difficult to understand the ODFs in three dimensional space, they are conveniently represented in two dimensional space using constant sections along one of the Euler angles in steps of 5°. For FCC materials ODF is represented in the constant $\varphi_2$ sections [42], whereas for body centered cubic (BCC) materials constant $\varphi_1$ sections are used for representation of texture [43].

(a)    (b)    (c)
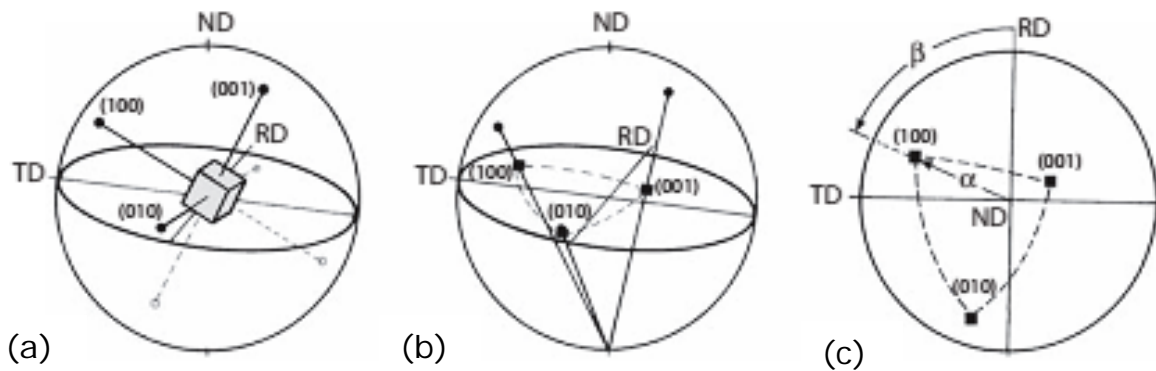
Fig.2.9: Representation of the {100} poles of a cubic crystal in the stereographic projection. (a) Crystal in the unit sphere, (b) projection of the {100} poles onto the equator plane, (c) {100} pole figure and definition of the pole figure angles α and β [41].

Specimen frame                     Crystalline frame

(a)



(b)

- A first rotation $\varphi_1$ around the normal direction ND transforming the transverse direction TD and the rolling direction RD into the new directions TD' and RD', respectively. $\varphi_1$ has to have such a value that RD' will be perpendicular to the plane formed by ND and [001].
- A second rotation $\phi$ around the new direction RD' with $\phi$ having such a value that ND is transformed into [001]] (=ND') and TD' into TD".
- A third rotation $\varphi_2$ around [00] (=ND') with $\varphi_2$ having such a value that RD' is transformed into [100] and TD" into [010].

Fig. 2.10: Schematic illustration of (a) reference system and (b) Euler angles [44].

Fig.2.11: Schematic representation of the three dimensional Euler space [45].

ODFs are generated from several experimentally measured PFs using diverse mathematical methods. Most widely accepted methods are developed independently by Bunge [46] and Roe [47] who have used generalized spherical harmonic functions for this purpose. A detailed analysis of the mathematical treatments for ODF calculation can be found elsewhere [48, 49].

Texture can also be conveniently represented in certain cases by plotting the orientation densities along certain characteristic paths or distinct crystallographic fibers [42]. In heavily rolled FCC materials texture is characterized by two important fibers i.e. α and β-fibers. The α-fiber ({011}//ND) extends from the Goss or G ({011}<100>) to the brass or $B_S$ ({011}<112>) orientation while the β fiber runs from the copper or Cu ({112}<111>) to the brass or $B_S$ ({011}<112>) through the S ({123}<634>) orientation. Fig.2.12 illustrates the positions of the texture fibers along with the main rolling texture components of FCC materials in the Euler space and Fig.2.13 indicates their ideal locations in the constant $\varphi_2$ sections.

The cold-rolling texture of FCC materials strongly depends on the stacking fault energy (SFE). Medium to high SFE FCC materials develop pure metal or copper type rolling texture characterized by the presence of strong Cu, S and $B_S$ components. In contrast, low SFE FCC materials develop predominantly brass type rolling texture characterized by the presence of stronger $B_S$ component [50]. The transition of texture from pure metal to brass type texture (Fig.2.13) has remained a classical topic in texture research [51]. This transition of texture has been interpreted by Wasserman in terms of the volume effect of deformation twins [52].
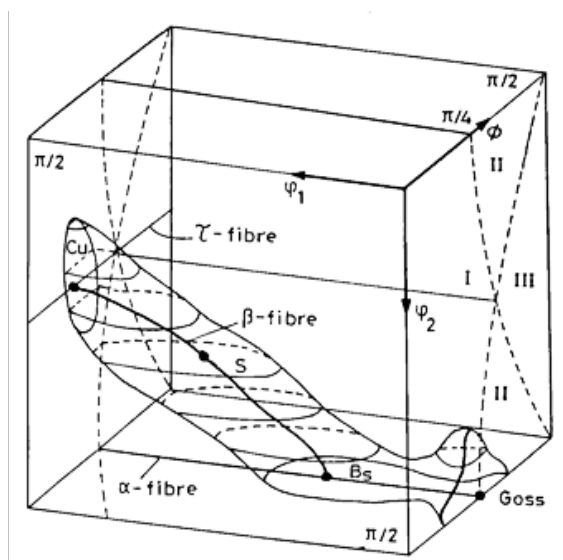
Fig.2.12: Three dimensional view of Euler space with locations of some important ideal orientations and texture fibres in FCC metals [42].
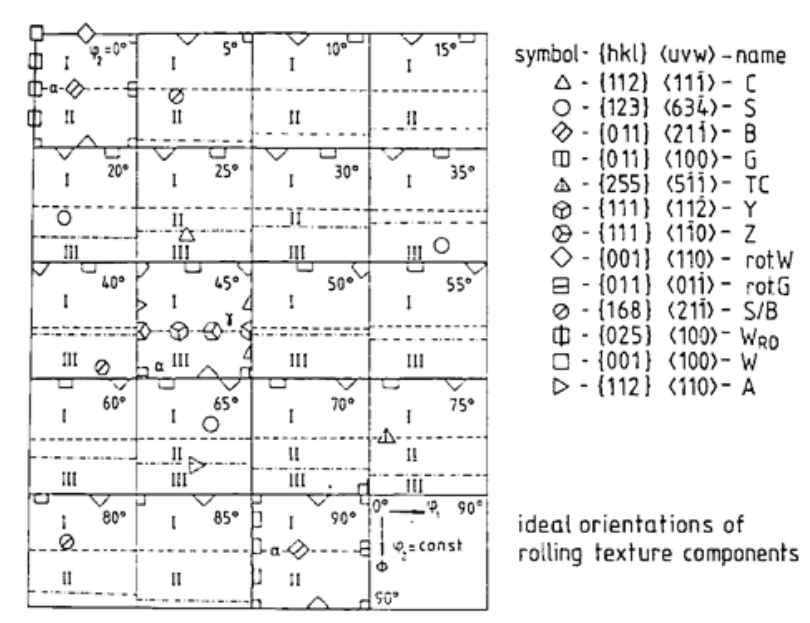


Fig.2.13: Several prominent orientations of FCC materials are shown in the constant $\varphi_2$ sections of the ODF [42].

According to this hypothesis the deformation twins forming at a later stage reorients the Cu oriented regions to {552}<115> oriented regions which finally reorient to the $B_S$ orientation. However, other researchers have negated the volume effect of deformation twins proposed by Wasserman in favor of the latent hardening effect of deformation twins [51].

The recrystallization texture of medium to high SFE FCC materials are characterized by the development of a sharp cube texture ({001}<100>). The origin of such sharp cube texture has been intensely debated [53, 54]. Two competing theories, namely oriented nucleation (ON) and oriented growth (OG) have been proposed. According to the ON theory the development of sharp cube texture is attributed to the preferential nucleation of cube oriented regions (cube bands) existing in the deformed matrix (frequency advantage). In contrast, the development of sharp cube texture is attributed to the preferential growth of cube grains due to high mobility misorientation relationship (e.g. 40°<111>) with a major component of the deformation texture.

The recrystallization textures of low SFE FCC material appear to be more complicated. 70:30 brass has been used as a model alloy in the past to understand the recrystallization texture of low SFE materials. Development of brass recrystallization component e.g. {236}<385> has been reported by several authors. The development of this component has been explained on the basis of preferential nucleation at shear bands followed by preferential growth [50]. However, detailed studies have shown rather complex dependence of strength of this component on the processing parameters including deformation level, prior grain size, annealing temperature and time [50]. The relevant results are summarized in Table 2.3.

Table.2.2: Effect of processing parameters on the evolution of annealing texture components in 70:30 brass [50].

| Effect of deformation level, prior grain size and annealing temperature | Texture components | | | |
|---|---|---|---|---|
| | Medium to heavy cold-rolling (~87-92%) | | Severe cold-rolling (≥95%) | |
| | Low temperature annealing (300°C(1hr)) | High temperature annealing (600°C(1hr)) | Low temperature annealing (300°C(1hr)) | High temperature annealing (600°C(1hr)) |
| Fine grained starting material (30 μm) [55] | {236}<385> | {110}<112> | {236}<385> | {113}<332> |
| Medium grained starting material (100 μm) [56] | Random | Brass-Goss (α-fiber) | {236}<385> | Brass-S, ND rotated cube |
| Coarse grained starting material (3000 μm) [55] | {110}<110> | {110}<112> | {236}<385> | {113}<332> |

## 2.4.2 Deformation and recrystallization behavior of the HEAs

Several studies have been carried out on microstructure and properties of HEAs. A critical review of the available literature suggests that majority of the early investigations have focused on hardness and compressive properties of as-cast HEAs at ambient and high temperatures [25, 57-66]. Overall, it has been observed that FCC structured HEAs show lower strength and higher ductility as compared to BCC HEAs. For example, the yield strength of FCC CoCrCuFeNiTi$_x$ ~ 300 MPa can be enhanced to ~3000 MPa in BCC structured AlCoCrCuFeNiTi$_x$ system [25, 67]. In addition, effects of different microalloying [25, 58, 68, 69] and cooling rate in enhancing the properties of HEAs have also been demonstrated [70].

Understanding the evolution of microstructure and properties during deformation and annealing has gained considerable momentum recently. The equiatomic CoCrFeMnNi with stable FCC structure has been used by several researchers for this purpose.

The microstructural evolution in CoCrFeMnNi alloy during heavy cold (Fig.2.14) and cryo-rolling (Fig.2.15) has been reported by Stepanov et al [71]. These authors have shown presence of extensive nano-twins in both cryo and cold-rolled materials. However, greater propensity for nano-twin formation is found during cryo-rolling as compared to cold-rolling (Fig.2.15). This leads to significantly faster microstructural evolution in the cryo-rolling route. This behavior is found consistent with other low SFE alloys in which formation of deformation twins is found to be an important deformation mechanism in addition to slip [72].

Otto et al [73] have studied the tensile deformation behavior of fine and coarse grained CoCrFeMnNi alloy at temperatures ranging from (-°C) 77 K to 1073 K (-°C). The development of deformation microstructure, particularly at the cryogenic temperature is characterized by the formation of extensive deformation nano-twins (Fig.2.16). Extensive deformation twinning results in increased work-hardening rate and remarkable

enhancement in strength, ductility at cryogenic temperatures for both coarse and fine grained materials (Fig.2.17) [73]. Excellent fracture toughness observed at cryogenic conditions is also attributed to the propensity for the formation of deformation nano-twins [74]. The extensive nano-twin formation has also been confirmed in C-containing CoCrFeMnNi HEA [75].

Therefore, formation of deformation nano-twins may be considered as a major feature of the deformation behavior of CoCrFeMnNi HEA which indicates the low SFE of this alloy. This is supported by recent report on experimentally and theoretically determined SFE of this alloy [76, 77].

The recrystallization and grain growth behavior of cold-rolled CoCrFeMnNi HEA has been reported recently by Liu et al [29]. The alloy is cold-rolled to 70% reduction in thickness and annealed at temperatures ranging from 850°C to 950°C. A fine recrystallized grain size (~4 μm) is observed after complete recrystallization at 850°C. Remarkable resistance to grain growth is manifested by rather high activation energy for grain growth (~321 kJ mol$^{-1}$) in this alloy. The high activation energy for grain growth is found to be in good agreement with the sluggish diffusion behavior reported in this system [28] and already highlighted as a core effect in HEAs. Very recently the evolution of a fine recrystallized microstructure after heavy deformation (~90% reduction in thickness) has been reported in other HEAs [78].

Otto et al [79] have also investigated the microstructure and grain boundary character evolution during recrystallization and grain growth. These authors have reported a linear dependence of twin fraction on grain size. The high activation energy for grain growth has also been confirmed by these authors.

The microstructure evolution in CoCrFeMnNi HEA during recovery, recrystallization and grain growth has been compared with pure Ni and a series of binary (Fe-Ni and Ni-Co), ternary (CoFeNi, FeNiCr, FeMnNi, CoNiCr, and CoMnNi) and quarternary (CoFeNiCr, CoFeMnNi and CoMnNiCr) systems developed based on the constituent components [80]. The quinary CoCrFeMnNi shows excellent phase stability and absence of abnormal grain growth which is found to occur in pure Ni and selected ternary alloys.

The deformation and annealing behavior of CoCrFeMnNi processed by high pressure torsion (HPT) to a very large strain has been reported recently. The alloy shows formation of ultrafine to nanostructure and excellent phase stability during HPT. However, transformation during annealing is observed which is attributed to faster kinetics due to the presence of nanostructure [81].

The dynamic recrystallization behavior and microstructure evolution during TMP by hot deformation of CoCrFeMnNi has recently been investigated by Stepanov et al [82] over a wide temperature range. These authors have reported the formation of dynamically recrystallized ultrafine grains (~0.2 μm) and activation energy for hot deformation comparable with that reported for grain growth [29].
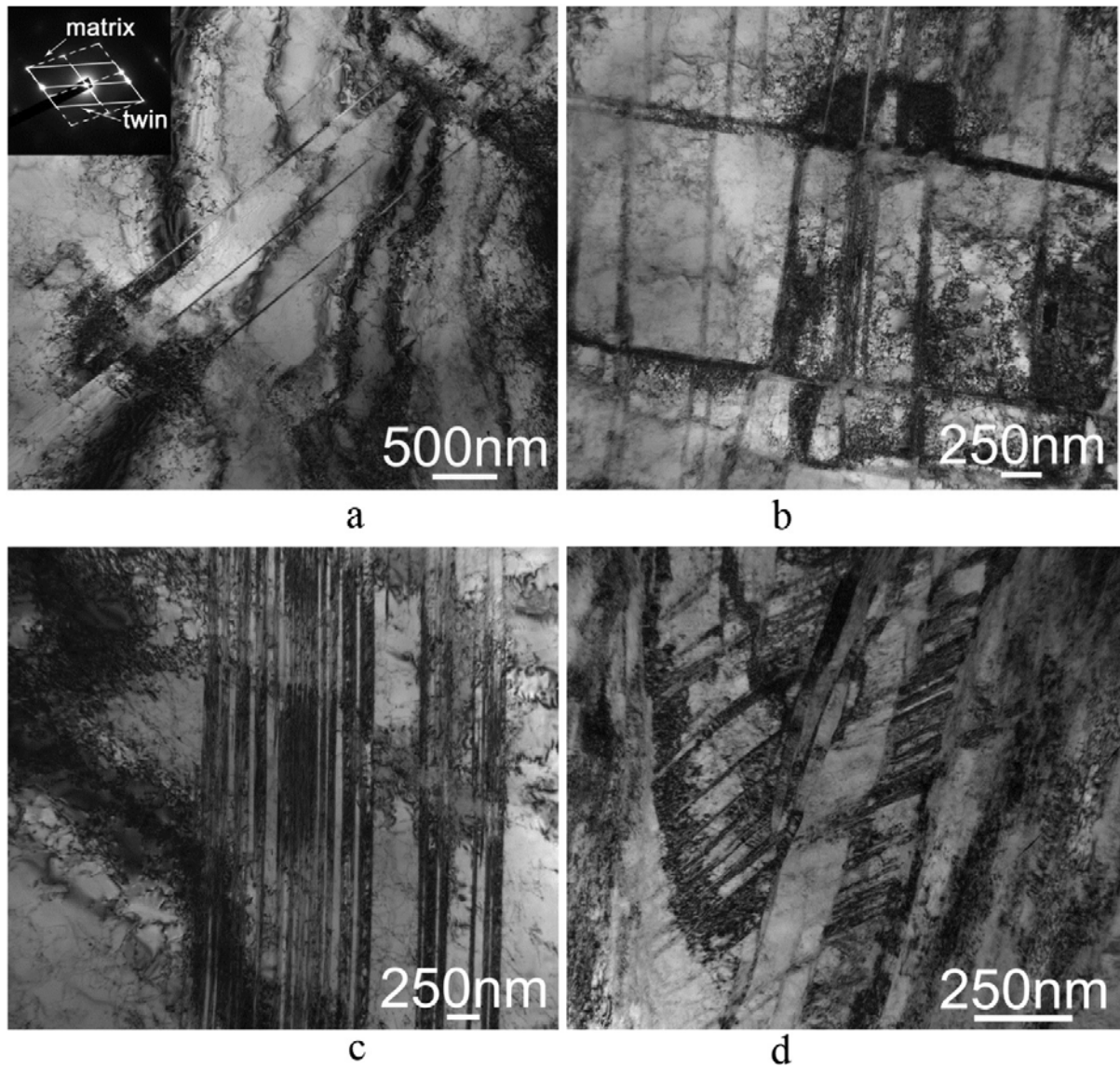
Fig.2.14: Bright-field TEM images of microstructure of the transversal plane of cold-rolled CoCrFeNiMn after (a) 5% (b) 25% (c) 40% and (d) 80% reduction in thickness [82].
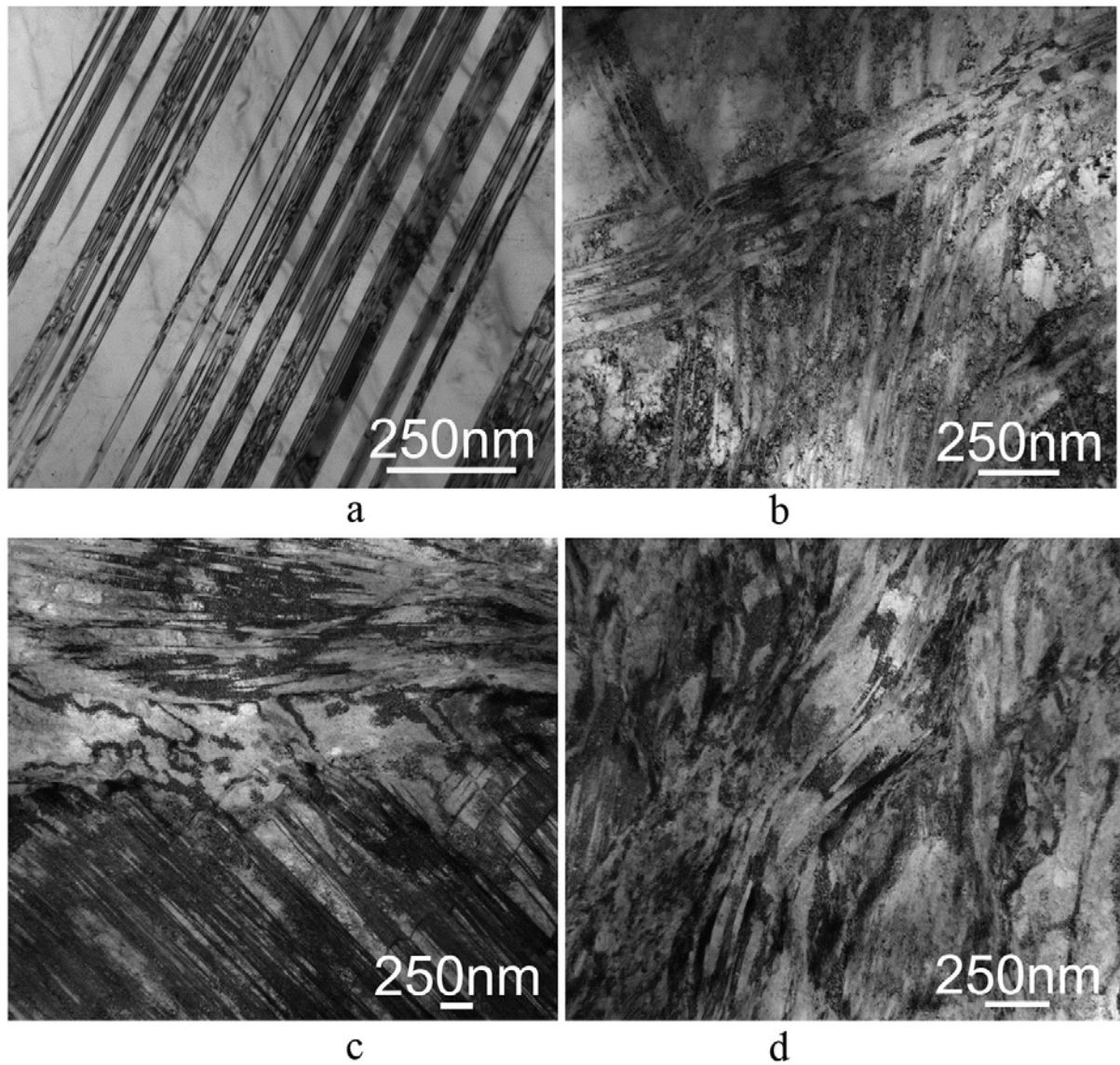
Fig.2.15: Bright-field TEM images of microstructure of the transversal plane of cryo-rolled CoCrFeNiMn after (a) 5% (b) 25% (c) 40% and (d) 80% reduction in thickness [82].
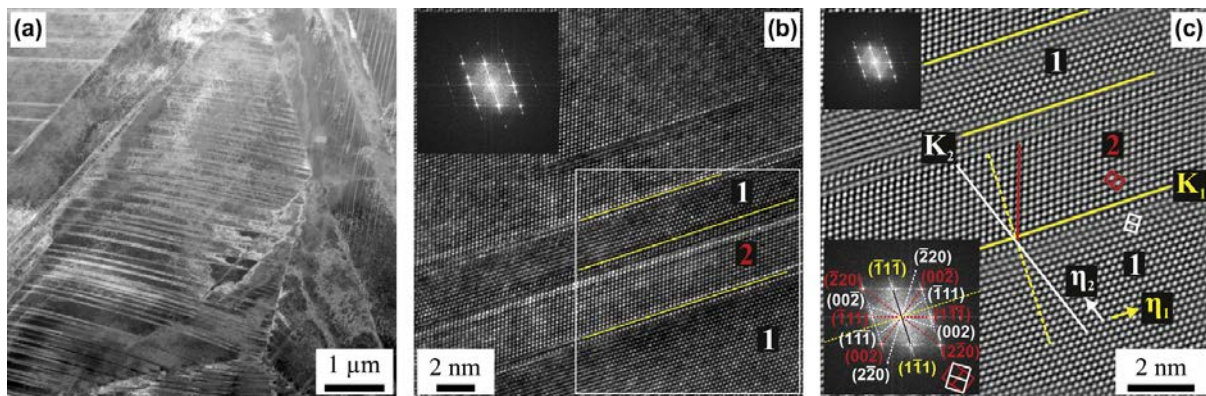
Fig.2.16: TEM micrographs showing deformation twins in a fine-grained CoCrFeMnNi alloy (grain size 4.4 µm) after a strain of 20.2% at 77 K. (a) The twinned microstructure is acquired in the HAADF mode. (b) High-resolution TEM image of twins denoted "1" and "2", with the corresponding FFT inset. (c) FFT-filtered image of the area outlined by the white square in (b) showing the corresponding twinning elements. The inset in the lower left corner of (c) shows the fully indexed intensity maxima in reciprocal space[73].
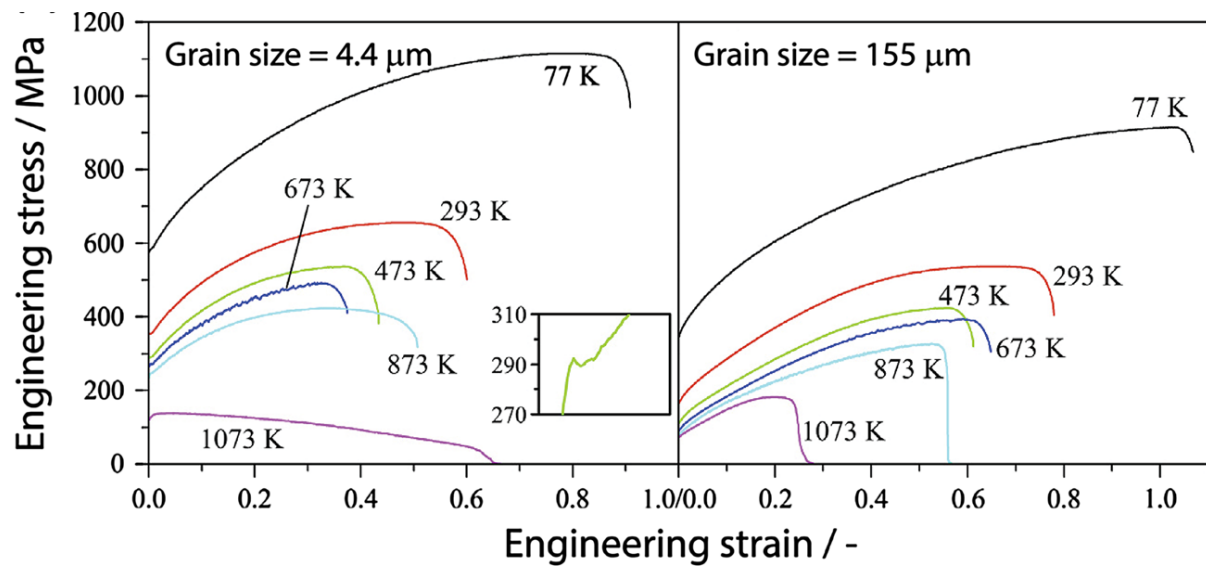
Fig.2.17: Engineering stress–strain curves of the CoCrFeMnNi alloy at the different testing temperatures for the fine-grained (grain size 4.4 μm) and coarse-grained (grain size 155 μm) materials [73].

## 2.5 Objectives and scope of the present work

The brief but critical and up-to-date literature review is presented here which suggests that the behavior of HEAs during TMP has been studied only to a limited extent. In particular, the evolution of texture after heavy cold-rolling and annealing has not been reported till date. This is surprising considering that understanding the evolution of texture during deformation and annealing can considerably help in tailoring the properties of the HEAs. Therefore, the systematic understanding of the evolution of texture due to heavy cold-rolling and annealing remains the focus of the present research. This also constitutes the prime novelty of this work.

The equiatomic CoCrFeMnNi having stable FCC structure has been used a model system in the present research. The effect of various processing parameters including strain, starting grain size and cryo-rolling has been systematically investigated. In addition, the evolution of texture during TMP has been appropriately compared and contrasted to highlight and understand the differences. It is envisaged that appropriate understanding of the evolution of texture in the experimental CoCrFeMnNi HEA would also be helpful for gaining insights into the texture formation behavior of other FCC single phase HEAs or multiphase HEAs having FCC as the major phase.

# -: CHAPTER 3 :-

# *Experimental*

## 3.1 Alloy preparation

The experimental equiatomic CoCrFeMnNi alloy for the present study was received from the department of Materials science and Engineering, National Tsing Hua University, Taiwan. It was prepared by vacuum arc melting technique from the mixture of elements with purities higher than 99.9%. A small excess amount of Mn was added to compensate for the loss during arc melting. The cast slabs were remelted three times. The as-cast slabs having dimensions of 40mm (length) × 20mm (width) × 10mm (thickness) (Fig.3.1) were homogenized for 6 hours (hrs) at 1100°C to enhance the chemical homogeneity.

## 3.2 Initial cold-rolling

Rectangular samples (40 mm length × 20 mm width × 5 mm thickness) were obtained from the homogenized slabs. In order to breakdown the cast structure, the homogenized pieces were cold-rolled to 50% reduction in thickness (corresponding to ~ 2.5 mm thickness) using a laboratory scale rolling equipment having 140 mm diameter rolls (SPX precision instruments, Fenn Division, USA). A constant rolling speed of 2 m min$^{-1}$ was maintained throughout this research work.

## 3.3 Thermo-mechanical processing

The effect of three different processing parameters was investigated namely cold-rolling strain, initial grain size and cryo-rolling. For this purpose the 50% cold-rolled samples (thickness ~2.5 mm) were annealed in a salt bath furnace at different temperatures and for different time intervals to prepare different recrystallized microstructure.

### 3.3.1 Effect of strain

The 50% cold-rolled samples (thickness ~2.5 mm) were annealed at 800°C for 1h. These fully recrystallized samples were subsequently cold-rolled up to 95% reduction in thickness (corresponding to a thickness of ~0.125 mm). The cold-rolling was carried out in steps of 20% reduction in each pass (with respect to the starting thickness of ~ 2.5 mm) up to 80%

Fig. 3.1: As-received homogenized slab of the CoCrFeMnNi HEA used in the present research.

reduction in thickness. Beyond this, the rolling was carried out using small incremental deformation in each pass. The deformation up to 90% deformation was achieved in three additional passes. Further 3-4 passes were needed to achieve 95% reduction in thickness. Thus, ~10-11 passes were used for achieving the desired 95% reduction in thickness.

Small samples were obtained from the 60%, 80% and 95% cold-rolled materials. These cold-rolled samples were isochronally annealed for 1 h at temperature ranging from 650°C to 1200°C. The annealed samples were immediately quenched in cold-water after the annealing treatments. In order to understand the early recrystallization behavior few samples were subjected to partial recrystallization treatment at 700°C for 60 seconds. In this case also, the heat treatment was followed by quenching in cold-water. The experimental procedure is summarized in the flowchart given in Fig. 3.2.

### 3.3.2 Effect of Initial grain size

The 50% cold-rolled samples were subjected to two different annealing treatments. A set of samples were annealed at 800°C for 1 h and the other set of samples were annealed at 1200°C for 6 hrs. This resulted in widely different recrystallized grain size in the two set of materials. The fine grained and and coarse grained starting materials (FGSM and CGSM, respectively) were cold-rolled up to 95% reduction in thickness (following the quite similar multi-pass rolling schedule described in section 3.4.1). Small samples were extracted from the cold-rolled sheets and were isochronally annealed for 1 h at temperature ranging from 700°C to 1200°C. The samples were immediately quenched in cold-water following the annealing treatments. The experimental procedure is summarized in the flowchart given in Fig. 3.3.

```
┌─────────────────────────────────────────────────────┐
│                 Starting as-cast slab                 │
└─────────────────────────────────────────────────────┘
                          ⇓
┌─────────────────────────────────────────────────────┐
│            Homogenized at 1100°C for 6 hrs            │
│  40 mm (length) × 20 mm (width) × 5 mm (thickness)   │
└─────────────────────────────────────────────────────┘
                          ⇓
┌─────────────────────────────────────────────────────┐
│         Cold-rolling to 50% reduction (2.5 mm)       │
└─────────────────────────────────────────────────────┘
                          ⇓
┌─────────────────────────────────────────────────────┐
│               Annealed at 800°C for 1 h              │
│ (Starting materials for subsequent thermo-mechanical │
│                     processing)                       │
└─────────────────────────────────────────────────────┘
                          ⇓
┌─────────────────────────────────────────────────────┐
│ Cold-rolled to 60% (1 mm), 80% (0.5 mm) and 95%      │
│        (0.12 mm) reduction in thickness              │
└─────────────────────────────────────────────────────┘
                          ⇓
┌─────────────────────────────────────────────────────┐
│ Isochronally annealed at temperatures ranging between│
│              650°C to 1200°C for 1 h                  │
└─────────────────────────────────────────────────────┘
                          ⇓
┌─────────────────────────────────────────────────────┐
│ Microstructural and textural characterization using  │
│                    SEM-EBSD                           │
└─────────────────────────────────────────────────────┘
```

Fig.3.2: Flow diagram for investigating the effect of strain on microstructure and texture evolution in the HEA during thermo-mechanical processing.

```
┌─────────────────────────────────────────┐
│          Starting as-cast slab            │
└─────────────────────────────────────────┘
                    ⇓
┌─────────────────────────────────────────┐
│       Homogenized at 1100°C for 6 hrs     │
│ 40 mm (length) × 20 mm (width) × 5 mm (thickness) │
└─────────────────────────────────────────┘
                    ⇓
┌─────────────────────────────────────────┐
│ Cold-rolling to 50% reduction in thickness (~ 2.5 mm) │
└─────────────────────────────────────────┘
          ⇓                         ⇓
┌──────────────────────┐   ┌──────────────────────┐
│ Annealed at 800°C for 1 h │   │ Annealed at 1200°C for 6 hrs │
│        (FGSM)         │   │        (CGSM)         │
└──────────────────────┘   └──────────────────────┘
          ⇓                         ⇓
┌─────────────────────────────────────────┐
│ Cold-rolled up to 95% reduction in thickness (~ 0.12 mm) │
└─────────────────────────────────────────┘
                    ⇓
┌─────────────────────────────────────────┐
│ Isochronally annealed at temperatures ranging between 700°C to │
│                 1200°C for 1 h            │
└─────────────────────────────────────────┘
                    ⇓
┌─────────────────────────────────────────┐
│ Microstructural and textural characterization using SEM-EBSD │
└─────────────────────────────────────────┘
```
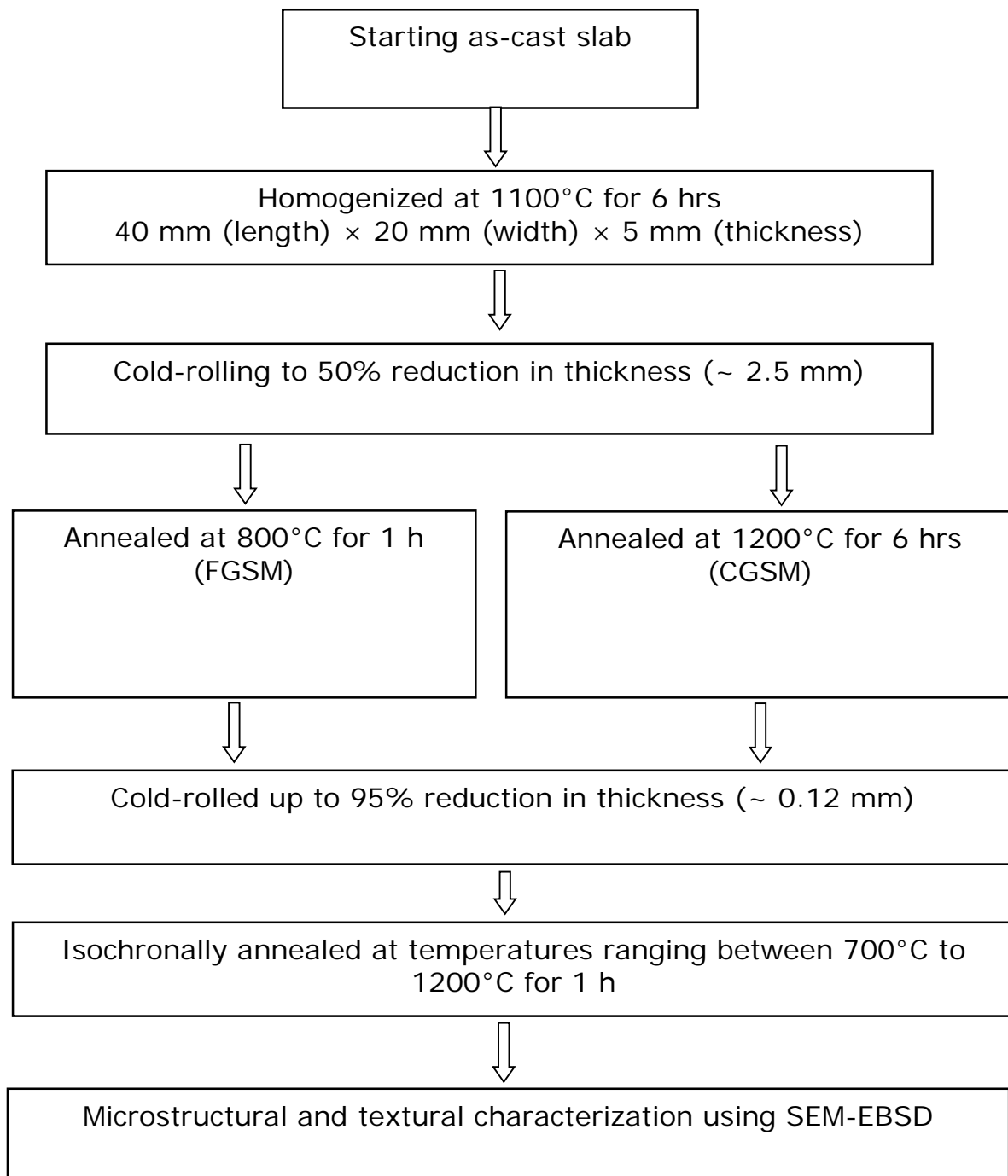
Fig.3.3: Flow diagram for investigating the effect of starting grain size on microstructure and texture evolution in the HEA during thermo-mechanical processing.

### 3.3.3 Effect of processing temperature

The effect of processing temperature was investigated by investigating the microstructure and texture evolution during cryo-rolling and subsequent annealing. For this purpose the 50% cold-rolled samples (thickness ~ 2.5 mm) were annealed at 800°C for 1 h. The fully recrystallized samples were cryo-rolled at liquid $N_2$ temperature. For the purpose of cryo-rolling, the samples were immersed in a liquid $N_2$ bath for 30 minutes before each pass. The cryo-rolled samples emerging from the exit side of the rolls were immediately transferred to the liquid $N_2$ bath. The cryo-rolling was carried up to 90% reduction in thickness following the quite similar deformation schedule described in section 3.3.1.

Rectangular samples were cut from the 90% cryo-rolled material and isochronally annealed at temperatures ranging from 700°C to 1200°C for 1 h. The annealed samples were quenched in cold-water after the heat treatments. The experimental procedure is summarized in the flowchart given in Fig. 3.4.

```
┌─────────────────────────────────────────┐
│            Starting as-cast slab          │
└─────────────────────────────────────────┘
                    ⇓
┌─────────────────────────────────────────┐
│        Homogenized at 1100°C for 6 hour   │
│  40 mm (length) × 20 mm (width) × 5 mm (thickness) │
└─────────────────────────────────────────┘
                    ⇓
┌─────────────────────────────────────────┐
│     Further cold-rolling to 50% reduction (2.5 mm) │
└─────────────────────────────────────────┘
                    ⇓
┌─────────────────────────────────────────┐
│            Annealed at 800°C for 1 h      │
└─────────────────────────────────────────┘
                    ⇓
┌─────────────────────────────────────────┐
│   Cryo-rolled to 90% (0.25 mm) reduction in thickness │
│ (samples were immersed in liquid N₂ bath for 30 minutes before each │
│                      pass)                 │
└─────────────────────────────────────────┘
                    ⇓
┌─────────────────────────────────────────┐
│  Isochronally annealed at temperatures ranging between 700°C to │
│                  1200°C for 1 h            │
└─────────────────────────────────────────┘
                    ⇓
┌─────────────────────────────────────────┐
│  Microstructural and textural characterization using SEM-EBSD │
└─────────────────────────────────────────┘
```

Fig.3.4: Flow diagram for investigating the effect of cryo-rolling on microstructure and texture evolution in the HEA during thermo-mechanical processing.

### 3.3.4 Thermo-mechanical processing of low SFE Ni-60 wt.%Co alloy

It is conceived to be important to clearly elucidate the thermo-mechanical processing behavior of the HEA with respect to other low SFE materials. For this purpose, Ni-60wt.%Co alloy was considered as a model low SFE alloy and microstructure and texture evolution during thermo-mechanical processing was investigated.

The Ni-60%Co alloy was procured from Testbourne Pvt. Ltd., U.K in the form of hot-rolled plates. Rectangular samples with dimensions of 50 mm (length) × 20 mm (Width) × 5 mm (thickness) were cut from the rolled plate and were subjected to multi-pass cold-rolling to ~ 50% reduction in thickness. The cold-rolled plates were subsequently annealed at 650°C for 10 minutes. These fully annealed samples were used as the starting materials for subsequent cold-rolling at room temperature up to 90% reduction in thickness (~ 0.25 mm). The same multi-pass rolling schedule was followed as discussed above for HEA.

Rectangular samples were cut from the 90% cold-rolled sheets and annealed in a salt bath furnace at temperature ranging from 700°C to 1000°C for 1h. The annealed samples were immediately quenched in cold-water. The processing steps could be summarized in Fig 3.5.

```
┌─────────────────────────────────────────────────────────────┐
│            Hot rolled slab (As received condition)            │
│   50 mm (length) × 20 mm (width) × 5 mm (thickness)           │
└─────────────────────────────────────────────────────────────┘
                              ⇩
┌─────────────────────────────────────────────────────────────┐
│      Cold-rolling to 50% reduction (thickness ~2.5 mm)        │
└─────────────────────────────────────────────────────────────┘
                              ⇩
┌─────────────────────────────────────────────────────────────┐
│            Annealed at 650°C for 10 minutes                   │
└─────────────────────────────────────────────────────────────┘
                              ⇩
┌─────────────────────────────────────────────────────────────┐
│    Cold-rolled to 90% reduction in thickness (~0.25 mm)       │
└─────────────────────────────────────────────────────────────┘
                              ⇩
┌─────────────────────────────────────────────────────────────┐
│  Isochronally annealed at temperatures ranging between 700°C to│
│                      1000°C for 1 h                           │
└─────────────────────────────────────────────────────────────┘
                              ⇩
┌─────────────────────────────────────────────────────────────┐
│   Microstructural and textural characterization using SEM-EBSD │
└─────────────────────────────────────────────────────────────┘
```
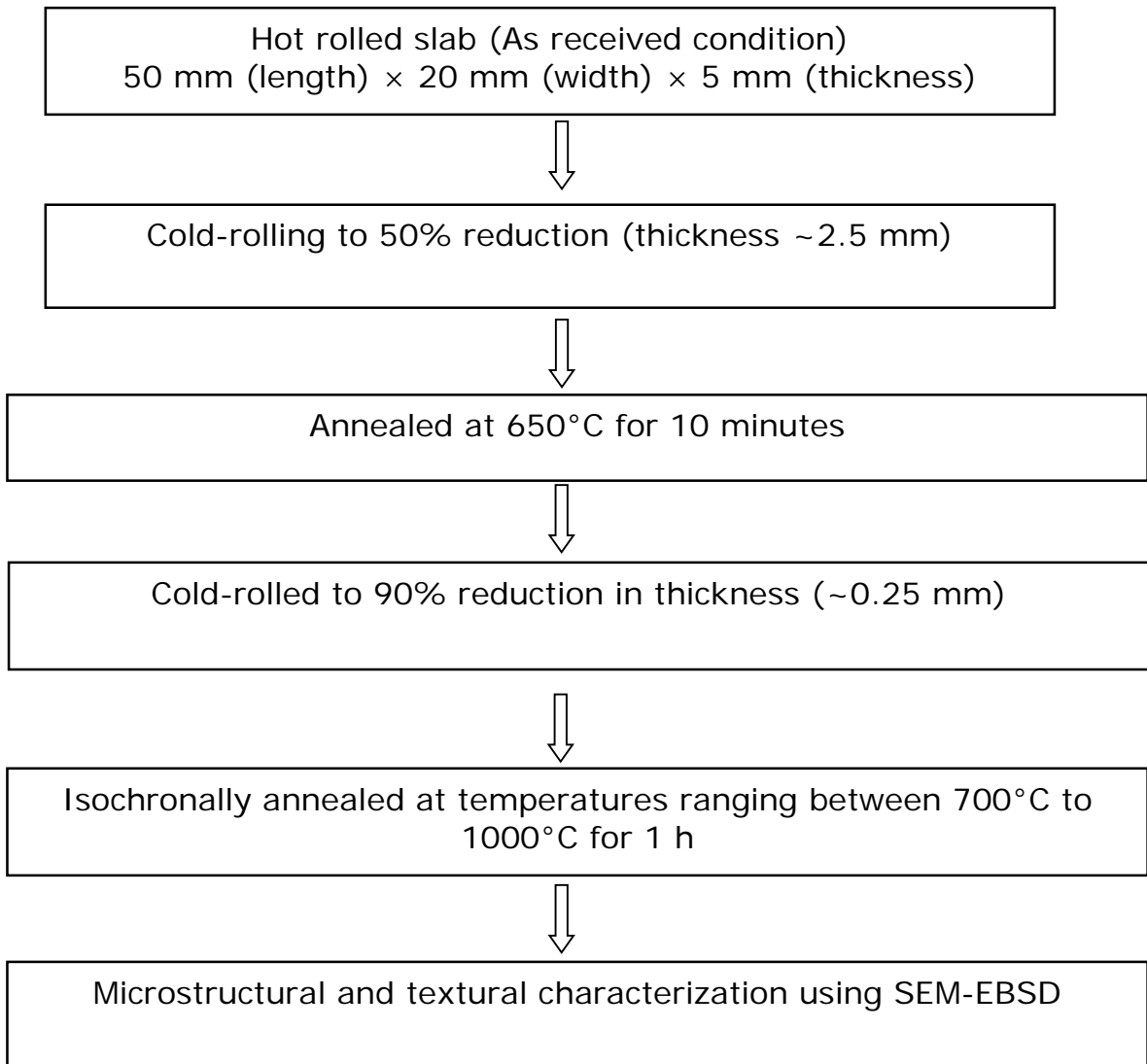
Fig.3.5: Flow diagram for investigating the effect of thermo-mechanical processing on the microstructure and texture evolution in Ni-60wt.%Co alloy.

## 3.4 Characterization

### 3.4.1 Thermal Characterization by Differential Scanning Calorimetry (DSC)

Thermal analysis of the HEA was carried out using DSC (Model: DSC 404, Make: NETZSCH, Germany). The DSC measurements were carried out under a flowing high purity argon atmosphere using a heating rate of 10°C min$^{-1}$.

### 3.4.2 Determination of chemical composition

Chemical composition analysis was carried out by energy dispersive spectroscopy (EDS) (EDAX Inc., USA) attached to a FEG-SEM (Field emission Gun; Scanning electron microscope) (Make: Carl Zeiss, Germany; Model: SUPRA – 40). EDS measurements were carried out using an accelerating voltage of 20 KV and working distance of approximately 8-10 mm. The EDS analysis was carried out using the point and area scan modes. The EDS data were collected from 10 individual points from the different locations of the sample. Area scan mode was used for revealing the elemental distribution. The samples for the chemical composition measurements were prepared by careful mechanical polishing with colloidal silica followed by ultrasonic cleaning.

### 3.4.3 Crystal structure and bulk texture measurement using X-ray diffraction (XRD)

The crystal structure was analyzed by X-ray diffraction (PANalytical, Model: X'pert PRO) using Cu-Kα radiation (1.5406 A°). The samples for XRD measurement were prepared using careful mechanical polishing with colloidal silica.

In the present investigation bulk texture measurements were carried out for selected heavily deformed specimens. The final thickness of 90% and 95% rolled specimens were 0.25 μm and 0.12 μm. Due to the thickness limitation, X-ray diffraction measurements were obtained from the rolling plane section bounded by the rolling (RD) and transverse directions (TD). For that purpose, the samples of dimension 10 × 15 mm were prepared by mechanical polishing with colloidal silica.

The bulk texture measurement of the deformed samples were carried out using X-ray diffraction technique using a PANalytical MRD system. The Cu-Kα radiation (1.54 Å) was used for the measurements. The orientation distribution function (ODF) was calculated using the series expansion method with series rank 22 [48]. Orthotropic sample symmetry was assumed for the ODF calculation.

### 3.4.4 Measurement of microtexture using EBSD

Electron Backscatter Diffraction (EBSD) is the most useful technique for simultaneous characterization of microstructure and texture. Due to this EBSD was used as the major technique for microstructural and textural characterization in the present work. The principles of automated EBSD could be summarized below.

Microtexture gives information regarding individual orientations along with their spatial distribution in polycrystalline materials. Microtexture determination by EBSD is achieved by analyzing the orientation information obtained from Kikuchi diffraction patterns. When an electron beam enters a crystalline solid it is diffusely scattered in all directions. Electrons which satisfy the Bragg's law at every set of lattice planes will diffract at an angle $\theta_B$ (Bragg angle) and will undergo elastic scattering to give a strong reinforced beam. Since diffraction of the electrons through the Bragg angle is occurring in all directions, the locus of the diffracted radiation is the surface of a cone (Kossel cone) that extends about the normal of the reflecting atomic planes with half apex angle $90° - \theta_B$.

The source of electron scattering can be considered to be between lattice planes, as shown in Fig.3.4, and hence two cones of radiation result from each family of planes. Calculations using typical values of electron wavelength and lattice interplanar spacing show that $\theta_B$ is approximately 0.5°. As a result, the apex angle of a diffraction cone is close to 180°, that is, the cones are almost flat. When the phosphor screen intercepts the diffracted cones a pair of parallel conic sections thus form. These sections
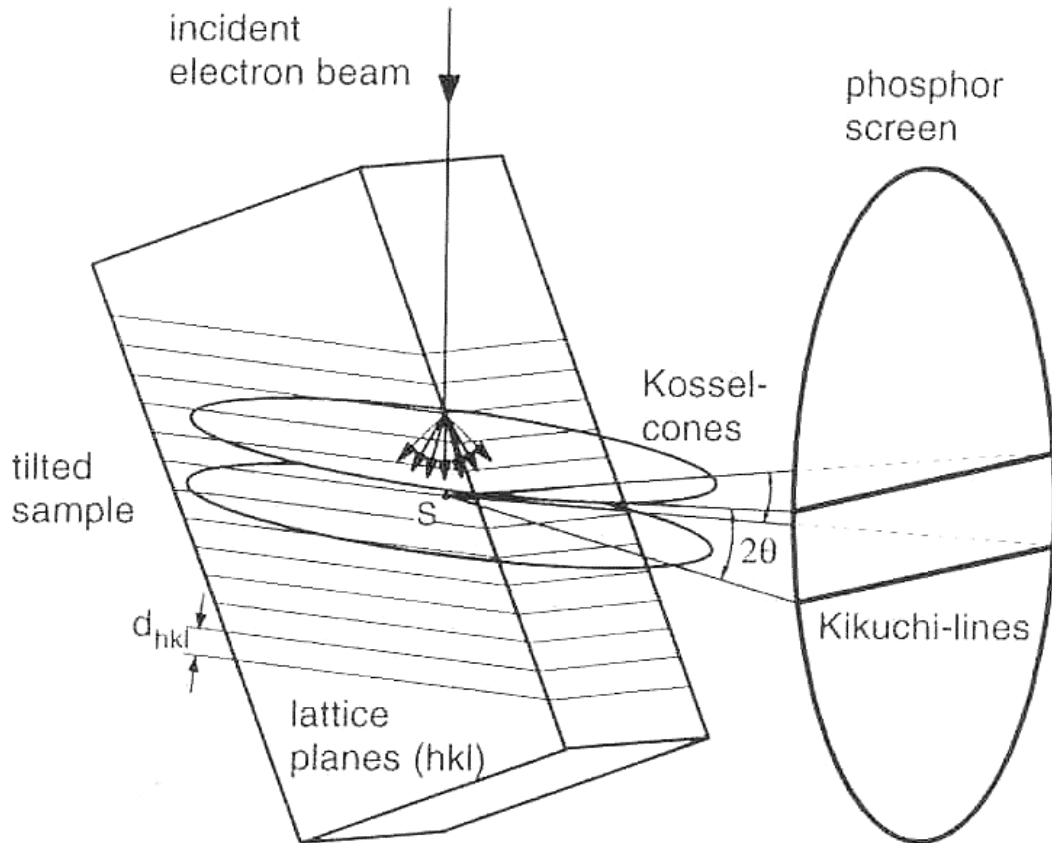
Fig. 3.4: Origin of Kikuchi lines from the EBSD perspective [41].

are nearly straight such that they generally appear to be parallel lines. These are the so called Kikuchi lines of Kikuchi bands. Spacing between the Kikuchi bands corresponds to an angular distance of $2\theta_B$ which in turn is proportional to the interplanar spacing.

In SEM the bulk specimen is to be tilted to about 20° about the vertical in order to obtain patterns of high intensity. Fully automated EBSD systems attached to SEM acquires and index Kikuchi patterns from a large number of individual grains and allows quantitative analysis of the orientation data. For acquisition of diffracted beam a phosphor screen is placed parallel to the incident beam, right in front of the tilted specimen. A pattern thus acquired spans over a wide angular range up to ±60° and contains several principal zones. Schematics of a commercial EBSD setup are shown in Fig.3.6.

Determination of individual orientation by fully automated EBSD system can be divided into the following steps [83]:

(A) Image Processing: Low signal to noise ratio of patterns needs to be improved for further analysis. This was done by applying image processing techniques. Background correction was one of the most common image processing techniques used in EBSD for improving the contrast of diffraction bands. This method usually eliminates any intensity gradients present in the image thereby improving the contrast.

 (B) Automatic Band detection: Kikuchi patterns would be automatically indexed once the bands in the Kikuchi patterns are detected. The detection of bands in EBSD was the most vital step. Lassen et al [84] suggested an algorithm for the first time for detecting Kikuchi bands called Hough transformation method which was the most commonly used algorithm for band detection.

During the Hough transformation each point $(x_i, y_i)$ of the original image is transformed into sinusoidal curve in the Hough space which is governed by the relation:

$$\rho(\varphi) = x_i \cos\varphi + y_i \sin\varphi, \quad \rho \in (0°, 180°), \quad \varphi \in (-R, R) \qquad (3.1)$$

The above relation specifies a line by the angle $\varphi$ between its normal and the pattern x-axis and its distance $\rho$ from the origin. The principle of Hough transformation has been schematically shown in Fig.3.7 for two bands which are defined by two points. Points which lie in the original image in Fig.3.7 (a) have the same distance $\rho$ and angle $\varphi$ with respect to the origin and hence, they all accumulate at the same point in the Hough space Fig.3.7 (b). Thus, by transforming an image into Hough space, lines in the image space become single points in the Hough space. This is done by first dividing Hough space into discrete bins. Then the intensity at every (x, y) pixel in the image is added into all discrete bins on the curve defined by Eq (3.1) (where $\rho$ is calculated for each discrete $\varphi$). The problem of finding a band in diffraction pattern is then reduced to finding a peak of high intensity in Hough space. The peak in Hough space has a characteristic butterfly shape - a peak surrounded by two valleys. In order to draw out peak of this shape, the Hough transformation is convoluted with a "butterfly mask".

(C) Indexing of the Bands: Automatic indexing of the bands is done by commercially available software packages and the algorithm implemented may vary depending on the system. The commercial software package HKL CHANNEL 5 used in this work for data acquisition employs simple Hough transformation for band detection as well as an "Advance Fit" algorithm to generate a short list of possible solution very quickly, compares the simulated EBSP for each possible solution in the short-list very accurately against the actual acquired EBSP [85].

(D) Orientation Determination: Once the miller indices associated with at least two bands are identified the orientation of the corresponding crystal lattice (with respect to some fixed reference frame) can be calculated in
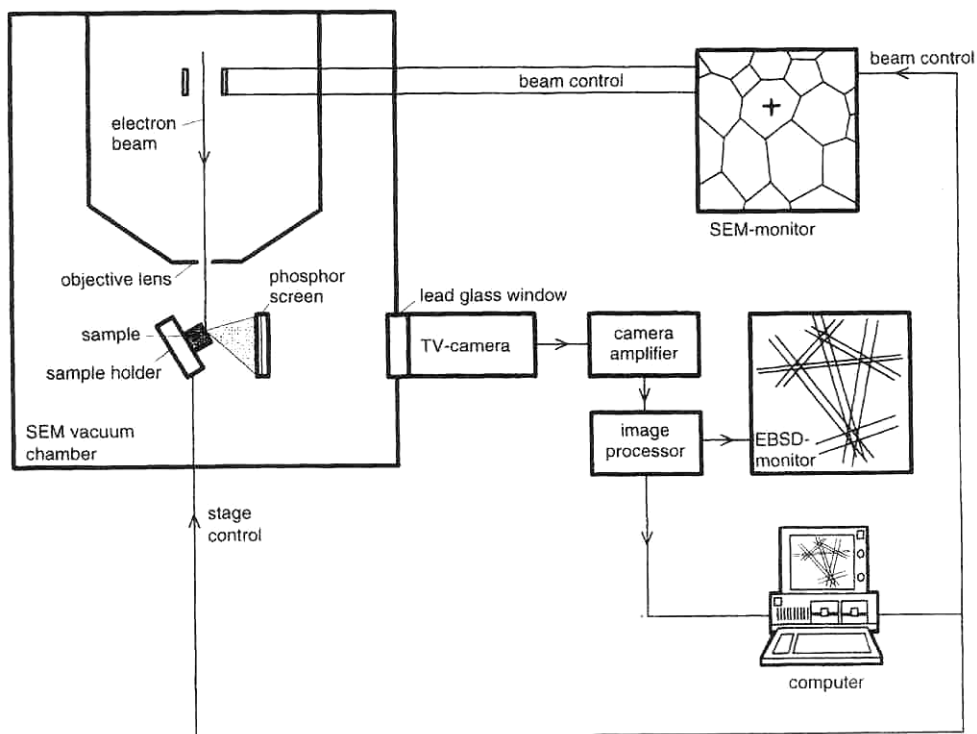
Fig.3.6: Components of a commercial EBSD system [41].



(a) Original image
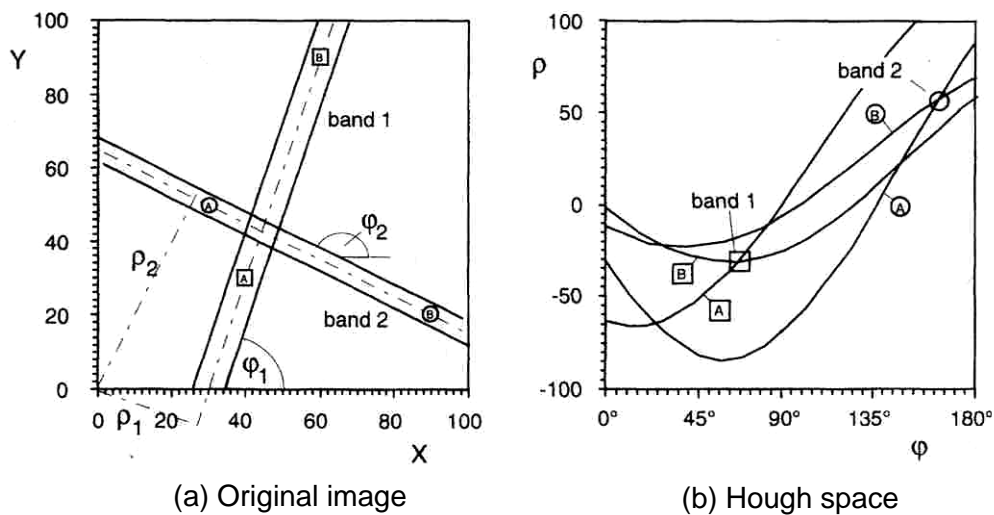
(b) Hough space

Fig.3.7: Schematic representation of the Hough transformation; (a) two bands in the original space, (b) the bands in the transformed Hough space. [41].

the following manner (Fig.3.8 (a) and (b)). Two vectors can be defined representing two plane normal in pattern coordinates:

$$\widehat{n_1}^p = \frac{\overline{OP} \, X \, \overline{OQ}}{\|\overline{OP} \, X \, \overline{OQ}\|} \qquad \text{and} \quad \widehat{n_2}^p = \frac{\overline{OR} \, X \, \overline{OS}}{\|\overline{OR} \, X \, \overline{OS}\|} \tag{3.2}$$

($\|V\|$ denotes the magnitude of vector $v$, i.e, $\|V\| = \sqrt{V.V} = \left(V_1 V_2 + V_2 V_2 + V_3 V_3\right)^{1/2}$ and V denotes a normalized vector, i.e, $\|V\| = 1$) From these two normalized vectors an orthogonal frame can be constructed as follows.

$$\hat{e}_1^{*p} = \hat{n}_1^p \quad \hat{e}_2^{*p} = \frac{\hat{n}_1^p \, X \, \hat{n}_2^p}{\left\|\hat{n}_1^p \, X \, \hat{n}_2^p\right\|} \quad \text{and} \quad \hat{e}_3^{*p} = \hat{e}_1^{*p} \, X \, \hat{e}_2^{*p} \tag{3.3}$$

Similarly, an orthogonal frame can be constructed in the crystal frame given the (hkl) indices associated with the bands used in the calculation of $\hat{n}_1^p$ and $\hat{n}_2^p$ shown previously.

This is done as follows:

$$\hat{e}_1^{*C} = \frac{(hkl)_1}{\|(hkl)_1\|}, \quad \hat{e}_2^{*C} = \frac{(hkl)_1 \, X \, (hkl)_2}{\|(hkl)_1 \, X \, (hkl)_2\|} \quad \text{and} \quad \hat{e}_3^{*C} = \hat{e}_1^{*C} \, X \, \hat{e}_2^{*C} \tag{3.4}$$

(a)                                                          (b)
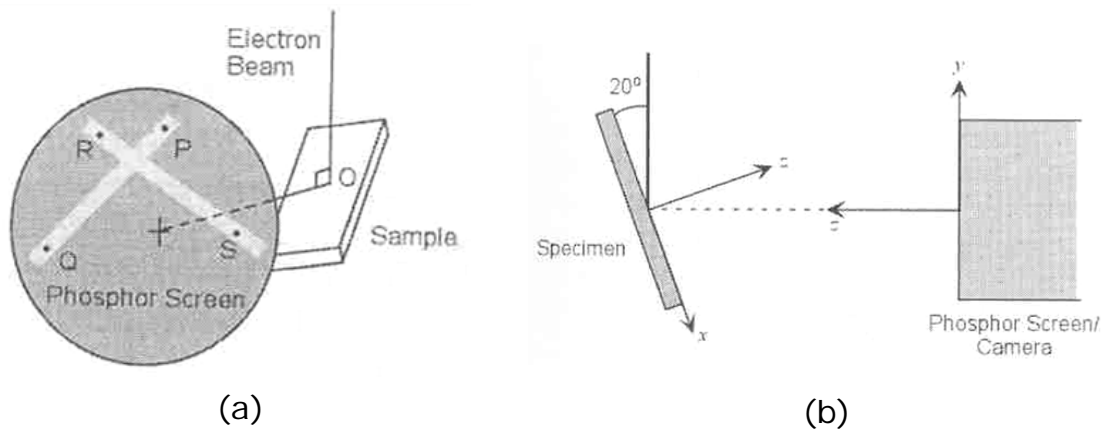
Fig.3.8: Schematic representation of the geometry of (a) diffraction and (b) EBSD [83].

Two sets of direction cosines can be determined relating the new (pattern) frame to the sample and crystal frames as follows:

$$g_{ij}^{s} = \hat{e}_{i}^{*P}.\hat{e}_{j}^{s} \text{ and } g_{ij}^{c} = \hat{e}_{i}^{c}.\hat{e}_{j}^{*C} \tag{3.5}$$

The vectors $\hat{e}_{j}^{s}$ is given as

$$\hat{e}_{1}^{s} = -Cos(20°)\hat{j} - \sin(20°)\hat{k} , \ \hat{e}_{2}^{s} = -\hat{i} \text{ and } \hat{e}_{1}^{s} = -Sin(20°)\hat{j} - Cos(20°)\hat{k} \tag{3.6}$$

And the vector $\hat{e}_{i}^{c}$ is simply

$$\hat{e}_{1}^{c} = \hat{i} , \ \hat{e}_{2}^{c} = \hat{j} \text{ and } \hat{e}_{3}^{c} = \hat{k} \tag{3.7}$$

The orientation matrix (representing the rotation required to bring the sample co-ordinate frame into coincidence with the crystal lattice reference frame) can be calculated as follows

$$g_{ij} = g_{ik}^{s}.g_{kj}^{c} \tag{3.8}$$

The microstructure and texture of the starting, deformed and annealed samples were characterized using fully automated Electron Backscatter Diffraction (EBSD) system (Oxford Instruments, UK) attached to a FEG-SEM (Make: Carl-Zeiss, Germany; Model: Supra-40) operated at 20 KV accelerating voltage. The working distance was 13-15 mm for the majority of the measurements. The samples for EBSD measurement were prepared using careful mechanical polishing with colloidal silica followed by electro-polishing at room temperature using a mixture of methanol and perchloric acids in a ratio of 1:9 (by volume).

The EBSD scans for the deformed samples were acquired from the longitudinal section (normal to the transverse direction (TD)) bounded by the normal direction (ND) and rolling direction (RD) close to the mid-thickness regions of the sheets. For deformed samples, several EBSD scans with a minimum area of around 20µm x 25µm were acquired from different areas located approximately at the mid-thickness of the sheets. Fine scan

step sizes ranging between 40 nm to 50 nm (0.04-0.05µm) were used for heavily deformed specimens.

The EBSD scans for the initial and different annealed samples were acquired from the rolling plane section (ND normal) bounded by the RD and TD. The step size of 0.2 µm -3 µm were used for annealed samples. Several EBSD scans were taken in the middle of the rolling plane section and merged together for the analysis purpose. This process ensured that at least 3000 grains recrystallized grains are considered for calculating the microstructural and textural parameters for each sample.

The EBSD scans were acquired using the Aztec HKL software (Oxford Instruments, UK). The scan dataset were imported into the TSL-OIM$^{TM}$ analysis software (EDAX Inc., The Netherlands) in the text file format (.ctf extension) for the analysis purpose. Orthotropic sample symmetry was assumed in calculating the orientation distribution functions (ODFs) from the microtexture data using the series expansion method of Bunge ($L_{max}$=22) [48]. The volume fractions of different texture components were determined using a tolerance angle of 15°.

### 3.4.5 Characterization of mechanical properties

Tensile tests were carried out for selected deformed and annealed specimens. A schematic drawing of a typical tensile test specimen could be shown in Fig.3.9. A table mounted tensile testing machine (Make: INSTRON, UK; Model: 5967) with 30KN capacity was used for tensile testing. The tensile testing was carried out using a constant strain rate of $10^{-3}$ s$^{-1}$. The tensile load was applied along the RD.
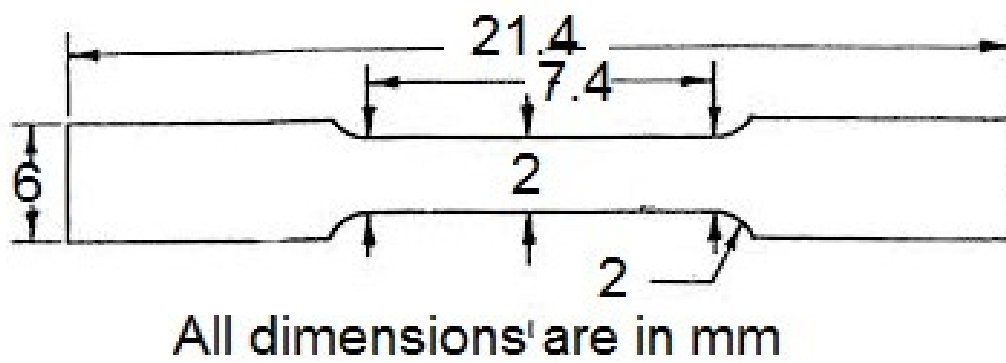
Fig.3.9: Schematic of the tensile test specimens.

# -: CHAPTER 4 :-

## *Microstructure and texture evolution after heavy cold-rolling and annealing*

## 4.1 Microstructure and texture of the cast and homogenized alloy

Fig.4.1 compares the XRD profile of the cast and homogenized HEA with that of the homogenized high-purity nickel. The XRD patterns clearly indicate that the homogenized HEA is having FCC crystal structure. However, the XRD peaks of the HEA (indicated in red color) are systematically shifted to the left as compared to the corresponding peaks of high purity nickel (indicated in black color). The systematic shift of the peaks of homogenized HEA towards the lower Bragg angle (2θ) indicates that the lattice parameter is larger than that of pure nickel. The lattice parameter is determined by using the following relation:

$$a^2 = \frac{\lambda^2 \ (h^2 + k^2 + l^2)}{(2 \ \sin\theta)^2} \qquad\qquad (4.1)$$

Considering the position of the (311) peak, the lattice parameters of the homogenized HEA (2θ = 90.73°) and homogenized Ni (2θ= 93.39°) are found to be 3.59 Å and 3.51 Å, respectively. The obtained lattice parameter value of the homogenized Ni (3.51 Å) is evidently similar to the reported value for high purity nickel (3.52 Å) (margin of error ~ 0.28%) [86]. Therefore, the lattice parameter of the HEA reported in the present study can be considered as reasonably precise. The observed increase of lattice parameter in the homogenized HEA is due to the formation of multicomponent solid solution in which Cr, Fe and Mn have larger atomic size than that of Ni.

Fig.4.2 shows the backscatter electron (BSE) micrograph of the cast and homogenized HEA. The micrograph reveals the presence of rather large grains. The average grain size measured from the micrograph is ~ 250 μm. The chemical composition analysis of the homogenized HEA is carried out by energy dispersive spectrometry (EDS) to determine the homogeneity and distribution of different elements. Fig.4.3 shows the X-ray area mapping of a typical region in the homogenized HEA which demonstrates rather homogenous distribution of the alloying elements. However, X-ray mapping has limitation and not able to detect atomic level segregation at the grain boundaries.
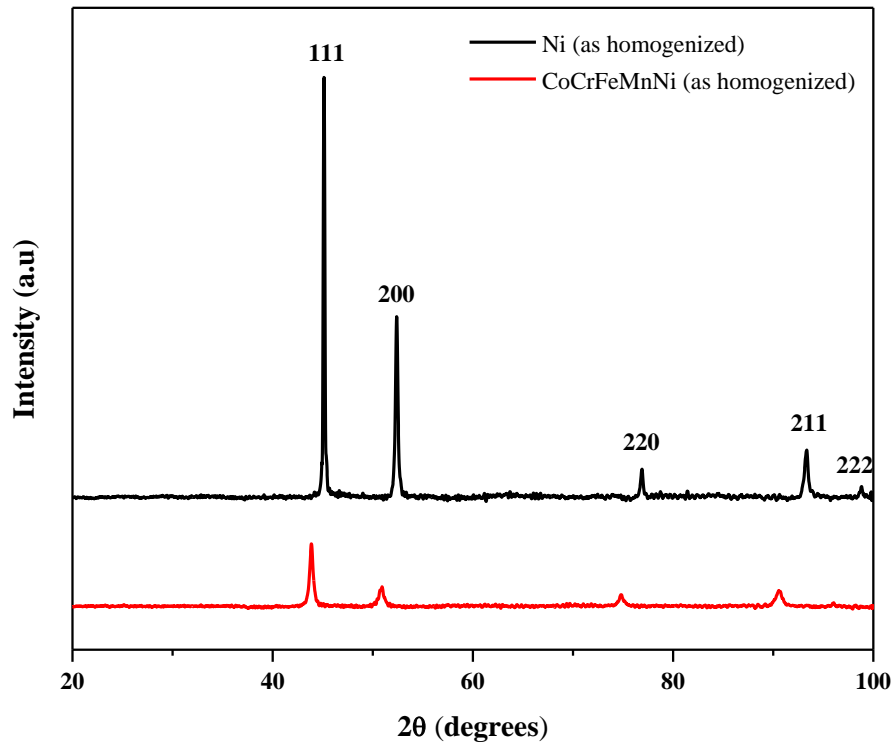
Fig.4.1: XRD patterns of homogenized HEA and high purity Ni.

Fig.4.2: BSE micrograph of the homogenized CoCrFeMnNi HEA.
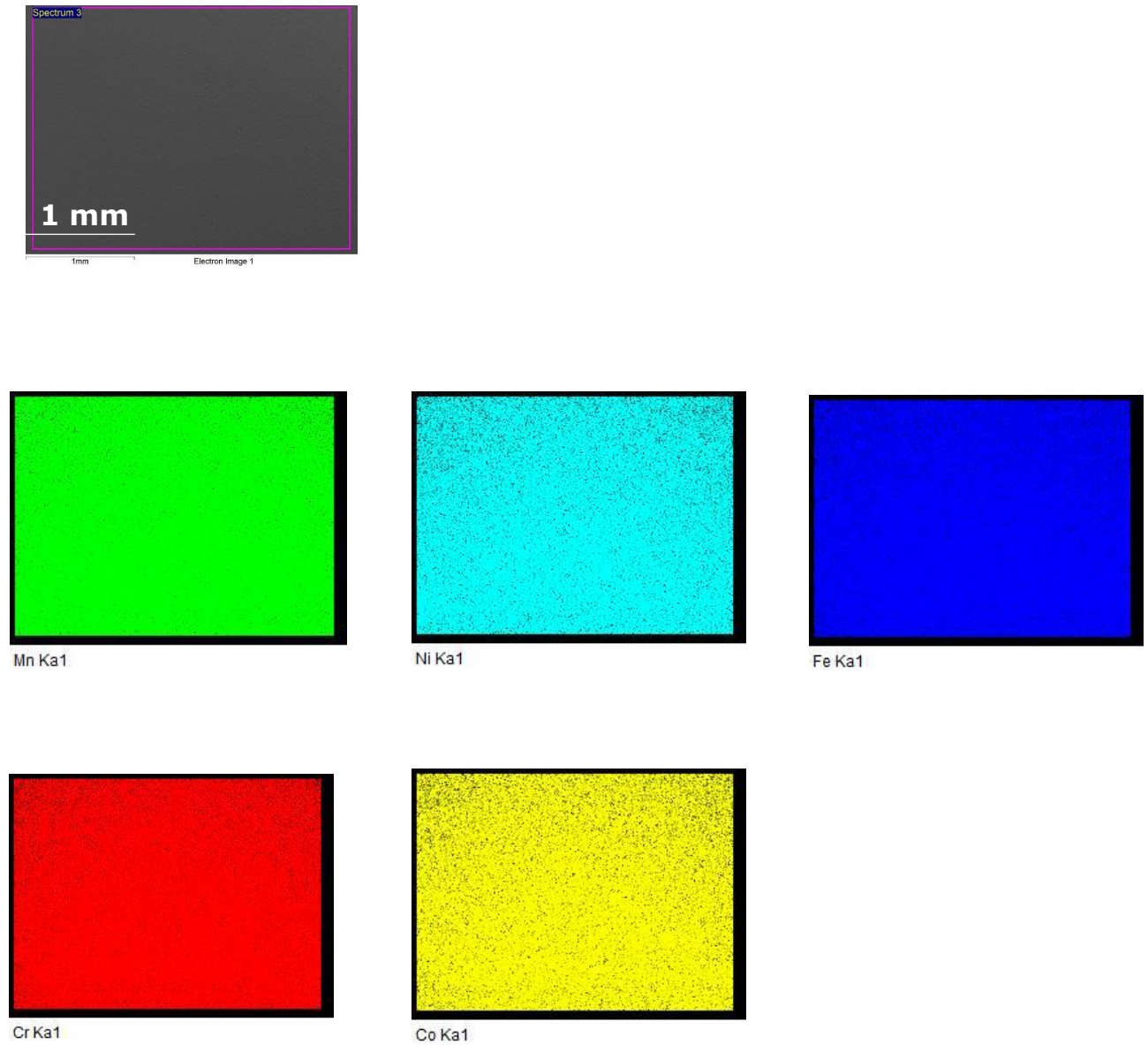
Fig.4.3: The X-ray area mapping of a typical region in the homogenized CoCrFeMnNi HEA.

Table 4.1 summarizes the average composition of the homogenized alloy in weight and atomic percentages.

Fig.4.4(a) shows the grain boundary (GB) map of the homogenized material following 50% cold-rolling and annealing at 800°C (it may be recalled that this is the starting condition for further TMP processing as already explained in Chapter 3). The high angle grain boundaries (HAGBs having a misorientation angle ($\theta$) > 15°) and low angle grain boundaries (LAGBs with 2°≤$\theta$≤15°) are highlighted in black and red, respectively. The GB map shows completely recrystallized state with an average grain size of ~ 7 μm (annealing twins are excluded in the grain size calculation). The microstructure shows the presence of large recrystallized grains along with clusters of small recrystallized grains. The presence of profuse Σ3 annealing twin boundaries (TBs; highlighted by red lines) could be easily observed in the microstructure. The appearance of the (111) pole figure (PF) suggests a rather weak and diffuse texture of the recrystallized starting material (Fig.4.4(b)).

Table.4.1: Chemical composition of the homogenized CoCrFeMnNi HEA.

| Element | wt.% | at.% |
|---------|------|------|
| Cr | 19.39 | 20.89 |
| Mn | 19.40 | 19.79 |
| Fe | 20.02 | 20.09 |
| Co | 20.75 | 19.73 |
| Ni | 20.44 | 19.50 |
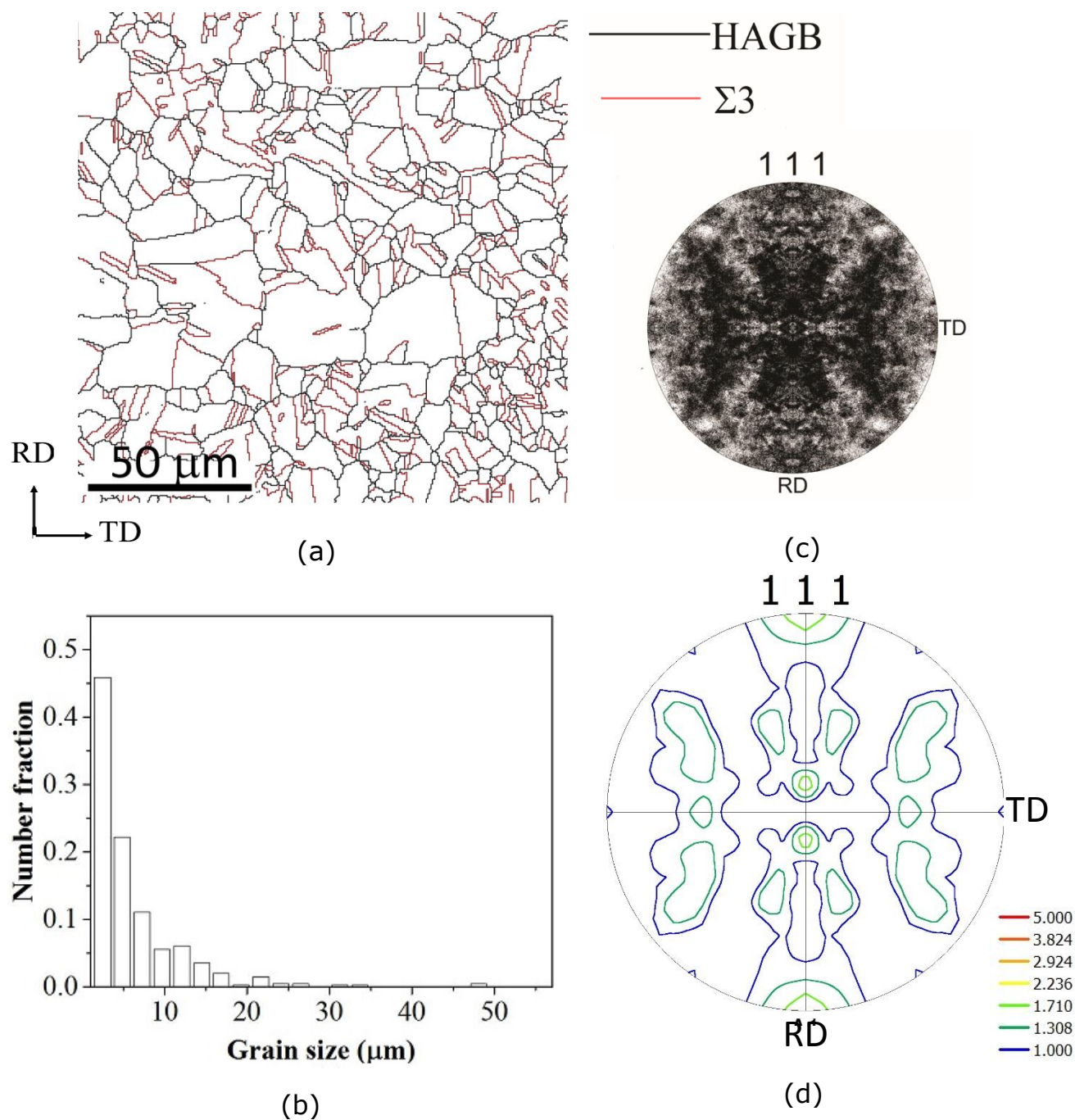
Fig.4.4: (a) GB map (b) grain size distribution and (c) discrete PF and (d) (111) PF of the homogenized HEA following 50% cold-rolling and annealing at 800°C for 1 h.

## 4.2 Microstructure and texture formation during cold–rolling

Fig.4.5 shows the image quality (IQ) maps of the 20% (Fig.4.5(a)), 40% (Fig.4.5(b)), 60% (Fig.4.5(c)) and 80% (Fig.4.5(d)) cold-rolled materials. The typical FCC rolling texture components are overlaid on the maps. Fig.4.5(e) through Fig.4.5(h) show the corresponding (111) PFs. Fig.4.7 shows the volume fraction of the typical FCC rolling texture components, namely, Cube (C; {001}<100>; highlighted in blue), Copper (Cu; {112}<111>; highlighted in red), S ({123}<634>; highlighted in yellow), Brass ($B_S$; {110}<112>; highlighted in green), Goss (G; {110}<001>; highlighted in orange) and an important orientation located in-between the G and $B_S$ (denoted as G/B; {011}<115>; highlighted in deep rose). Table 4.2 summarizes the important texture components along with their respective set of Euler angles (Table 4.2 also includes the important recrystallization texture components which would be discussed later).

After 20% deformation (Fig.4.5(a)), the starting recrystallized grains are still easily distinguished. Few of the starting grains already appear flattened along the RD. This is also clearly observed after 40% deformation (Fig.4.5(b)). Further cold-rolling to 60% (Fig.4.5(c)) and 80% (Fig.4.5(d)) reduction in thickness results in the evolution of lamellar banded microstructure elongated along the RD.

The comparison of the ideal (111) PF (Fig.4(i)) with that of the 20% cold-rolled material (Fig.4.5(e)) indicates the presence of weak pure metal or copper type texture. The PFs of the 40% (Fig.4.5(f)) and 60% (Fig.4.5(g)) cold-rolled materials appear very similar to that of the 20% cold-rolled material. However, the PF of the 80% (Fig.4.5(h)) cold-rolled material appears distinctly different that the other PFs, thus indicating fundamental changes in texture.
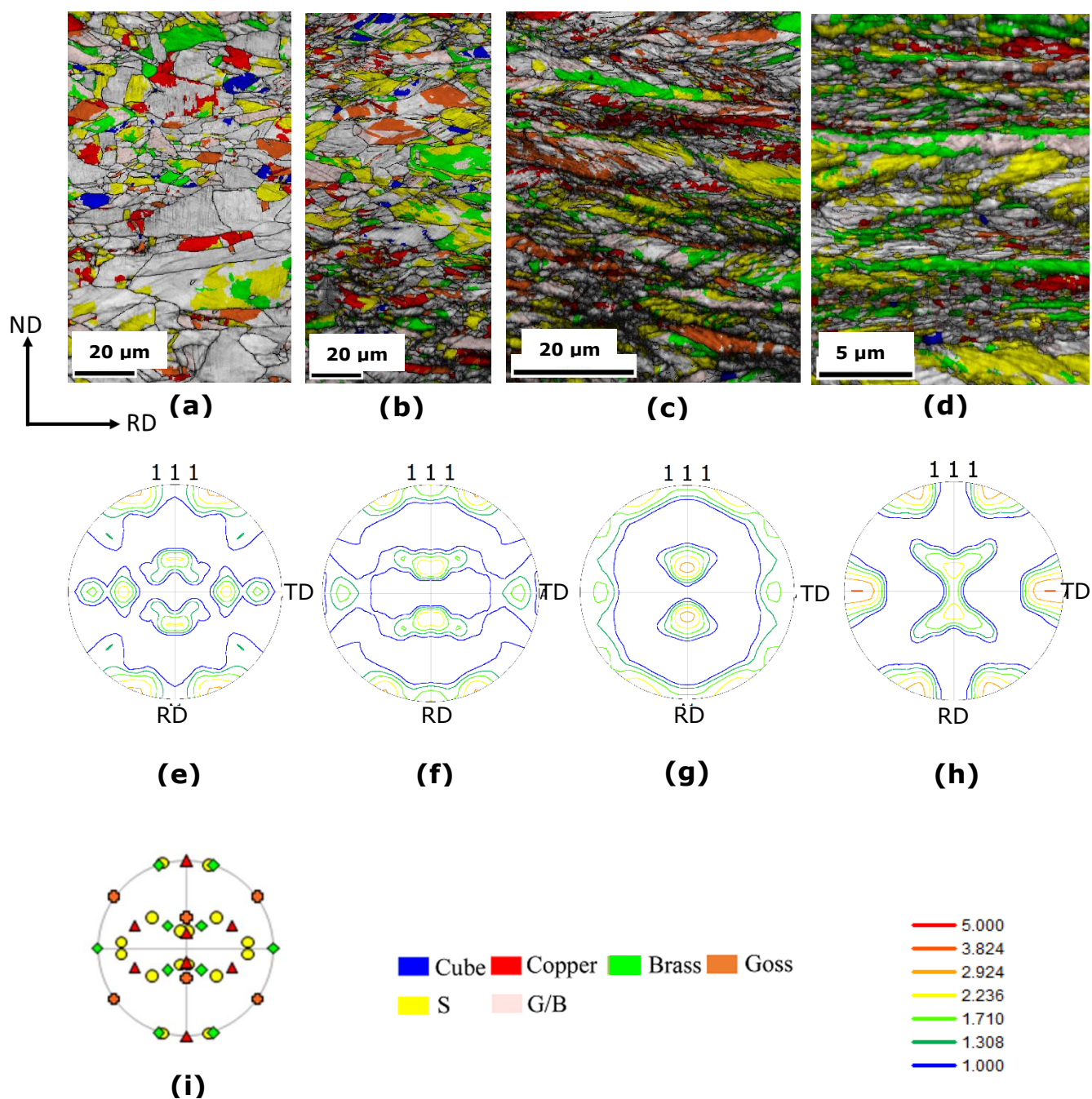
Fig.4.5: Grain orientation map ((a)-(d)) and (111) PF ((e)-(h)) of 20% ((a), (e)), 40% ((b), (f)), 60% ((c), (g)) and 80% ((d), (h)) cold-rolled materials; (i) is the (111) PF showing the ideal locations of different texture components.

Table 4.2 Euler angles and Miller indices of the important deformation and recrystallization texture components [50].

| Texture component | Symbol | Euler angle | | | Miller indices |
|---|---|---|---|---|---|
| | | $\varphi_1$ | $\phi$ | $\varphi_2$ | |
| Cube (C) | ■ | 0, 0, 0 | | | {001} <100> |
| Copper (Cu) | ● | 90, 35, 45 | | | {112} <111> |
| S | ▲ | 59, 37, 63 | | | {123} <634> |
| Bs | ▼ | 35, 45, 0 | | | {110} <112> |
| G | ◆ | 0, 45, 0 | | | {110} <001> |
| Rt - G | ★ | 90, 45, 0 | | | {110} <110> |
| G/B | ◄ | 17, 45, 0 | | | {110} <1 1 5> |
| G/B(T) | ▶ | 55, 45, 0 | | | {110} <111> |
| BR | ⬢ | 80, 31, 34 | | | {236} <385> |
| D | ♨ | 90, 27, 45 | | | {1 1 3} <3 3 2> |
| K | ▨ | 27, 64, 14 | | | {142} <211> |
| M | ⊠ | 80, 30, 65 | | | {13 6 25} <20 15 14> |

Fig.4.6 shows the microstructure and texture after 90% cold-rolling obtained from the two different regions. The IQ maps (Fig.4.6(a) and Fig.4.6(b)) are obtained from the ND-RD section close to the mid-thickness regions. The IQ maps show lamellar morphology elongated along the RD. Presence of thin, but deep shear bands (marked with the arrow mark) inclined to the RD about ~30° could be observed in the IQ map in Fig.4.6(a). The appearance of the (111) PFs (Fig.4.6(c) and Fig.4.6(d)) clearly reveals the development of a predominantly brass or alloy type texture after 90% deformation. In good agreement with this observation, the orientation maps (Fig.4.6(a) and Fig4.6(b)) clearly show significant presence of the $B_S$ (green), S (yellow) and G (orange) components, but much weaker presence of the Cu (red) component. The volume fractions of individual texture components obtained from the two different regions are compared in Fig. 4.7. The plot clearly indicates that the respective volume fractions of the texture components obtained from the two regions are rather similar. This confirms the development of rather homogenous brass texture after heavy cold-rolling.

In order to further drive home this point, the X-ray texture measurements are obtained from the rolling plane section (normal to the ND and bounded by the rolling direction (RD) and transverse direction (TD)) of the 90% cold-rolled material. The ODF obtained from X-ray texture measurement is shown in Fig.4.8. The $\varphi_2=0°$ section of the ODF shows the spread of intensities along the α-fiber from the G to the $B_S$ orientation through the intermediate G/B orientation. The $\varphi_2=45°$ section of the ODF clearly shows strong stronger intensity at the $B_S$ location as compared to the Cu location. This again confirms the development of a strong brass type texture. Evidently, this is in excellent agreement with the results obtained from microtexture measurements by EBSD (Fig.4.6 and Fig.4.7). Therefore, with increasing cold-rolling reduction, the texture of the HEA is transformed from pure metal type (after 60% deformation as shown in Fig.4.5(g)) to brass type after 90% cold-rolling (Fig.4.6(c), Fig.4.6(d) and

Fig.4.9) through a transition type texture observed in 80% cold-rolled material (Fig.4.5(h)). These changes are quantitatively summarized in Fig.4.9 by the volume fraction analysis of individual components. The plot (Fig.4.9) clearly shows the gradual strengthening of the $B_S$ component at the expense of the Cu component with increasing thickness reduction.
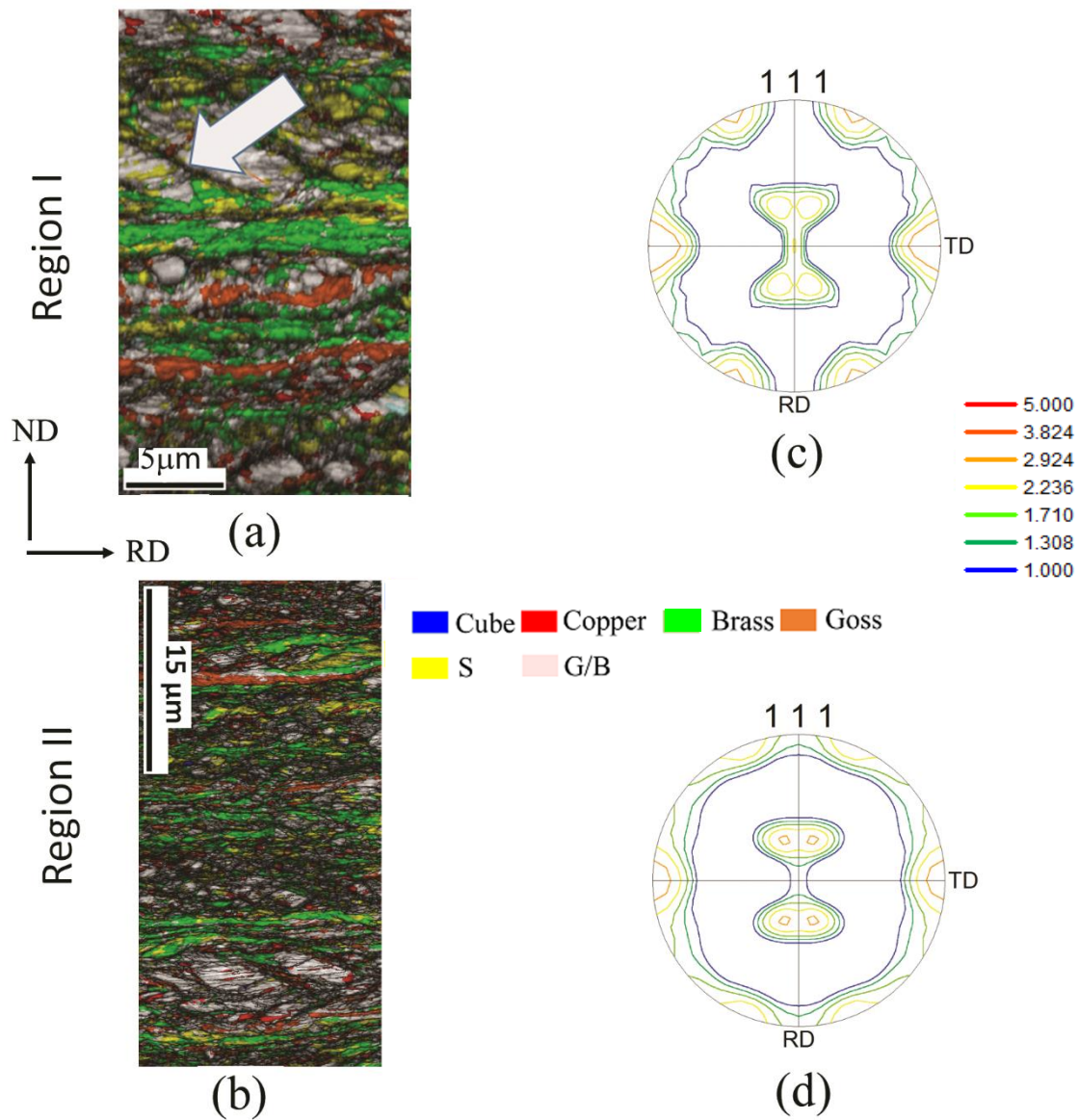
Fig.4.6: (a) and (b) are the IQ maps (with overlaid orientations) of two different regions in the 90% cold-rolled HEA; (c) and (d) are the corresponding (111) PFs.
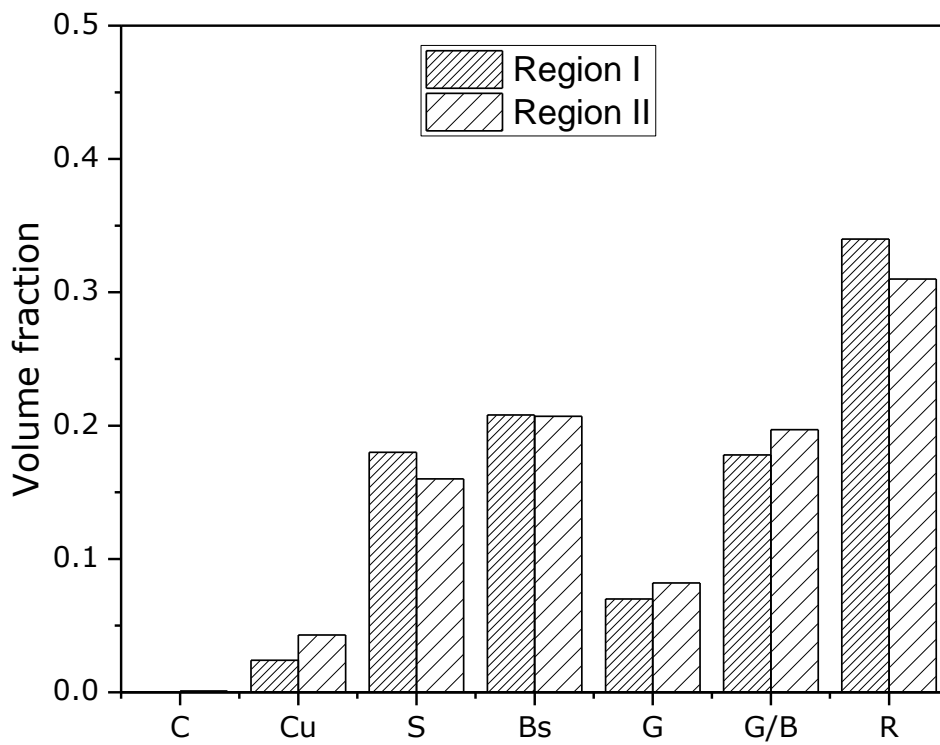
Fig.4.7: Volume fractions of different texture components obtained from the two different regions in the 90% cold-rolled material.
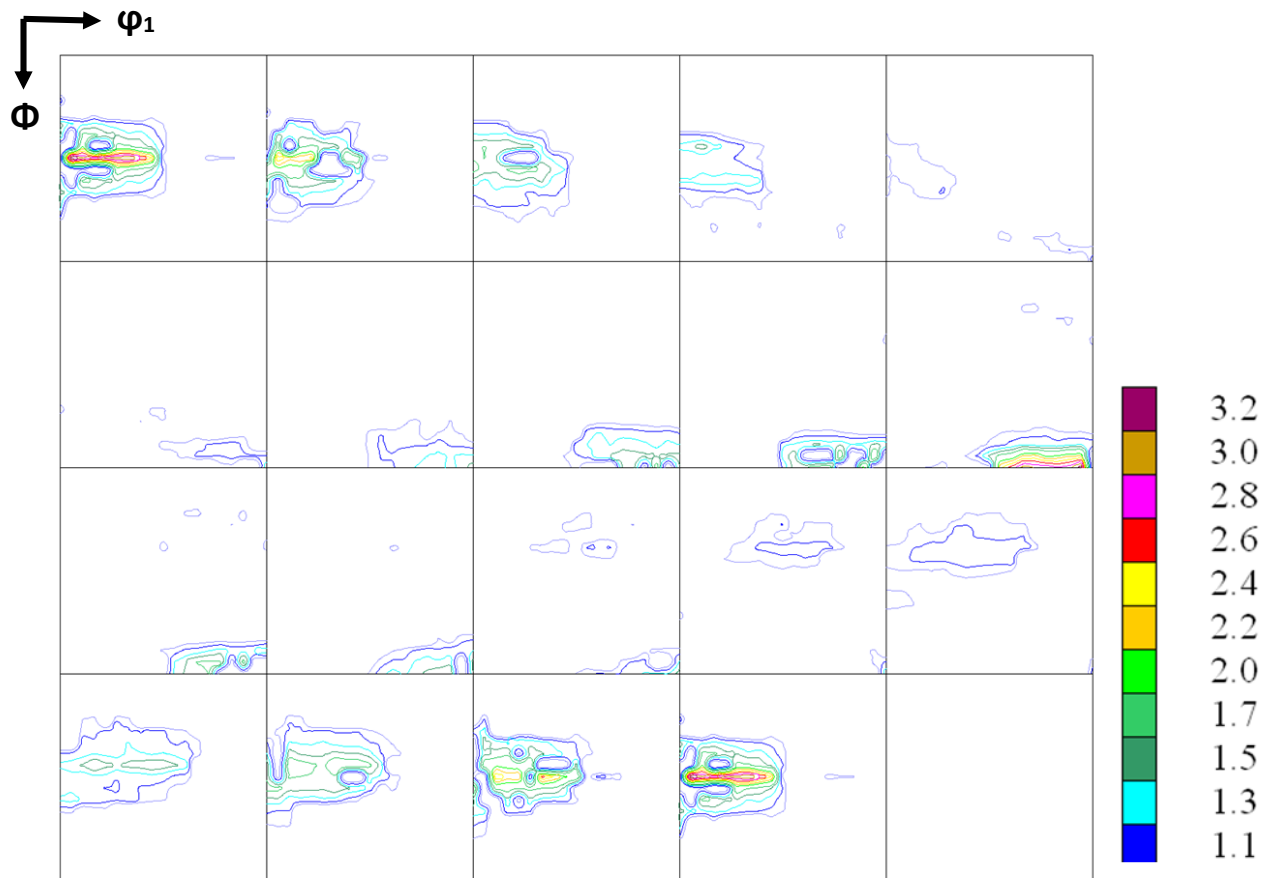
Fig.4.8: The φ₂ sections of the ODF (measured by XRD) obtained from the rolling plane section of the 90% cold-rolled material.
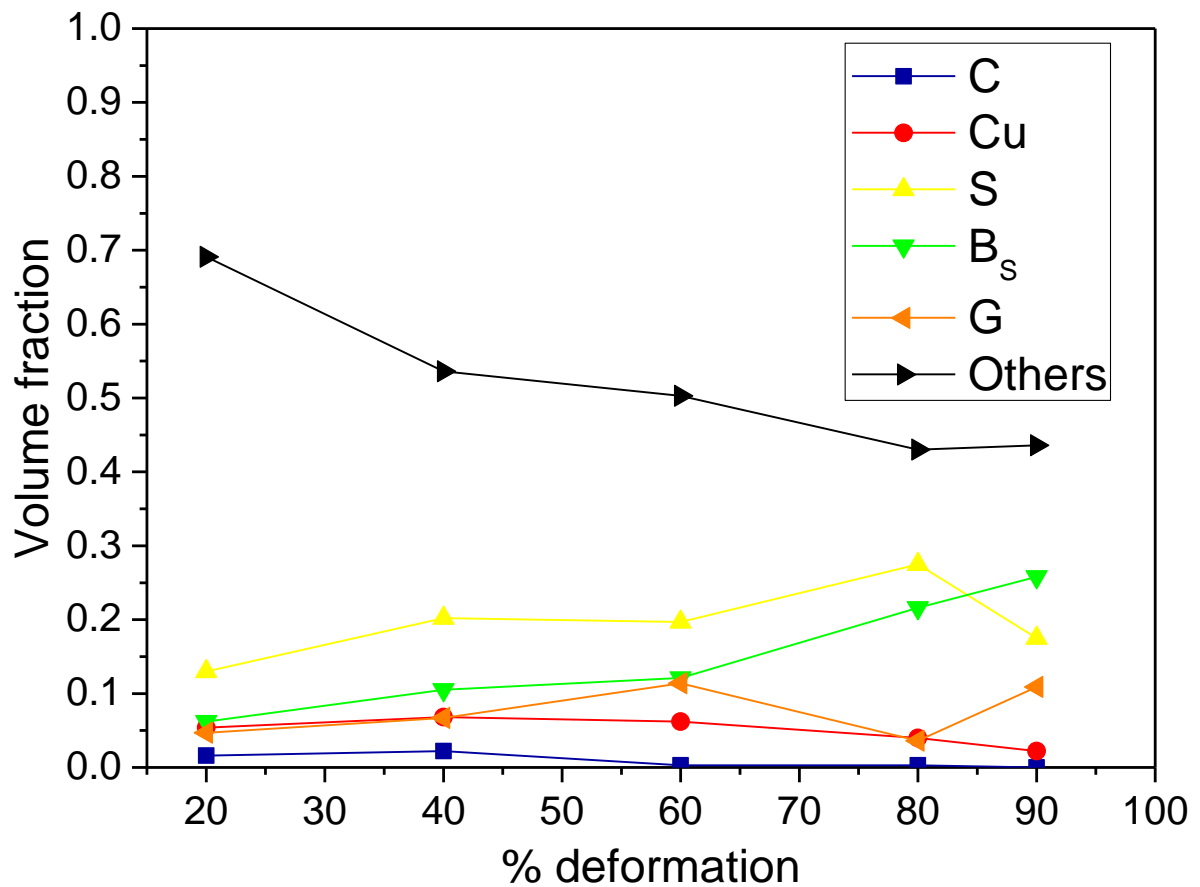
Fig.4.9: Variation of volume fraction of different texture components with thickness reduction during cold-rolling (The volume fraction of individual texture components was determined using a cut-off angle of 15°).

## 4.3. Evolution of microstructure and texture during annealing

Fig.4.10 shows the microstructures of the 90% cold-rolled material following different annealing treatments. The microstructure after annealing at 650°C appears mostly recrystallized (Fig.4.10(a)). However, few isolated Bs-oriented regions are found to be in the deformed state. This is clearly evidenced by the presence of the internal LAGB network in the Bs oriented regions (indicated by the arrow mark). Fig.4.10(a) also shows the presence of profuse annealing TBs. The average recrystallized grain size (excluding the annealing TBs) is ~1.1 µm. Annealing at 700°C yields a fully recrystallized microstructure consisting of grains separated by HAGBs (Fig. 4.10(b)). However, the average recrystallized grain size remains rather small ~ 1.5 µm. Annealing at increasingly higher temperatures results in gradual grain growth (Fig.4.10(c) to Fig.4.10(e)).

The evolution of key microstructural parameters during annealing is shown in Fig.4.11(a). The variation of average grain size shows insignificant grain growth up to annealing temperature of 800°C. Noticeable grain growth is observed only after annealing at 1000°C. The average grain size is found to be ~24 µm after annealing at 1000°C. The misorientation distribution plot shown in Fig.4.11(b) reveals a very strong peak at the misorientation angle of 60° for all the annealed materials. This peak corresponds to the annealing TBs defined by the 60°<111> angle-axis misorientation relationship. This is in good agreement with the presence of profuse annealing TBs (Fig.4.10). Fig.4.11(c) shows the variation of annealing TBs with annealing temperature. It is observed that the annealing TBs do not show any significant variation up to the annealing temperature of 800°C. Beyond that, the TB fraction increases consistently with increasing annealing temperature.

The (111) PFs of different annealed materials are shown in Fig.4.12. The (111) PF of the materials annealed at 650°C (Fig.4.12(a)) is calculated only from the recrystallized grains. The appearance of the different PFs suggests the retention of deformation texture components.
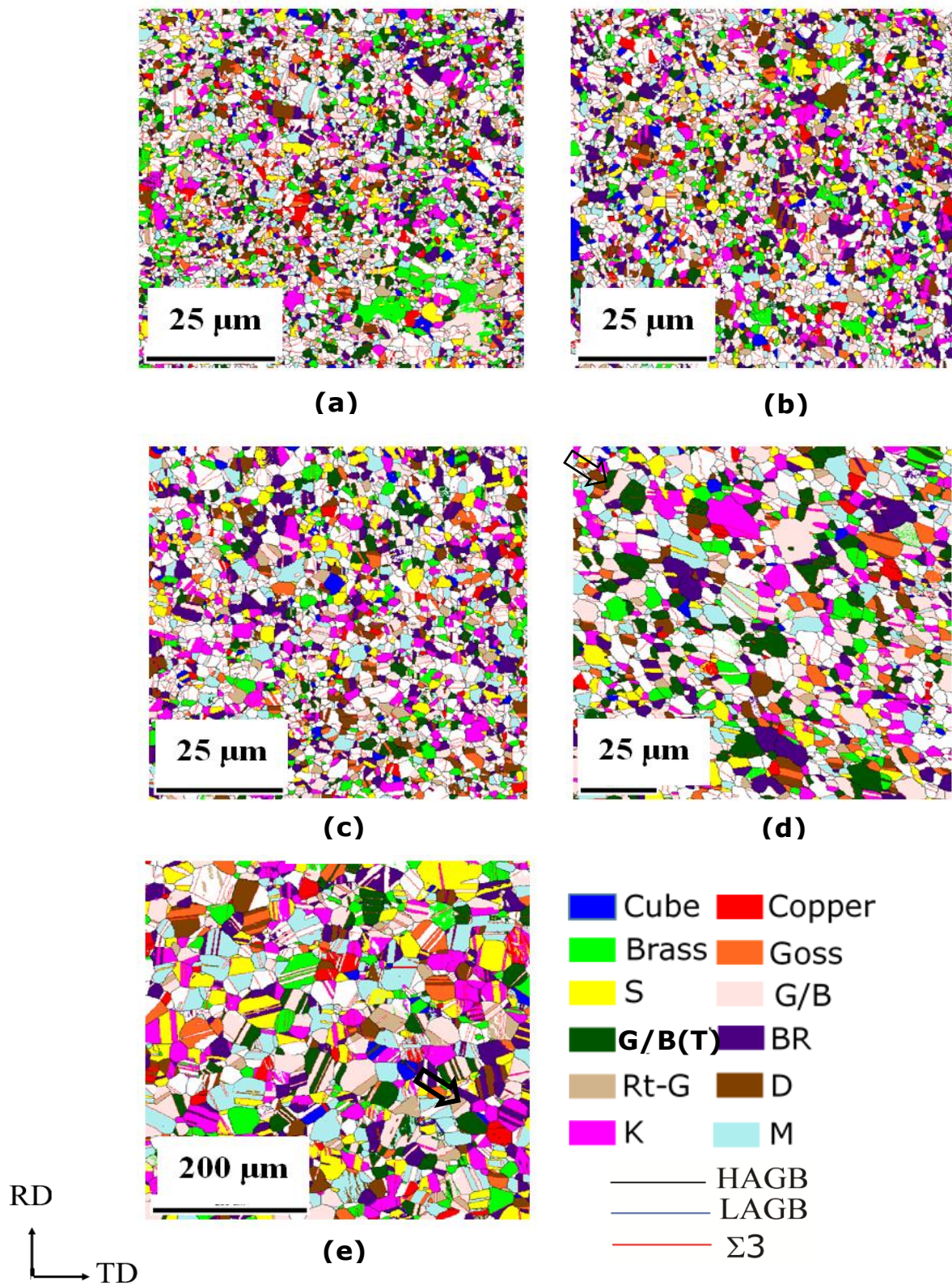
Fig.4.10: Orientation maps of 90% cold-rolled material after annealing at (a) 650°C, (b) 700°C, (c) 800°C, (d) 900°C and (e) 1000°C.

(a)



(b)



(c)
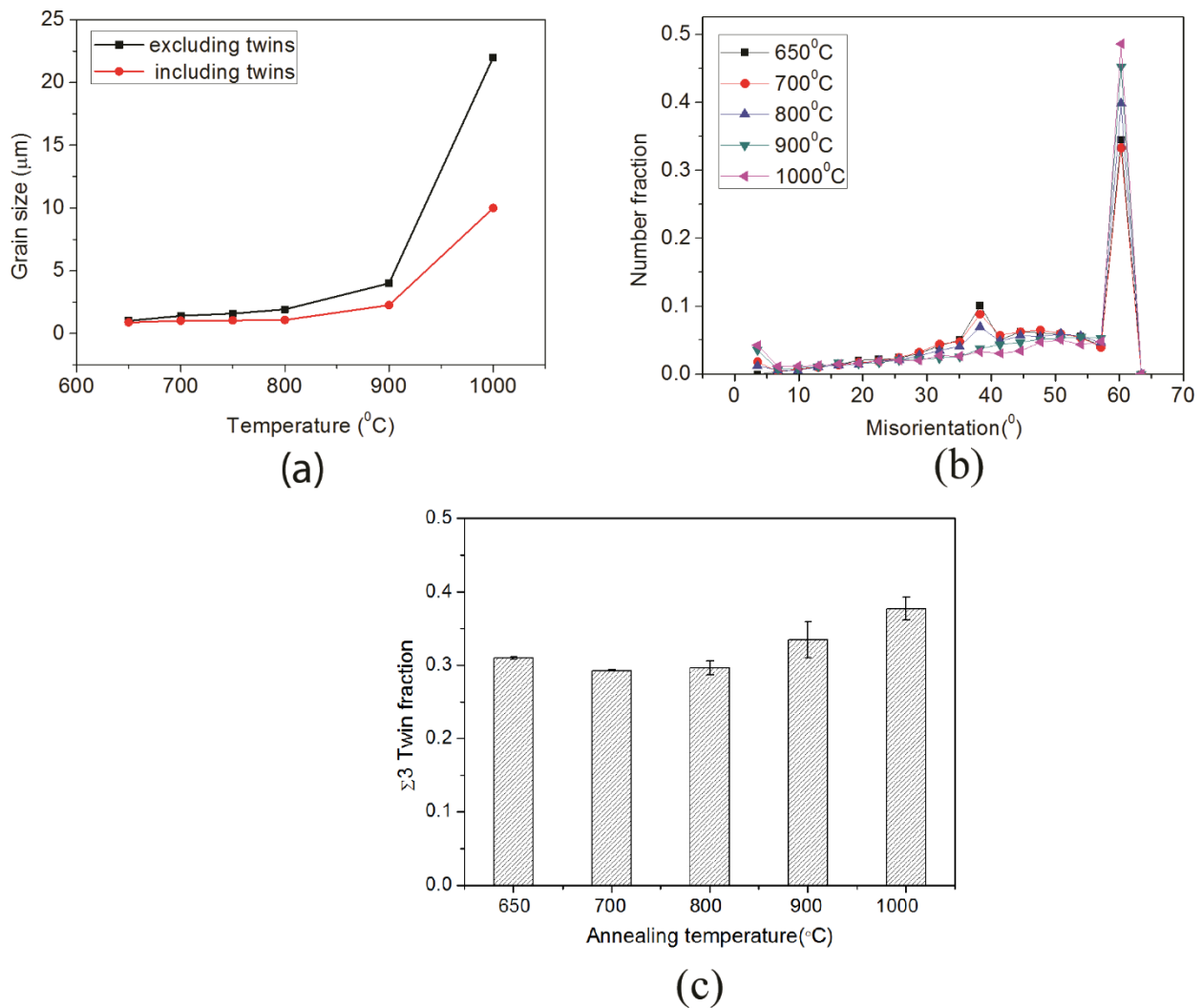
Fig.4.11: Variation of (a) grain size, (b) misorientation angle and (c) fraction of TBs with annealing temperature.
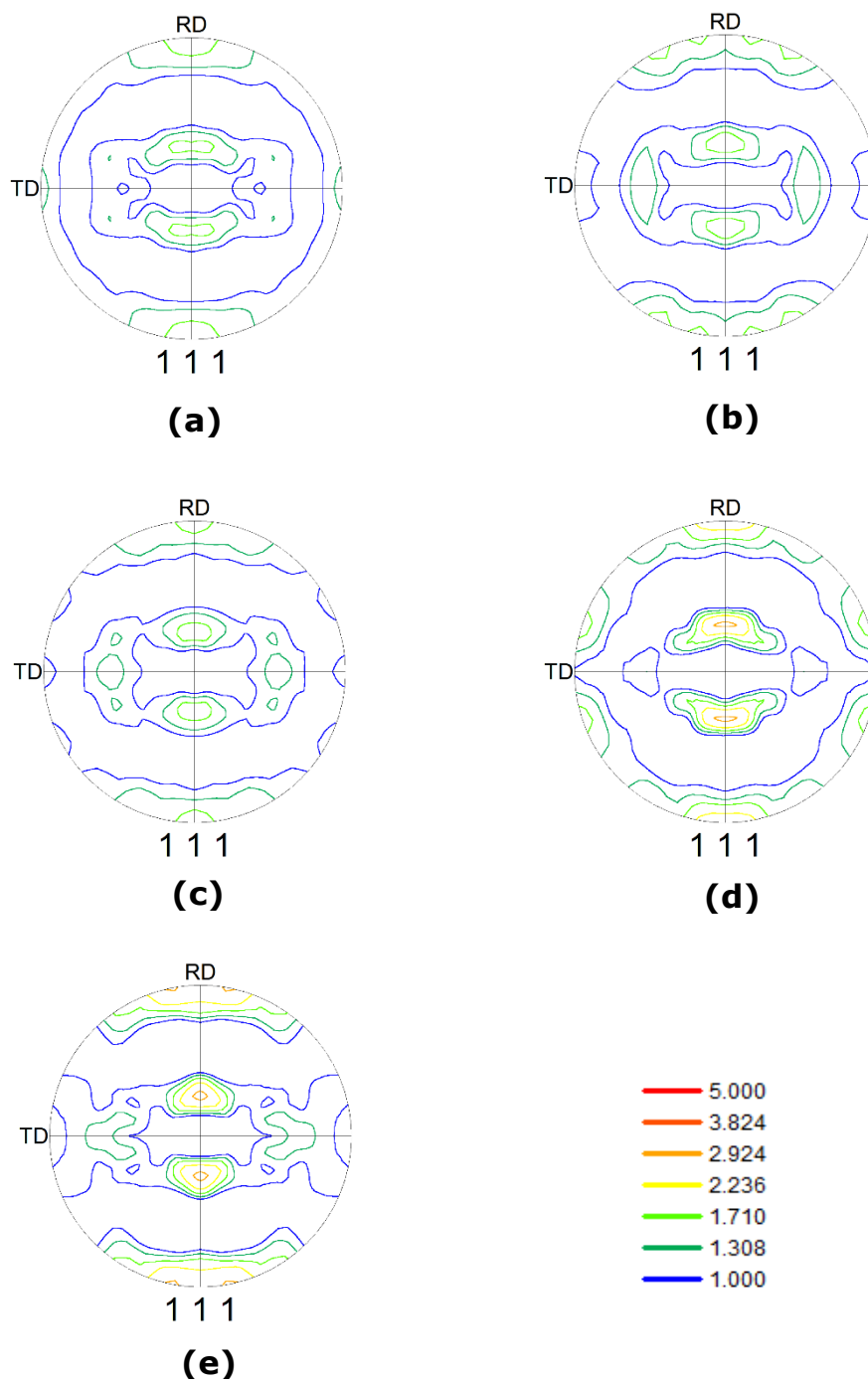
Fig.4.12: (111) PFs of 90% cold-rolled material annealed at (a) 650°C, (b) 700°C, (c) 800°C, (d) 900°C and (e) 1000°C.

In order to further understand the evolution of recrystallization texture, Fig.4.13 is presented which shows the relevant ODF sections ($\varphi_2$=0°, 15°, 35°, 45° and 65°) of the 90% cold-rolled specimen after different annealing treatments. Fig.4.13(a) shows the ODF sections of the 90% cold-rolled specimen after annealing at 650°C. The intensity around the cube location is rather weak, which is also consistent with the very low cube volume fraction (~2%). Since low cube volume fractions are observed in other annealed materials, this aspect will not be discussed further. However, the $\varphi_2$=0° section clearly indicates the development of the α-fiber (<110>// normal direction (ND)) which is shown as the skeleton line extending from the G to the Rt-G through G/B, $B_S$ and G/B(T) (Refer to Table 4.2 for ideal notations for these orientations). The intensity distribution along the α-fiber shows relatively strong intensity at the G/B location (Fig.4.13(a)). The significant presence of the G/B orientation could also be confirmed from the orientation map in Fig.4.10(a) (highlighted in rose). The significant presence of the Bs component (highlighted in green) is also noticed in the orientation map while other α-fiber orientations, such as, G (highlighted in orange), G/B(T) (highlighted in dark green) and Rt-G (highlighted in tan) are present as minor components. This is also in good agreement with the intensity distribution along the α-fiber. However, the volume fraction of the Bs component at 650°C annealed condition is much lower than the volume fraction observed in 90% cold-rolled condition. The total volume fraction of the α-fiber components (defined by the sum of the volume fractions of G, G/B, Bs, A and Rt-G) is ~25%. The $\varphi_2$=15° section (Fig.4.13(a)) shows noticeable intensity at the vicinity of ($\varphi_1,\Phi,\varphi_2$=27°,64°,15°), corresponding to {142}<211> (K). The volume fraction of this component is ~7%. The $\varphi_2$=35° section shows intensity at the ($\varphi_1,\Phi,\varphi_2$=80°,31°,35°) location corresponding to the brass recrystallization texture component (BR) {236}<385>. The orientation map reveals significant presence of this component (highlighted in indigo, volume fraction ~ 7%). The $\varphi_2$=45°, $\varphi_2$=65° sections of the ODFs and the orientation map (Fig.4.10(a)) show the presence of the Cu (highlighted in

red) and S (highlighted in yellow) orientations. The volume fractions of these two components are ~3% and 5%, respectively. However, another orientation at ($\varphi1,\Phi,\varphi2=80°,31°,65°$) corresponding to {13 6 25}<-20 -15 4} (designated as the M orientation) is observed (highlighted in cyan in Fig.4.10(a)) having volume fraction ~7%. The {113}<332> orientation (highlighted in wine) shows a volume fraction of ~4%. The total volume fraction of the random components (other than those listed in Table 4.2) is rather high in different annealed conditions.

The ODF sections of the materials annealed at different temperatures show evident similarities amongst them. The $\varphi_2=0°$ sections of the ODFs of different annealed materials continue to show the presence of discontinuous α-fiber. The intensity distribution along the α-fiber indicates strong intensities at the G/B and G/B(T) locations after annealing at 900°C. The orientation maps show the spatial distribution of different orientations belonging to the α-fiber (Fig.4.13). The apparent similarities of the ODF sections of different annealed materials indicate the presence of the same texture components. The orientations maps confirm the presence of these components in different annealed materials (Fig.4.10).

The variation of volume fraction of different texture components with annealing temperature is shown in Fig.4.14(b). The plot reveals only minor changes in the volume fractions of different texture components with annealing temperature. The total volume fraction of α-fiber and random components are rather high in all the annealed conditions, as already pointed out.
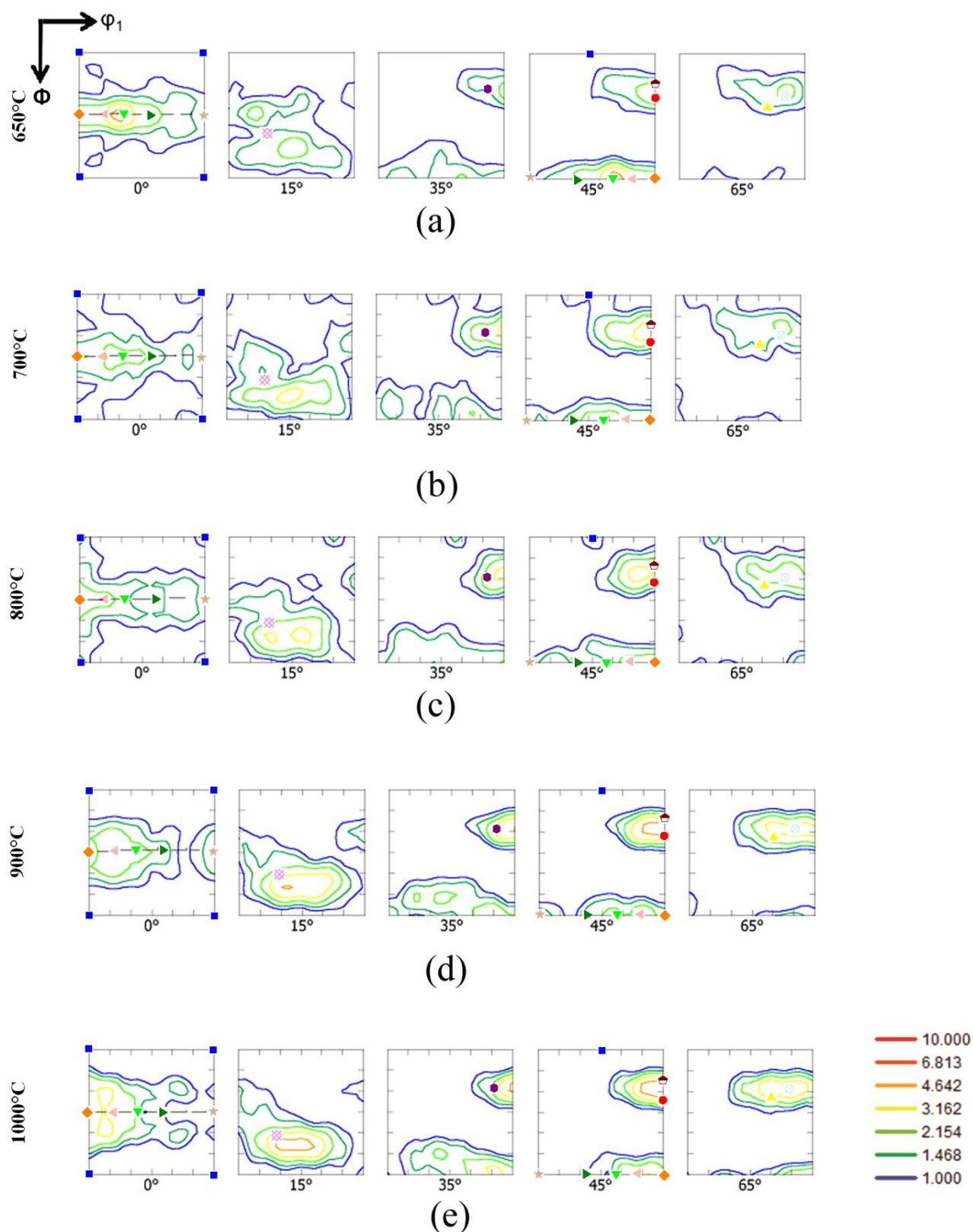
Fig.4.13: φ2=0°, 15°, 35°, 45° and 65° sections of the ODFs of different annealed materials (Refer to Table 4.2 for symbols used in the ODF sections).
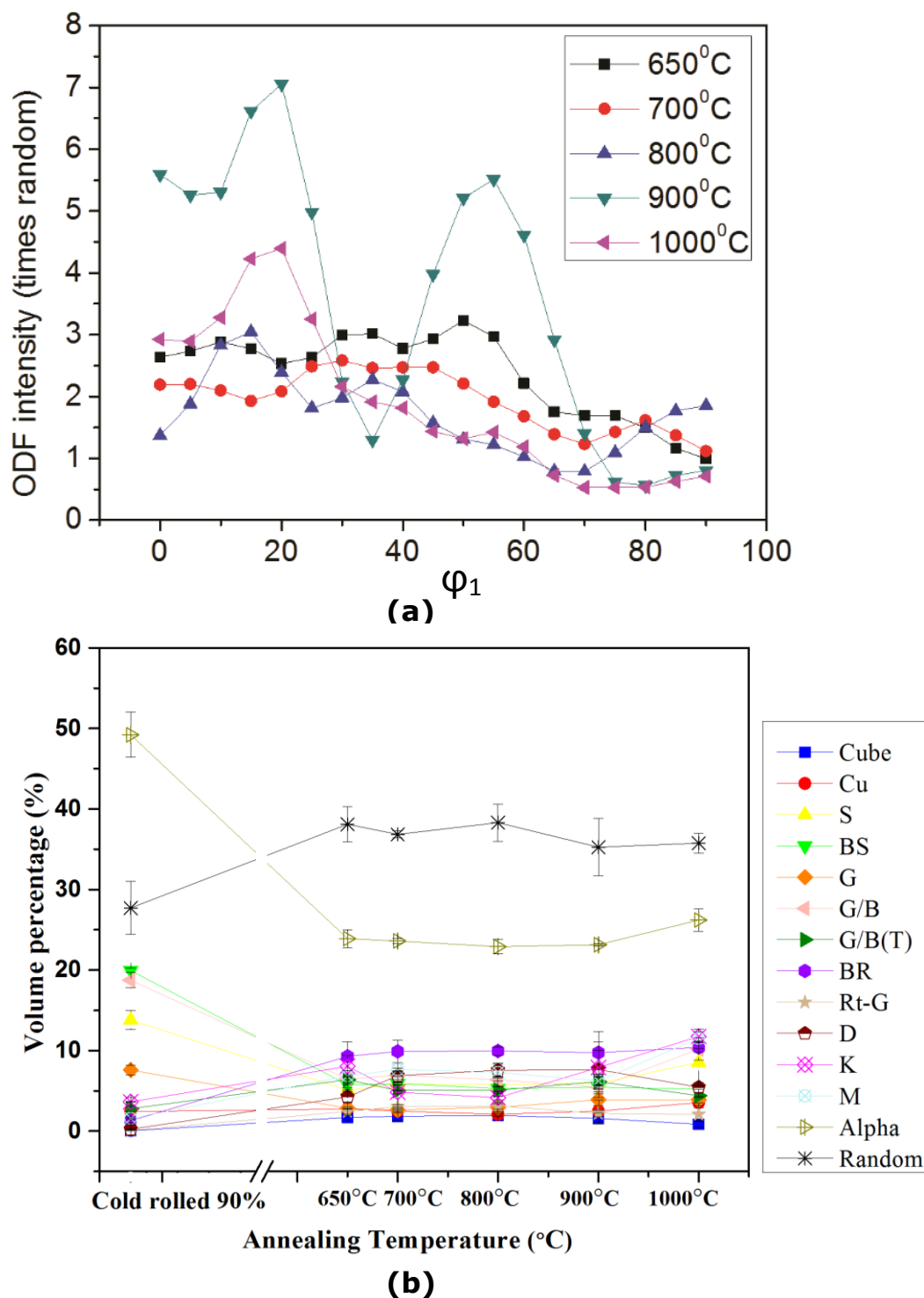
Fig.4.14: Variation of (a) intensity along the α-fiber and (b) volume fraction of different texture components with annealing temperature.

## 4.4 Evolution of mechanical properties during TMP

Tensile tests are selectively carried out to unveil the effect of TMP processing on the evolution of mechanical properties. For this purpose tensile tests are carried out for the 90% cold-rolled and subsequently annealed specimens. Fig.4.15 depicts the engineering stress-strain plots of the cold-rolled and different annealed HEA.

After 90% reduction in thickness, the UTS value and elongation to failure is ~ 1520 MPa and ~ 4 %. Therefore, the strength is definitely in the ultrahigh strength regime but the ductility is rather limited. Following annealing at 700°C the UTS decreases to ~ 1050 MPa (i.e. still in the ultrahigh strength regime) but the ductility is enhanced appreciably (~ 11%). Interestingly the stress-strain plot also shows a discontinuous yielding behavior (enclosed in circle). Upon annealing at 800°C the UTS is decreased further (~900 MPa) accompanied by remarkable increase in ductility (~26 %). Further annealing at 1000°C results in drastic decrease in strength (~650 MPa) with concurrent increase in ductility (~30%). The tensile test data are summarized in the Table 4.3.
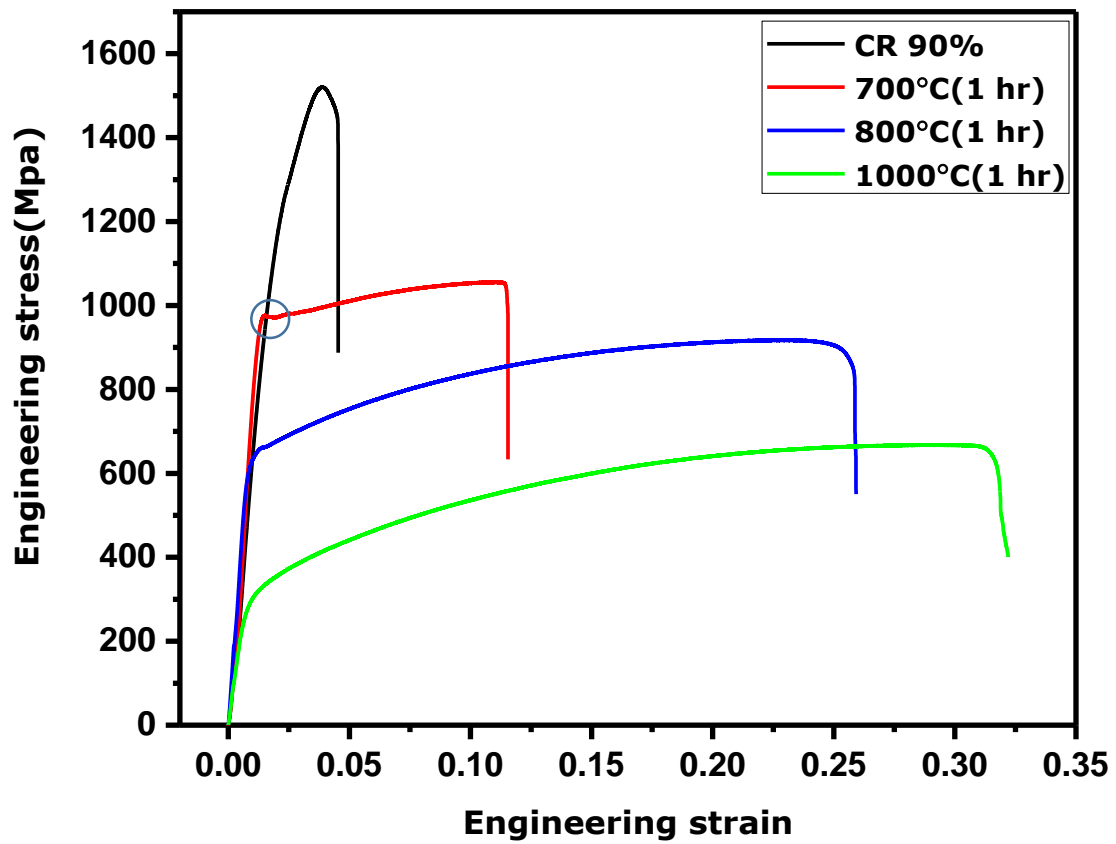
Fig.4.15: Engineering stress-strain plots of the 90% cold-rolled and annealed HEAs. CR is abbreviated for the as cold-rolled condition.

Table 4.3: Mechanical properties of 90% cold-rolled and annealed materials.

| TMP Conditions | YS (MPa) | UTS (MPa) | Elongation to failure (%) |
|---|---|---|---|
| 90% Cold-rolled | 1135 | 1520 | 4 |
| 90% cold-rolled and annealed at 700°C for 1hr | 972 | 1055 | 11 |
| 90% cold-rolled and annealed at 800°C for 1hr | 631 | 917 | 26 |
| 90% cold-rolled and annealed at 1000°C for 1hr | 294 | 667 | 31 |

## 4.5 Discussion

*4.5.1 Evolution of microstructure and texture during cold-rolling*

The major observation concerning the development of deformation microstructure in the HEA is the presence of lamellar microstructure co-existing with heavily fragmented regions. The deformation texture appears to be predominantly copper type up to 60% deformation and transforms to predominantly brass type after 90% reduction in thickness. The texture after 80% reduction in thickness appears to be intermediate, where the volume fraction of the Bs component is comparable to that of the S component.

It might be noted that solid solution formation usually lowers the SFE and in a multicomponent HEA system significant reduction of SFE might be expected. The SFE of the present alloy estimated through first principle calculation is ~18-25 mJ m$^{-2}$ [76, 77]. The transition of texture from predominantly copper type to predominantly brass type, thus indirectly confirms the rather low SFE of the HEA.

The phenomenon of texture transition has been investigated extensively [51, 87]. It has been hypothesized by Wasserman [88] that the texture transition is due to a volume effect of deformation twins. Accordingly Hirsch et al [89] have proposed that irrespective of the SFE, a copper type rolling texture develops at initial stages of deformation. At higher strains (>50% reduction in thickness) deformation twins rotates copper oriented grains into the {552} <115> orientation, which finally leads to the development of brass texture following a sequence of complex crystal rotation path. Although, deformation twins are observed in low SFE materials, the volume effect of deformation twins has been negated by other researchers. Leffers et al [51]  have consistently argued that low SFE materials deviate from pure copper type texture at very early stages of deformation thereby negating the volume effect of deformation twins [88]. They have emphasized the importance of latent-hardening caused due to the closely spaced twin lamellae. On the other hand, Duggan et al [90] concluded that

while the phenomenon of texture transition is evident and amply corroborate the presumed, the actual mechanism of texture transition remains inconclusive.

In the present HEA deformation twins could not be identified in the heavily deformed condition due to the very fine and closely spaced nature of these twins, often beyond the resolution limit of EBSD. However, extensive formation of deformation twins has been reported by careful TEM studies [73, 81] which is consistent with the observed texture transition in the present study.

### 4.5.2 Evolution of microstructure during annealing

The development of near ultrafine microstructure is observed during annealing. Remarkable resistance against grain coarsening is observed during annealing at least up to 800°C (Fig.4.9). The Recrystallization temperature of the present alloy is around 700°C as observed in Fig.4.10 (b). As a rule of thumb, the upper bound of recrystallization temperature is approximately ~0.5 $T_m$ ($T_m$ is the melting point in Kelvin temperature). Thus, the predicted upper-bound recrystallization temperature is around 508°C because the solidus temperature of the present alloy as determined by using DSC measurement (Fig.4.16) is 1289°C whereas the liquidus temperature is 1339°C. It is apparent that the temperature for complete recrystallization is 700°C or ~0.62$T_m$, which is higher than the usual upper bound ~0.5 $T_m$. Similar observation of recrystallization temperature much higher than 0.5$T_m$ has been reported in high-entropy alloy Al0.5CoCrCuFeNi [91]. For a further comparison, Ni with melting point 1453°C has a recrystallization temperature range of 300°–600°C (0.33 – 0.5$T_m$) depending on its impurity [50]. In addition, TWIP steels with low SFE show much lower recrystallization temperature and can be completely recrystallized in 100 seconds at 700°C [92].
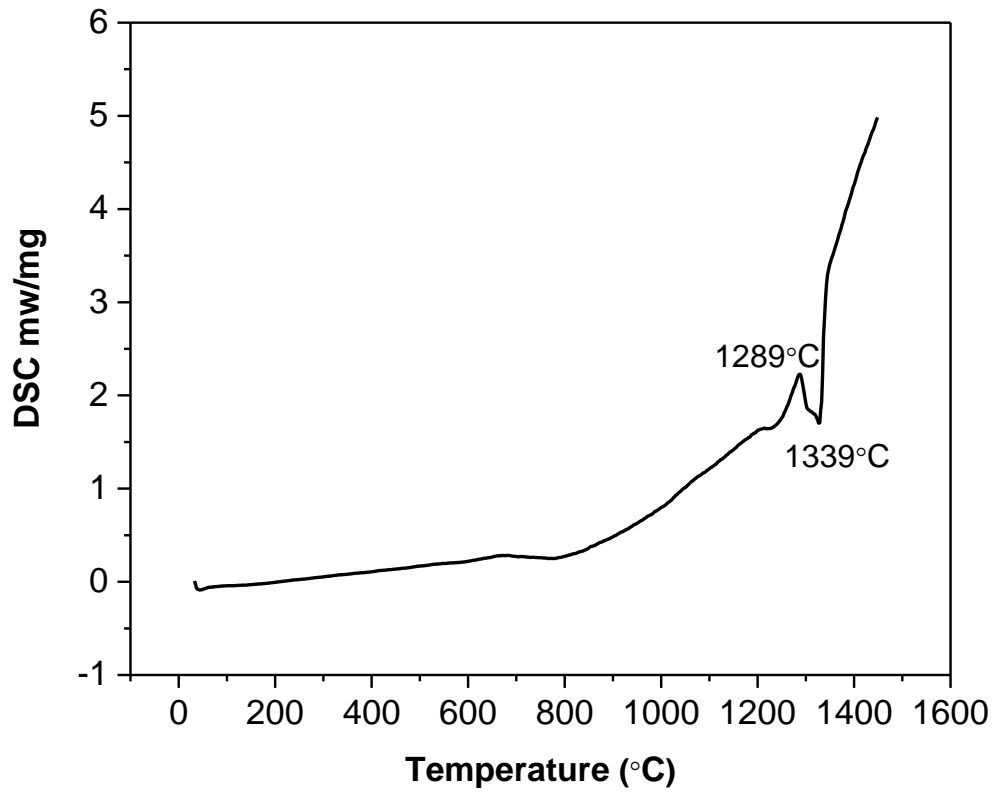
Fig.4.16: DSC plot of the 90% cold-rolled material.

Evolution of fine grain size and high recrystallization temperature in the present HEA could be explained by the formation of the whole–solute matrix. Three affecting routes are proposed:

1. decrease in the driving force for nucleation of new grains and grain growth.
2. decrease in the grain boundary migration rate
3. increase in the density of potential nucleation sites

Firstly, the whole-solute matrix inherently has severe lattice distortion because of the fact that each and every atom in the matrix has strain energy due to the atomic size differences from its neighboring atoms. The dislocation energy, SFE and grain boundary energy would be lowered by the amount of strain energy associated with the severely distorted matrix. As a result, driving force for recrystallization in eliminating dislocations and stacking faults, and grain growth in reducing total boundary energy is effectively reduced [50].

Secondly, sluggish diffusion due to the whole-solute matrix reduces the grain boundary migration rate since boundary migration requires atoms jumping across the boundaries i.e. ease of diffusion in the matrix. Recently, the sluggish diffusion behavior of the present HEA system has been reported and discussed [28]. Liu et al [29] have investigated the present HEA and reported a rather high value of activation energy ($\sim$ 321 kJ mol$^{-1}$) and slow grain growth kinetics during annealing, which is in good agreement with the sluggish diffusion effect. These two factors account for the high recrystallization temperature and low grain growth, resulting in the formation of near ultrafine grain size after recrystallization. Moderate grain coarsening is observed after annealing at 1000°C. It could be attributed to the sufficiently high thermal energy at such higher temperatures, which gradually reduces the sluggish diffusion effect in the whole-solute matrix.

The evolution of the GBCD during annealing in the present HEA is an interesting aspect and shown in Fig.4.11 (c). The GBCD is not vastly different during annealing at 650°C, 700°C and 800°C. Almost similar fractions of annealing TBs are observed at these annealing temperatures. Since the grain growth is very limited at these annealing conditions, the GBCD distribution is not affected. After annealing at 900°C, the fraction of annealing TBs increases significantly with increasing annealing temperatures while the HAGB fraction decreases. In addition, the fraction of LAGBs is not affected during annealing at different temperatures and remains almost unchanged. This is consistent with the fact that reduction of grain boundary energy during grain growth is achieved by increasing the TB fraction with an accompanying decrease in the HAGB fraction. This is understandable based on the fact that the TB energy is rather small as compared to those of the random HAGBs [92]. The tendency to eliminate the HAGBs as compared to the annealing TBs is stronger in this present HEA.

The observed increase in the TB fraction with increasing grain size is consistent with the mechanism proposed by Fullman and Fischer [93]. They have explained that the annealing TB formation during grain growth is promoted by the migration of triple points which results in lowering of the total boundary energy. During the continued migration of the triple points, the original grains are replaced by new grains, resulting in the formation of new twins and further lowering of energy. This process is evidently related to the migration distances which are comparable to the grain size. As a consequence, the twin density is expected to be proportional to the grain size.

### 4.5.3 Evolution of texture

It is instructive to compare and contrast the observed recrystallization texture of the HEA with those of the other known low SFE alloys, for example, the 70:30 brass and TWIP steels. It must be pointed out that while the development of a brass-type texture during cold-rolling in low

SFE alloys is widely recognized [51, 87], there is much less clarity regarding the recrystallization texture of cold-rolled low SFE alloys. Focusing on the heavy deformation regime (which is of greatest interest for the present study), low temperature annealing of heavily deformed 70:30 brass results in the formation of the well-known brass recrystallization component {236}<385>. However, the recrystallization texture is strongly influenced by starting grain size, annealing temperatures and imposed strain. Besides, alloy composition is also an important factor. Bracke et al [92] have recently summarized the literature pertaining to the effects of processing and microstructural parameters on the recrystallization texture of various grades of TWIP and austenitic stainless steels having low SFE values 15-45 mJ m$^{-2}$. The majority of the published work report the retention of the rolling texture components with particularly strong B$_S$ and development of α-fiber components (include G, G/B, B$_S$ and G/B(T)) in the recrystallization texture [92, 94, 95].

While continuous recrystallization or extended recovery can result in the retention of deformation texture, this has been ruled out by clear evidence of the presence of recrystallization front [92]. The most plausible explanation of retention of deformation texture components in the recrystallization texture of low SFE alloys seems to be a consequence of nucleation of recrystallization in a rather energetically homogenous deformation structure which is effective in suppressing preferential nucleation [92, 96]. In contrast, some researchers have reported very weak or even randomized texture in TWIP steels upon cold-rolling and annealing [97, 98]. The weak or randomized texture has been attributed to the nucleation at micro shear bands [97, 99], large starting grain size prior to cold-rolling [96] or profuse annealing TB formation during recrystallization owing to low SFE [100].

In the present case the recrystallization texture of the HEA shows the presence of the deformation texture components, such as S and α-fiber components. The volume fraction of the BR component is not significantly

greater than other components. As already pointed out, the volume fractions of different components do not reveal any significant variation with annealing temperature.

It would be particularly interesting to compare and contrast the present observations with those reported by Haase et al [101] in a Fe-28Mn-0.8C TWIP alloy cold-rolled to 80% reduction in thickness and annealed at 700°C for 300 seconds to achieve complete recrystallization. The authors have observed that the volume fraction $B_S$ is definitely more than that of the S and other α-fiber components in the fully-recrystallized state. The high fraction of $B_S$ is attributed to the preferential nucleation from shear bands present in the heavily deformed materials [94, 101]. However, unlike the TWIP steels, $B_S$ and G are not particularly strong in the HEA.

In order to reveal the reasons for the observed similarity and differences with the TWIP steels, it is necessary to investigate the early stages of recrystallization. The EBSD map and (111) PF of a 90%-deformed sample annealed at 700°C for 60 seconds is shown in Fig.4.17(a) and Fig.4.17(c), respectively. The deformed regions show internal LAGB network. The average recrystallized volume fraction is low (~15%) in this annealed condition. The deformed regions are separated from the recrystallized regions by using internal misorientation (defined as Kernel Average Misorientation or KAM). The local misorientation within a grain can be characterized by using the KAM approach [83]. Fig.4.18 shows the schematic diagram of KAM approach. Here misorientation between a grain at the center of the kernel and all points at the perimeter of the kernel are measured. The local misorientation value assigned to the center point is the average of these misorientations. Options are available to use only the points at the perimeter of the kernel or to use all the points in the kernel. In the present work up to the third nearest neighbor is considered for calculating the KAM with tolerance angle of 5°.

The recrystallized grains are defined as those having KAM<1° and grain size (area) ≥ 0.2 μm². Additionally, a further check is carried out to ensure

that such grains are bounded by HAGBs. It is clearly seen from the orientation map (Fig.4.17(b)) and the (111) PF (Fig.4.17(d)) that the recrystallized grains at an early stage of recrystallization have orientations very close to those already present in the deformed matrix. The retention of the deformation texture components even at the early stages of nucleation rules out the possibility of strong preference for orientation selection during recrystallization. This is further corroborated by the partitioning of different texture components (except the $B_S$ component which will be discussed later) rather equally between the recrystallized and deformed fraction (Fig.4.17(e)). The nucleation of recrystallization happens rather homogenously throughout the deformed microstructure having rather homogenous microtexture (Fig.4.17). Thus, in the absence of strong preferential orientation selection, the deformation texture components are retained. The evident similarities of the (111) PF of recrystallized fraction at an early stage of recrystallization (Fig.4.17(d)) and those of fully recrystallized materials annealed at different temperatures (Fig.4.12) clearly indicate that it is a characteristic of the recrystallization process in HEA which is consistent over a wide range of temperatures. This indicates similar recrystallization texture formation mechanism affected by the energetically homogenous deformed matrix as proposed by Bracke et al [92].
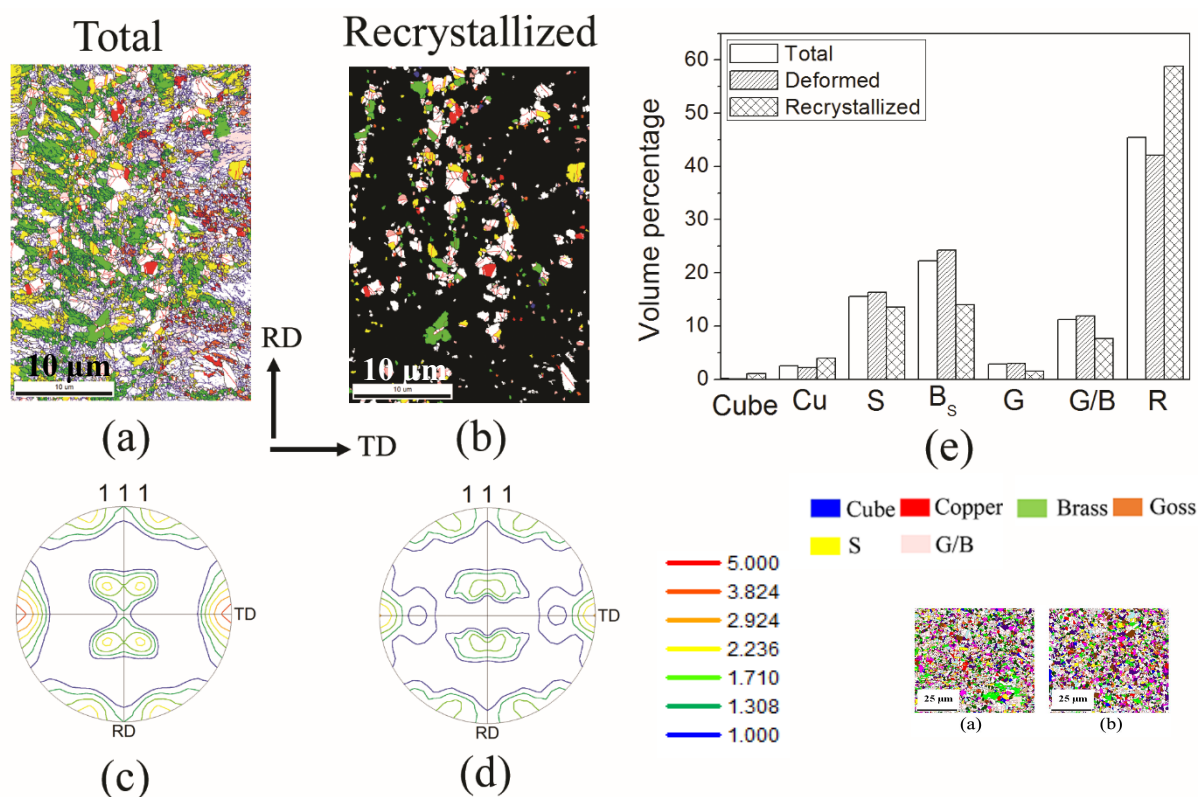
Fig.4.17: (a) Orientation map of partially recrystallized HEA following annealing at 700°C for 60 s. (b) shows the recrystallized regions in 90% cold-rolled material; (c) and (d) are the corresponding (111) PFs (e) shows the distribution of volume fractions of different texture components in total, deformed, and recrystallized regions.
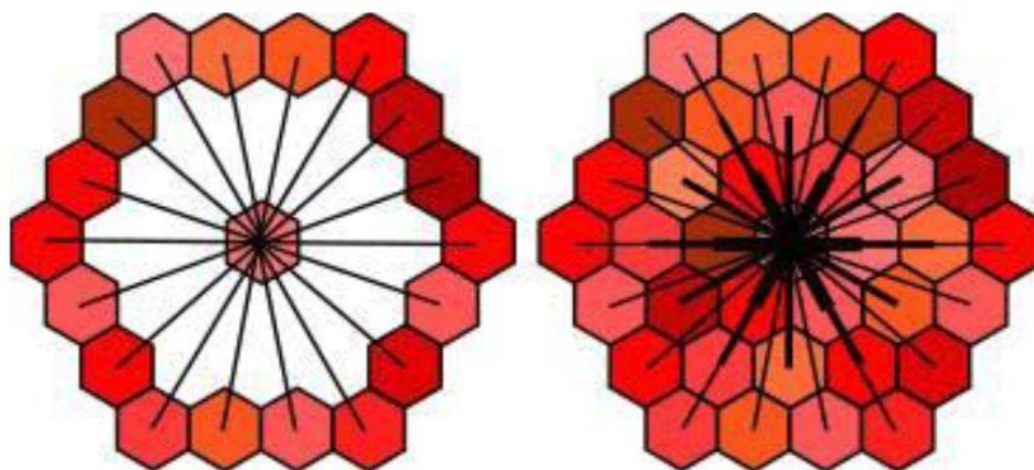
Fig.4.18: Schematic diagram showing the (a) misorientation between a grain at the center and all other points at the perimeter of the kernel and (b) misorientation between a grain at the center and all points in the kernel.

However, it is noted that even at the early stages of nucleation the $B_S$ is not the dominant component. This is convincingly supported by the comparison of the (111) PFs obtained from the total scan area (Fig.4.17(c)) and the (111) PF obtained from the recrystallized fraction (Fig.4.17(d)) and distribution of the different texture components amongst the deformed and recrystallized fractions (Fig.4.17(e)). It is easily observed that while the texture components other than $B_S$ are more or less equally distributed amongst the deformed and recrystallized fractions, $B_S$ has a significantly higher presence in the deformed fraction as compared to that in the recrystallized fraction. The possible reason for this is attributed to the slower recrystallization rate in the near $B_S$-oriented regions which are gradually consumed by the neighboring growing recrystallized grains. This is amply corroborated by the orientation map of the 650°C-annealed condition (Fig.4.10(a)), where the remaining deformed regions exclusively possess near $B_S$-orientation. Thus, the observed differences in recrystallization texture of HEA with those of the TWIP and austenitic steels i.e. weaker $B_S$ component in the HEA appears to be due to the slower recrystallization rate of the near $B_S$- oriented regions. From the results reported on TWIP steel by Haase et al [101] and on 316 steel by Donadille et al [94] where presence of stronger $B_S$ and G component in the recrystallization texture could be attributed to the preferential nucleation of this component from shear bands, it appears that shear bands in the HEA do not have near $B_S$-orientation (Fig.4.16(a)) and such preferential nucleation of $B_S$-oriented grains from shear bands does not occur in HEA.

The development of strong BR component also involves preferential nucleation at shear bands and subsequent growth. Therefore, the absence of strong BR component is also consistent with the absence of strong preferential nucleation in the experimental HEA. In the similar way, the origin of strong {113}<332> component also necessitates preferential growth. As already observed, the different texture components do not

reveal any significant change with annealing temperature which rules out the possibility of strong preferential growth.

It is important to note the development of strong α-fiber (<110>//ND) component A ($(110)[1\bar{1}1]$). The absence of a large fraction of the A component in the deformation texture (~2-5%) shows that formation of profuse annealing twins plays an important role in the formation of this significant α-fiber component. Formation of a near complete α-fiber due to annealing twins has also been reported in cold-rolled and annealed TWIP steels [101]. In particular, the α-fiber component A ($(110)[1\bar{1}1]$) is twin related to G/B orientation [95]. This is most clearly visible from the orientation map of the 900°C- and 1000°C-annealed materials (shown by the arrow marks in Fig.4.10(d,e)). The low SFE of the present alloy enhances the formation of annealing twins, which in turn enhances the formation of the α-fiber component A. Few of the other orientations mentioned in the present study for e.g. the K and M orientations have also been observed and reported in the recrystallization texture of austenitic stainless steels [102].

*4.5.4 Evolution of mechanical properties during TMP*

The tensile tests have been carried out mainly to quantify the changes during TMP processing. It is clearly observed from the Fig.4.15 that a remarkable combination of strength ductility may be achieved after annealing the 90% cold-rolled material at 700°C and 800°C. It is interesting to note that both these annealed conditions correspond to the formation of ultrafine recrystallized microstructure. The enhancement of ductility at the expense of strength at higher annealing temperatures follow the usual behavior.

An interesting observation is the discontinuous yielding behavior of the material annealed at 700°C. This phenomenon has also been observed in other ultrafine grained materials. However, an in-depth analysis is beyond the scope of this work and needs to be investigated further. Overall, it is apparent that controlled TMP processing routes yielding ultrafine microstructure may be very effective means for tuning the properties of single phase FCC HEAs.

# -: CHAPTER 5 :-

## *Comparison of microstructure and texture evolution during grain growth in low SFE CoCrFeMnNi HEA and Ni-60wt.%Co*

## 5.1 Comparison with low SFE Ni-60wt.%Co alloy

In Chapter 4, the evolution of microstructure and texture in CoCrFeMnNi HEA during heavy deformation and annealing is analyzed. In order to achieve that, the CoCrFeMnNi HEA is heavily cold-rolled to 90% reduction in thickness and then isochronally annealed for 1hr at different temperature ranging from 650°C to 1000°C. The characteristic differences with the recrystallization texture of low SFE alloys, such as TWIP and austenitic steels have also been highlighted. While such comparisons are quite useful, these steels are evidently different from the multicomponent HEAs.

Recently, Zaddach et al has estimated that the SFE of CoCrFeMnNi HEA alloy is ~ 18 mJ m$^{-2}$ to 25 mJ m$^{-2}$ [76, 77]. The SFE, thus, appears to be very similar to the SFE of the FCC Ni-60wt.%Co alloy ~15 mJ m$^{-2}$ to 20 mJ m$^{-2}$ [103-105]. Secondly, Ni-60wt.%Co is also a highly solute rich alloy, very similar to the HEA. However, unlike the whole solute matrix HEA, the Ni-60wt.%Co alloy is not a multicomponent system. It is anticipated that the effect of multicomponent solid solution formation on microstructure and texture evolution of the present HEA could be understood in depth by way of comparison with Ni-60wt.%Co alloy. Consequently, the major focus of the present chapter is to compare and contrast the microstructure and texture formation during grain growth in equiatomic CoCrFeMnNi HEA and Ni-60wt.%Co alloy.

## 5.2 Starting Microstructure of Ni-60wt.%Co and HEA

Fig.5.1(a) and Fig.5.1(b) show the GB maps of the starting Ni-60wt.%Co and CoCrFeMnNi alloys, respectively. The GB maps show fully recrystallized conditions. The presence of few large recrystallized grains along with the clusters of small recrystallized grains can be observed in both the maps. The recrystallized grains are separated by HAGBs (indicated in black color in Fig.5.1(a) and Fig.5.1(b)). The microstructures also show the presence of profuse Σ3 annealing twin boundaries (TBs). The number fraction of the Σ3 annealing TBs in the starting Ni-60wt.%Co is ~ 33% and in CoCrFeMnNi HEA is ~36%. Fig.5.1(c) and Fig.5.1(d) show the grain size distribution of the two starting materials. In both the cases similar distribution characterized by a large fraction of grains in the smaller size range (<10μm) and a small fraction of grains in the larger size range could be observed. The average grain size of the two starting materials is very similar ~ 7 μm (excluding the annealing twins).

## 5.3 Deformation microstructure and texture of Ni-60wt.%Co and HEA

Fig.5.2 shows the microstructure (IQ maps) of the two starting materials following cold-rolling to 90% reduction in thickness. The microstructure of the cold-rolled Ni-Co (Fig.5.2(a)) and HEA (Fig.5.2(b)) show lamellar banded morphology extended parallel to the RD. The $\varphi_2$=0°, 45° and 65° sections of the ODFs of 90% cold-rolled Ni-Co and HEA is shown in Fig.5.2(c) and Fig.5.2(d), respectively. The color codes and symbols used in the ODFs and the orientation maps are already shown in Chapter 4 but reproduced here in Table 5.1 for ease of referencing.

The respective ODF sections of the two materials appear similar and indicate the presence of typical FCC rolling texture components, namely brass or Bs ({110}<112>)(highlighted in green), S ({123}<634>) (highlighted in yellow), Goss or G ({110}<001>) (highlighted in orange) and copper or Cu ({112}<111>) (highlighted in red).

The $\varphi_2$ = 0° and 45° sections of the ODFs of Ni-Co (Fig.5.2(c)) and HEA (Fig.5.2(d)) show higher intensities at the Bs location as compared to the Cu and S locations. The volume fractions of typical rolling texture components in the two cold-rolled materials are compared in Fig.5.3. The plot shows the presence of much stronger $B_S$ component than Cu ({112}<111>) and S ({123}<634>) components. In addition, Fig.5.3 also shows a noticeable volume fraction of the G/B component ({110}<115>) which lies on the α-fiber midway between the G and Bs locations, as may be clearly seen from the $\varphi_2$=0° section. Fig.5.2 and Fig.5.3 clearly show that the cold-rolling texture of the two materials may be considered rather similar, qualitatively and quantitatively.
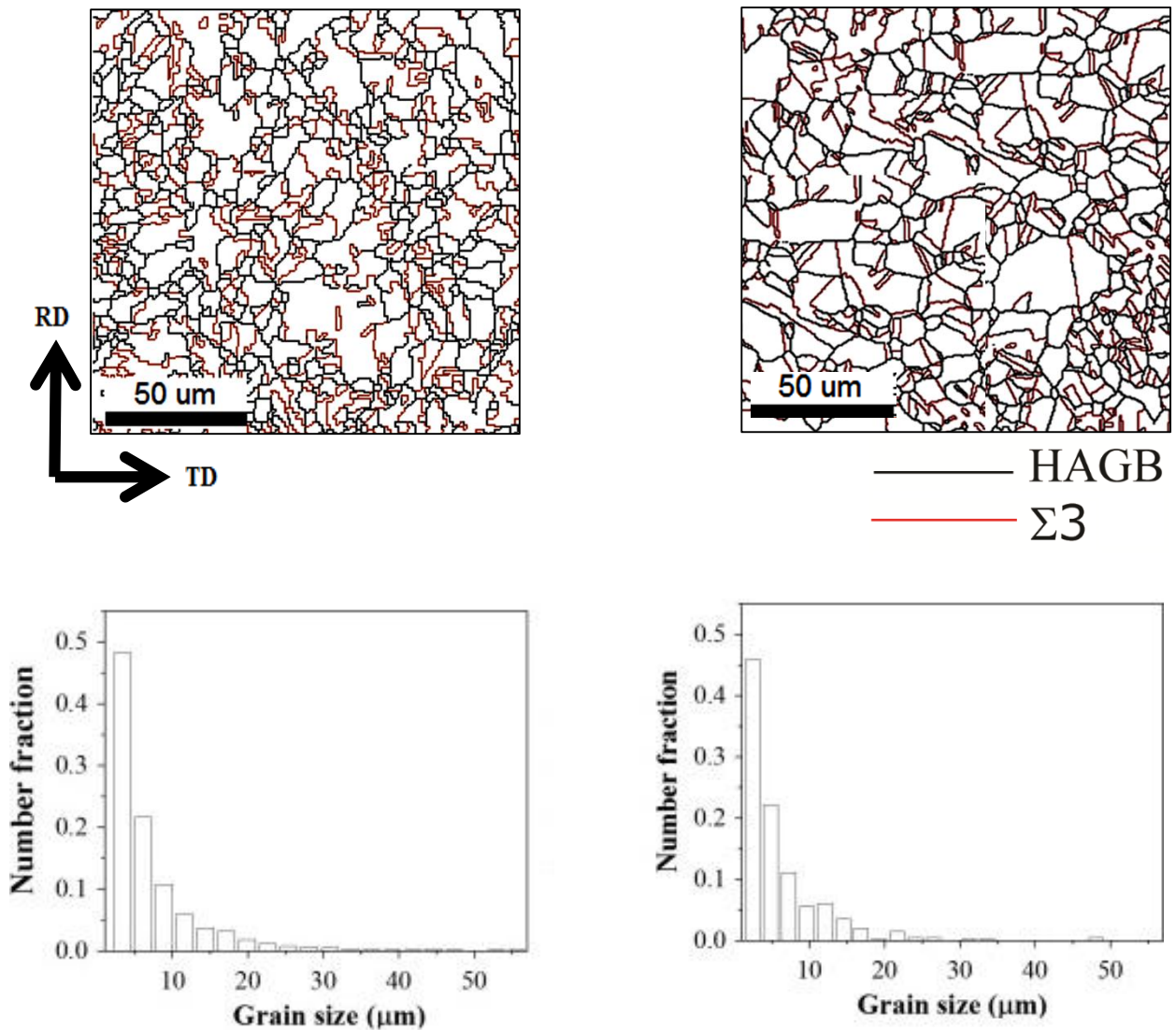
Fig.5.1: Microstructure of starting materials of (a) Ni–Co and (b) HEA (RD is the rolling direction and ND is the normal direction); (c) and (d) show the grain size distribution of starting Ni–Co and HEA, respectively.
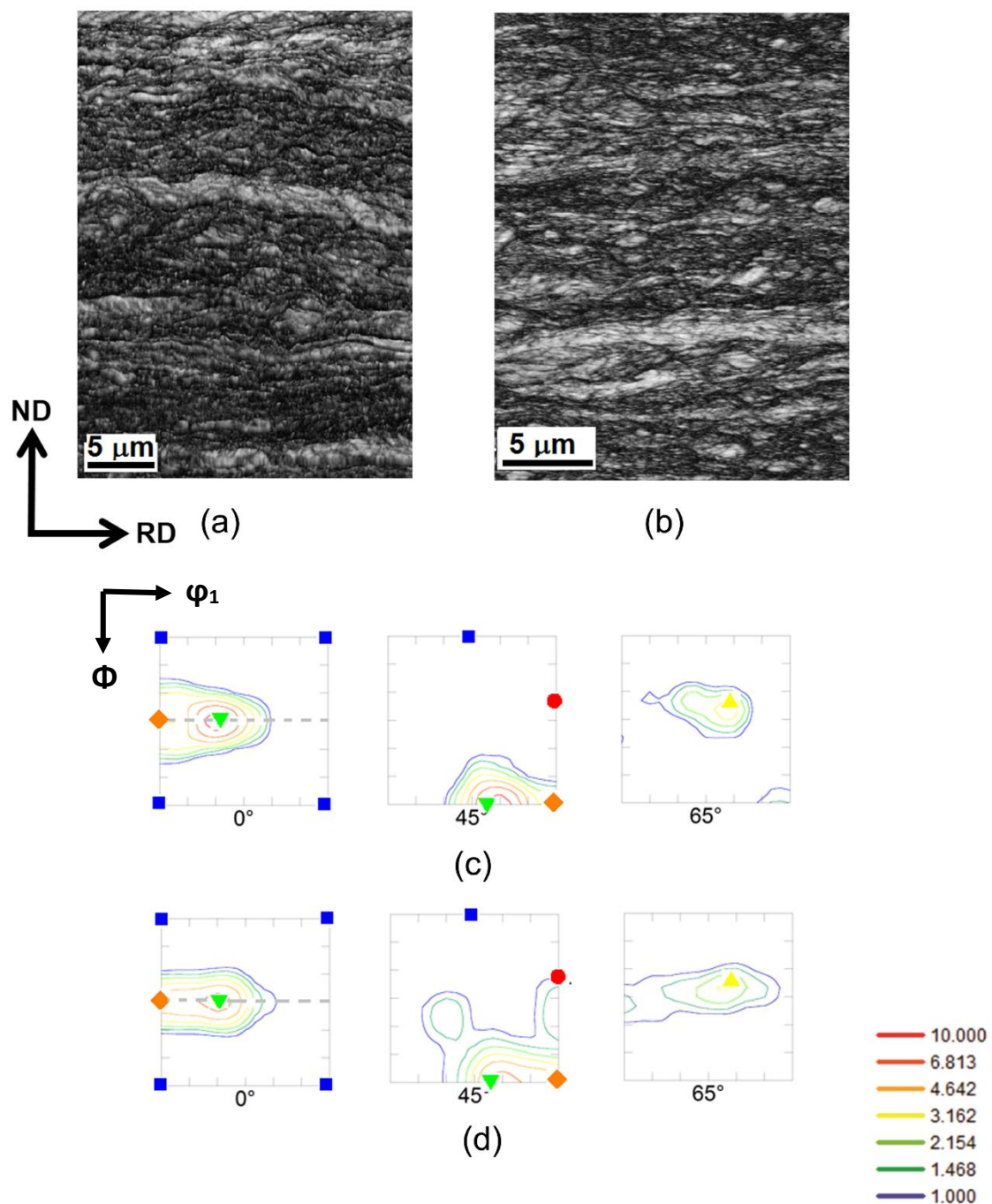
Fig.5.2: IQ maps of 90% cold-rolled (a) Ni–Co and (b) HEA. (c) and (d) show the relevant ODF φ₂ sections of 90% cold-rolled Ni–Co and HEA, respectively.

Table 5.1: Euler angles and Miller indices of the important deformation and recrystallization texture components.

| Texture component | Symbol | Euler angle | | | Miller indices |
|---|---|---|---|---|---|
| | | φ₁ | φ | φ₂ | |
| Cube (C) | ■ | 0, 0, 0 | | | {001} <100> |
| Copper (Cu) | ⬟ | 90, 35, 45 | | | {112} <111> |
| S | ▲ | 59, 37, 63 | | | {123} <634> |
| Bs | ▼ | 35, 45, 0 | | | {110} <112> |
| G | ◆ | 0, 45, 0 | | | {110} <001> |
| Rt - G | ★ | 90, 45, 0 | | | {110} <110> |
| G/B | ◀ | 17, 45, 0 | | | {110} <1 1 5> |
| G/B(T) | ▶ | 55, 45, 0 | | | {110} <111> |
| BR | ⬢ | 80, 31, 34 | | | {236} <385> |
| D | ♔ | 90, 27, 45 | | | {1 1 3} <3 3 2> |
| K | ▨ | 27, 64, 14 | | | {142} <211> |
| M | ⊠ | 80, 30, 65 | | | {13 6 25} <20 15 14> |

Fig.5.3: Quantitative analysis of texture components in 90% cold-rolled Ni–Co and HEA.

## 5.4 Evolution microstructure and texture of Ni-60wt.%Co and HEA during annealing

In order to compare the microstructure and texture evolution during grain growth, the 90% cold-rolled samples of the two alloys are subjected to different annealing treatments in a salt bath furnace at temperatures ranging from 600°C to 1000°C for holding time ranging from 1 h to 16 hrs. The objective is to obtain similar average grain size in the two materials. Table 5.2 shows the specific annealing treatments (temperature and time) for the two cold-rolled materials in order to obtain the similar average grain size. For the ease of discussion, heat treatments which yield similar average recrystallized grain size in the two alloys are designated with the same heat-treated condition for e.g. H1 refers to the heat treated condition which yield the average recrystallized grain size of ~5.0 μm in the two alloys. It is clearly observed that in order to achieve similar average grain size, the heat treatment temperature/time is consistently higher in the case of the HEA.

Table 5.2: Heat treatment conditions for obtaining similar average grain size in 90% cold-rolled Ni–Co and HEA.

| Designation | Heat treatment conditions | | Grain size | |
|---|---|---|---|---|
| | Ni-Co | HEA | Ni-60Co | HEA |
| H1 | T = 700°C t= 1h | T=800°C t = 6h | 5.22± 0.03µm | 5.0± 0.10µm |
| H2 | T = 800°C t= 1h | T = 1000°C t= 30 min | 23.75± 0.37µm | 23.73± 1.43µm |
| H3 | T = 1000°C t= 1h | T = 1000°C t= 16h | 58± 6.50µm | 56.68± 6.28µm |

## *5.4.1 Evolution of microstructure during annealing*

Fig.5.4 shows the microstructures of the 90% cold-rolled and annealed Ni-Co (Fig.5.4(a)-(c)) and HEA (Fig.5.4(d)-(f)). The microstructure of Ni-Co in the H1 condition (Fig.5.4(a)) reveals a fully recrystallized state with a large fraction annealing TBs. The microstructure reveals few isolated largely grown grains (marked by arrows) along with grains having much smaller sizes (shown by enclosing circles). The microstructures of the Ni-Co alloy in the H2 (Fig.5.4(b)) and H3 (Fig.5.4(c)) treated conditions continue to show inhomogeneity, evidently distinguished by the presence of preferentially grown large recrystallized grains (marked by arrows).

The microstructure of the HEA in the H1 treated condition also shows slight inhomogeneity as revealed by the regions composed of relatively large recrystallized grains (marked by arrows in Fig.5.4(d)) existing with regions consisting of small grains (enclosed by circles in Fig.5.4(d)). The grain size distribution plots of the two alloys appear similar in the H1 treated condition (Fig.5.5((a),(d)) indicated by similar standard deviation (S.D.) values. The microstructures of the HEA in the H2 (Fig.5.4(e)) and H3 (Fig.5.4(f)) treated conditions appear more uniform as compared to the Ni-Co alloy in the similar treated conditions (Fig.5.4(b)-(c)). The S.D. of the HEA in the H2 treated condition (Fig.5.5(e)) is slightly lower than that of the Ni-Co alloy in the H2 treated condition (Fig.5.5(b)). However, the most remarkable difference could be observed in the H3 treated condition (Fig.5.5 (f)). The largest grains are having a diameter of ≤ 175 μm which is much smaller than that observed in the case of the Ni-Co alloy (~400 μm) in the same treated condition (Fig.5.5 (c)). This is also amply supported by the standard deviation (S.D.) of the grain size distribution of the HEA ~ 34 which is much smaller than that of the Ni-Co alloy ~56 (Fig.5(c)), indicating much narrower or more uniform grain size distribution in the H3 treated condition. Annealing TBs could be clearly distinguished in all the microstructures.
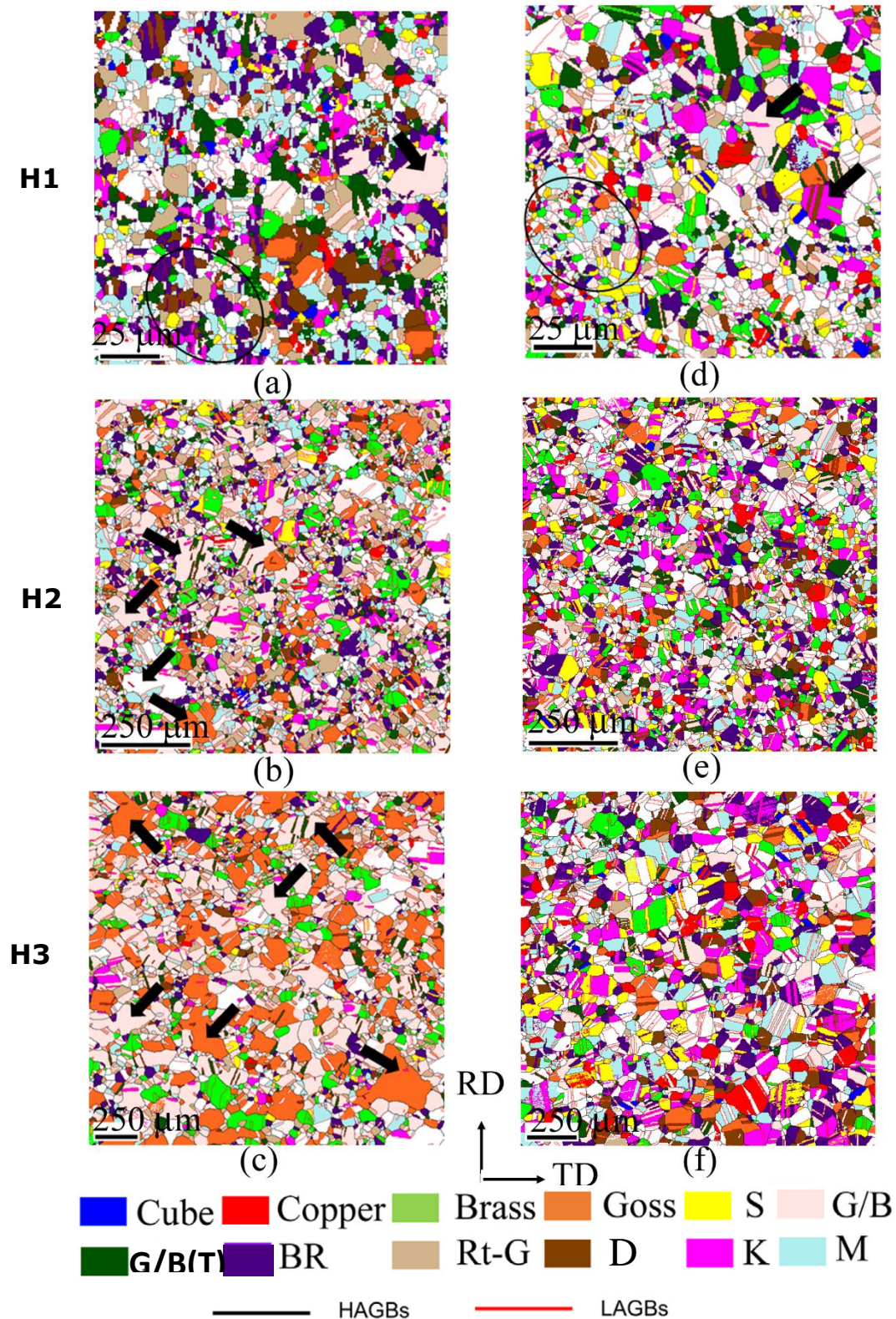
Fig.5.4: Orientation maps of ((a)–(c)) Ni–Co and ((d)–(f)) HEA in different heat-treated conditions.
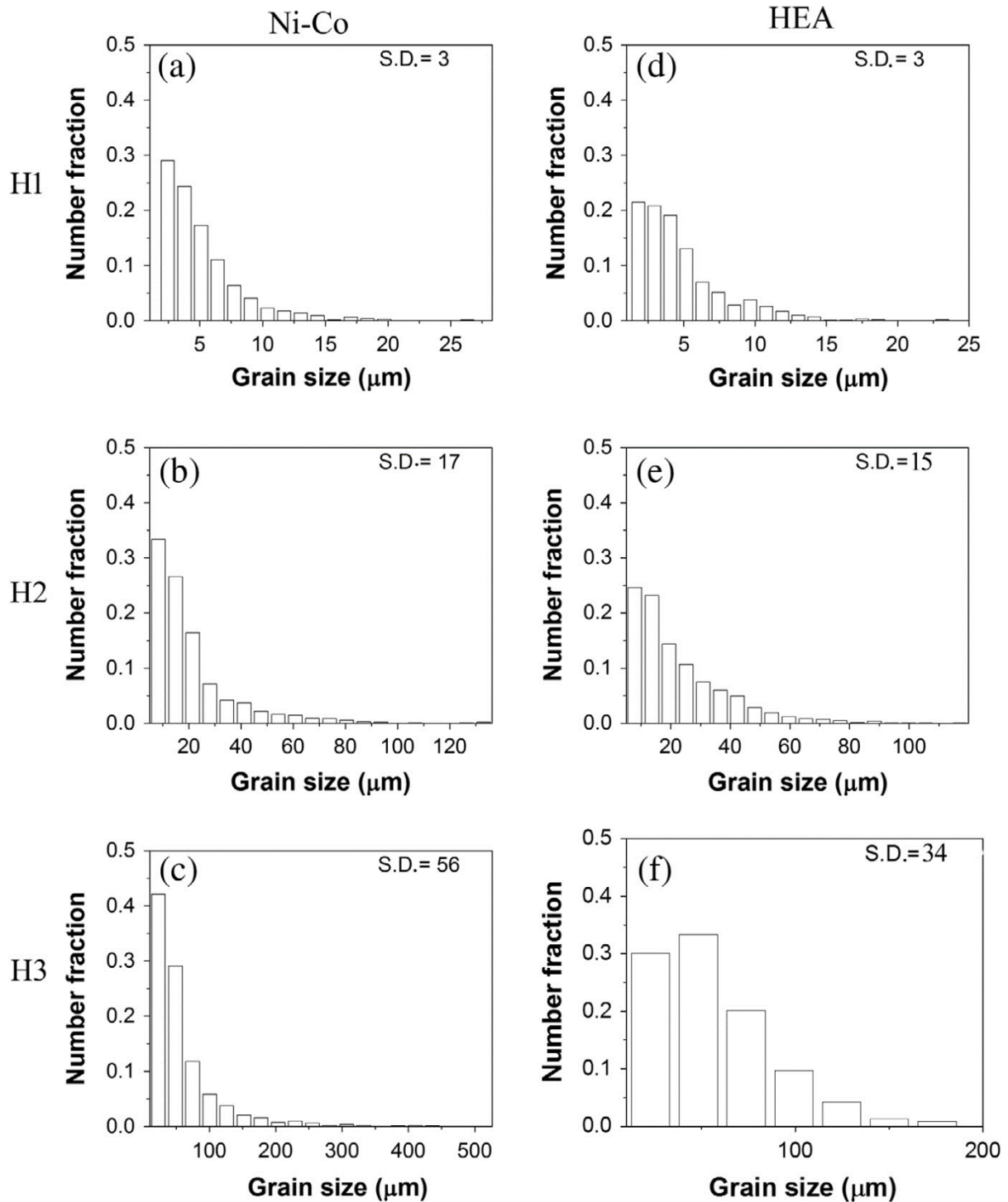
Fig.5.5: The grain size distribution plots of ((a)–(c)) Ni–Co and ((d)–(f)) HEA in ((a), (d)) H1, ((b), (e)) H2 and ((c), (f)) H3 treated conditions (S.D. is the standard deviation of the distribution).

The evolution of TB fraction (defined as the ratio of the number of twin boundaries to the total number of grain boundaries) in the two materials is compared in Fig.5.6. The plot clearly shows that with increasing grain size the annealing TB fraction increases in the two alloys. The increase in the TB fraction is more significant in case of the H1 and H2 treated conditions. Most importantly, the TB fractions in the two alloys in any given heat-treated condition are quite similar. In other words, for similar grain size the annealing TB fractions in the two alloys are also similar.

*5.4.2 Evolution of texture during annealing*

In order to have a detailed understanding of the texture in the two alloys, the ODFs of annealed Ni–Co (Fig.5.7(a)–(c)) and HEA (Fig.5.8(a)-(c)) are studied carefully. The $\varphi_2=0°$ section of the ODF of Ni–Co alloy in the H1 treated condition (Fig.5.7(a)) shows the presence of intensity only at the Rt-G location. The orientation map (Fig.5.4 (a)) shows the presence of this component (highlighted in tan) having volume fraction ~6.5%. The other components along the α-fiber, such as, G (highlighted in orange), G/B (highlighted in rose), Bs (highlighted in green) and the first order twin of G/B (G/B(T); highlighted in deep green) are rather weak (refer to Table 5.1 for details). Noticeable intensity is observed at the ($\varphi_1$, Φ, $\varphi_2$ = 27°, 64°, 15°) location corresponding to the {142}<211> orientation (K; highlighted in magenta in Fig.5.4). The $\varphi_2=35°$ section shows the presence of the brass recrystallization component (BR) {236}<385> (highlighted in violet) having volume fraction of ~12%. The $\varphi_2=45°$ section shows stronger {113}<332> orientation (D; highlighted in maroon). The D component is having a volume fraction of ~ 8%. The $\varphi_2=65°$ section shows noticeable presence of S and {13 6 25}<20 15 14> (M; highlighted in turquoise) orientations having volume fractions of ~8% and ~14%, respectively.

Perceptible change in texture is observed in the H2 treated condition (Fig.5.7(b)). The $\varphi_2=0°$ section of the ODF (Fig.5.7(b)) shows that the G/B orientation is much stronger than G and B$_S$ orientations along the α-fiber. Remarkably, the preferentially grown large recrystallized grains in the

microstructure (Fig.5.4 (b)) are having the α-fiber orientations, such as G/B, G and Bs, resulting in an increased fraction of the α-fiber (defined as the sum of volume fraction of components lying on the α-fiber, namely, G, G/B, BS, G/B(T) and Rt-(G)). In contrast, other orientations observed in the H1 treated condition, such as the BR, K and M orientations are diminished in strength in the H2 treated condition, which is clearly visible from the orientation map (Fig.5.4(b), respective ODF sections (Fig.5.5(b) and the quantitative description shown in the Fig.5.9. The volume fractions of α-fiber orientations G/B and G increases further in the H3 treated condition (Fig.5.9). The orientation map (Fig.5.4(c)) and ODF sections (Fig.5.7(c)) also clearly show the strong presence of G and G/B orientations, but only a minor presence of other components. The strengthening of the α-fiber results in the diminished strength of the random components (Fig.5.9).

The $\varphi_2=0°$ section of the ODF of HEA in the H1 treated condition clearly shows the development of a α-fiber with discrete intensity peaks close to the G/B (the intensity peak is only slightly shifted from the orientation {011}<155>) and B$_S$ orientations (Fig.5.8(a)). The $\varphi_2=15°$ section shows the presence of the K orientation, but it is somewhat shifted from its original position. The BR orientation shows intensity levels very similar to that of the K orientation and consequently these two orientations show very similar volume fractions in the orientation map (Fig.5.4(d)). The $\varphi_2=45°$ section (Fig.5.8(a)) shows week presence of Cu and D orientations. The presence of the M orientation is observed in the $\varphi_2=65°$ section of the ODF and also confirmed from the orientation map (Fig.5.4(d)). The respective ODF sections of the HEA in the H2 (Fig.5.8(b)) and H3 (Fig.5.8(c)) treated conditions appear quite similar revealing only marginal variation in the intensities of the individual texture components. Consequently, in sharp contrast to Ni-Co alloy, which shows remarkable strengthening of α-fiber components (e.g. G and G/B) during grain growth (Fig.5.9), the orientation maps of HEA in the H2 or H3 treated conditions (Fig.5.4((e)-(f)) show much

weaker G or G/B components. Fig.5.10 shows the quantitative analysis of different texture components. Note that the volume fractions of the texture components are plotted against the grain size for clarity. The quantitative analysis of the volume fractions of texture components with grain growth shows only marginal variation (Fig.5.10). This is also quite consistent with the appearance of the same texture components in the orientation maps of different annealed HEA samples (Fig.5.4((d)-(f)). These observations clearly show that the texture evolution during grain growth in the two alloys are remarkably different.
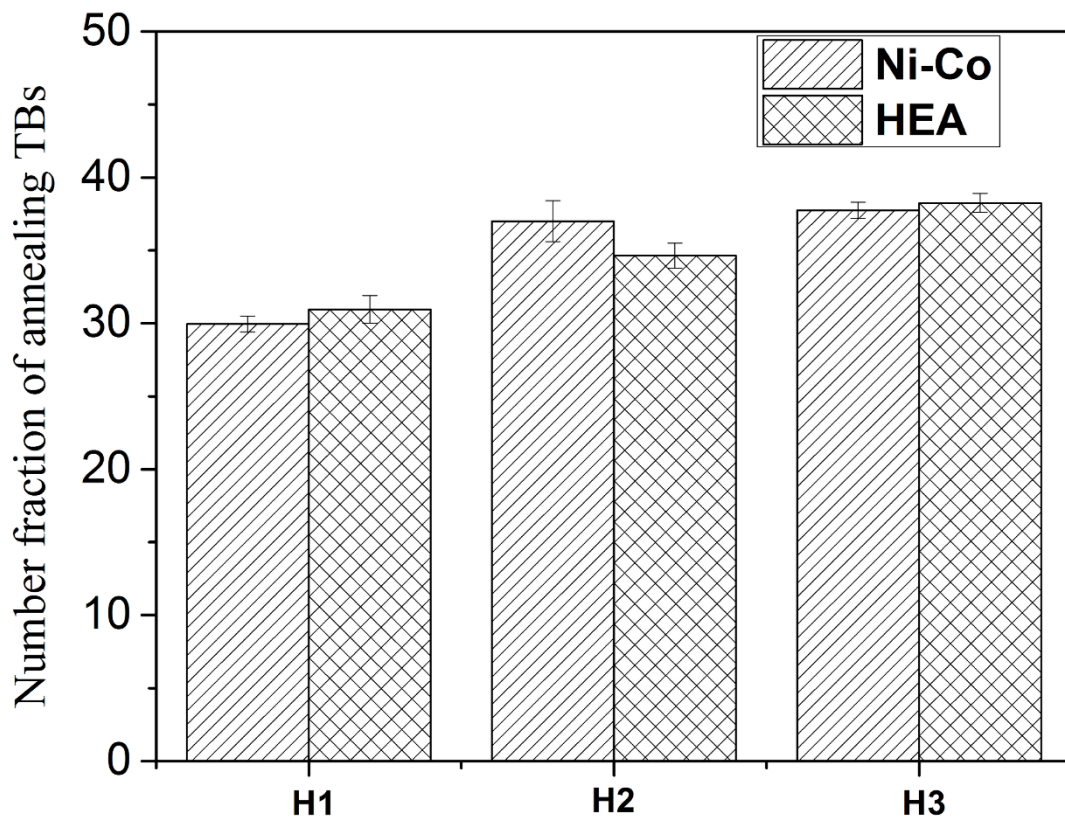
Fig.5.6: Comparison of Σ3 annealing TB fraction in Ni–Co and HEA in different heat-treated conditions.
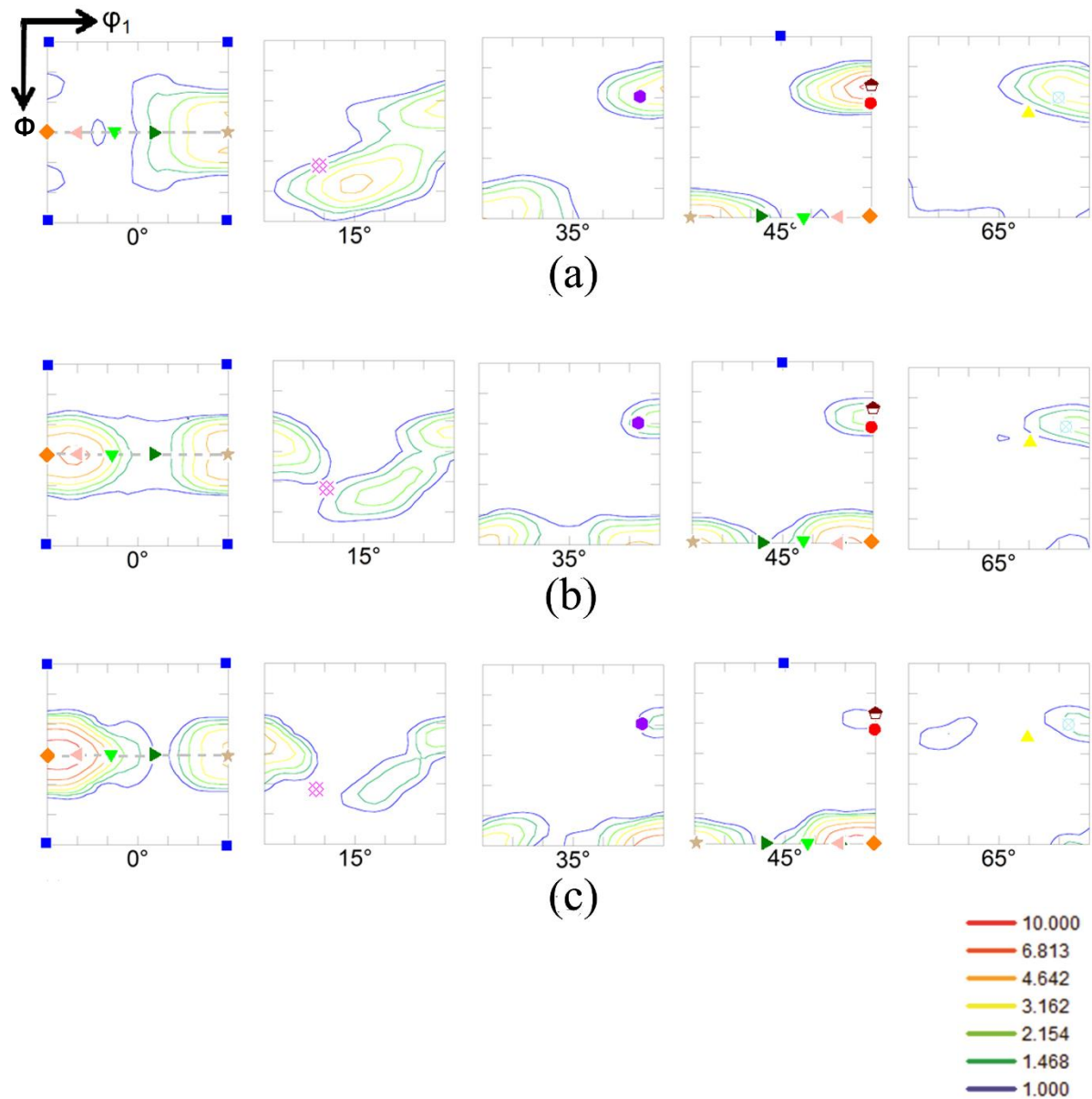
Fig.5.7: Relevant ODF sections of Ni–Co alloy in (a) H1, (b) H2 and (c) H3 treated conditions (Refer to Table 5.1 for symbols used in the ODF sections).
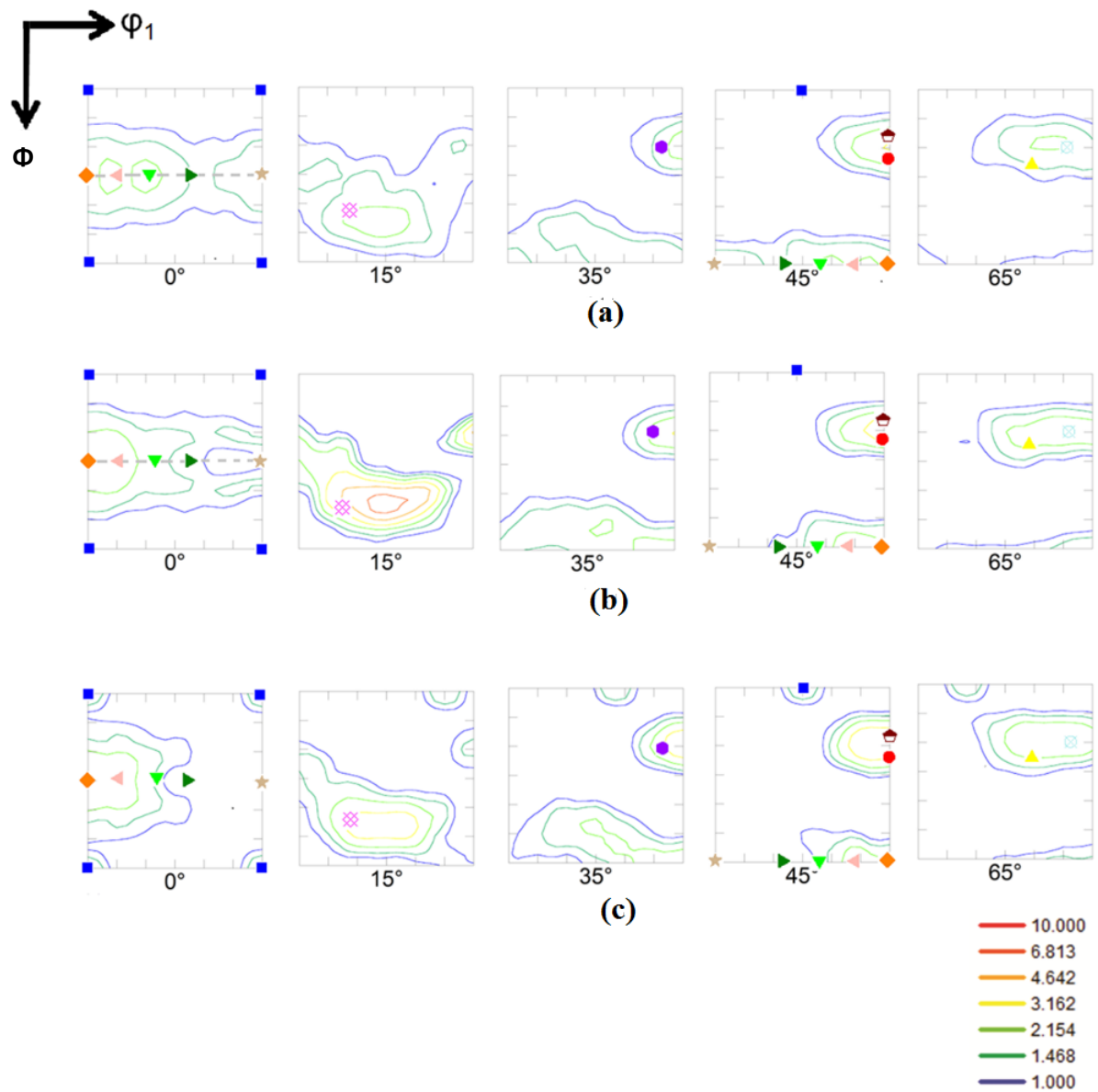
Fig.5.8: Relevant ODF sections of HEA in (a) H1, (b) H2 and (c) H3 treated conditions (Refer to Table 5.1 for symbols used in the ODF sections).
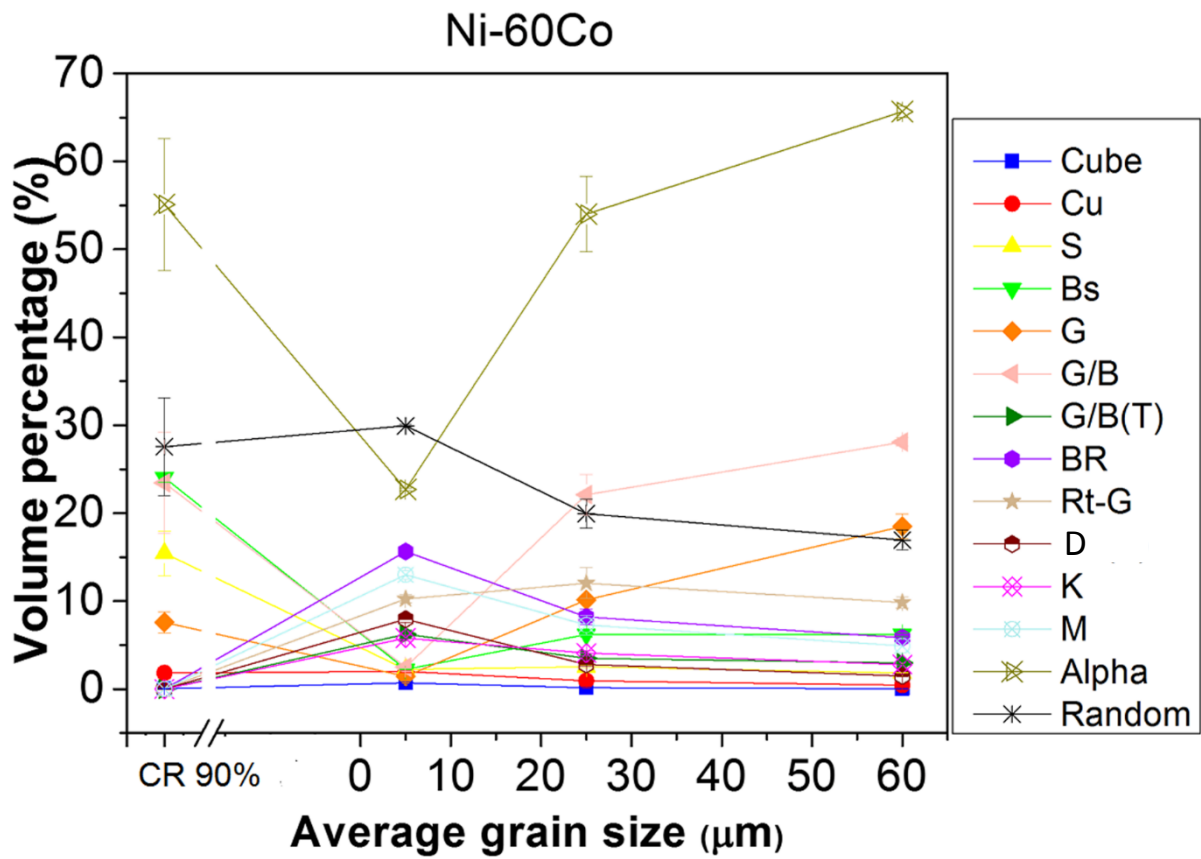
Fig.5.9: Quantitative analysis of texture components in Ni–Co.
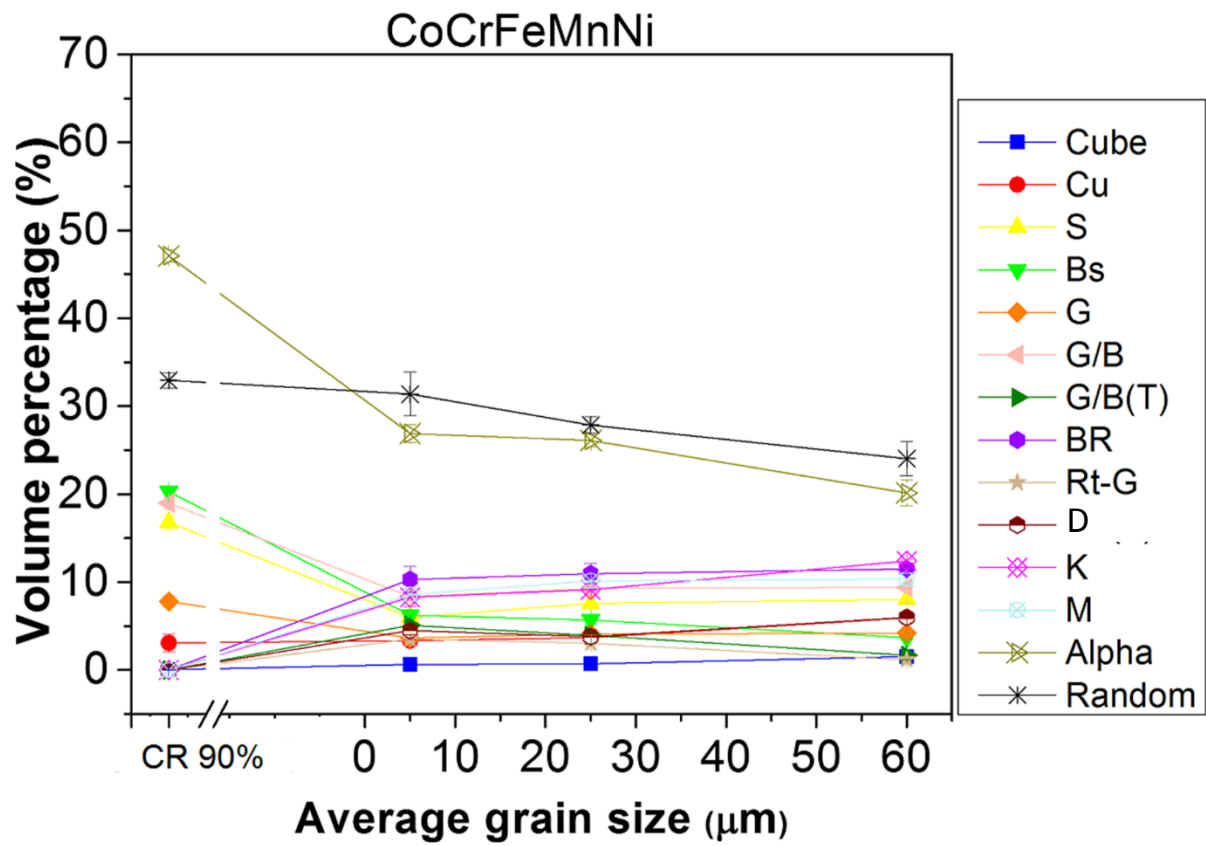
Fig.5.10: Quantitative analysis of texture components in HEA.

## 5.5 Discussion

In order to achieve similar average grain size, the 90% cold-rolled HEA has to be annealed at significantly higher temperatures or for significantly longer durations as compared to the 90% cold-rolled Ni-Co alloy (Table 5.2). Hence, the resistance to recrystallization and grain growth in the present HEA is significantly higher than Ni-Co. The sluggish recrystallization and grain growth behavior is attributed to the whole solute matrix of HEAs which renders atomic diffusion and grain boundary movement difficult. These explanations are also quite consistent with higher activation energies (Q) and lower diffusivities (D) of Ni and Co in HEA (calculated for H3 treatment temperature i.e. 1000°C which is same for both Ni-Co and HEA) as compared to those in Ni-Co alloy as shown in Table 5.3 [28, 106, 107]. For the same reason the present HEA also shows much higher activation energy for grain growth (~322 kJ mol$^{-1}$) as compared to other low SFE materials [29].

Although the two alloys are having low SFE, the microstructure evolution during grain growth is remarkably different. The Ni-Co alloy shows an inhomogeneous (or less uniform) microstructure in the H1 treated condition i.e. when the grain growth is limited so that the average grain size is significantly lower than the other two heat treated conditions. The microstructures of Ni-Co alloy continue to show inhomogeneity or non-uniformity during subsequent grain growth i.e. in the H2 and H3 treated conditions as revealed by the presence of large preferentially grown recrystallized grains (Fig.5.4((a)-(c)). In sharp contrast, the HEA shows significantly homogenous microstructure after grain growth i.e. in the H2 and H3 treated conditions.

The fundamental difference in the microstructural evolution of Ni-Co and HEA may be attributed to the whole solute matrix of HEAs which affects the recrystallization and grain growth. The inherently sluggish diffusion in the HEA can significantly diminish the grain boundary mobility. This would evidently result in more homogenous growth in HEA which should lead to a

more homogenous microstructure as compared to Ni-Co alloy. These fundamental differences in the two alloys also are consistent with texture evolution during grain growth which would be discussed shortly.

Table 5.3: The diffusion related parameters of Ni and Co in Ni−60 wt.%Co and HEA.

| Element | Diffusion related parameters | | | | | |
|---|---|---|---|---|---|---|
| | Pre-exponential term (Do) $(10^{-4}$ m$^2$ s$^{-1})$ | | Activation energy (Q) $(kJ$ mol$^{-1})$ | | Diffusivity (D) at 1000°C $(10^{-16}$ m$^2$ s$^{-1})$ | |
| | Ni−60 wt.%Co [106, 107] | CoCrFeMnNi [28] | Ni−60 wt.%Co | CoCrFeMnNi | Ni−60 wt.%Co | CoCrFeMnNi |
| Ni | 6.309 | 19.7 | 303.75 | 317.5 | 2.165 | 1.907 |
| Co | 0.112 | 9.26 | 246.85 | 306.9 | 8.311 | 2.361 |

The annealed microstructures of the two alloys reveal profuse Σ3 annealing TBs in good agreement with the low SFE of the two alloys. However, an interesting feature is that the two alloys show very similar fraction of Σ3 annealing TBs when the average grain size of the two materials are similar. Since different temperature or time has been used in this work to achieve similar average grain size in the two materials, these observations indicate that the fraction of annealing TBs depends on the final recrystallized grain size.

Recently, Otto et al [79] have investigated the evolution of Σ3 annealing TBs in the present HEA. They have cold-rolled the alloy to different strains and annealed at different temperatures. It has been reported that the fraction of Σ3 annealing TBs depends on the final recrystallized grain size if the starting materials for grain growth have completely recrystallized microstructure [79]. However, no such relationship is found to hold good during recrystallization. These observations are explained by the authors [79] based on the theories of annealing TB formation by Fullman and Fischer [93] who have postulated that the formation of annealing TBs during grain growth is promoted by the migration of triple points, resulting in the lowering of the total boundary energy. During the continued migration of the triple points the original grains are replaced by new grains, leading to the formation of new twins and further lowering of energy. This process is evidently related to the migration distances which are comparable to the order of the grain size. As a consequence, the TB fraction should be proportional to the grain size.

Very similar TB fractions in the two materials in the H2 and H3 treated conditions seem to support the observations of Otto et al [79]. Since the starting materials are in the cold-rolled state, this could indicate that a large fraction of the TBs might have been actually created during grain growth. However, an interesting case is the H1 treated condition. Since the average grain size in the two alloys is similar but small in this heat-treated condition, it is presumed that a considerable fraction of annealing TBs in this case is

formed before appreciable grain growth sets in. Since the SFE values of the two alloys are quite similar, similar annealing TB fractions indicate a possible role of SFE in determining the limiting TB fraction for a given grain size. Although, this point needs to be further investigated and clarified.

The heavily cold-rolled Ni-Co and HEA show the development of strong brass type texture which is confirmed by the qualitative and quantitative texture analyses. This behavior is anticipated for low SFE materials. In contrast to Ni-Co alloy, the HEA shows much stronger retention of deformation texture components during annealing. However, the Bs component is not the major component of the recrystallization texture in both Ni-Co and HEA. In case of HEA, experimental observations suggest that this could be attributed to the slower recrystallization kinetics of the near $B_S$ oriented regions, due to which they are consumed by other orientations (already shown in Chapter 4). Absence of strong $B_S$ component in the recrystallization texture of Ni-Co alloy also indicates a very similar mechanism. Some of the observed recrystallization texture components originate through the formation of annealing twins. The D component is twin related to Cu [102] and also symmetrically related to the Cu orientation. Therefore, a substantial overlap with Cu orientation is possible and few of these grains may not be generated through twinning of the Cu component.

The formation of the brass recrystallization component (BR) which is observed in both the alloys needs to be discussed further. The strong presence of this component in brass is attributed to the nucleation at shear bands and subsequent twinning if the parent orientation is assumed to be the G/B orientation [108]. The growth of this component is favored due to a high mobility 40°<111> relationship with the Bs, which is the main component of the deformation texture. However, this component is not significantly strong in either of the two alloys. This indicates that the contribution of shear bands to recrystallization is limited. Alternatively, the recrystallization happens in a more homogeneously deformed matrix which

helps in retention of the deformation texture components. This mechanism has already been discussed in Chapter 4 in the case of the present HEA and TWIP steel [92].

The texture of the two alloys in the H1 treated condition is similar, characterized by the presence of the same components. The most remarkable difference in the recrystallization texture of the two materials is, however, the much stronger α-fiber components G/B and G in Ni-Co alloy as compared to those in the HEA after grain growth (i.e. in the H2 and H3 treated conditions). The significant presence of G/B and G components can be attributed to the preferential growth of these grains as is clearly evidenced from the microstructures (Fig.5.4). It might be noted that these components have the least volume fractions in the H1 treated condition (Fig.5.9) i.e. after complete recrystallization but rather limited grain growth. Therefore, these components will have the best chance to grow amongst a spectrum of different orientations. This is due to the fact that their growth is least likely to be affected by the presence of grains of the same orientations i.e. these grains can maintain mobile high angle grain boundaries over large migration distances. This process is similar to the orientation pinning effect which is used to explain the preferred growth of certain texture components [54].

In case of the HEA, the α-fiber components, G/B and G do not show any preferential growth as is observed in the case of Ni-Co. The microstructure remains more homogenous (or uniform) after grain growth as already pointed out before and the texture component plot (Fig.5.10) clearly reveals only minor changes in the volume fractions of individual components confirming a more homogenous grain growth behavior. This sharply contrasting behavior of the two alloys could be explained on the basis of two facts, namely, nucleation in a homogeneously deformed matrix which reproduces same orientations and inherently sluggish diffusion in multicomponent HEA systems [54]. Since boundary migration will depend upon the diffusion in and across the grain boundaries, sluggish diffusion

would greatly diminish the mobility of boundaries and affect the preferential growth of grains. This would evidently result in more homogenous or uniform grain growth and no significant variation in strength of different texture components as compared to Ni-Co alloy. These are evidently consistent with experimental observations.

The present study clearly indicates that while the two low SFE materials develop similar deformation texture after heavy cold-rolling, the texture after annealing and grain growth can be quite different. It might be noted that although Ni-Co is also a highly solute rich single phase alloy, unlike HEA is not a multicomponent system, therefore diffusion is considerably easier. Therefore, the present results clearly show that inherently sluggish diffusion in the multicomponent HEA systems can have a great influence on microstructure and texture development during grain growth.

# -: CHAPTER 6 :-

## Effect of cold-rolling strain on the evolution of microstructure and texture during annealing of an equiatomic CoCrFeMnNi high entropy alloy

## 6.1 Effect of cold-rolling strain

In Chapter 5, it has been clarified that the HEA shows significantly different texture formation behavior during grain growth as compared to low SFE Ni-60wt.%Co alloy. In the low SFE Ni-60wt.%Co alloy, preferential growth of grains significantly alters the recrystallization texture. In contrast, absence of preferential growth in the HEA leads to only minor changes in the volume fraction of texture components with annealing temperature.

It is well known that in conventional low SFE alloys, the processing parameters including imposed strain, starting grain size and deformation temperature greatly influence the formation of texture [50]. Therefore, it is of interest to see how these parameters affect the recrystallization texture formation behavior of the present HEA. The present chapter presents the effect of cold-rolling strain on the formation of recrystallization texture in the equiatomic CoCrFeMnNi HEA. For this purpose CoCrFeMnNi HEA is first cold-rolled to 60%, 80% and 95% reduction in thickness and then annealed at different temperatures. The recrystallization texture formation is then systematically investigated.

## 6.2 Effect of strain on microstructure and texture during cold-rolling

Evolution of microstructure and texture during cold-rolling of the HEA has already been discussed in Chapter 4. However, the main results are summarized in Fig.6.1 for clarity. The microstructures after 60% (Fig.6.1(a)) and 80% (Fig.6.1(b)) cold-rolling reveal lamellar banded structure. Further cold-rolling to 95% reduction results in significant fragmentation of the microstructure. It is clearly seen that the deformation texture changes from copper type (after 60% cold-rolling as shown by the (111) PF in Fig.6.1(d)) to predominantly brass type (after 95% cold-rolling as shown by the (111) PF in Fig.6.1(f)) through a transition type texture (after 80% cold-rolling as shown by the (111) PF in Fig.6.1(d)). The texture transition is amply corroborated by the quantitative analysis of volume

fractions of different texture components (Fig.6.2). Gradual strengthening of the $B_S$ component accompanied by the decrease in strength of the Cu component is clearly observed.
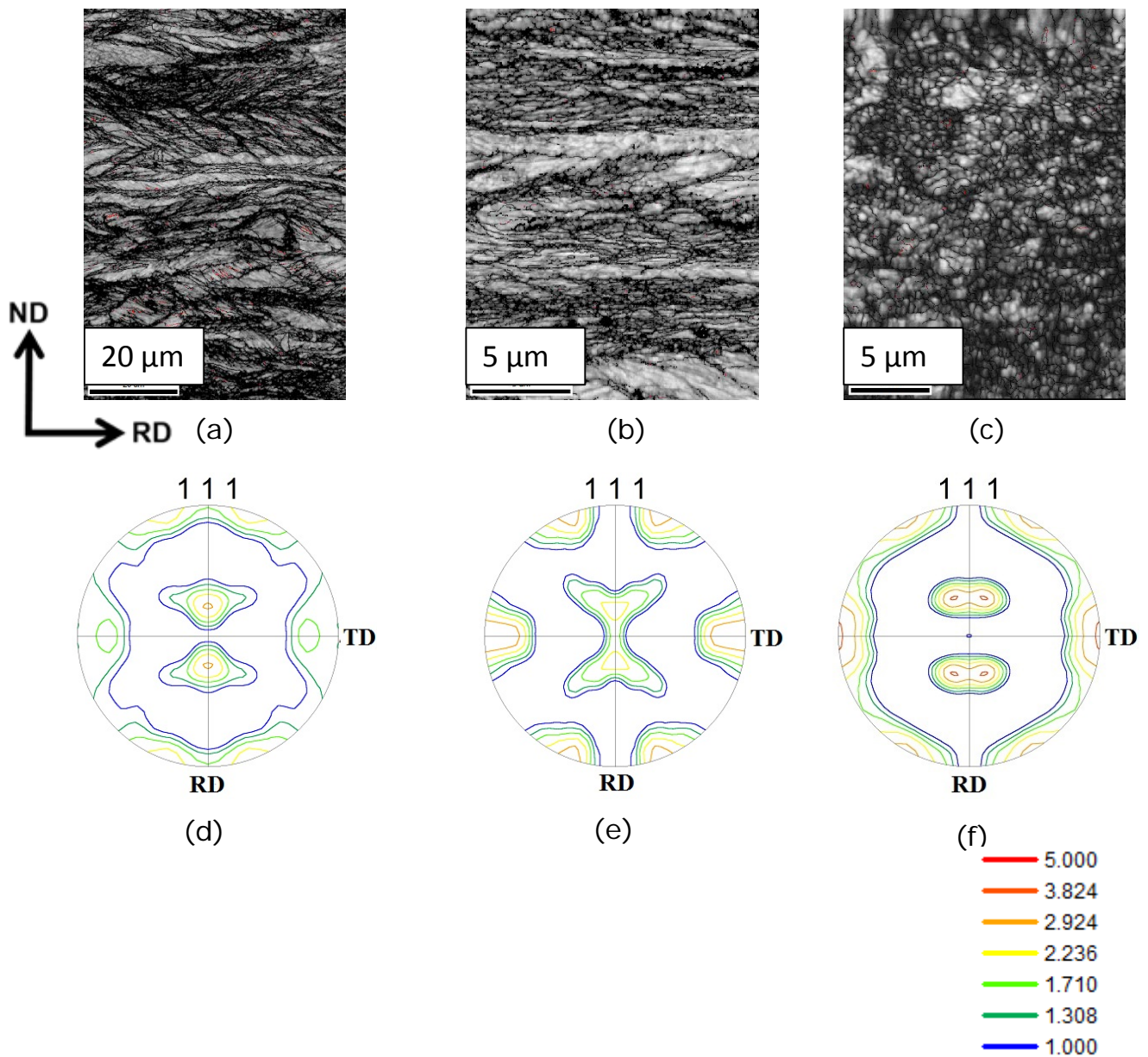
Fig.6.1: The IQ maps of (a) 60%, (b) 80% and (c) 95% cold-rolled materials; (d), (e) and (f) show the corresponding (111) PFs.

Table.6.1: Euler angles and Miller indices for the observed texture components.

| Texture component | Symbol | Euler angle | | | Miller indices |
|---|---|---|---|---|---|
| | | $\varphi_1$ | $\phi$ | $\varphi_2$ | |
| Cube (C) | ■ | 0, 0, 0 | | | {001} <100> |
| Copper (Cu) | ● | 90, 35, 45 | | | {112} <111> |
| S | ▲ | 59, 37, 63 | | | {123} <634> |
| Bs | ▼ | 35, 45, 0 | | | {110} <112> |
| G | ◆ | 0, 45, 0 | | | {110} <001> |
| Rt - G | ★ | 90, 45, 0 | | | {110} <110> |
| G/B | ◀ | 17, 45, 0 | | | {110} <1 1 5> |
| G/B(T) | ▶ | 55, 45, 0 | | | {110} <111> |
| BR | ⬟ | 80, 31, 34 | | | {236} <385> |
| D | ♨ | 90, 27, 45 | | | {1 1 3} <3 3 2> |
| K | ※ | 27, 64, 14 | | | {142} <211> |
| M | ⊗ | 80, 30, 65 | | | {13 6 25} <20 15 14> |

Fig.6.2: Variation of volume fraction of texture components with cold-rolling reduction.

## 6.3 Evolution of microstructure and texture during annealing

Fig.6.3 shows the orientation maps of the 60%, 80% and 95% cold-rolled materials after annealing at different temperatures. The GB map of the 60% cold-rolled material annealed at 700°C (Fig.6.3(a)) shows fully recrystallized microstructure consisting of clear recrystallized grains fully bounded by HAGBs (highlighted by black lines). The microstructure shows the presence of profuse annealing TBs (highlighted in red). The average recrystallized grain size is ~ 3 µm. The grain size is increased to ~ 20 µm after annealing at 1000°C (Fig.6.3(b)). A remarkable increase in grain size (~90 µm) is observed after annealing at 1200°C (Fig.6.3(c)).

The evolution of microstructure in the 80% (Fig.6.3(d) -(f)) and 95% (Fig.6.3 (g)-(i)) cold-rolled and annealed materials follow the somewhat similar trend. Recrystallized grains fully bounded by HAGBs could be observed in the microstructures of the 80% (Fig.6.3(d)) and 95% (Fig.6.3(g)) deformed materials after annealing at 700°C. The microstructures of the 80% (Fig.6.3(e)) and 95% (Fig.6.3(h)) cold-rolled materials after annealing at 1000°C shows grain growth, resulting in an average grain size ~ 20-23 µm, which is quite similar to that of the 60% cold-rolled material annealed at the same temperature (~ 20 µm). Remarkable grain growth is observed after annealing at 1200°C. The grain size of the 80% (Fig.6.3(f)) and 95% (Fig.6.3(i)) cold-rolled materials after annealing at 1200°C are found to be ~ 70 µm and 60 µm, respectively.

Fig.6.4 shows the variation in grain size with annealing temperature. The difference in the average recrystallized grain size is rather insignificant and fall within the scatter around the mean size up to the annealing temperature of 1000°C. However, annealing at 1200°C, which leads to remarkable grain growth, the final recrystallized grain size depends strongly on the prior cold-rolling strain; decreasing consistently with increasing cold-rolling strain.
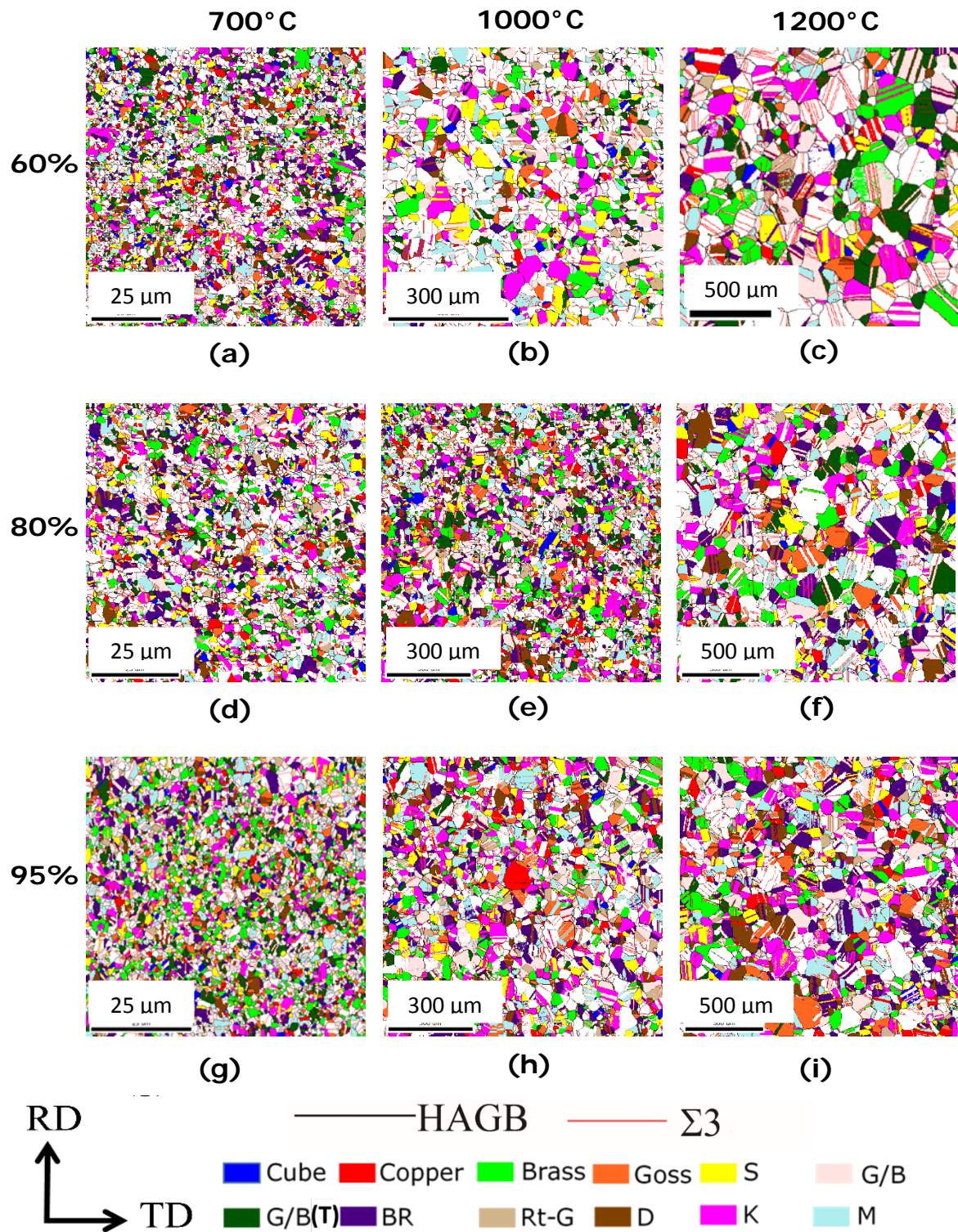
Fig.6.3: Orientation maps of ((a)-(c)) 60%, ((d)-(f)) 80% and ((g)-(i)) 95% cold-rolled FGSM annealed at ((a),(d),(g)) 700°C, ((b),(e),(h)) 1000°C and ((c),(f),(i)) 1200°C for 1h.
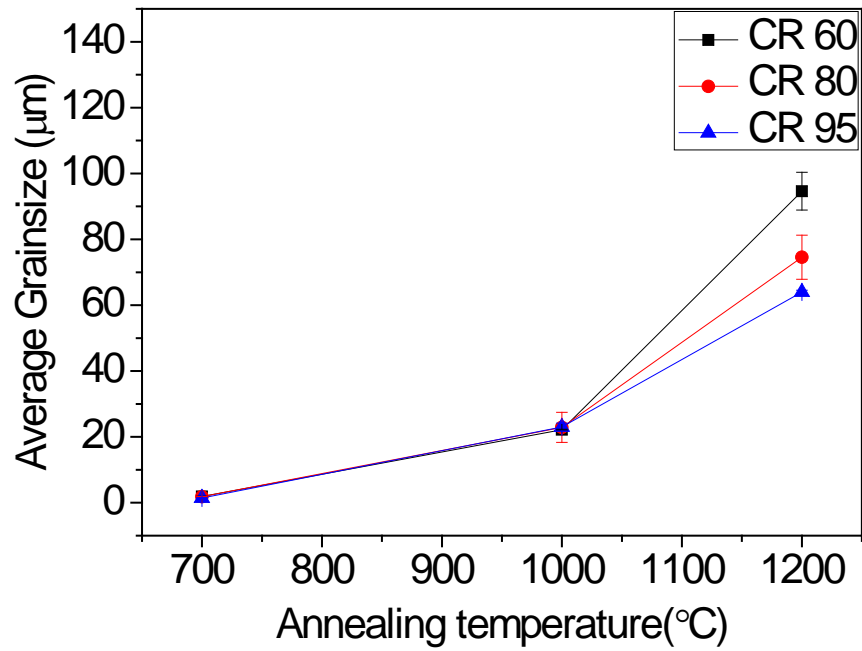
Fig.6.4: Grain size dependence on annealing temperature in different cold-rolled materials.

Fig.6.5 shows the relevant ODF sections of the 60% cold-rolled material after annealing at different temperatures. Development of a weak and discontinuous α-fiber extending from the G to the Rt-G through the G/B, $B_S$, and G/B(T) orientations (refer to Table 6.2 for the symbols used for different orientations) is observed after annealing at 700°C (Fig.6.5(a)). The spatial distribution of the different α fiber components could be seen in the orientation map in Fig.6.3(a). The $\phi_2=35°$ section of the ODF shows the location of the BR and the orientation map (Fig.6.3(a)) clearly shows the presence of this orientation. The $\phi_2=45°$ and 65° sections of the ODF show the presence of the Cu and S components and these components are also noticed in the orientation map (Fig.6.3(a)). The presence of the K and M components is noticed in the respective ODF sections and in the orientation map. The texture remains more or less unchanged after annealing at higher temperatures. Only minor differences, such as, strengthening of the α-fiber is noticed after annealing at 1000°C (Fig.6.5(b)) and 1200°C (Fig.6.5(c)).

Fig.6.6 and Fig.6.7 show the relevant ODF sections of the 80% and 95% cold-rolled materials, respectively after different annealing treatments. The appearance of the ODF sections indicates the development of very similar texture components as already described for the 60% cold-rolled and annealed materials. The presence of these components in the 80% and 95% cold-rolled materials after different annealing treatments is also confirmed from the respective orientation maps shown in Fig.6.3.

Fig.6.8 shows the variation of texture components with annealing temperature in 60% (Fig.6.8(a)), 80% (Fig.6.8(b)) and 95% (Fig.6.8(c)) cold-rolled materials. Annealing of the different cold-rolled materials results in the decrease of the intensity of the volume fraction of the α-fiber (sum of the volume fractions of the components along the α-fiber, namely G, G/B, $B_S$, G/B(T) and Rt-G) and other deformation texture components as compared to the deformed material. The K and M components, however, show increase in strength as compared to that in the deformed condition.

In good agreement with the ODF observations, the individual texture components show only minor variation with annealing temperature. Consequently, the total volume fraction of the α-fiber and random components (sum of volume fraction of components other than those shown in Table 6.1) do not reveal any significant changes. This is also in good agreement with the strength of annealing texture in different annealed conditions measured by the texture index (Fig.6.8(d)). It is clearly observed that the texture index does not show any significant variation with annealing temperature.

Fig.6.9 shows the variation of volume fraction of BR {236}<385> and D {113}<332> components in 60%, 80% and 95% cold-rolled materials after annealing at different temperatures. No significant strengthening with annealing temperature is observed for these components.
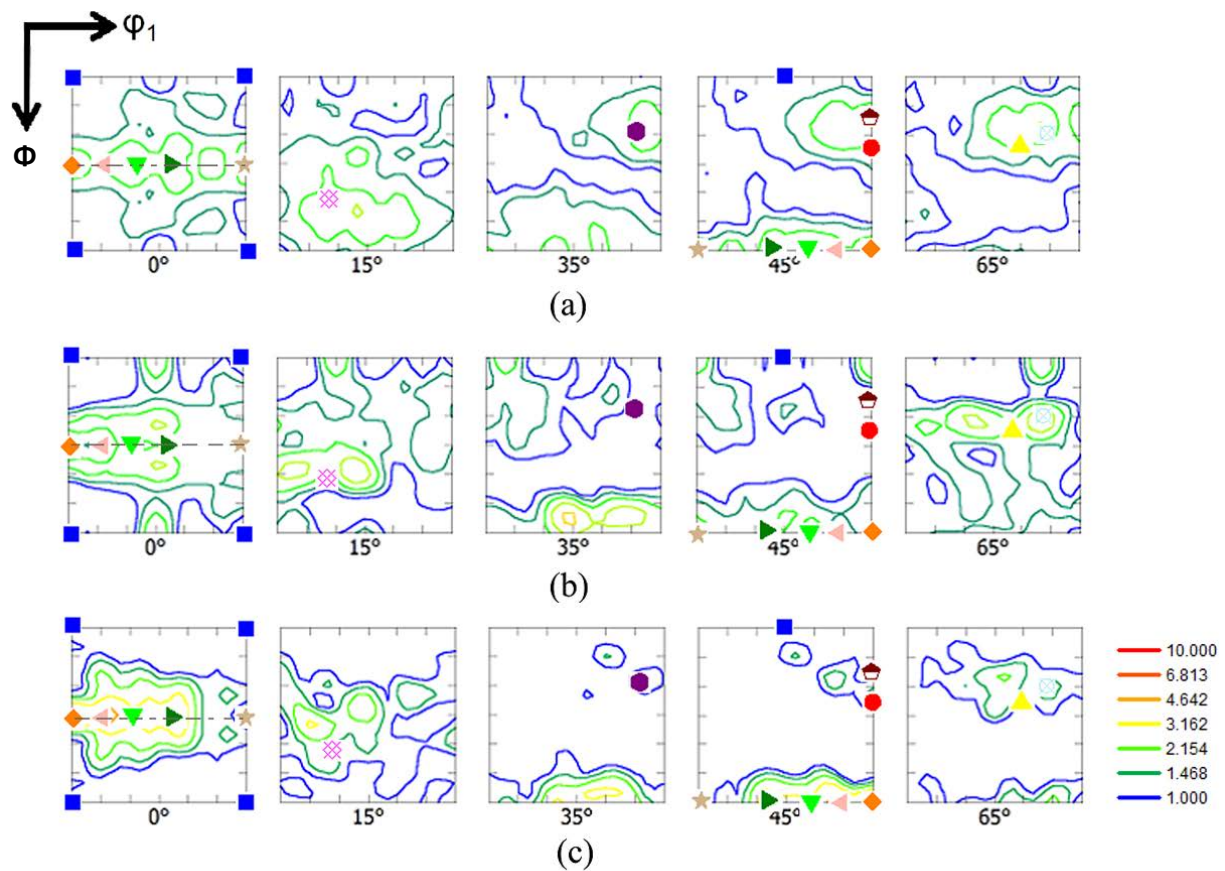
Fig.6.5: The relevant ODF sections of 60% cold-rolled material annealed at (a) 700°C, (b) 1000°C, (c) 1200°C for 1h (Refer to Table 6.1 for symbols used in the ODF sections).
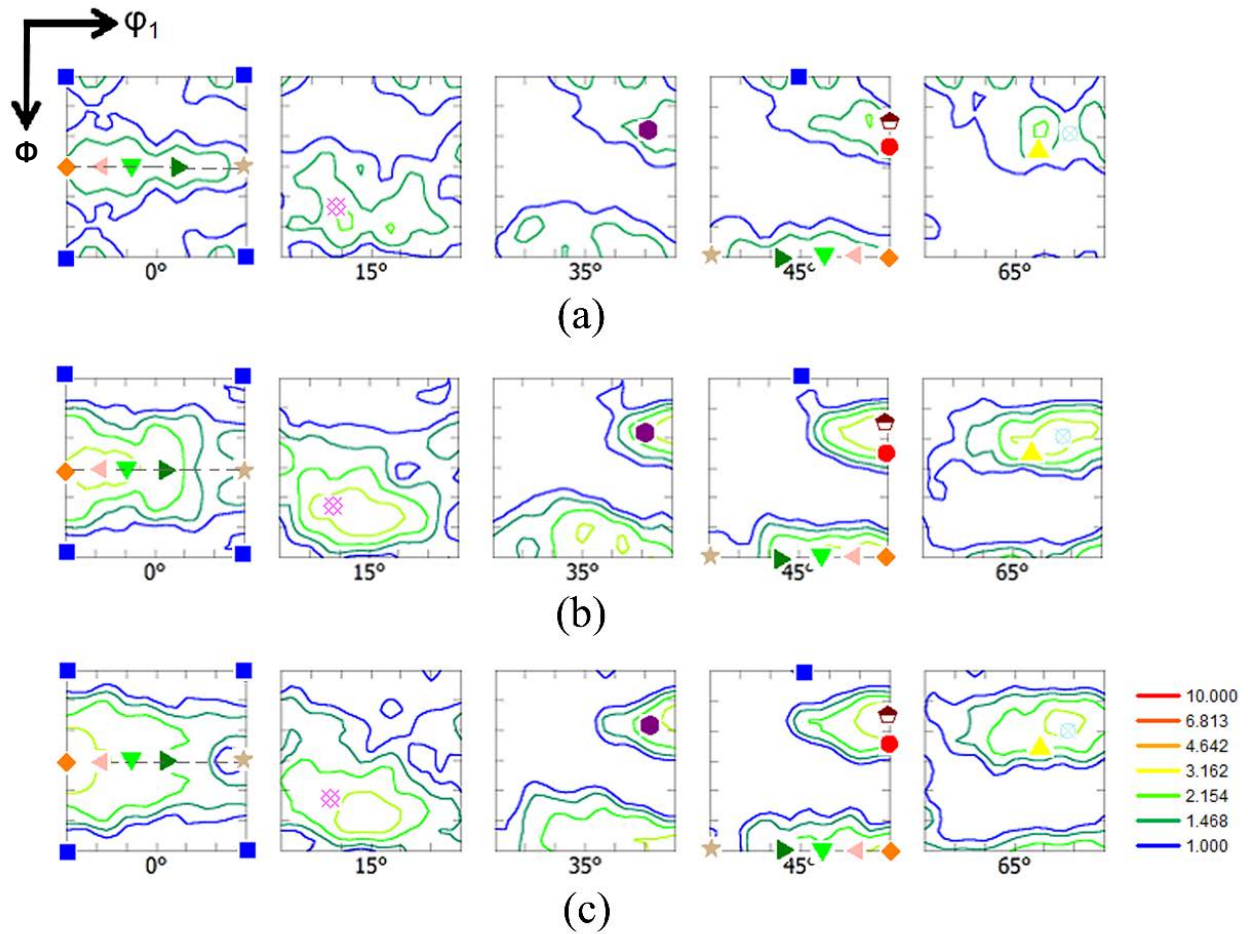
Fig.6.6: The relevant ODF sections of 80% cold-rolled material annealed at (a) 700°C, (b) 1000°C, (c) 1200°C for 1h (Refer to Table 6.1 for symbols used in the ODF sections).
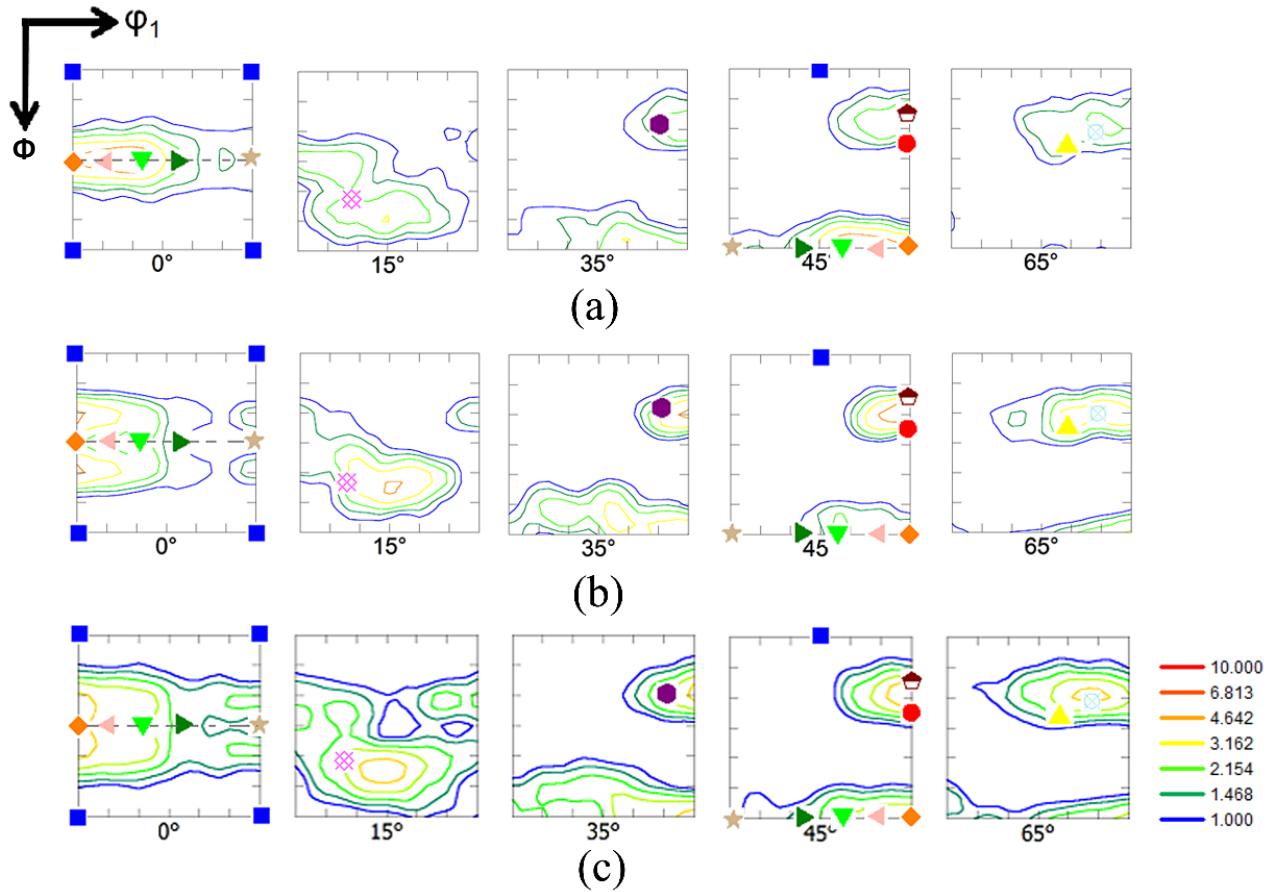
Fig.6.7: The relevant ODF sections of 95% cold-rolled material annealed at at (a) 700°C, (b) 1000°C, (c) 1200°C for 1h (Refer to Table 6.1 for symbols used in the ODF sections).
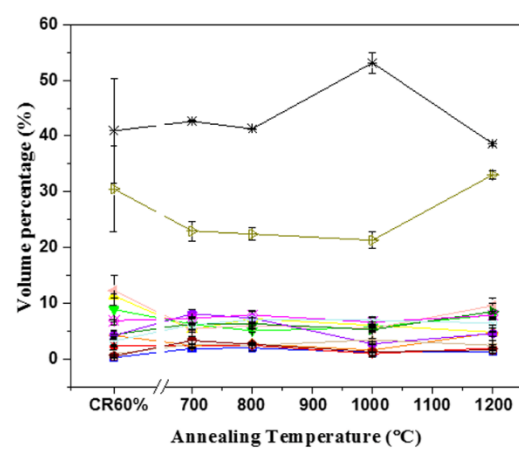
(a)
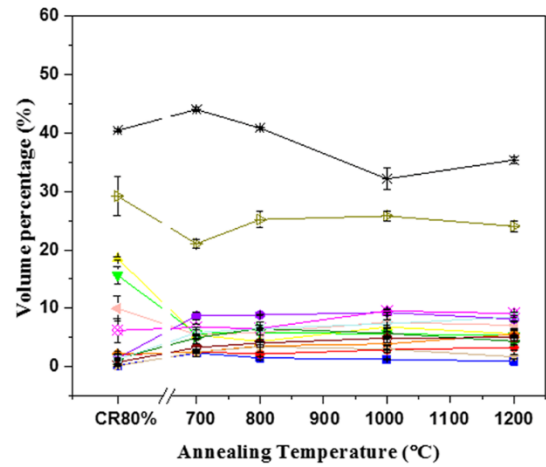
(b)
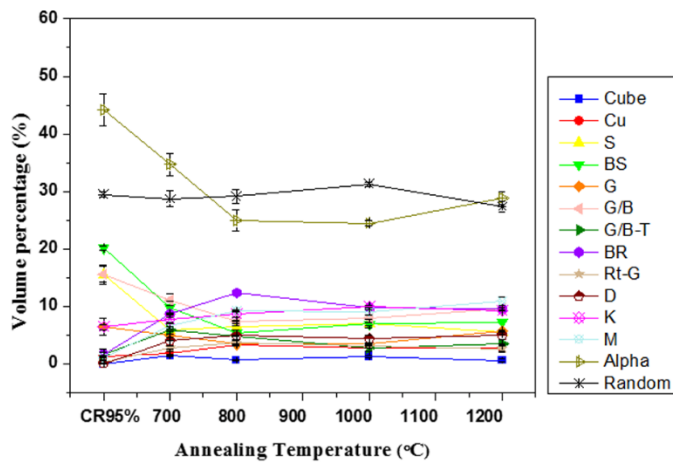
(c)
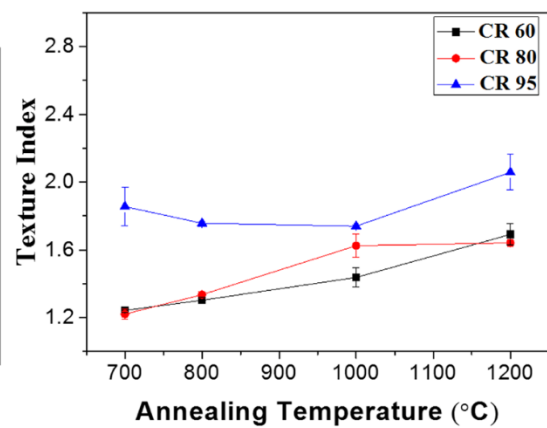
(d)

Fig.6.8: Variation of texture components with annealing temperature in (a) 60%, (b) 80% and (c) 95% cold-rolled HEA; (d) shows the variation of the texture index with annealing temperature in the HEA cold-rolled to different strain levels.

(a)   (b)
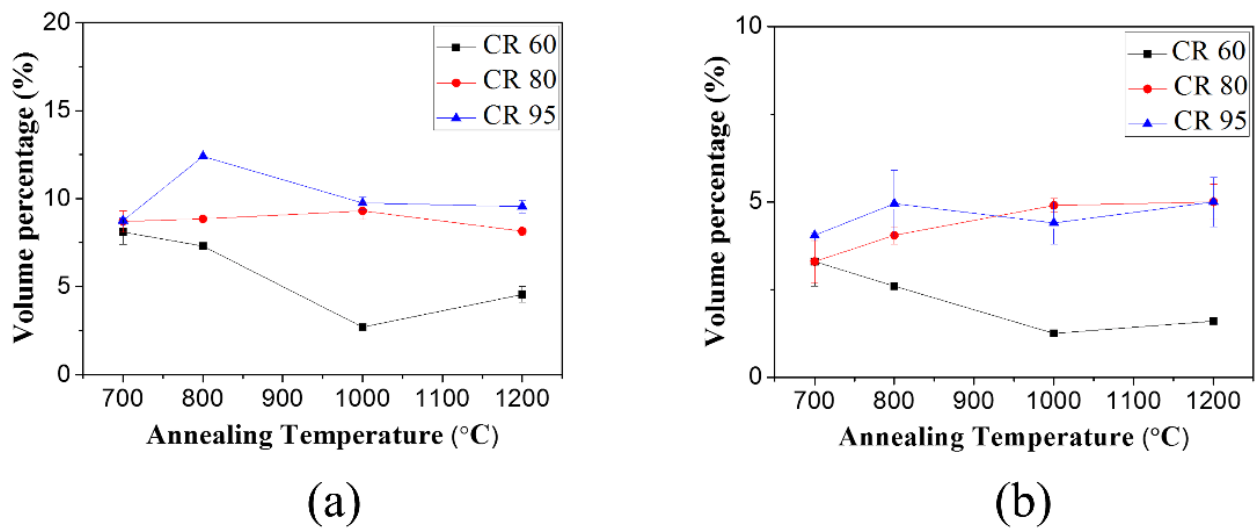
Fig.6.9: Variation of (a) BR and (b) {113}<332> components with annealing temperature in the HEA cold-rolled to different strain levels.

## 6.4 Discussion

*6.4.1 Evolution of microstructure during annealing*

The mechanism of recrystallization in low SFE alloys is described by the discontinuous recrystallization process which proceeds through the typical nucleation and growth stages [50]. The discontinuous recrystallization process in the present HEA has already been demonstrated in the Chapter 4. Consequently, the available nucleation sites and the subsequent growth behavior of the recrystallized grains would affect the final recrystallized grain size. In heavily deformed materials, such nucleation sites include grain boundaries and deformation heterogeneities including deformation bands, transition bands and shear bands [50]. In general, the final recrystallized grain size decreases with increasing prior deformation. This behavior is explained by the fact that the density of nucleation sites increases with increasing prior deformation [50].

The differences in average grain sizes of the 60%, 80% and 95% cold-rolled materials after annealing at lower temperatures e.g. after annealing at 700°C are rather insignificant. This observation is very consistent with that of Otto et al [79]. However, the grain sizes of different cold-rolled materials are found to be quite similar up to the annealing temperature of 1000°C. This might be due to the sluggish diffusion and different microtexture in the 95% cold-rolled material as compared to the 60% and 80% cold-rolled materials. However, this needs to be investigated further. During annealing at 1200°C, the recrystallization is completed much faster and the effect of prior strain is quite evident. The grain size after annealing at 1200°C shows the typical behavior, decreasing with increasing prior cold-rolling reduction, which is accounted for by the increasing nucleation density with increasing prior rolling strain. The detailed analysis of grain growth has not been attempted and should be investigated in future work.

In contrast, after annealing at high temperatures e.g. 1200°C, where recrystallization is followed by significant grain growth, the final recrystallized grain size decreases remarkably. However, the recrystallized

grain size in the similarly cold-rolled and annealed conditions are somewhat smaller in the present work as compared to those reported by Otto et al [79]. This could possibly be due to the large starting grain size of the as cast and homogenized material used by Otto et al [79].

The materials selected for annealing treatments (i.e. 60%, 80% and 95% deformed materials) have different deformation textures, mainly differentiated by the relative strength of the $B_S$ component. The observed transition from pure metal to copper type texture with increasing deformation is typical of low SFE materials [51] and has already been highlighted and discussed in Chapter 6.

### 6.4.2 Evolution of texture during annealing

In spite of the differences in the deformation texture, the main features of the annealing texture i.e. the development of the α-fiber and retention of deformation texture components (e.g. S component) are similar in all the three different cold-rolled materials after annealing at different temperatures. It has already been pointed out that for low SFE brass with small starting grain size, the annealing texture at lower annealing temperatures is characterized by the presence of typical BR component. At higher annealing temperatures, the materials deformed up to medium strain levels develop the $B_S$ component, while heavily deformed materials developed the D ({113}<332>) component. The evolution BR component in brass and conventional low SFE materials is explained by the nucleation at shear bands followed by preferential growth. Mechanism of the brass type shear bands and their contribution to texture development has been intensively investigated in different medium to low SFE materials [109-111]. However, less propensity for shear band formation results in more homogenous deformed microstructure of HEA. This ensures that preferential nucleation at deformation heterogeneities including shear bands does not significantly affect the formation of recrystallization texture. This explains the absence of a strong BR component. The absence of strong preferential nucleation is also consistent with the retention of the

deformation texture components (e.g. S) in the annealing texture. This behavior is somewhat similar to the behavior observed in low SFE TWIP steels as already pointed out in Chapter 4 [96]. It might be noted that although the $B_S$ component is strong in the deformation texture of 95% cold-rolled material, this component is found to be much weakened after annealing due to the slower recrystallization kinetics in the $B_S$ oriented regions (as shown in Chapter 4).

The insignificant variation of different texture components with annealing temperature further indicates quite similar growth rate of different texture components. It may be noted that the preferential growth of texture components, proposed as a mechanism for the evolution of strong recrystallization texture, involves rapid migration of boundaries, which in turn, depends strongly on the rapid diffusivity of atoms across the boundaries. As clarified recently, the present HEA shows the remarkably sluggish diffusion behavior [28] with rather high activation energy for grain growth [29]. Therefore, the sluggish diffusion in HEA greatly diminishes the possibility of preferential growth of texture components. It might be noted that these factors fundamentally differentiates the evolution of recrystallization texture in HEA to that of conventional low SFE binary Ni-60wt.%Co alloy, as clarified in Chapter 5. Since the formation of the {113<332> component also involves preferential growth [50], this component also does not dominate the annealing texture of HEA, unlike the low SFE brass.

It may thus be apparent that even though the deformation texture of the three cold-rolled materials are different, the annealing textures consist of similar components. Absence of preferential nucleation (due to the more homogenous deformed microstructure) and preferential growth (due to sluggish diffusion in HEA) lead to the formation of similar annealing texture components in HEA cold-rolled to different strain levels. In other words, the prior cold-rolling strain affects the grain size after recrystallization, but has only limited effect on the formation of texture.

# -: CHAPTER 7 :-

## *Effect of starting grain size on the evolution of microstructure and texture*

## 7.1 Effect of initial grain size

The present chapter investigates the effect of starting grain size on the formation of recrystallization texture in the equiatomic CoCrFeMnNi HEA. For this purpose two different starting grain size materials with average grain size ~7 µm (fine grained starting material or FGSM) and ~200 µm (coarse grained starting material or CGSM) are cold-rolled up to ~95% reduction in thickness and isochronally annealed at temperatures ranging from 700°C to 1200°C. The experimental details of the processing routes are already discussed in chapter 3. The texture evolution in the FGSM has already been discussed in chapter 4. However, important results will be reproduced here in order to highlight the effect of starting grain size.

Fig.7.1 shows the grain boundary (GB) maps of the FGSM (Fig.7.1(a)) and CGSM (Fig.7.1(b)). The two maps reveal fully recrystallized microstructure and presence of annealing twins. The high angle grain boundaries (HAGBs with misorientation angle ($\theta$) $\geq$ 15°) are depicted by black lines, while the $\Sigma$3 annealing twin boundaries (TBs) are highlighted in red lines. The average grain size (twins are not considered as separate grains) is found to be ~7 µm and 200 µm for the FGSM and CGSM, respectively from the GB maps. The rather weak texture of the FGSM has been reported in Chapter 4. The texture of the CGSM is also found to be rather weak and hence not shown here separately.

## 7.2 Effect of initial grain size on microstructure and texture evolution during heavy cold-rolling

Fig.7.2(a) and Fig.7.2(b) show the microstructures (IQ maps) of 90% and 95% cold-rolled FGSM, respectively. The lamellar morphology could be observed after 90% cold-rolling (Fig.7.2(a)). Further cold-rolling to 95% reduction in thickness results in significant microstructural fragmentation (Fig.7.2(b)). The $\varphi_2$=0° sections (Fig.7.2(c) and (d)) of the ODFs (determined using XRD) of the two cold-rolled materials clearly show the presence of the strong B$_S$ component. The intensity distribution in the $\varphi_2$=45° and 65° sections of the ODF show weaker Cu and S components than B$_S$. This clearly indicates the development of a predominantly brass (or alloy) type texture. Table 7.1 is reproduced here which shows the important deformation and recrystallization texture components.
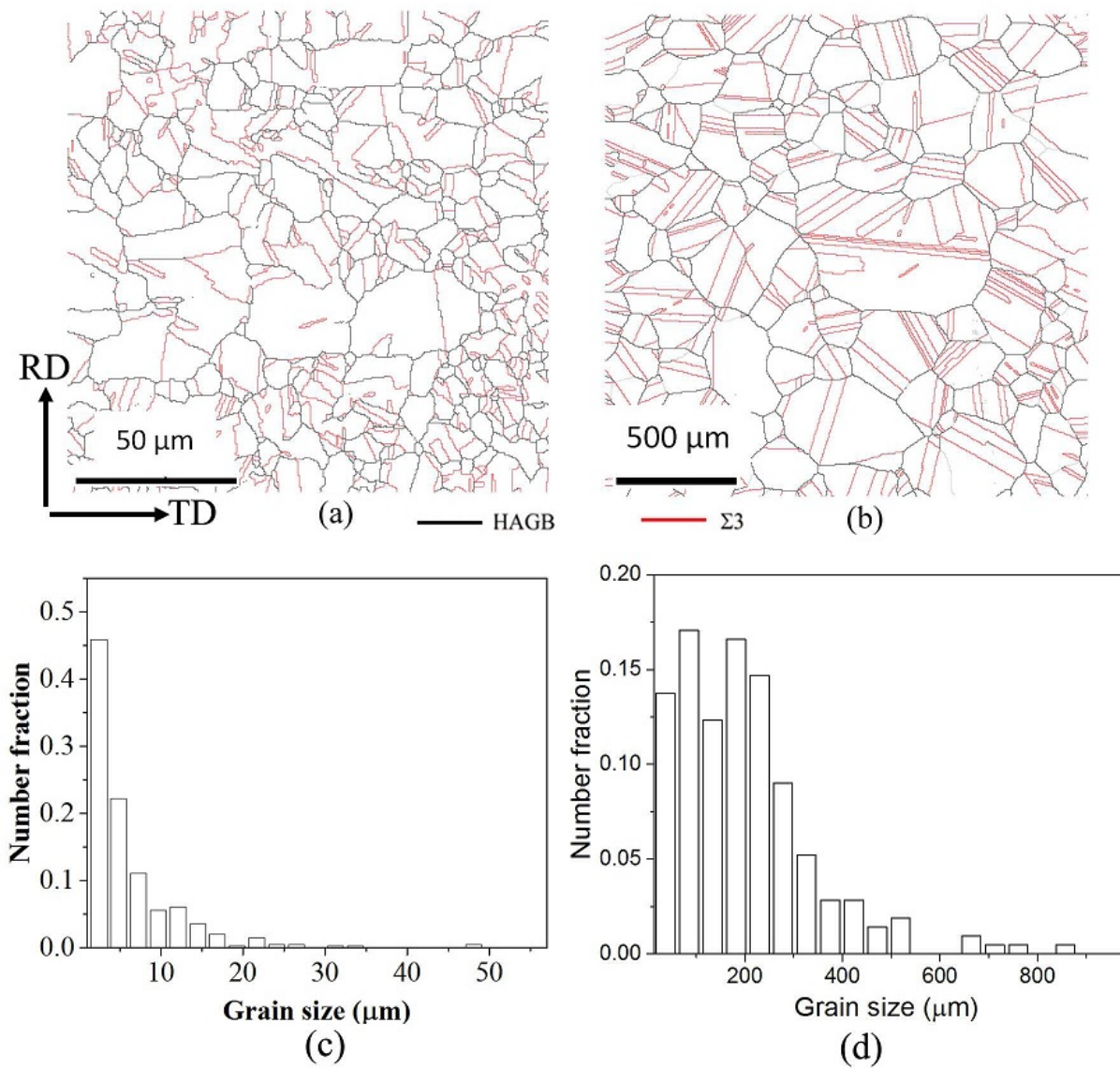
Fig.7.1: ((a)-(b)) Grain boundary maps and ((c)-(d)) Grain size distributions of FGSM and CGSM.
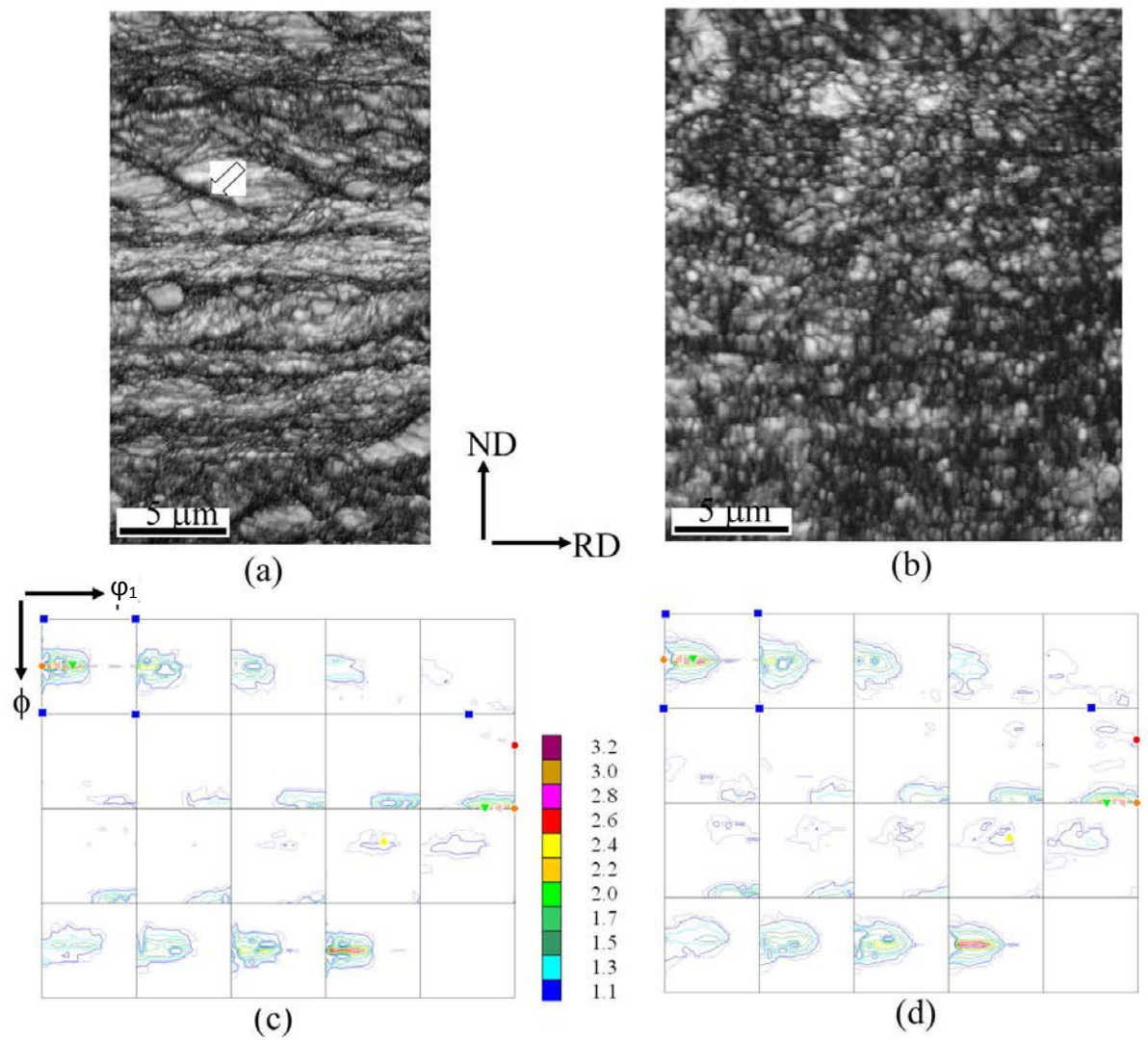
Fig.7.2: ((a)-(b)) IQ maps and ((c)-(d)) ODFs (determined by XRD) of FGSM after ((a),(c)) 90% and ((b),(d)) 95% cold-rolling (Refer to Table 7.1 for legends of the orientations in the ODFs).

Table.7.1: Euler angles and Miller indices for the observed texture components.

| Texture component | Symbol | Euler angle | | | Miller indices |
|---|---|---|---|---|---|
| | | φ₁ | φ | φ₂ | |
| Cube (C) | ■ | 0, 0, 0 | | | {001} <100> |
| Copper (Cu) | ⬢ | 90, 35, 45 | | | {112} <111> |
| S | ▲ | 59, 37, 63 | | | {123} <634> |
| Bs | ▼ | 35, 45, 0 | | | {110} <112> |
| G | ◆ | 0, 45, 0 | | | {110} <001> |
| Rt - G | ★ | 90, 45, 0 | | | {110} <110> |
| G/B | ◀ | 17, 45, 0 | | | {110} <1 1 5> |
| G/B(T) | ▶ | 55, 45, 0 | | | {110} <111> |
| BR | ⬟ | 80, 31, 34 | | | {236} <385> |
| D | ⬖ | 90, 27, 45 | | | {1 1 3} <3 3 2> |
| K | ※ | 27, 64, 14 | | | {142} <211> |
| M | ⊠ | 80, 30, 65 | | | {13 6 25} <20 15 14> |

The microstructures of the 90% and 95% (Fig.7.3) cold-rolled CGSM also show very similar development. The microstructure of the 90% cold-rolled material (Fig.7.3(a)) shows thick bands elongated along the RD. After 95% cold-rolling, the microstructure shows massive fragmentation (Fig.7.3(b)). The ODFs (obtained from the rolling plane or RD-TD section using XRD) of the 90% (Fig.7.3(c)) and 95% (Fig.7.3(d)) cold-rolled materials appear very similar to those of the FGSM. Strong presence of the $B_S$ orientation is confirmed from the $\varphi_2=0°$ section of the ODFs. The $\varphi_2=45°$ and 65° sections clearly show the presence of much stronger $B_S$ component than Cu and S components. Therefore, the cold-rolled FGSM and CGSM develop rather homogenous brass type texture throughout the volume.
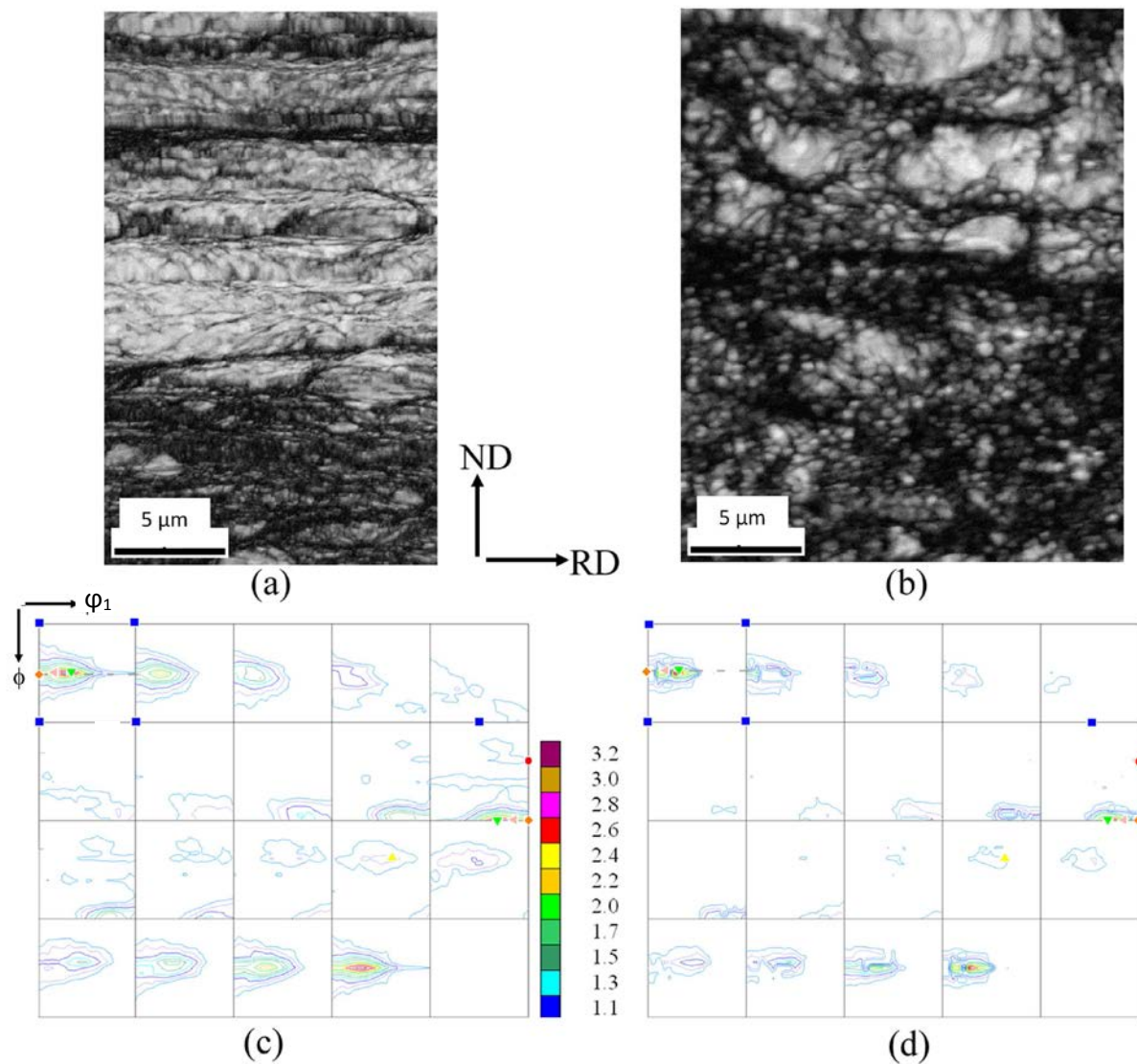
Fig.7.3: ((a)-(b)) IQ maps and ((c)-(d)) ODFs (determined by XRD) of CGSM after ((a),(c)) 90% and ((b),(d)) 95% cold-rolling (Refer to Table 7.1 for legends of the orientations in the ODFs).

## 7.3 Evolution of microstructure during annealing

Fig.7.4 shows the microstructures of the 90% (Fig.7.4(a)-(c)) and 95% (Fig.7.4(d)-(f)) cold-rolled FGSM after annealing at different temperatures. The microstructure of the FGSM (Fig. 4(a)) after annealing at 700°C shows fully recrystallized grains completely bounded by HAGBs. The average grain size is found to be approximately ~1.40 ± 1 μm. The microstructure shows profuse annealing twin boundaries (highlighted in red). Fig.7.5(a) indicates the presence of a large fraction of grain in the ultrafine range (<1 μm). The grain growth is rather limited below the annealing temperature of 1000°C (Fig.7.4(b)). Annealing at 1200°C (Fig.7.4(c)) results in extensive grain growth. The grain size distributions after annealing 1000°C (Fig.7.5(b)) and 1200°C (Fig.7.5(c)) show greater spread.

Very similar pattern of microstructural evolution is observed in the 95% cold-rolled FGSM in these annealed conditions. The material annealed at 700°C (Fig.7.4(d)) shows fully recrystallized microstructure (average grain size ~1 ± 0.5 μm) having large fraction of grains in the ultrafine regime (Fig.7.5(d)). Moderate coarsening is observed after annealing at 1000°C (Fig.7.4(e)) but extensive grain growth is observed after annealing at 1200°C (Fig.7.4(f)). Increasing spread of the distribution with increasing annealing temperature is understood (Fig.7.5((e)-(f)).

Fig.7.6 shows the microstructures of the 90% and 95% cold-rolled CGSM after annealing. The microstructures of the 90% (Fig.7.6(a)) and 95% (Fig.7.6(d)) cold-rolled CGSM after annealing at 700°C appear fully recrystallized having average grain size of ~1.6 ± 1 μm and ~1 ± 0.40 μm, respectively. The grain size distribution corresponding to these two annealing conditions show large fraction of grains in the ultrafine range (Fig.7.7(a) and Fig.7.7(d)). The microstructures after annealing at 1000°C (Fig.7.6(b) and Fig.7.6(e) corresponding to 90% and 95% cold-rolled materials, respectively) show moderate coarsening, but extensive grain growth is noticed after annealing at 1200°C (Fig.7.6(c) and Fig.7.6(f) corresponding to 90% and 95% cold-rolled materials, respectively). Here

also, the grain size distributions of the 90% and 95% cold-rolled materials annealed at the same temperature appear quite similar except for the annealing temperature of 1200°C, where few large grains (having size up to 400 mm) are observed in the 95% cold-rolled material (Fig.7.7(f)) but not in the 90% cold-rolled material (Fig.7.7(c)).

Fig.7.8 shows the comparison of key microstructural parameters in the different annealed conditions. The plot (Fig.7.8(a)) does not show any significant difference in grain size amongst different materials after annealing at 700°C. Two important observations after annealing at higher temperatures can be highlighted. Firstly, the final recrystallized grain size is strongly affected by the starting grain size, so that the 90% and 95% cold-rolled FGSM annealed at 1000°C and 1200°C show decidedly lower grain size as compared to their CGSM counterparts. Secondly, the grain size is not vastly different for 90% and 95% rolled FGSM up to the annealing temperature of 1200°C. Very similar behavior is observed for the CGSM up to the annealing temperature of 1000°C. However, after annealing at 1200°C the 95% cold-rolled CGSM shows higher grain size than 90% cold-rolled CGSM. The fraction of annealing TBs (Fig.7.8(b)) is increased with increasing annealing temperature. The TB fraction is not significantly different at lower annealing temperatures where the grain growth effect is limited. However, after annealing at 1000°C, when the average grain size in FGSM is considerably smaller than CGSM, the TB fraction is also found to be lower in the FGSM. In addition, the 95% cold-rolled CGSM which shows considerably larger grain size, the TB fraction is also found to be greater.

Fig.7.4: Orientation maps of ((a)-(c)) 90% and ((d)-(f)) 95% cold-rolled FGSM following annealing at ((a),(d)) 700°C, ((b),(e)) 1000°C and ((c),(f)) 1200°C for 1 h (Refer to Table 7.1 for the legends of the orientations).
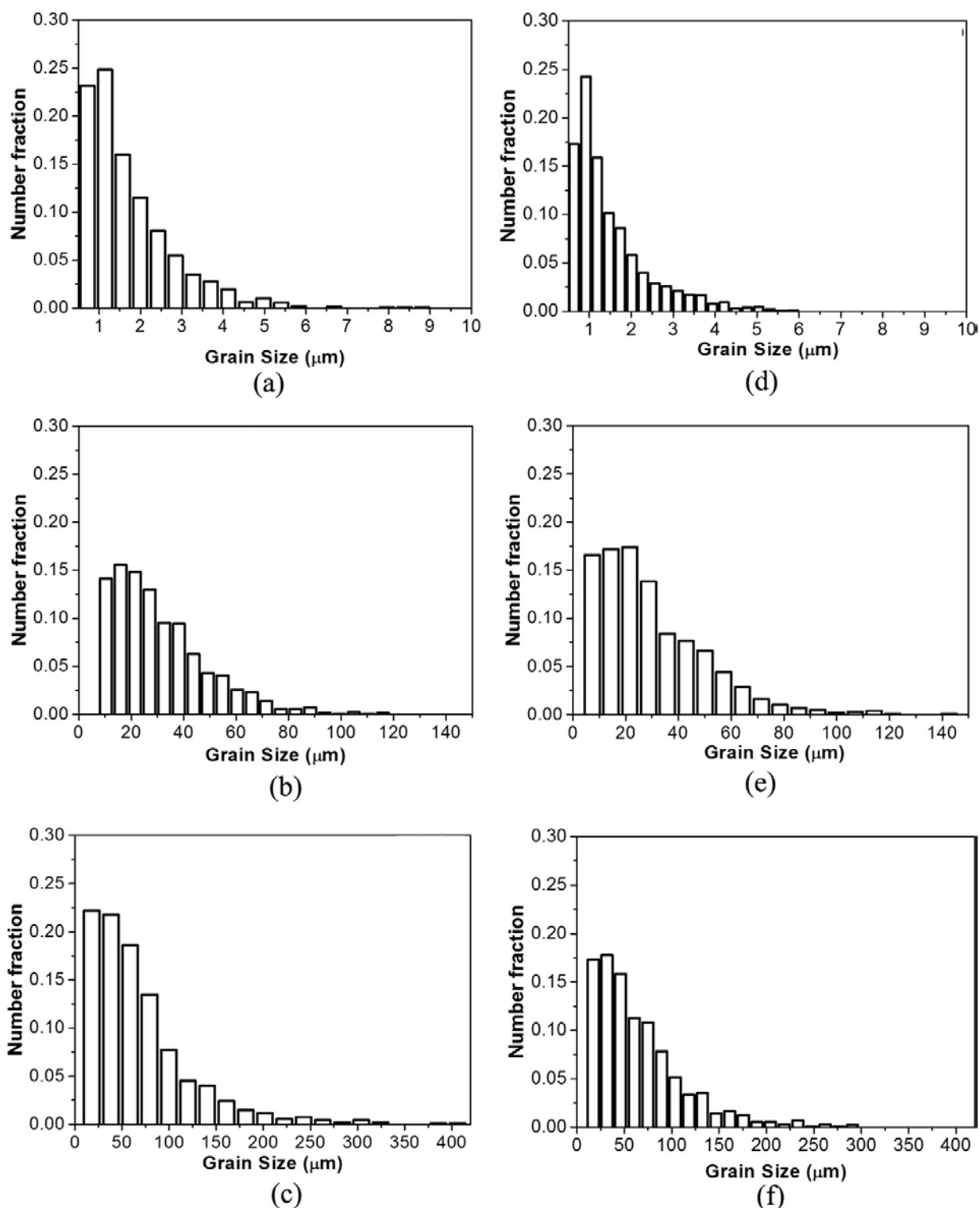
Fig.7.5: Grain size distribution of ((a)-(c)) 90% and ((d)-(f)) 95% cold-rolled FGSM following annealing at ((a),(d)) 700°C, ((b),(e)) 1000°C and ((c),(f)) 1200°C for 1 h.
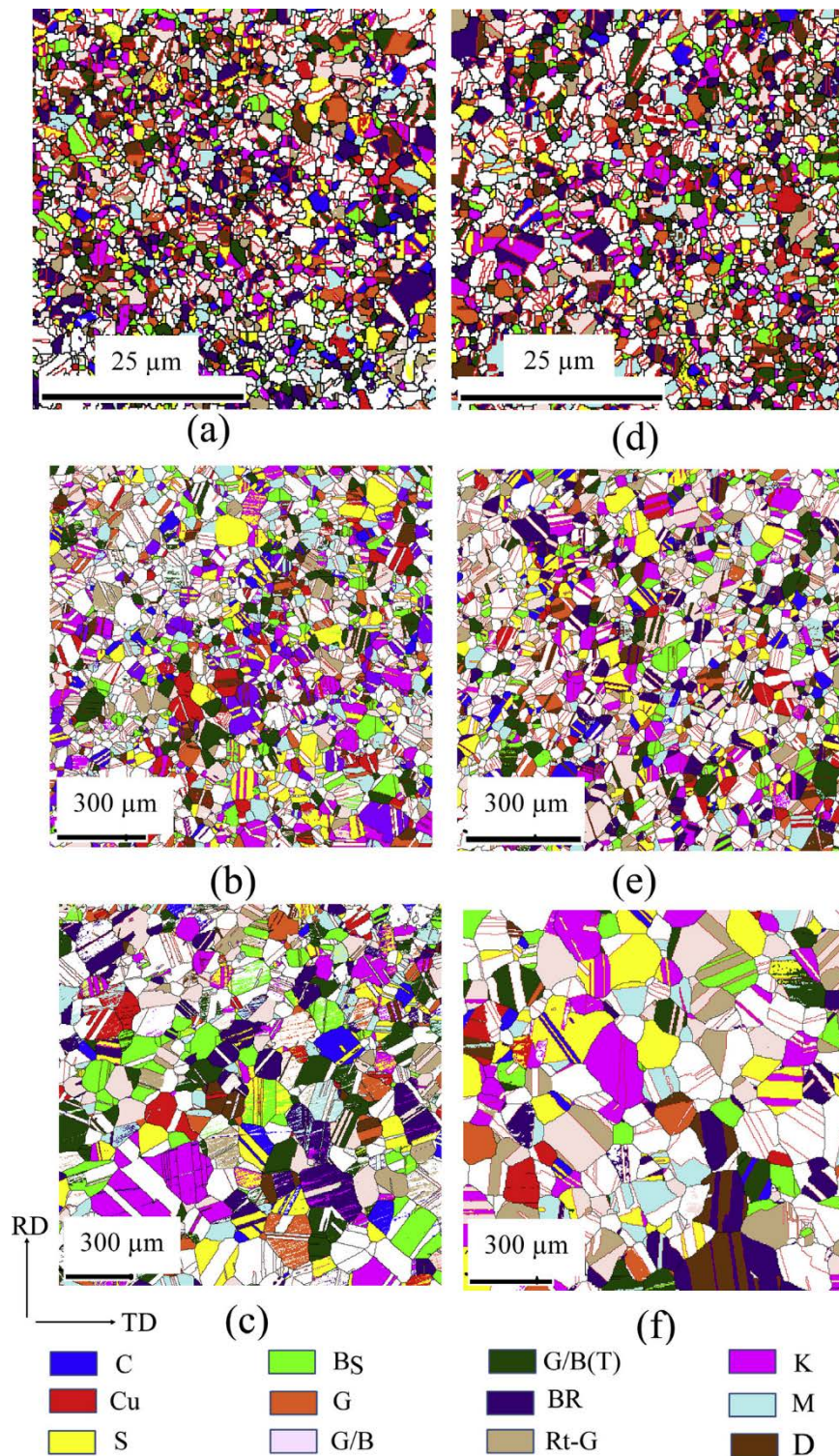
Fig.7.6: Orientation maps of ((a)-(c)) 90% and ((d)-(f)) 95% cold-rolled CGSM following annealing at ((a),(d)) 700°C, ((b),(e)) 1000°C and ((c),(f)) 1200°C for 1 h (Refer to Table 7.1 for legends of the orientations).
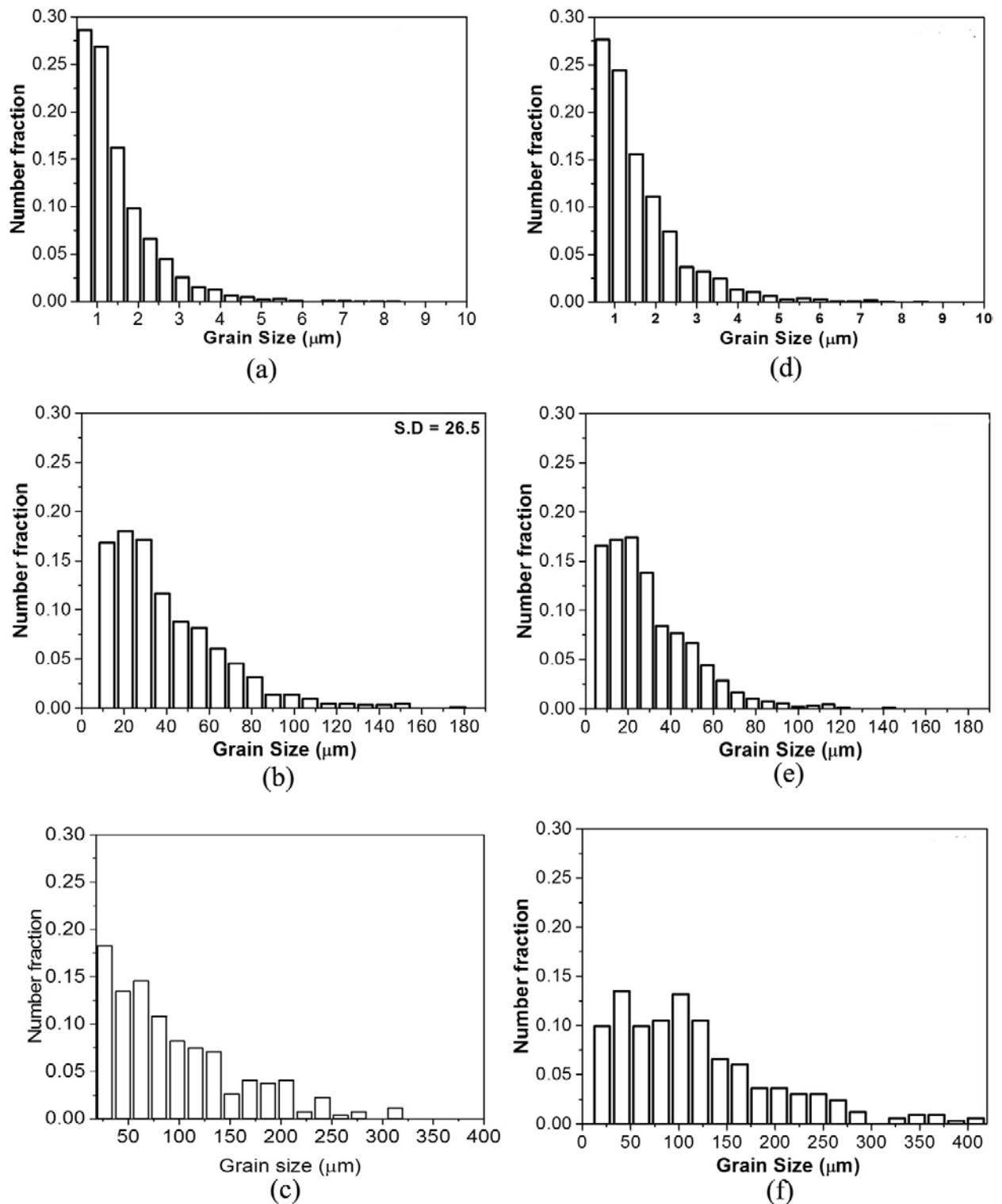
Fig.7.7: Grain size distribution of ((a)-(c)) 90% and ((d)-(f)) 95% cold-rolled CGSM following annealing at ((a),(d)) 700°C, ((b),(e)) 1000°C and ((c),(f)) 1200°C for 1 h.

(a)



(b)
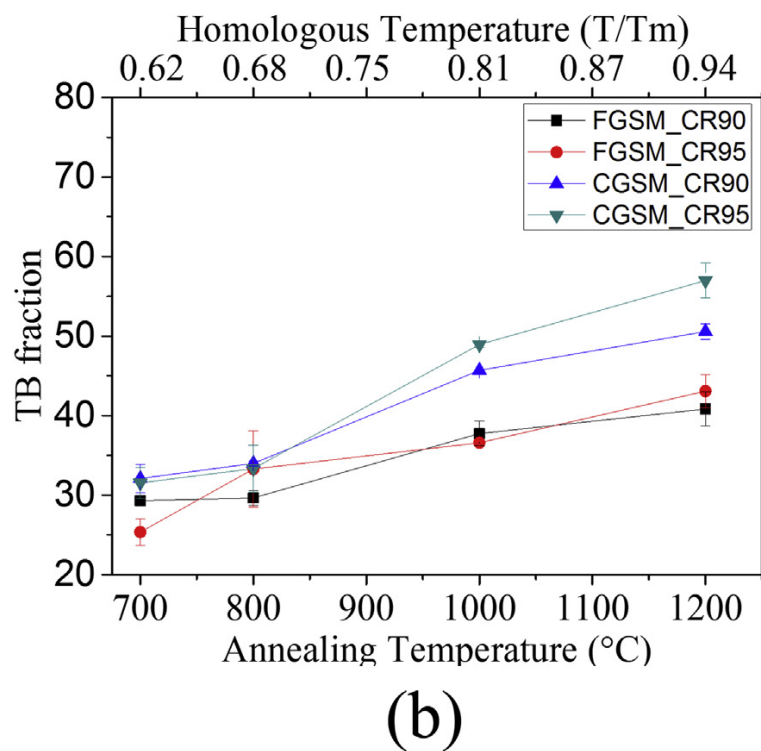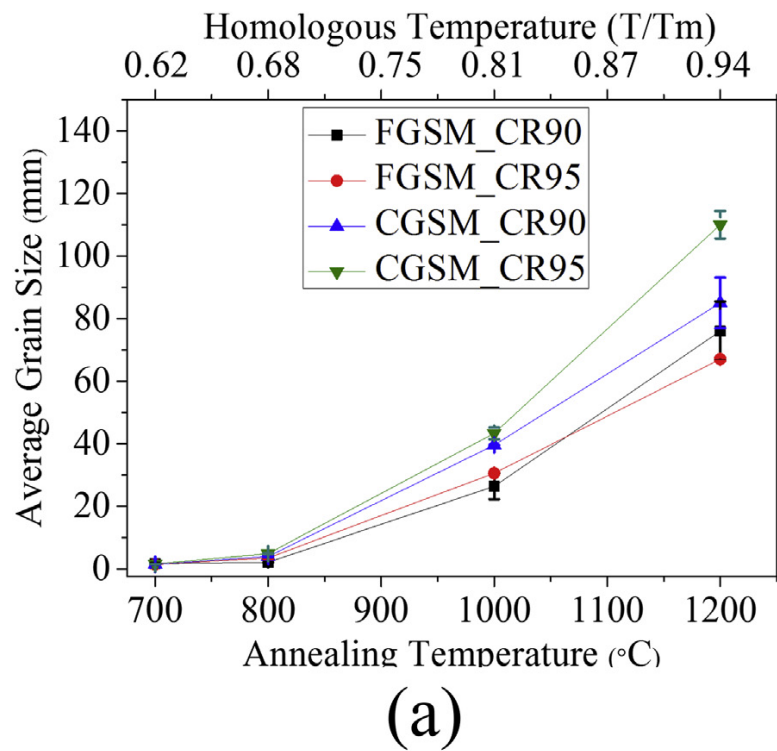
Fig.7.8: Variation of (a) grain size and (b) TB fraction with annealing temperature in FGSM and CGSM.

## 7.4 Evolution of microtexture during annealing

In order to understand the evolution of recrystallization texture, the ODFs (determined by EBSD) of annealed FGSM and CGSM specimens are examined carefully. Fig.7.9 shows the relevant ODF sections ($\varphi_2$=0°, 15°, 35°, 45° and 65°) of 90% (Fig.7.9((a)-(c)) and 95% (Fig.7.9((d)-(f)) cold-rolled FGSM after different annealing treatments. The $\varphi_2$=0° section of the ODF of the 90% cold-rolled FGSM after annealing at 700°C (Fig.7.9(a)) shows the presence of a discontinuous α-fiber which is shown as the skeleton line extending from the G to the Rt-G through the G/B, Bs and G/B(T) orientations. The presence of the G/B orientation could be confirmed from the orientation map (highlighted in rose) shown in Fig.7.4(a). The presence of the Bs component is also noticed in the orientation map (highlighted in green) while the other α-fiber orientations, such as, G (highlighted in orange), G/B(T) (highlighted in dark green) and Rt-G (highlighted in tan) are present only as minor components. The $\varphi_2$=15° section (Fig.7.9(a)) shows noticeable intensity at the vicinity of the {142}<211> component (K). The volume fraction of this component is found to be ~8% from the orientation map. The $\Phi_2$=35° section shows strong intensity at the ($\varphi_1$, $\Phi$, $\varphi_2$=80°,31°,35°) location corresponding to the brass recrystallization component (BR) {236}<385>. The orientation map reveals significant presence of this component (highlighted in indigo, volume fraction ~ 17%). The $\varphi_2$=45° and $\varphi_2$=65° sections of the ODFs and the orientation map in Fig.7.4(a) show the presence of the Cu (highlighted in red) and S (highlighted in yellow) orientations. The volume fraction of these two components are found to be ~2% and 5%, respectively. However, M orientation ({13 6 25}<20 15 4}) is observed in the orientation map (highlighted in cyan) (Fig.7.4(a)) having volume fraction ~6%. The D orientation ({113}<332>) (highlighted in wine) shows a volume fraction of ~4% in the orientation map. The presence of the discontinuous α-fiber is clearly observed in the $\varphi_2$=0° section of the ODF of FGSM annealed at 1000°C (Fig.7.9(b)) and 1200°C (Fig.7.9(c)). The ODF sections show the presence of the same texture components, namely K, BR, Bs, Cu, S and M

components at their respective locations. Presence of these components could also be easily observed in the orientation maps of the materials annealed at 1000°C (Fig.7.4(b)) and 1200°C (Fig.7.4(c)).

The corresponding ODF sections of the 95% cold-rolled FGSM (Fig.7.9(d)-(f)), 90% (Fig.7.10(a)-(c)) and 95% (Fig.7.10(d)-(e)) cold-rolled CGSM after annealing at different temperatures appear very similar amongst them and also show evident similarities with the corresponding ODF sections of the 90% cold-rolled and annealed FGSM (Fig.7.9((a)-(c)). This indicates the presence of very similar texture components. However, the ODF sections of the 95% cold-rolled CGSM annealed at 1200°C (Fig.7.10(f)) appear somewhat different than those of the 90% cold-rolled/annealed CGSM (Fig.7.10(d)) and 95% cold-rolled/annealed FGSM (Fig.7.9(f)). In particular, the ODF sections appear quite diffuse indicating weakening of texture. Notably, the {113}<332> component (D) does not show any noticeable increase in the 95% cold-rolled material even after annealing at 1200°C which is evident from the ODF sections and the relevant orientation maps (Fig.7.4 and 7.6).
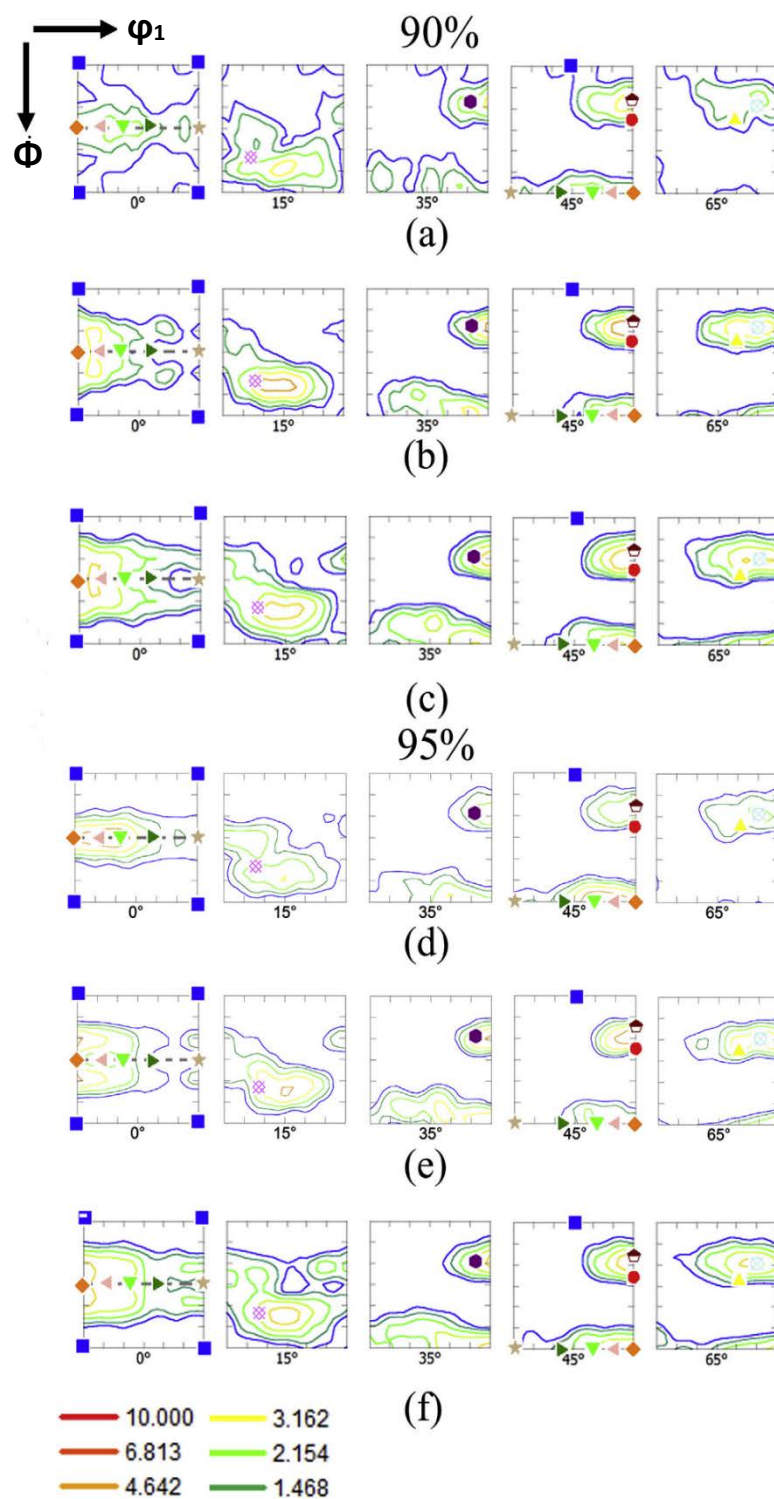
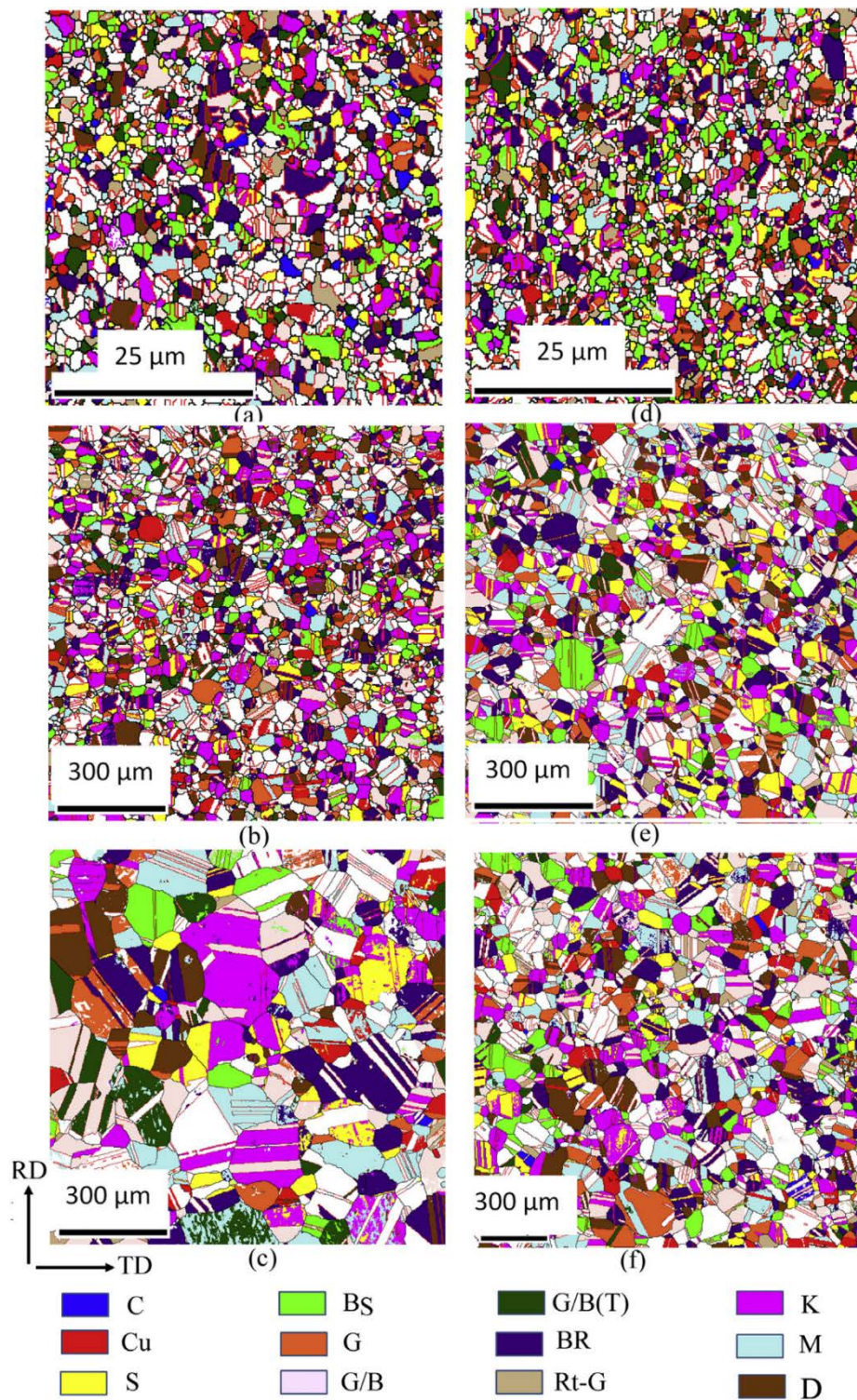Fig.7.9: The relevant ODF sections (determined by EBSD) of ((a)-(c)) 90% and ((d)-(f)) 95% cold-rolled FGSM following annealing at ((a),(d)) 700°C, ((b),(e)) 1000°C, ((c),(f)) 1200°C for 1 h (Refer to Table 7.1 for symbols used in the ODF sections).
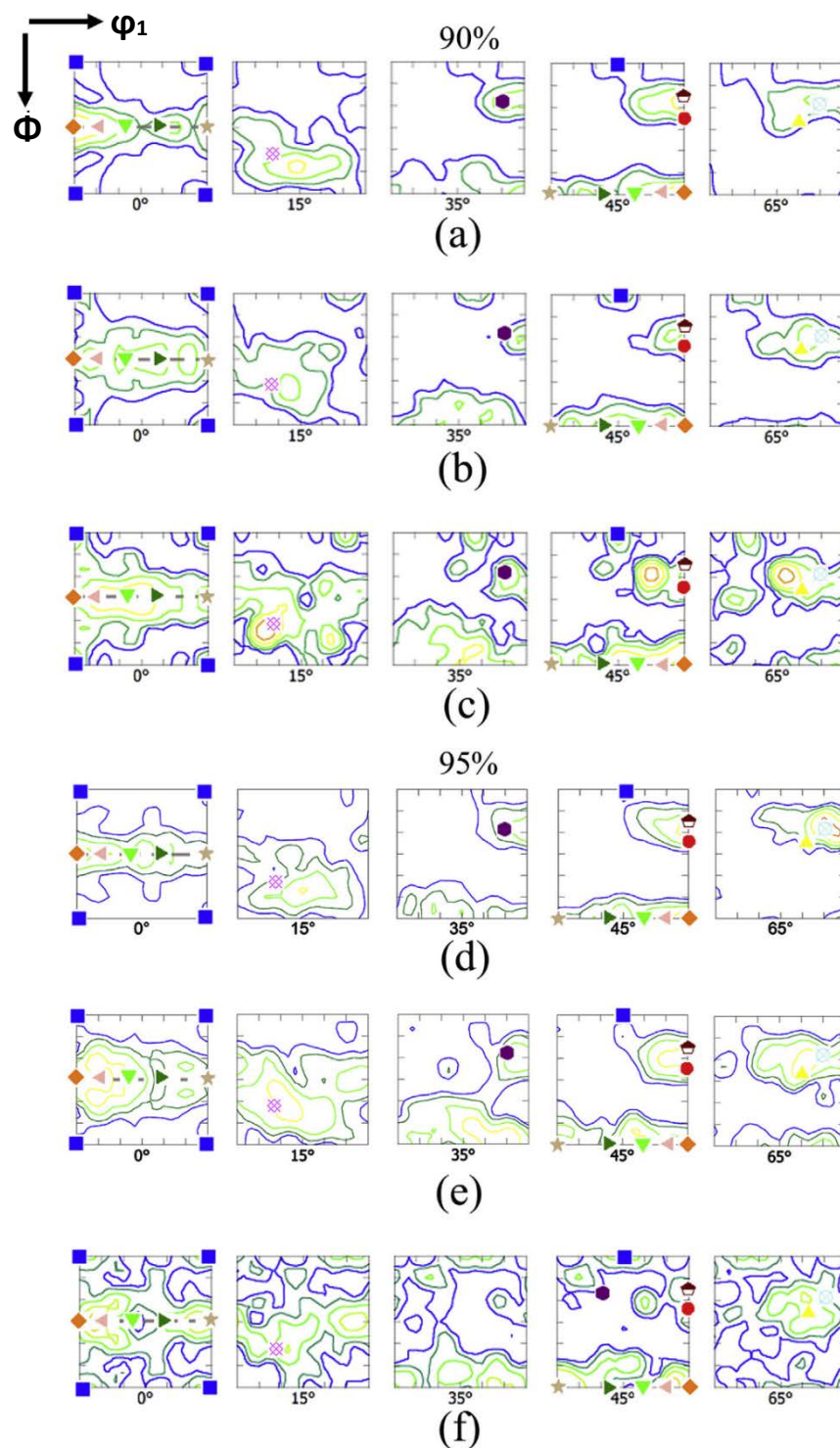
Fig.7.10: The relevant ODF sections (determined by EBSD) of ((a)-(c)) 90% and ((d)-(f)) 95% cold-rolled CGSM after annealing at ((a),(d)) 700°C, ((b),(e)) 1000°C, ((c),(f)) 1200°C for 1 h (Refer to Table 7.1 for symbols used in the ODF sections).

Fig.7.11 shows the variation of texture components with annealing temperature in 90% and 95% cold-rolled FGSM and CGSM. It is clearly observed that the individual texture components in the 90% and 95% cold-rolled and annealed FGSM (Fig.7.11(a) and Fig.7.11(b), respectively) do not show any major variation with annealing temperature. This is also evident in case of the 90% cold-rolled and annealed CGSM (Fig7.11(c)). The plot of 95% cold-rolled and annealed CGSM (Fig.7.11(d)) shows decrease in the volume fraction of the BR component and increase in the volume fraction of the random components. This is consistent with the diffuse ODF sections (Fig.7.10(f)) observed after annealing at 1200°C. The variation of the two important texture components, namely the BR and {332}<113> are shown separately in Fig.7.12(a) and 7.12(b), respectively. The volume fractions of these components are not significantly different in FGSM or CGSM. Thus, the volume fractions of different texture components are not significantly affected by the starting grain size or annealing temperature.
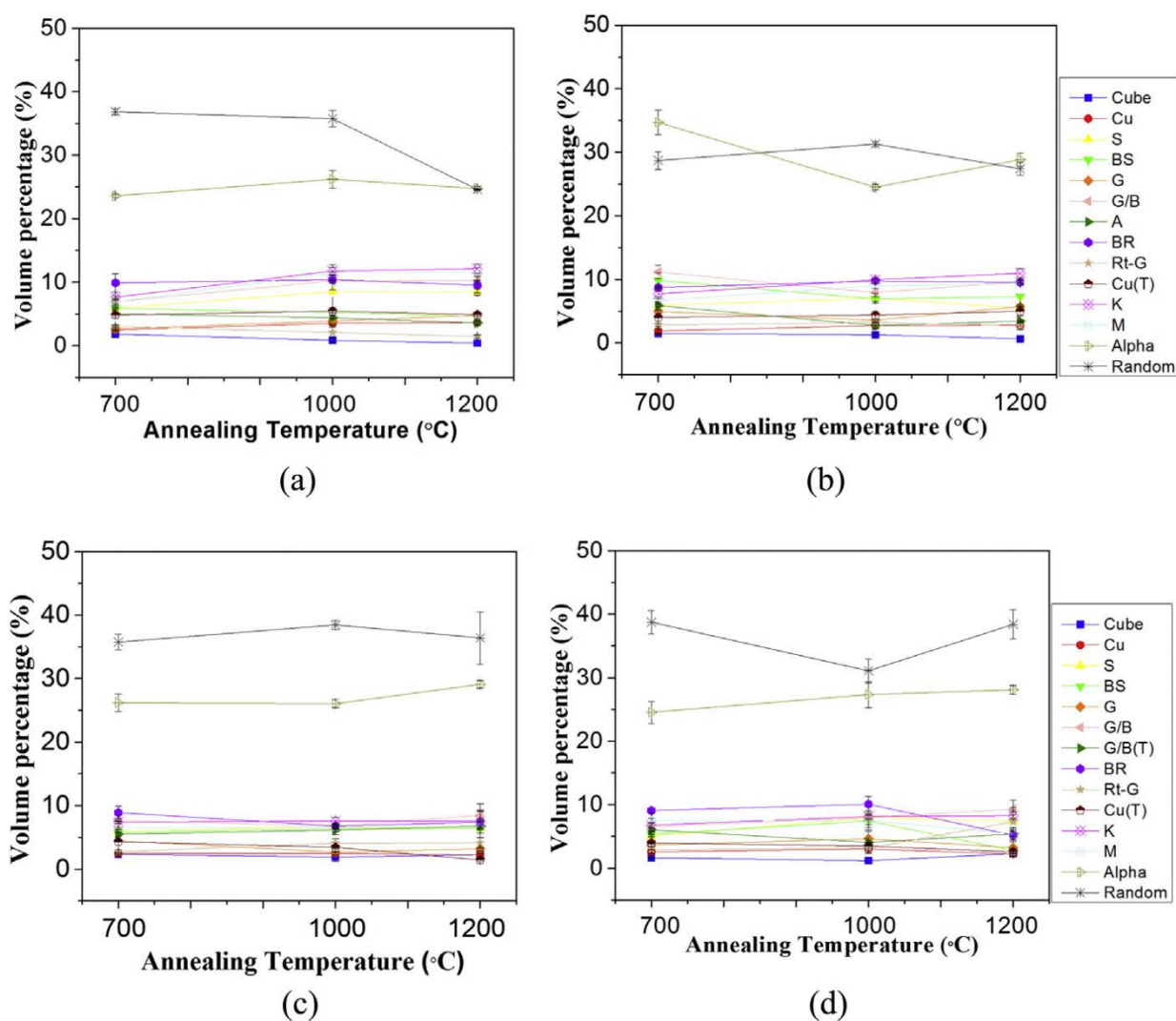
Fig.7.11: Variation of volume fraction of texture components with annealing temperature in (a) 90% and (b) 95% cold-rolled FGSM; (c) and (d) show the variation of texture components with annealing temperature in 90% and 95% cold-rolled CGSM, respectively.
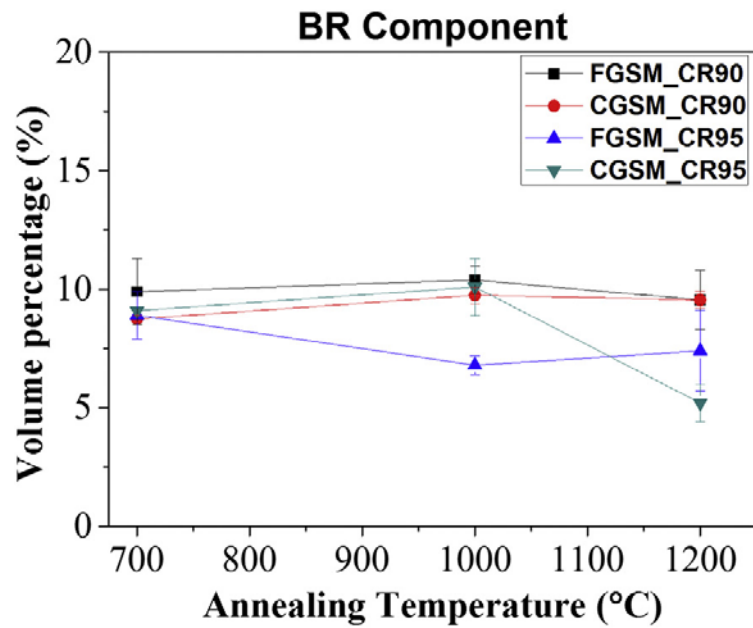
(a)
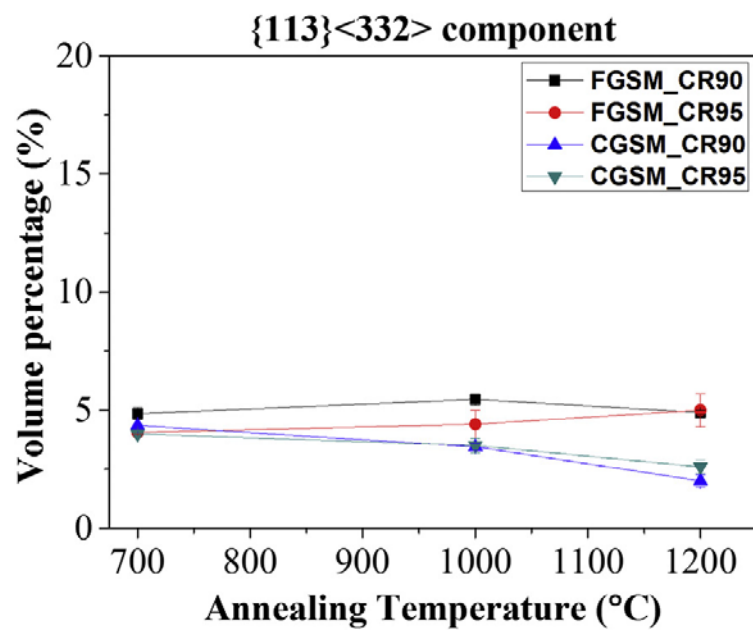


Fig.7.12: Variation of (a) BR {236}<385> and (b) D {113}<332> components with annealing temperature (CR is abbreviated for cold-rolled).

## 7.5. Discussion

Duggan et al [112] have studied in detail the effect of starting grain size on the formation of recrystallization texture in low SFE ɑ-brass. These authors have reported a rather complex behavior. After medium to heavy rolling (~90%) and annealing at low temperature (e.g. at 300°C), the {110}<110> component is strengthened at the expense of the BR component with increasing starting grain size. However, after high temperature annealing, the textures of the fine and coarse grained materials show prominent {110}<112> component. In the severe deformation regime (≥95% cold-rolling), the BR or {236}<385> component dominates the texture of both fine and coarse grained materials after low temperature annealing. The {113}<332> component dominates the recrystallization texture of both fine and coarse grained materials after high temperature annealing. Thus, over a wide grain size range, the texture of the heavily rolled materials (>95% thickness reduction) is dominated by the BR component after low temperature annealing and {113}<332> after high temperature annealing, respectively [50]. These results are summarized in Table 7.2.

The softening behavior in heavily deformed low SFE materials, such as HEAs, is characterized by the discontinuous recrystallization process which proceeds through the typical nucleation and growth stages [50]. Therefore, the available nucleation sites and growth conditions would determine the final recrystallized grain size. In deformed materials such nucleation sites may be the grain boundaries and deformation heterogeneities (e.g. deformation bands, transition bands and shear bands) [50]. The starting grain size significantly affects the final recrystallized grain size by affecting the density of potential nucleation sites. In general, finer is the starting grain size finer is the grain size after recrystallization. This behavior is usually attributed to finer microstructure or greater number of available nucleation sites in deformed condition in initially fine grained materials [50].

Table 7.2: Summary of annealing texture development in low SFE 70:30 brass having different starting grain size [50].

| Initial grain size | Texture components | | | |
|---|---|---|---|---|
| | Medium to heavy cold-rolling (~90%) | | Severe cold-rolling (≥95%) | |
| | Low temperature annealing | High temperature annealing | Low temperature annealing | High temperature annealing |
| Fine grained | {236}<385> | {110}<112> | {236}<385> | {113}<332> |
| Coarse grained | {110}<110> | {110}<112> | {236}<385> | {113}<332> |

The microstructures of the two cold-rolled materials appear fully recrystallized after annealing at 700°C. The average recrystallized grain size does not differ significantly (Fig.7.8(a)). This may be attributed to the sluggish diffusion in HEA system which restricts grain growth [28]. At higher annealing temperatures (≥1000°C) where nucleation is followed by significant grain growth, the grain size of the CGSM is significantly higher than that of the FGSM. This clearly indicates that the FGSM is having greater number of potential nucleation sites as compared to that in the CGSM. It may also be noted that a larger starting grain size is expected to result in more deformation heterogeneities in the heavily cold-rolled condition. Despite this, the finer recrystallized grain size in the annealed FGSM indicates that preferential nucleation at shear bands is not a very dominant mechanism in HEAs. The texture evolution during annealing will further clarify these issues.

An interesting point is that the grain size of the 95% cold-rolled CGSM annealed at 1200°C is greater than that of the 90% cold-rolled CGSM annealed at the same temperature (Fig.7.8(a)). This apparent anomaly could be explained by the rather small thickness of the 95% cold-rolled sheet which restricts grain growth but leads to the growth of more randomly oriented grains, which is also observed in the orientation map (Fig.7.6(f)). Further support for this phenomenon is obtained from the texture development which will be discussed later.

It might be noted that the annealing TB fraction is not vastly different at lower annealing temperatures due to quite similar average grain size in different annealed materials. However, after annealing at 1200°C the fraction of annealing TBs is noticeably higher in the CGSM as compared to that in the FGSM. At the same time the average grain size is also higher in the CGSM as already discussed. Thus, annealing TB fraction shows strong dependence on the final average recrystallized grain size as reported recently by Otto et al [79].

These observations are analyzed by the authors [79] based on the theory of annealing twin formation of Fullman and Fischer [93]. According to this theory, formation of annealing TBs during grain growth is promoted by the migration of triple points, which results in lowering of the total boundary energy. During the continued migration of the triple points, the original grains are replaced by new grains, resulting in the formation of new twins and further lowering of the energy. This process is evidently related to the migration distances which is comparable to the scale of grain size. As a consequence, the twin boundary fraction should be proportional to the final grain size. This convincingly explains higher TB fractions in the CGSM than FGSM after annealing at 1000°C and 1200°C. This is also consistent with higher TB fraction in the 95% cold-rolled CGSM as compared to that in the 90% cold-rolled CGSM after annealing at 1200°C (Fig.7.8(b)).

In the present case, the deformation textures of the FGSM and CGSM show very similar strong brass type texture despite widely different starting grain size. Remarkably, the annealing textures of the two materials do not reveal any significant dependence on the annealing temperature and starting grain size. In addition, although the BR component is present in FGSM and CGSM cold-rolled to different thickness reduction after annealing, the strength of this component is not significantly greater than the other texture components. The {113}{332} (D) component also does not show any considerable increase in the 95% cold-rolled and annealed materials as compared to that in the 90% cold-rolled and annealed materials, irrespective of the starting grain size (i.e. true for both FGSM and CGSM). The present observations are thus clearly at variance with annealing texture formation in α-brass [112]. In the case of α-brass, strong dependence of recrystallization texture formation on starting grain size, strain and annealing temperature may be easily noticed (Table 7.2).

The mechanism of evolution of annealing texture of HEA can now be analyzed. The evolution BR component in low SFE brass includes nucleation at shear bands followed by preferential growth. Similarly, the Rt-G or

{110}<110> component also involves nucleation at special deformation heterogeneities [50]. However, more homogenous microstructures of deformed FGSM and CGSM ensure that nucleation at deformation heterogeneities does not play a decisive role on the formation of recrystallization texture in HEA. As a result, preferential nucleation of {110}<110> and BR oriented grains is not promoted in the present HEA unlike low SFE brass. The marginal or insignificant variation of the volume fractions of different texture components with annealing temperature further indicates similar growth rate of different texture components. It may be noted that the preferential growth of texture components, as noted in the mechanism of strong BR texture evolution, involves rapid migration of boundaries, which in turn, depends on rapid diffusivity of atoms across the boundaries. As clarified recently, the present HEA shows sluggish diffusion [28] with rather high activation energy for grain growth [29]. Therefore, the sluggish diffusion in HEA greatly diminishes the possibility of preferential growth of texture components [113]. Since the formation of the {113}<332> component also involves preferential growth [65], this component does not dominate the annealing texture of FGSM or CGSM unlike the low SFE brass (Table.7.2).

The 95% cold-rolled CGSM after annealing at 1200°C shows slightly different features. More diffuse ODFs, decrease in the BR component concomitant with the increase in the random fraction are already pointed out. These effects can be explained on the basis of rather small thickness of the 95% cold-rolled sheet (~125 μm) where the grain size (~110 μm) approaches the sheet thickness introducing the growth of randomly oriented grains. It may be noted that in the case of 90% cold-rolled CGSM, although the grain size is rather large (~85 μm), this effect is not very pronounced due to relatively larger sheet thickness (~250 μm).

In summary, irrespective of the starting grain size, development of a strong brass type texture is observed during heavy cold-rolling. However, the recrystallization texture is not significantly affected by the prior grain size or annealing temperature. Absence of preferential nucleation and growth restrict the development of strong BR and {113}<332> components, leading to the formation of similar annealing texture components. In other words, starting grain size affects the microstructure evolution after annealing but has only limited effect on the formation of annealing texture.

# -: CHAPTER 8 :-

## *Effect of heavy cryo-rolling on the evolution of microstructure and texture*

## 8.1 Effect of heavy cryo-rolling

The current chapter presents the results concerning the effect of heavy cryo-rolling on the microstructure and texture formation in the equiatomic CoCrFeMnNi HEA. For this purpose cryo-rolling up to 90% reduction in thickness is followed by annealing at different temperatures varying from 700°C to 1200°C (the experimental details are already discussed in chapter 3). The microstructure and texture evolution in the cryo-rolled alloy is compared with the behavior of cold-rolled alloy in order to highlight the effect of heavy cryo-rolling. Although, the results on cold-rolled alloy have already been discussed in Chapter 4 and Chapter 7, relevant results will be reproduced here for the ease of comparison.

## 8.2 Effect of heavy cryo-rolling on microstructure and texture evolution

Fig.8.1(a) shows the microstructure of the starting recrystallized material showing the presence of profuse annealing twin boundaries. The high angle grain boundaries (HAGBs with misorientation angle ($\theta$) $\geq$ 15°) are depicted by black lines, while the $\Sigma$3 annealing twin boundaries (TBs) are highlighted in red lines. The average grain size (neglecting annealing twins as separate grains) of the starting material is ~7 μm.

The microstructure of the 90% cryo-rolled material (Fig.8.1(b)) appears much more fragmented resulting in much finer microstructure as compared to the cold-rolled material (Fig.8.1(c)). Cryo-rolled microstructure reveals many interconnecting micro shear bands (marked by arrows in the Fig.8.1(b)). Local fragmentation resulting in the cell structure can be observed in the both the deformed microstructures. The cell size is much smaller in lamellar boundaries and shear bands than that in between them.

Fig.8.1(d) shows the (111) PF of the starting material which reveals a rather weak texture. The (111) PFs of the 90% cryo- (Fig.8.1(e)) and cold-rolled materials (Fig.8.1(f)) indicate the presence of strong brass (Bs) component ({110} <112>). The bulk texture (obtained by XRD) is represented by the complete ODFs of the 90% cryo- (Fig.8.2(a)) and cold-rolled materials (Fig.8.2(b)). The corresponding ODF sections appear quite similar. The Development of incomplete α-fiber (RD//<110>), defined as the skeleton line extending from the Goss (G, {011}<100>) to the rotated-Goss orientation (Rt-G, {011}<110>), is easily noticed in the $\varphi_2$=0° section of both the ODFs with particularly strong intensities around the ideal Bs location. Thus, the texture evolution of both cryo and cold-rolled materials follow the similar trend. The important texture components observed in deformed and different annealed conditions are summarized in Table 8.1.
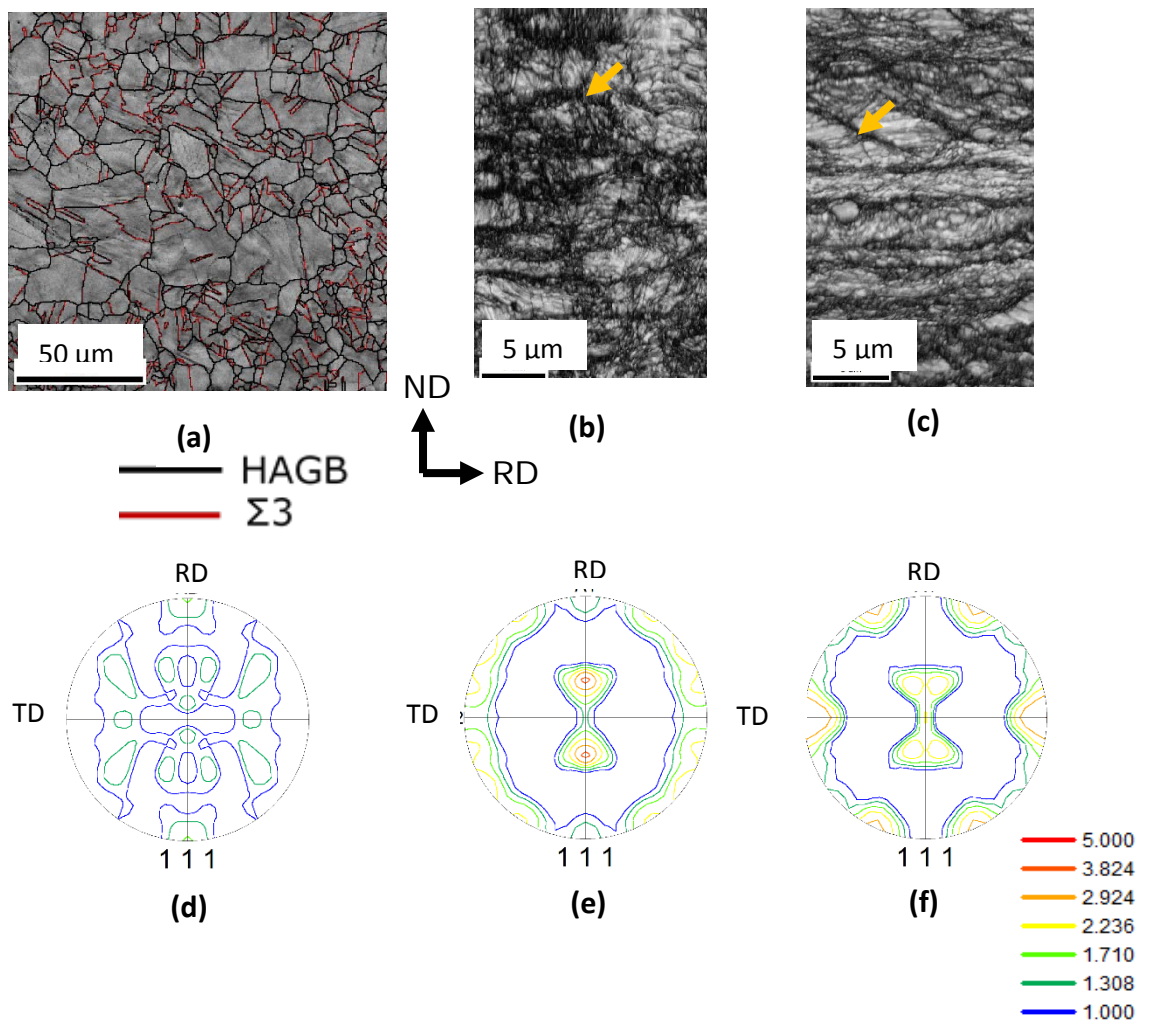
Fig.8.1: Microstructures of (a) starting, (b) 90% cryo-rolled and (c) 90% cold-rolled materials; (d), (e) and (f) show the corresponding (111) PFs.

(a)



(b)
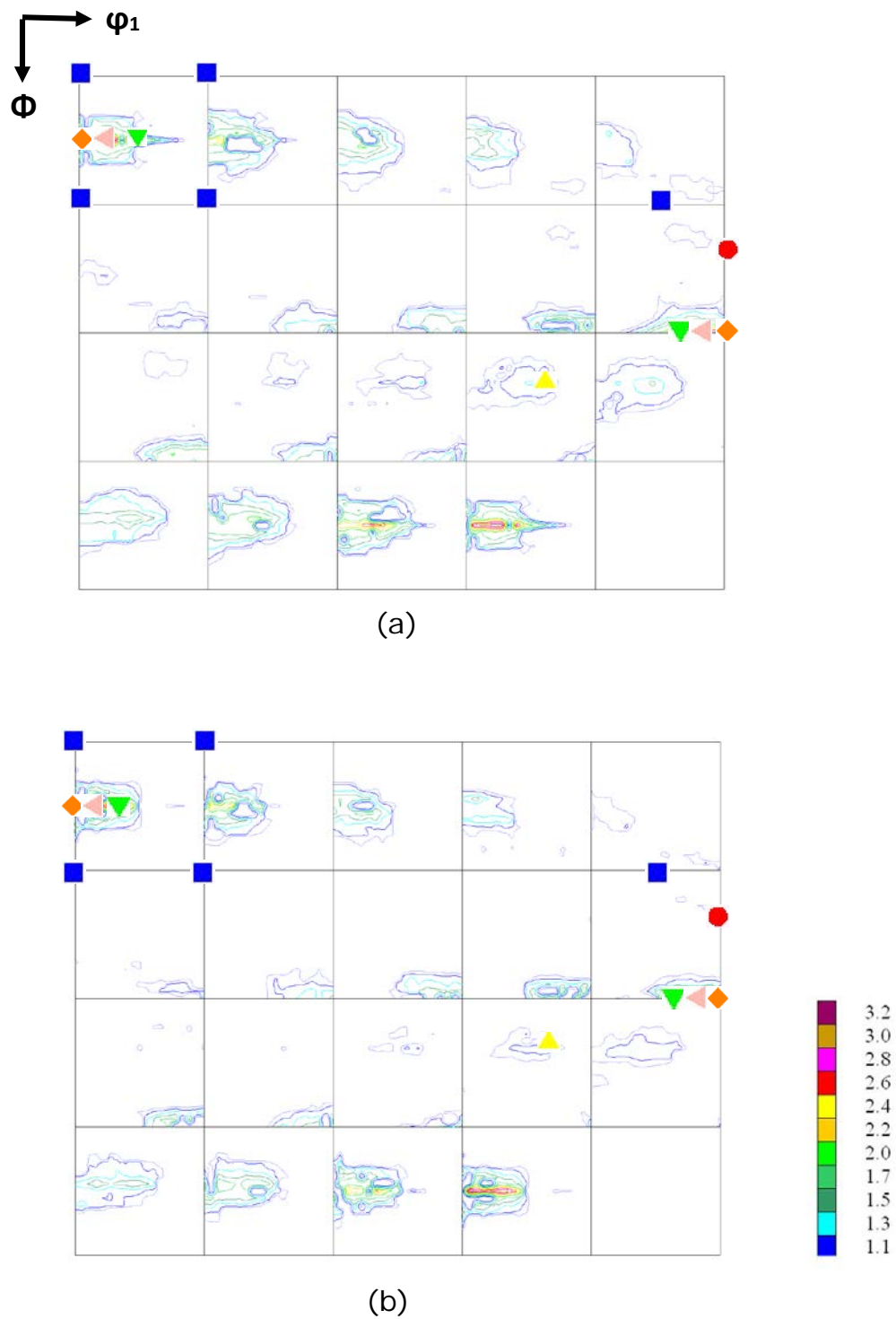
Fig.8.2: ODFs (determined by XRD) of (a) 90% cryo-rolled (b) 90% cold-rolled materials (Refer to Table 8.1 for legends of the orientations in the ODFs).

Table.8.1: Miller indices and corresponding set of Euler angles for important deformation and recrystallization texture components.

| Texture component | Symbol | Euler angle | | | Miller indices |
|---|---|---|---|---|---|
| | | $\varphi_1$ | $\phi$ | $\varphi_2$ | |
| Cube (C) | ■ | 0, 0, 0 | | | {001} <100> |
| Copper (Cu) | ⬟ | 90, 35, 45 | | | {112} <111> |
| S | ▲ | 59, 37, 63 | | | {123} <634> |
| Bs | ▼ | 35, 45, 0 | | | {110} <112> |
| G | ◆ | 0, 45, 0 | | | {110} <001> |
| Rt - G | ★ | 90, 45, 0 | | | {110} <110> |
| G/B | ◄ | 17, 45, 0 | | | {110} <1 1 5> |
| G/B(T) | ▶ | 55, 45, 0 | | | {110} <111> |
| BR | ⬣ | 80, 31, 34 | | | {236} <385> |
| D | ⬠ | 90, 27, 45 | | | {1 1 3} <3 3 2> |
| K | ✳ | 27, 64, 14 | | | {142} <211> |
| M | ⊗ | 80, 30, 65 | | | {13 6 25} <20 15 14> |

## 8.3 Microstructure evolution during annealing

Fig.8.3 shows the evolution of microstructures during isochronal annealing of the 90% cryo- and cold-rolled materials. The orientation maps of the cryo- (Fig.8.3(a)) and cold-rolled materials (Fig.3(d)) annealed at 700°C reveal fully recrystallized state. Annealing at 1000°C and 1200°C results in perceptible grain growth in both cryo- (Fig.8.3((b)-(c)) and cold-rolled materials (Fig.8.3((e)-(f)).

Fig.8.4 shows the grain size as a function of annealing temperature. The cryo-rolled material consistently shows lower average grain size as compared to the cold-rolled material. This holds true for average grain size calculated disregarding (i.e. twins are not considered as separate grains) or considering annealing twins (twins are considered as separate grains). It may be noted that the average grain size of the cryo- and cold-rolled materials after annealing at 700°C is ~ 1.3 μm and 1.6 μm, respectively. Therefore, the absolute difference is quite negligible, although the relative difference is appreciable (~23%). In contrast, the difference is quite remarkable after annealing at higher annealing temperature. Annealing at higher annealing temperatures (1000°C and 1200°C) leads to considerable difference in grain size between cold- and cryo-rolled materials.
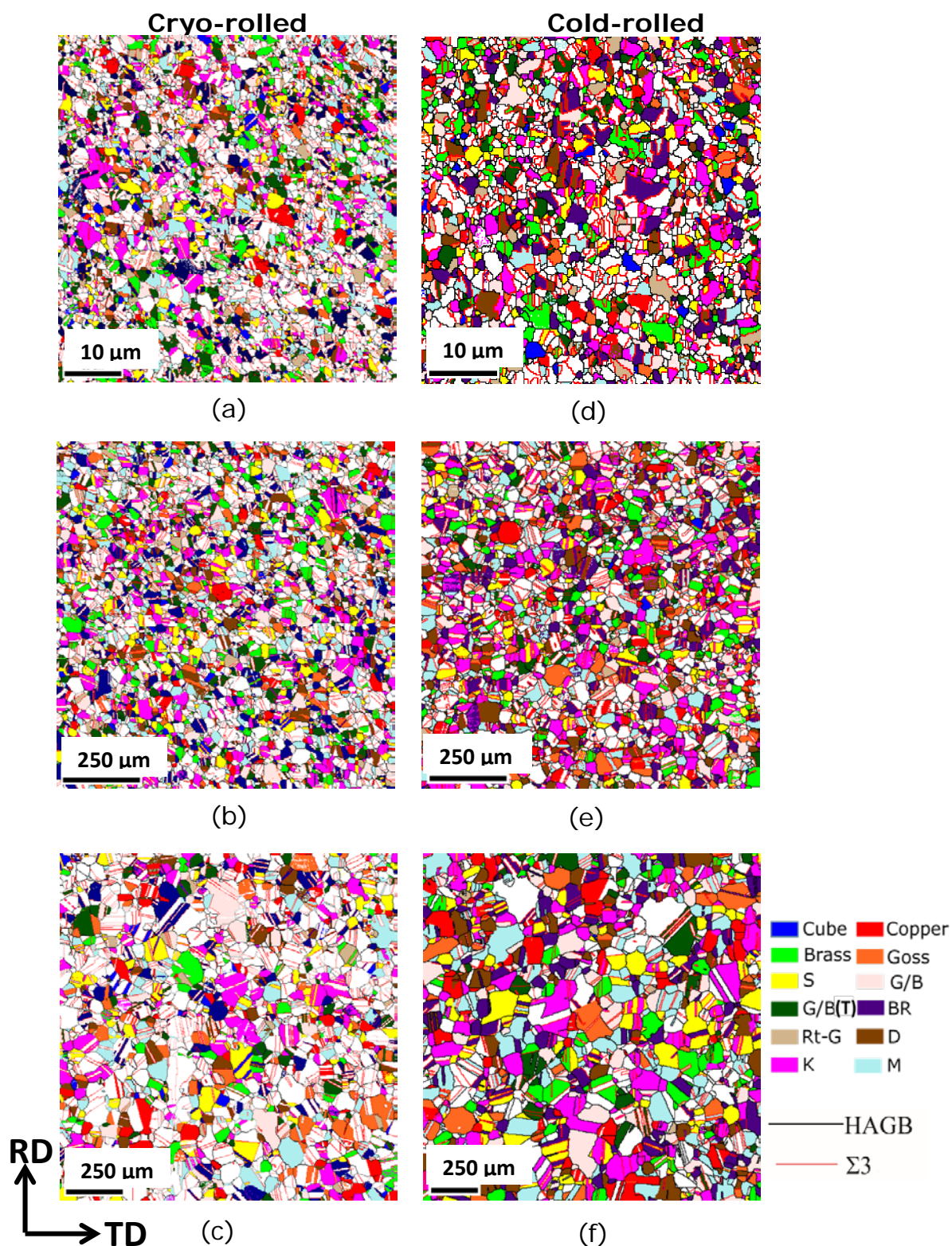
Fig.8.3: The orientation maps of cryo- ((a)-(c)) and cold-rolled HEAs ((d)-(f)) after annealing at 700°C ((a), (d)), 1000°C ((b),(e)) and 1200°C ((c), (f)).
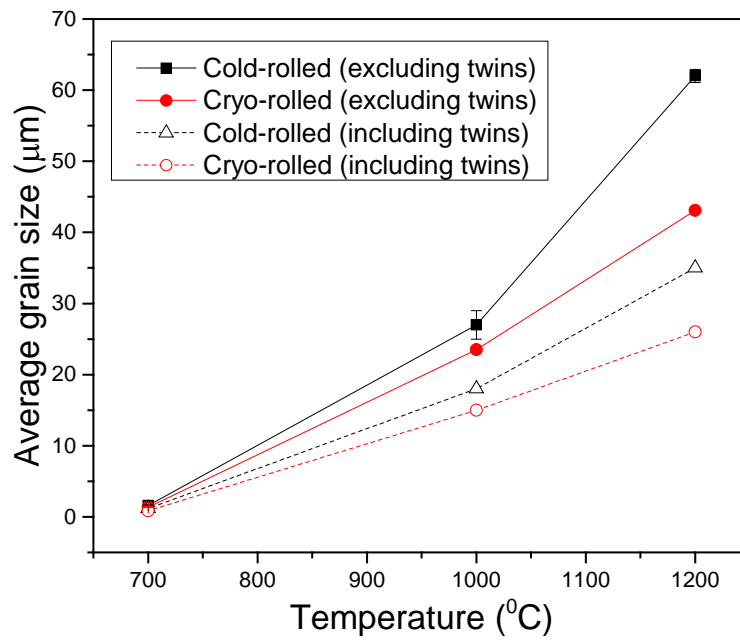
Fig.8.4: Variation of grain size with annealing temperature in cryo and cold-rolled materials.

## 8.4 Microtexture evolution during annealing

In order to understand the evolution of texture after annealing, ODFs (determined by EBSD) of the annealed cryo-rolled and cold-rolled materials (Fig.8.5) are examined carefully along with the orientation maps (Fig.8.3). Fig.8.5(a) shows the $\varphi_2=0°$ section of the ODF of the 90% cryo-rolled specimen after annealing at 700°C. It shows the presence of a discontinuity α-fiber, which is already introduced as the skeleton line extending from the G to the Rt-G through the G/B, $B_S$ and G/B(T) orientations. The presence of the G/B orientation could be confirmed from the orientation map (highlighted in rose) shown in Fig.8.3(a). The volume fractions of the G/B and G/B(T) components are similar ~5% as determined from the orientation map (Fig.8.3(a)). The intensity distribution at the locations of the K and BR components is also found to be quite comparable. Accordingly, the volume fractions of these two components are found to be quite similar ~6% (Fig.8.3(a)). Intensity peak may be observed associated with the M component in the $\varphi_2=65°$ section of the ODF (Fig.8.3(a)). The volume fraction of this component is ~ 6.5%, which is slightly greater than the volume fraction of the S component (~5%). The volume fractions of the Cu (~2%) and D (~2.7%) components are quite low. The ODF sections of the cryo-rolled materials annealed at 1000°C (Fig.8.5(b)) and 1200°C (Fig.8.5(c)) show the presence of very similar texture components, namely K, BR, BS, Cu, S and M components, as in the case of the material annealed at 700°C.

The presence of the discontinuous α-fiber is continued to be observed in the $\varphi_2=0°$ section of the ODF of the cold-rolled materials annealed at 700°C (Fig.8.5(d), 1000°C (Fig.8.5(e)) and 1200°C (Fig.8.5(f)). Only minor change in intensities or shift from the ideal locations of the different texture components could be observed in the cold-rolled materials. Therefore, the texture of the cryo-rolled material does not show significant variation with annealing temperature which is quite similar to the behavior observed in the case of the cold-rolled material.
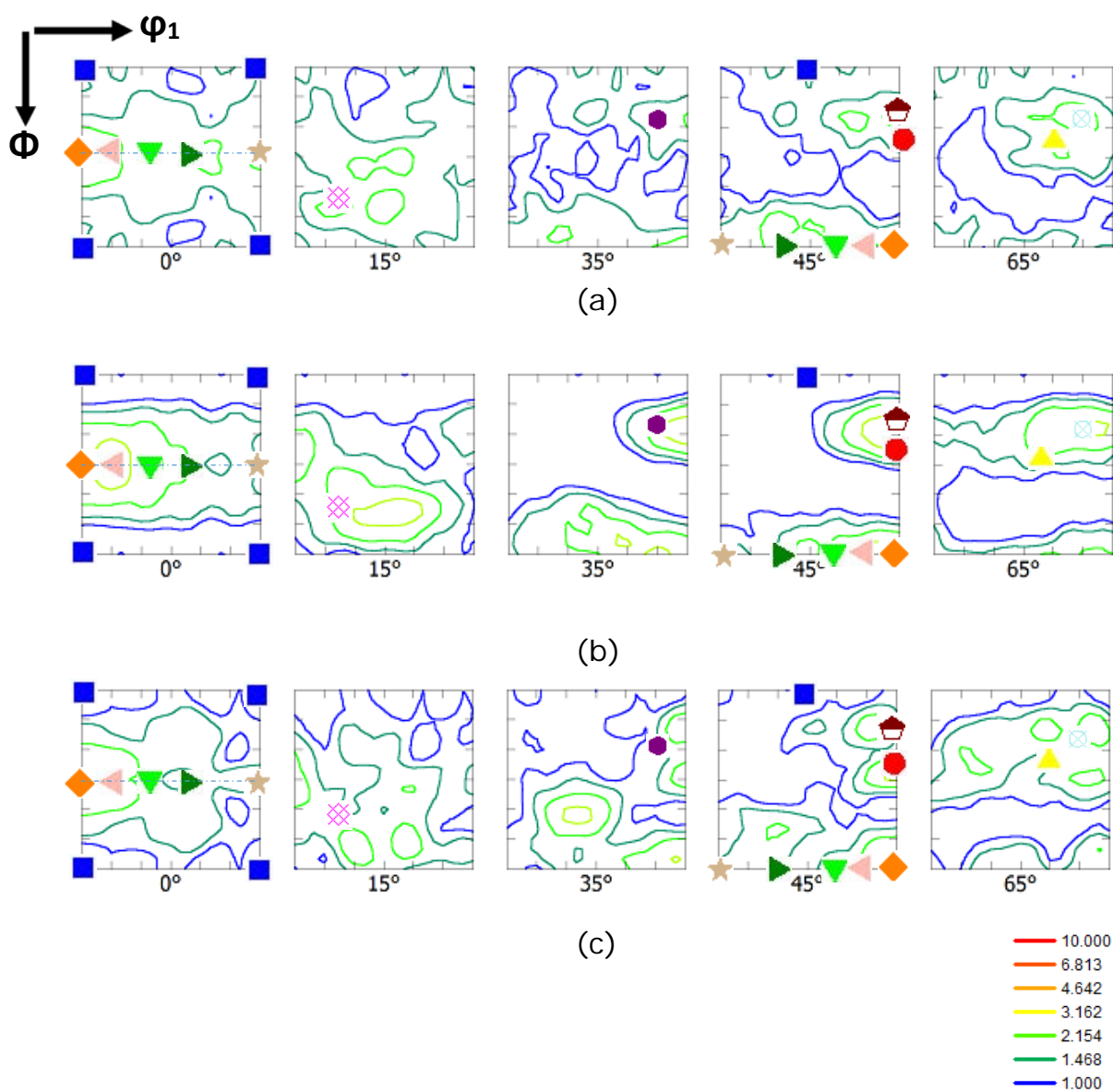
Fig.8.5: Relevant ODF sections of cryo-rolled material annealed at (a) 700°C, (b) 1000°C and (c) 1200°C (Refer to Table 8.1 for symbols used in the ODF sections).
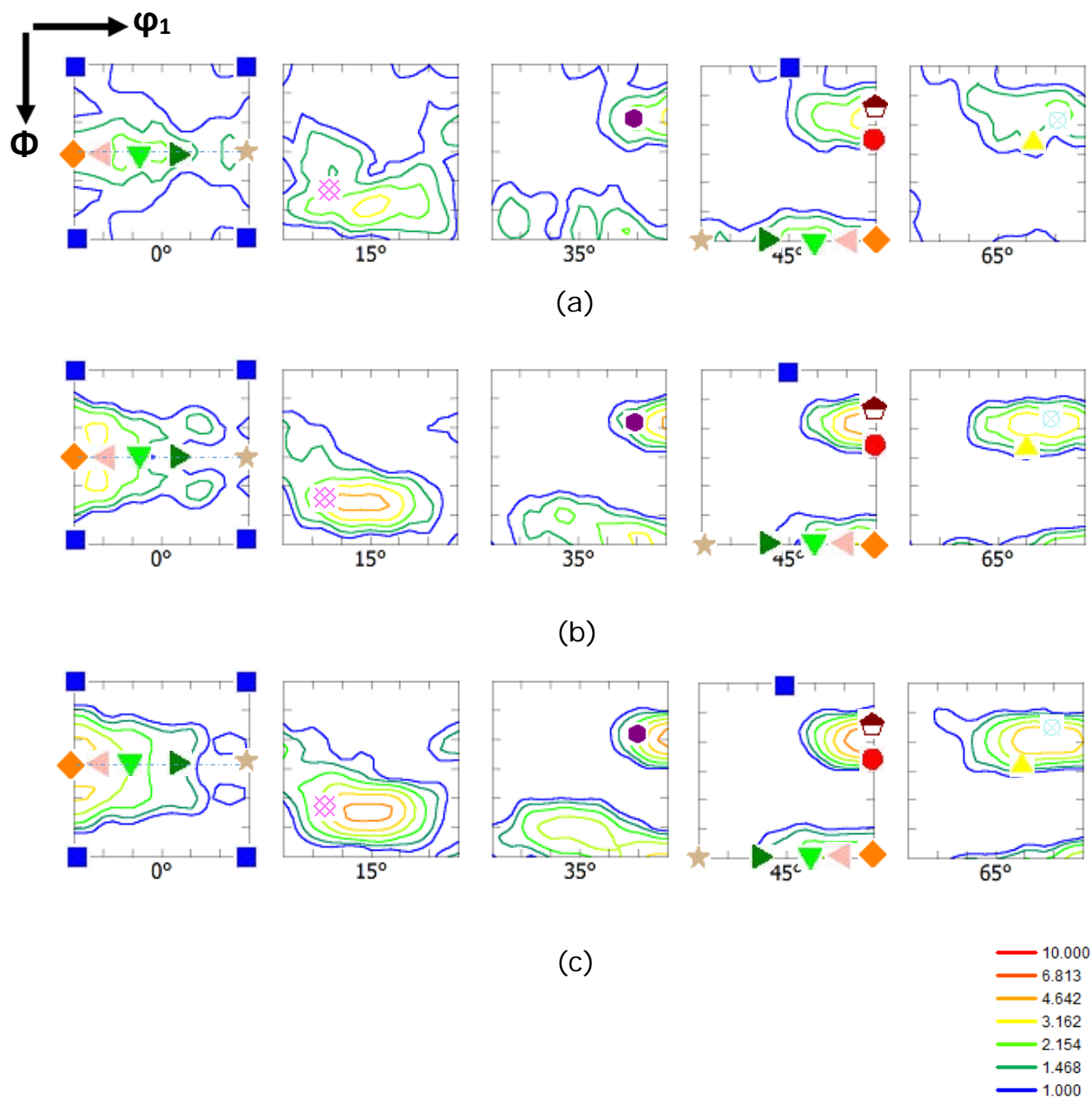
Fig.8.6: Relevant ODF sections of cold-rolled material annealed at (a) 700°C, (b) 1000°C and (c) 1200°C (Refer to Table 8.1 for symbols used in the ODF sections).

Fig.8.7 shows the variation of texture components with annealing temperature in the cryo- (Fig.8.7(a)) and cold-rolled (Fig.8.7(b)) materials. Higher fraction of random components but weaker α-fiber component are seen in the annealed cryo-rolled material as compared to the annealed cold-rolled material. It is clearly observed that texture components do not show significant variation with annealing temperature for both cryo (Fig.8.7(a)) and cold-rolled materials (Fig.8.7(b)). Further, this behavior is quite consistent with the information already obtained from the respective ODFs of these materials. Fig.8.7(c) shows the variation of texture index (which indicates the strength of texture) with annealing temperature. In case of the cold-rolled material, the texture index shows consistent increase with increasing annealing temperature. In contrast, the texture index of the cryo-rolled materials increases after annealing at 1000°C but decreases after annealing at 1200°C.
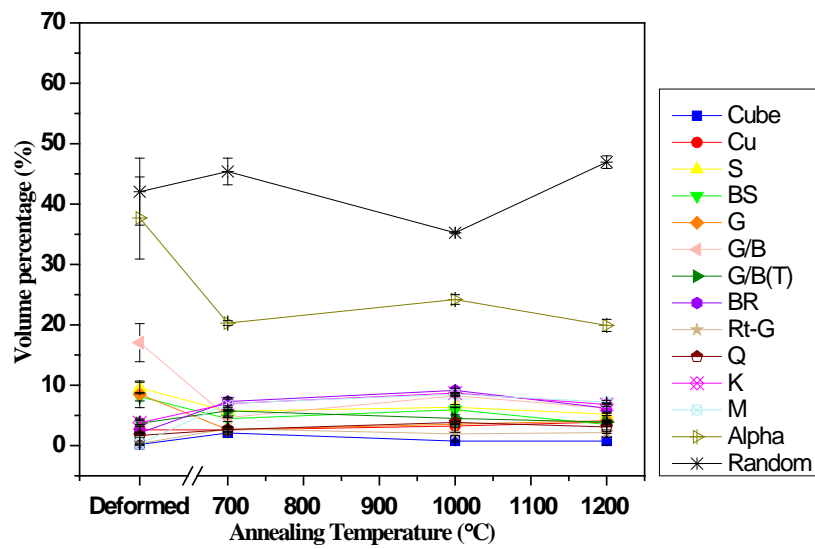
(a)
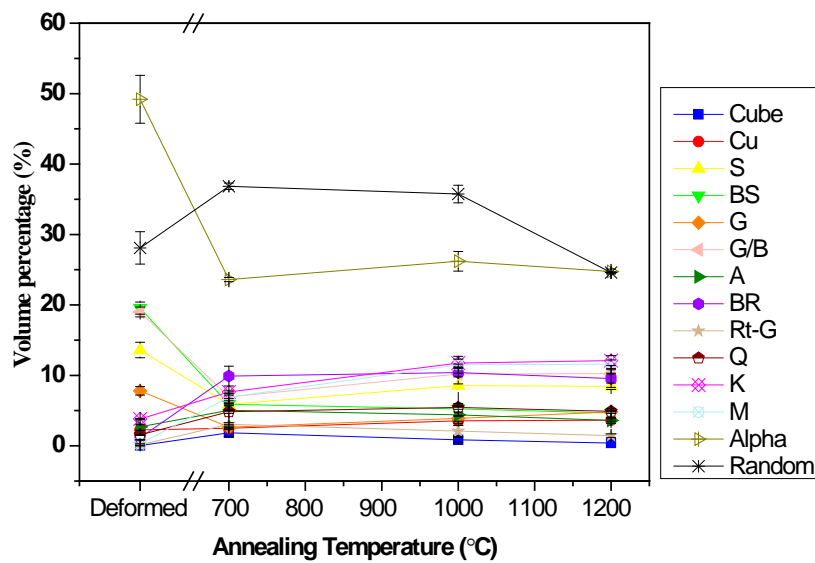


(b)

Fig.8.7: Variation of volume fractions of texture components with annealing temperature in (a) cryo- and (b) cold-rolled materials.
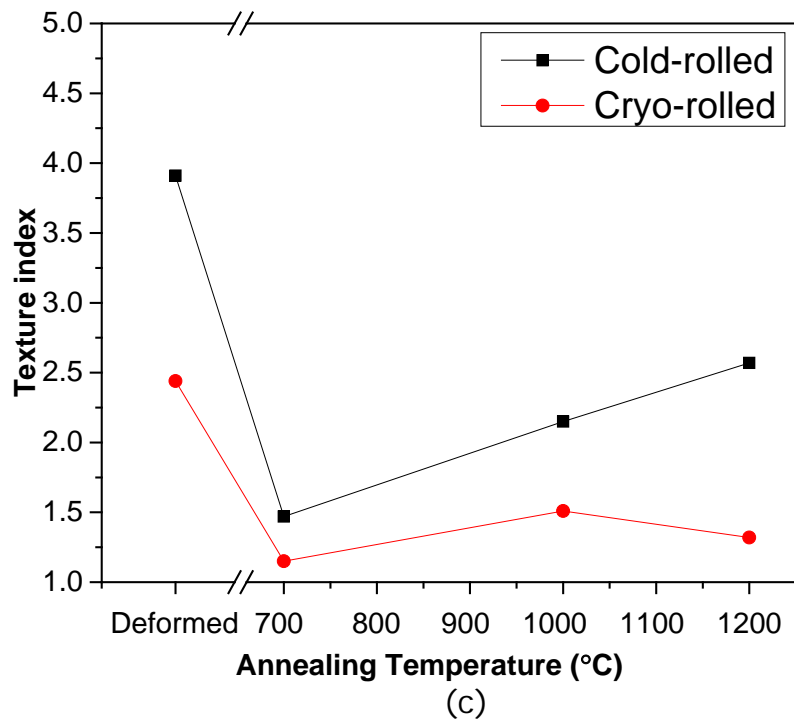
Fig.8.7: (c) the variation of texture index with annealing temperature in cryo- and cold-rolled materials.

**8.5 Discussion**

Cryo-rolling of materials constitutes an interesting thermo-mechanical processing route which can introduce significant microstructural refinement and enhance the mechanical properties. Consequently, the effect of cryo-rolling has been investigated in a wide variety of materials [114-122] . Recently, the effect of cryo-rolling has also been investigated in HEAs and significant enhancement in strength has been reported by Stepanov et al [71]. They have reported that microstructure evolution during rolling at room temperature and cryo-rolling conditions follows similar trend characterized by an elongation of grains, twinning and rotation of the twin lamellae towards the rolling direction. During cryo-rolling, micro-shear bands were observed at early stages of deformation (40%) as compared to room temperature rolling [71]. Occurrence of deformation twinning was certainly more pronounced in the cryo-rolled material, thereby providing faster microstructural refinement.

The bulk textures of the two materials processed by the two different routes show very similar strong brass type texture, typical of low SFE materials [123]. The crucial role of deformation twins affecting the texture transition behavior has also been highlighted. Even though the deformation twins could not be imaged in the present work in the heavily deformed materials, presumably due to their fine scale structure (beyond the resolution limit of EBSD), formation of profuse nanoscale deformation twins has been extensively reported in the present HEA [77, 124]. Greater propensity for the formation of nano-twins during cryo-rolling, particularly at the early stages of deformation has been reported recently [71]. The relative difference in the ease of nano-twin formation in the two different processing routes does not seem to affect the evolution of bulk texture after heavy deformation. However, cryo-rolling yields larger volume fraction of random component but weaker α-fiber components than cold-rolling. This suggests that larger amount of nano-twins in cryo-rolled HEA increases the volume fraction of random components.

The microstructures of the cold and cryo-rolled materials show certain differences after 90% deformation. The evidently more fragmented and finer microstructure in the cryo-rolled material appears to be consistent with the retention of higher dislocation density and the greater propensity towards the formation of nano-twins during cryo-rolling. Further, finer microstructure in the cryo-rolled material may originate from enhanced nano-twin formation where the formation of deformation TBs can greatly accelerate microstructural refinement [125]. However, further investigation must be carried out to fully understand the observed differences.

As already highlighted in Chapter 6 and Chapter 7, the density of available nucleation sites should affect the final recrystallized grain size. As already mentioned previously (Chapter 6 and Chapter 7), in heavily deformed materials the potential nucleation sites include grain boundaries, deformation heterogeneities e.g. deformation bands, transition bands and shear bands . The cryo-rolled material shows consistently lower grain size as compared to the cold-rolled material. In view of the preceding discussion, this observation clearly indicates that cryo-rolled material has greater number of potential nucleation sites. This appears consistent with the significantly fragmented microstructure of the cryo-rolled material (Fig.8.1(b)). In addition, the formation of nano-twins is considerably favored in cryo-rolled material [71, 74]. These twin boundaries can also act as potential nucleation sites for recrystallization. Therefore, the process of nucleation should dominate growth to a greater extent in the cryo-rolled material. Consequently, the grain size in different annealed cryo-rolled material should be expected to be lower as compared to their counterparts in the cold-rolled material.

The difference in grain size is small after low temperature annealing (e.g. at 700°C) and quite remarkable after annealing at higher temperatures (e.g. at 1200°C). At low temperatures, due to the sluggish diffusion in the HEA, the grain growth is rather limited. This results in only minor difference

in the recrystallized grain size in absolute terms but the enhanced nucleation in the cryo-rolled material is easily understood when the relative difference is considered. At higher annealing temperatures where appreciable grain growth takes place, the effect of greater number of available nucleation sites in the cryo-rolled material is manifested by the much lower average grain size in this material as compared to the similarly annealed cold-rolled material.

The recrystallization texture of brass usually shows a strong brass recrystallization component {236}<385> (BR component in Table 8.1) [50] but the strength of this component is affected by grain size, deformation level and annealing temperature. For a fine starting grain size (which is of interest to us in the present work as the starting grain size is ~7 µm) and deformation level ≤ 90% reduction in thickness, the recrystallization texture after low temperature annealing is dominated by the BR component while the {110}<112> component dominates the texture after high temperature annealing. For severe deformation levels (≥95% reduction in thickness), the recrystallization texture is dominated by the {113}<332> (D component in Table 8.1) [50]. The origin of the BR component in the recrystallization texture is explained on the basis of preferential nucleation of these components at the shear bands and subsequent growth of these components. Likewise, the origin of the {113}<332> component also involves preferential growth [50].

The recrystallization texture of both cryo- and cold-rolled materials do not show dominant BR or D components. These components are present along with the retained deformation texture components, such as, S and other α-fiber components. Thus, the absence of strong BR or D components in the recrystallization texture of the HEA indicates absence of strong preferential nucleation or preferential growth. This behavior has already been explained on the basis of the characteristic nucleation and growth behavior in the present HEA. The absence of strong preferential nucleation in the HEA is explained on the basis of more energetically homogenous

deformed matrix similar to the behavior observed in case of low SFE twinning induced plasticity steels (TWIP) [92]. Although, fully developed and micro shear bands are observed in both the deformed materials, their contribution in terms of preferential nucleation appears to be rather limited.

The sluggish diffusion in HEA [28] retards the rapid preferential movement of boundaries which restricts the possibility of preferential growth of texture components unlike other low SFE, such as Ni-60wt.%Co alloy (Chapter 5). The absence of preferential growth is quite evident from the minor changes in the volume fractions of different texture components with annealing temperature (Fig.8.7(a) and Fig.8.7(b), respectively for cryo and cold-rolled materials). Expectedly, this also results in only minor change in the strength of texture with annealing temperature (Fig.8.7(c)).

In summary, cryo-rolling affects the evolution of microstructure during deformation and annealing as compared to cold-rolling at room temperature. More fragmented and finer microstructure is formed in the cryo-rolled HEA. This possibly relates to the greater propensity for the formation of nano-twins in the cryo-rolled HEA. Grain size of the cryo-rolled and annealed HEA is smaller than the cold-rolled and annealed HEA when annealed at 700°C, 1000°C and 1200°C. This is due to the greater number of available nucleation sites in the cryo-rolled HEA. In the aspect of texture, the texture of cryo-rolled HEA contains higher fraction of random component than that of cold-rolled HEA. This appears consistent with significantly more microstructural fragmentation. However, the volume fractions of different texture components show minor change with annealing temperature for both cold-rolled and cryo-rolled HEAs. This could be attributed to the sluggish diffusion behavior of the present HEA which greatly hinders preferential boundary movement, thus eliminating preferential growth of texture components.

# -: CHAPTER 9 :-

## *Summary and Conclusions*

The present work investigates the evolution of microstructure and texture during deformation and annealing of equiatomic CoCrFeMnNi HEA. The evolution of deformation and annealing textures of the HEA is compared with other low stacking fault materials.

The major conclusions that may be drawn are:

I.    The HEA develops a predominantly brass-type texture and an ultrafine lamellar microstructure characterized by the presence of deep shear bands and locally fragmented regions after heavy cold-rolling. This indirectly supports the low SFE of the alloy.

II.   Annealing at low temperatures can yield fully recrystallized near ultrafine grained microstructure. The HEA is found to have a high recrystallization temperature and strong resistance against grain coarsening during annealing.

III.  Significantly high recrystallization temperature (700°C), low grain growth, and fine-grained structure of the HEA could be attributable to the whole-solute distorted matrix which is featured by high lattice distortion energy, sluggish diffusion effect and low SFE.

IV.   Retention of deformation texture components and the development of strong α-fiber (<011>//ND) is observed after annealing. Annealing twins play an important role in the development of these α-fiber components. The texture components show only minor variation with annealing temperature.

V.    The typical recrystallization texture components of low SFE brass, namely BR and {113} <332> components do not show a strong presence in the annealing texture.

A critical comparison with model low SFE Ni-60wt.%Co alloy has been carried out to further understand the unique texture formation behavior of the HEA. For this purpose the two alloys are deformed to the same thickness

level and annealed in such a manner to have similar average grain size at different stages of grain growth. The following conclusions may be drawn:

I.   Ni-Co and HEA show strong brass type deformation texture after heavy cold-rolling, but very different annealing texture formation behavior.

II.  Ni-Co alloy shows strong α-fiber orientations G/B and G after grain growth, which is attributed to the preferential growth of these grains. In sharp contrast, only minor variation of texture components in HEA and more homogenous grain growth could be observed in HEA.

III. The sharply different texture during grain growth in the two materials is attributed to the sluggish diffusion in multicomponent HEA which greatly diminishes mobility of boundaries and effectively prevent preferential growth of grains.

IV.  The absence of strong preferential nucleation and growth is found consistent with the absence of strong BR or {113}<332> components.

The effect of different processing parameters, namely cold-rolling strain, starting grain size and cryo-rolling has been systematically investigated on the microstructure and texture formation behavior of the HEA. In order to investigate the effect of cold-rolling strain the HEA is cold-rolled up to 95% reduction in thickness and annealed at different temperatures. The main outcomes are summarized below:

I.   The HEA shows fragmented microstructure and transition from pure metal to brass type texture with increasing cold-rolling reduction. Development of predominantly brass type texture is observed after 95% cold-rolling.

II.   The recrystallized grain size is not affected significantly by prior cold-rolling strain at a lower annealing temperature, which is attributed to sluggish diffusion in HEAs which restricts grain growth at low annealing temperatures. Remarkable effect of prior strain is observed only after significant grain growth.

III.  The recrystallization textures of different cold-rolled materials show the presence of similar texture components. BR or {113}<332> components do not have a dominant presence in the recrystallization texture. The volume fractions of different texture components are not significantly affected by the annealing temperature.

IV.   Absence of strong preferential nucleation or preferential growth of texture components in HEA is not affected by the prior cold-rolling strain.

The effect of prior grain size on the evolution of microstructure and texture is investigated using two starting materials with widely different average grain size ~7 µm (FGSM) and 200 µm (CGSM). Both these starting materials are cold-rolled to 90% and 95% reduction in thickness and annealed at different temperatures. The following conclusions may be drawn:

I.    The FGSM and CGSM develop a predominantly brass type texture after heavy cold-rolling. Lamellar deformation structure is observed up to 90% cold-rolling, but microstructural fragmentation is revealed in the 95% cold-rolled materials.

II.   After low temperature annealing the grain size differences in FGSM and CGSM are not significant which is attributed to sluggish diffusion in HEAs which restricts grain growth at low annealing temperatures. The FGSM shows much finer grain size than CGSM after high temperature annealing.

III.    The annealing texture of both FGSM and CGSM are characterized by development of α-fiber and retention of deformation texture components. The recrystallization textures do not show dominant BR or {113}<332> components unlike low SFE brass. This is attributed to nucleation in a more homogeneous deformed matrix and inhibition of preferential growth of texture components due to sluggish diffusion in HEA systems.

IV.    The volume fractions of the texture components in FGSM and CGSM are negligibly affected by starting grain size and annealing temperature. Minor variation of texture components with annealing temperature indicates absence of preferential growth of texture components.

The effect of cryo-rolling is investigated by comparing the microstructure and texture development with those during deformation at room temperature. The following conclusions may be drawn:

I.    More fragmented and finer microstructure is formed in the heavily cryo-rolled HEA. This possibly relates to the greater propensity for the formation of nano-twins in the cryo-rolled HEA but needs to be investigated further.

II.    The grain size of the cryo-rolled and annealed HEA is smaller than the cold-rolled and annealed HEA when annealed at 700°C, 1000°C and 1200°C. This is due to the greater number of available nucleation sites in the cryo-rolled HEA.

III.    In the aspect of texture, the cryo and cold-rolled materials show the development of very similar deformation and grain growth textures. The volume fractions of different texture components show only minor changes with annealing temperature for both cold-rolled and cryo-rolled HEAs. This is attributable to the sluggish diffusion, which

retards rapid boundary movement and thus preferential growth of texture components during annealing.

Overall, it may be concluded that different processing parameters may greatly impact the microstructure development during deformation and annealing. However, the characteristic annealing texture formation behavior of the HEA featured by the absence of strong preferential nucleation and growth is not affected by the processing parameters to any significant extent.

*References*

1.  Cantor, B., Chang, I.T.H., Knight, P. and Vincent, A.J.B., *Microstructural development in equiatomic multicomponent alloys*. Materials Science and Engineering: A, 2004. **375**: p. 213-218.

2.  Yeh, J.W., Chen, S.K., Lin, S.J., Gan, J.Y., Chin, T.S., Shun, T.T., Tsau, C.H. and Chang, S.Y., *Nanostructured High-Entropy Alloys with Multiple Principal Elements: Novel Alloy Design Concepts and Outcomes*. Advanced Engineering Materials, 2004. **6(5)**: p. 299-303.

3.  Murty, B., Yeh, J.W. and Ranganathan, S., *High-entropy alloys*. 2014: Butterworth-Heinemann.

4.  Yeh, J.W., Chen, Y.L., Lin, S.J. and Chen, S.K., *High-entropy alloys–a new era of exploitation*. in Materials Science Forum, Trans Tech Publication, 2007. **560**: p. 1-9.

5.  Zhang, Y., Zuo, T.T., Tang, Z., Gao, M.C., Dahmen, K.A., Liaw, P.K. and Lu, Z.P., *Microstructures and properties of high-entropy alloys*. Progress in Materials Science, 2014. **61**: p. 1-93.

6.  Liu, Y., Li, Y., Chen, X. and Chen, M., *High-entropy Alloy with Multi-principal Elements - State of the Art*. Materials Review, 2006. **4**: p. 002.

7.  Tsai, M.H. and Yeh, J.W., *High-entropy alloys: a critical review*. Materials Research Letters, 2014. **2(3)**: p. 107-123.

8.  Liang, X.b., Wei, M., Cheng, J.B., Zhang, W. and Xu, B.S., *Research Progress in Advanced Materials of High-entropy Alloys*. Journal of Materials Engineering, 2009. **12**: p. 020.

9.  Yeh, J.W., R*ecent progress in high-entropy alloys*. Annales de chimie - Science des matériaux, 2006. **31(6)**: p. 633-648.

10. Gao, M.C., *Progress in High-Entropy Alloys*. Journal of Materials Science, 2013. **65(12)**: p. 1749-175.

11. Tsai, M.H., *Physical properties of high entropy alloys*. Entropy, 2013. **15(12)**: p. 5338-5345.

12. Yeh, J.W., *Physical Metallurgy of High-Entropy Alloys.* Journal of Materials Science, 2015. **67(10)**: p. 2254-2261.

13. Miracle, D., *High entropy alloys and their development as structural materials.* Materials Science and Technology, 2015: p. 1142-1147.

14. Gludovatz, B., George, E.P. and Ritchie, R.O., *Processing, Microstructure and Mechanical Properties of the CrMnFeCoNi High-Entropy Alloy.* Journal of Materials Science, 2015. **67(10)**: p. 2262-2270.

15. Jablonski, P.D., Licavoli, J.J., Gao, M.C. and Hawk, J.A., *Manufacturing of High Entropy Alloys.* Journal of Materials Science, 2015. **67(10)**: p. 2278-2287.

16. Lu, Z.P., Wang, H., Chen, M.W., Baker, I., Yeh, J.W., Liu, C.T. and Nieh, T.G., *An assessment on the future development of high-entropy alloys: Summary from a recent workshop.* Intermetallics, 2015. **66**: p. 67-76.

17. Swalin, R.A. and King, A.L., *Thermodynamics of solids.* American Journal of Physics, 1962. **30(10)**: p. 778-778.

18. Yeh, J.W., *Alloy design strategies and future trends in high-entropy alloys.* Journal of Materials Science, 2013. **65(12)**: p. 1759-1771.

19. Lucas, M.S., Wilks, G.B., Mauger, L., Munoz, J.A., Senkov, O.N., Michel, E., Horwath, J., Semiatin, S.L., Stone, M.B. and Abernathy, D.L., *Absence of long-range chemical ordering in equimolar FeCoCrNi.* Applied Physics Letters, 2012. **100(25)**: p.1-4.

20. Singh, S., Wanderka, N., Murthy, B.S., Glatzel, U. and Banhart, J., *Decomposition in multi-component AlCoCrCuFeNi high-entropy alloy.* Acta Materialia, 2011. **59(1)**: p. 182-190.

21. Ma, D., Yao, M., Pradeep, K.G., Tasan, C.C., Springer, H. and Raabe, D., *Phase stability of non-equiatomic CoCrFeMnNi high entropy alloys.* Acta Materialia, 2015. **98**: p. 288-296.

22. Yao, M.J., Pradeep, K.G., Tasan, C.C. and Raabe, D., *A novel, single phase, non-equiatomic FeMnNiCoCr high-entropy alloy with exceptional phase stability and tensile ductility.* Scripta Materialia, 2014. **72–73**: p. 5-8.

23. Yeh, J.W., Chang, S.Y., Hong, Y., Chen, S.K. and Lin, S.J., *Anomalous decrease in X-ray diffraction intensities of Cu-Ni-Al-Co-Cr-Fe-Si alloy systems with multi-principal elements.* Materials Chemistry and Physics, 2007. **103(1)**: p. 41-46.

24. Zhang, Y., Yang, X. and Liaw, P.K., *Alloy design and properties optimization of high-entropy alloys.* Journal of Materials Science, 2012. **64(7)**: p. 830-838.

25. Zhou, Y.J., Zhang, Y., Wang, Y.L. and Chen, G.L., *Solid solution alloys of AlCoCrFeNiTix with excellent room-temperature mechanical properties.* Applied Physics Letters, 2007. **90(18)**: p. 181904.

26. Senkov, O.N., Wilks, G.B., Scott, J.M. and Miracle, D.B., *Mechanical properties of $Nb_{25}Mo_{25}Ta_{25}W_{25}$ and $V_{20}Nb_{20}Mo_{20}Ta_{20}W_{20}$ refractory high entropy alloys.* Intermetallics, 2011. **19(5)**: p. 698-706.

27. Senkov, O.N., Wilks, G.B., Miracle, D.B., Chuang, C.P. and Liaw, P.K., *Refractory high-entropy alloys.* Intermetallics, 2010. **18(9)**: p. 1758-1765.

28. Tsai, K.Y., Tsai, M.H. and Yeh, J.W., *Sluggish diffusion in Co–Cr–Fe–Mn–Ni high-entropy alloys.* Acta Materialia, 2013. **61(13)**: p. 4887-4897.

29. Liu, W., Wu, Y., He, J.Y., Nieh, T.G. and Lu, Z.P., *Grain growth and the Hall–Petch relationship in a high-entropy FeCrNiCoMn alloy.* Scripta Materialia, 2013. **68(7)**: p. 526-529.

30.  Tsai, M.H., Yuan, H., Cheng, G., Xu, W., Tsai, K.Y., Tsai, C.W., Jian, W.W., Juan, C.C., Shen, W.J. and Chuang, M.H., *Morphology, structure and composition of precipitates in $Al_{0.3}CoCrCu_{0.5}FeNi$ high-entropy alloy.* Intermetallics, 2013. **32**: p. 329-336.

31.  Tsai, M.H., Yuan, H., Cheng, G., Xu, W., Jian, W.W., Chuang, M.H., Juan, C.C., Yeh, A.C., Lin, S.J. and Zhu, Y., *Significant hardening due to the formation of a sigma phase matrix in a high entropy alloy.* Intermetallics, 2013. **33**: p. 81-86.

32.  He, J.Y., Wang, H., Huang, H.L., Xu, X.D., Chen, M.W., Wu, Y., Liu, X.J., Nieh, T.G., An, K. and Lu, Z.P., *A precipitation-hardened high-entropy alloy with outstanding tensile properties.* Acta Materialia, 2016. **102**: p. 187-196.

33.  Ranganathan, S., *Alloyed pleasures: Multimetallic cocktails.* Current Science, 2003. **85(5)**: p. 1404-1406.

34.  Wu, J.-M., Lin, S.J., Yeh, J.W., Chen, S.K., Huang, Y.S. and Chen, H.C., *Adhesive wear behavior of $Al_xCoCrCuFeNi$ high-entropy alloys as a function of aluminum content.* Wear, 2006. **261(5)**: p. 513-519.

35.  Takeuchi, A. and Inoue, A., *Calculations of mixing enthalpy and mismatch entropy for ternary amorphous alloys.* Materials Transactions, Japan Institute of Metals, 2000. **41(11)**: p. 1372-1378.

36.  Takeuchi, A. and Inoue, A., *Quantitative evaluation of critical cooling rate for metallic glasses.* Materials Science and Engineering A, 2001. **304-306(1-2)**: p. 446-451.

37.  Zhang, Y., Zhou, Y.J., Lin, J.P., Chen, G.L. and Liaw, P.K., *Solid-Solution Phase Formation Rules for Multi-component Alloys.* Advanced Engineering Materials, 2008. **10(6)**: p. 534-538.

38.  Ren, B., Liu, Z.X., Li, D.M., Shi, L., Cai, B. and Wang, M.X., *Effect of elemental interaction on microstructure of CuCrFeNiMn high-*

*entropy alloy system.* Journal of Alloys and Compounds, 2010. **493**: p. 148-153.

39. Zhang, K. and Z. Fu, *Effects of annealing treatment on phase composition and microstructure of CoCrFeNiTiAl$_x$ high-entropy alloys.* Intermetallics, 2012. **22**: p. 24-32.

40. Yang, X. and Zhang, Y., *Prediction of high-entropy stabilized solid-solution in multi-component alloys.* Materials Chemistry and Physics, 2012. **132(2-3)**: p. 233-238.

41. Randle, V. and O. Engler, *Introduction to Texture Analysis: Macrotexture, Microtexture and Orientation Mapping.* 2014: CRC Press.

42. Hirsch, J. and Lucke, K., *Mechanism of Deformation and Development of Rolling Textures in Polycrystalline Fcc Metals-I. Description of Rolling Texture Development in Homogeneous CuZn Alloys.* Acta Metallurgica, 1988. **36(11)**: p. 2863-2882.

43. Raabe, D. and Lucke, K., *Rolling and annealing textures of bcc metals.* Materials Science Forum, 1994. **157-6**: p. 597-610.

44. Hansen, N. and Bay, B., *Initial stages of recrystallization in aluminium containing both large and small particles.* Acta Metallurgica, 1981. **29(1)**: p. 65-77.

45. Ray, R.K., Butron-Guillen, M.P., Jonas, J.J. and Savoie, J., Transformation textures in steels. ISIJ International, 1994. **34**: p. 927-942.

46. Klein, H. and Bunge, H.J., *Advances and Applications of Quantitative Texture Analysis*, ed. Bunge, H.J. 1989, Oberursel DGM.

47. Roe, R.J., *Description of crystallite orientation in polycrystalline materials. III. General solution to pole figure inversion.* Journal of Applied Physics, 1965. **36(6)**: p. 2024-2031.

48. Bunge, H.J., *Mathematische Methoden der Texturanalyse.* 1969: Academic Verlag, Berlin, Germany.

49. Bunge, H.J., *Texture analysis in materials science: Mathematical methods.* 1982: Butterworths, London, UK.

50. Humphreys, F.J. and Hatherly M., *Recrystallization and related annealing phenomena (second edition).* 2004: Elsevier, Oxford.

51. Leffers, T. and Ray, R.K., *The brass-type texture and its deviation from the copper-type texture.* Progress in Materials Science, 2009. **54(3)**: p. 351-396.

52. Wassermann, G. and Grewen, J., Texturen metallischer werkstoffe. 1962: Springer, Berlin.

53. Doherty, R.D., *Recrystallization and Texture.* Progress in Materials Science, 1997. **42**: p. 39-58.

54. Doherty, R.D., Hughes, D.A., Humphreys, F.J., Jonas, J.J., Juul Jensen D., Kassner, M.E., King, W.E., McNelley, T.R., McQueen, H.J. and Rollett A.D., *Current issues in recrystallization: A review.* Materials Science and Engineering A - Structural Materials Properties Microstructure and Processing, 1997. **238(2)**: p. 219-274.

55. Lee, W. and Duggan, B., *Effects of Grain Size on Rolling and Annealing Textures in 82%–92% Cold Rolled α-Brass.* Texture, Stress, and Microstructure, 1988. **8**: p. 155-172.

56. Yeung, W., Hirsch, J. and Hatherly, M, in ICOTOM 8, eds. Kallend and Gottstein, 1988: TMS, Warrendale, 631.

57. Zhang, Y., *Mechanical Properties and Structures of High Entropy Alloys and Bulk Metallic Glasses Composites.* Materials science forum, 2010. **654-656**: p. 1058-1061.

58. Zhu, J.M., Fu, H.M., Zhang, H.F., Wang, A.M., Li, H. and Hu, Z.Q., *Microstructures and compressive properties of multicomponent $AlCoCrFeNiMo_x$ alloys.* Materials Science and Engineering A - Structural Materials Properties Microstructure and Processing, 2010. **527(26)**: p. 6975-6979.

59.   Zhu, J.M., Zhang, H.F., Fu, H.M., Wang, A.M., Li, H. and Hu, Z.Q., *Microstructures and compressive properties of multicomponent AlCoCrCuFeNiMoₓ alloys.* Journal of Alloys and Compounds, 2010. **497(1-2)**: p. 52-56.

60.   Zhang, K.B., Fu, Z.Y., Zhang, J.Y., Shi, J., Wang, W.M., Wang, H., Wang, Y.C. and Zhang, Q.J., *Annealing on the structure and properties evolution of the CoCrFeNiCuAl high-entropy alloy.* Journal of Alloys and Compounds, 2010. **502(2)**: p. 295-299.

61.   Zhu, J.M., et al., Synthesis and properties of multiprincipal component AlCoCrFeNiSix alloys. Materials Science and Engineering A - Structural Materials Properties Microstructure and Processing, 2010. **527(27-28)**: p. 7210-7214.

62.   Zhang, Y., Wang, X.F., Chen, G.L. and Qiao, Y., *Effect of ti on the microstructure and properties of CoCrCuFeNiTiₓ high-entropy alloys.* Annales De Chimie-Science Des Materiaux, 2006. **31(6)**: p. 699-709.

63.   Zhou, Y.J., Zhang, Y., Wang, Y.L. and Chen, G.L., *Microstructure and compressive properties of multicomponent Al-x(TiVCrMnFeCoNiCu)(100-x) high-entropy alloys.* Materials Science and Engineering A - Structural Materials Properties Microstructure and Processing, 2007. **454**: p. 260-265.

64.   Li, C., Li, J.C., Zhao, M. and Zhang, L., *Microstructure and properties of AlTiNiMnBx high entropy alloys.* Materials Science and Technology, 2008. **24(3)**: p. 376-378.

65.   Kao, Y.F., Chen, T.J., Chen, S.K. and Yeh, J.W., *Microstructure and mechanical property of as-cast, -homogenized, and -deformed AlxCoCrFeNi (0 ≤ x ≤ 2) high-entropy alloys.* Journal of Alloys and Compounds, 2009. **488(1)**: p. 57-64.

66.   Shun, T.T. and Du, Y.C., *Microstructure and wear resistance of FCC Al0.3CoCrFeNiC x high entropy alloys.* Journal of Alloys and Compounds, 2009. **479(1-2)**: p. 157-160.

67. Wang, X.F., Zhang, Y., Qiao, Y. and Chen, G.L., *Novel microstructure and properties of multicomponent CoCrCuFeNiTi$_x$ alloys.* Intermetallics, 2007. **15(3)**: p. 357-362.

68. Zhu, J.M., Fu, H.M., Zhang, H.F., Wang, A.M. and Li, H., *Microstructure and compressive properties of multiprincipal component AlCoCrFeNiC$_x$ alloys.* Journal of Alloys and Compounds, 2011. **509(8)**: p. 3476-3480.

69. Ma, S.G. and Zhang, Y., *Effect of Nb addition on the microstructure and properties of AlCoCrFeNi high-entropy alloy.* Materials Science and Engineering: A, 2012. **532**: p. 480-486.

70. Wang, F.J., Zhang, Y., Chen, G.L. and Davies, H.A., *Cooling Rate and Size Effect on the Microstructure and Mechanical Properties of AlCoCrFeNi High Entropy Alloy.* Journal of Engineering Materials and Technology, 2009. **131(3)**: p. 034501

71. Stepanov, N., Tikhonovsky, M., Yurchenko, N., Zyabkin, D., klimova, M., Zherebtsov, S., Efimov, A. and Salishchev, G., *Effect of cryo-deformation on structure and properties of CoCrFeNiMn high-entropy alloy.* Intermetallics, 2015. **59**: p. 8-17.

72. Zhao, Y., Liao, X.Z., Zhu, Y.T., Horita, Z. and Langdon, T.G., Influence of stacking fault energy on nanostructure formation under high pressure torsion. Materials Science and Engineering: A, 2005. **410**: p. 188-193.

73. Otto, F., Dlouhý, A., Somsen, C., Bei, H., Eggeler, G. and George, E.P., *The influences of temperature and microstructure on the tensile properties of a CoCrFeMnNi high-entropy alloy.* Acta Materialia, 2013. **61(15)**: p. 5743-5755.

74. Gludovatz, B., Hohenwarter, A., Catoor, D., Chang, E.H., George, E.P. and Ritchie, R.O., *A fracture-resistant high-entropy alloy for cryogenic applications.* Science, 2014. **6201**: p. 1153-1158.

75.    Wu, Z., Parish, C.M. and H. Bei., Nano-twin mediated plasticity in carbon-containing FeNiCoCrMn high entropy alloys. Journal of Alloys and Compounds, 2015. **647**: p. 815-822.

76.    Huang, S., Li, W., Lu, S., Tian, F., Shen, J., Holmström, E. and Vitos. L., *Temperature dependent stacking fault energy of FeCrCoNiMn high entropy alloy.* Scripta Materialia, 2015. **108**: p. 44-47.

77.    Zaddach, A., Niu, C., Koch, C.C. and Irving, D.L., *Mechanical properties and stacking fault energies of NiFeCrCoMn high-entropy alloy.* Journal of Materials Science, 2013. **65(12)**: p. 1780-1789.

78.    Park, N., Watanabe, I., Terada, D., Yokoyama, Y., Liaw, P.K. and Tsuji, N., *Recrystallization Behavior of CoCrCuFeNi High-Entropy Alloy.* Metallurgical and Materials Transactions A: Physical Metallurgy and Materials Science, 2015. **46(4)**: p. 1481-1487.

79.    Otto, F., Hanold, N.L. and George, E.P., *Microstructural evolution after thermomechanical processing in an equiatomic, single-phase CoCrFeMnNi high-entropy alloy with special focus on twin boundaries.* Intermetallics, 2014. **54**: p. 39-48.

80.    Wu, Z., Bei, H., Otto, F., Pharr, G.M. and George, E.P., *Recovery, recrystallization, grain growth and phase stability of a family of FCC-structured multi-component equiatomic solid solution alloys.* Intermetallics, 2014. **46**: p. 131-140.

81.    Schuh, B., Mendez-Martin, F., Völker, B., George, E.P., Clemens, H., Pippan, R. and Hohenwarter, A., *Mechanical properties, microstructure and thermal stability of a nanocrystalline CoCrFeMnNi high-entropy alloy after severe plastic deformation.* Acta Materialia, 2015. **96**: p. 258-268.

82.    Stepanov, N.D., Shaysultanov, D.G., Yurchenko, N.Y., Zherebtsov, S.V., Ladygin, A.N., Salishchev, G.A. and Tikhonovsky, M.A., *High temperature deformation behavior and*

*dynamic recrystallization in CoCrFeNiMn high entropy alloy.* Materials Science and Engineering: A, 2015. **636**: p. 188-195.

83. Schwartz, A.J., Kumar, M., Adams, B.L. and Field, D.P., *Electron Backscatter Diffraction in Materials Science.* 2013: Springer US.

84. Krieger Lassen, N.C., Jensen, J.D. and Conradsen, K., *Image processing procedures for analysis of electron back scattering patterns.* Scanning Microscopy, 1992. **6**: p. 115-121.

85. Mesquita, T.J., Chauveau, E., Mantel, M. and Nogueira, R.P., *A XPS study of the Mo effect on passivation behaviors for highly controlled stainless steels in neutral and alkaline conditions.* Applied Surface Science, 2013. **270**: p. 90-97.

86. Jordan, L. and Swanger, W.H., *The Properties of Pure Nickel.* Journal of Research of the National Bureau of Standards, 1930. **5**: p. 1291-1307.

87. Ray, R.K., *Rolling textures of pure nickel, nickel-iron and nickel-cobalt alloys.* Acta Metallurgica et Materialia, 1995. **43(10)**: p. 3861-3872.

88. El-Danaf, E., Kalidindi., Doherty, R.D. and Necker, C., *Deformation texture transition in brass: critical role of micro-scale shear bands.* Acta Materialia, 2000. **48(10)**: p. 2665-2673.

89. Hirsch, J. and Lucke, K., *Mechanism of Deformation and Development of Rolling Textures in Polycrystalline Fcc Metals .II. Simulation and Interpretation of Experiments on the Basis of Taylor-Type Theories.* Acta Metallurgica, 1988. **36(11)**: p. 2883-2904.

90. Duggan, B., Hatherly, M., Hutchinson, W.B. and Wakefield, P.T., *Deformation structures and textures in cold-rolled 70: 30 brass.* Metal Science, 1978. **12(8)**: p. 343-351.

91. Tsai, C.W., Chen, Y.L., Tsai, M.H., Yeh, J.W., Shun, T.T. and Chen, S.K., *Deformation and annealing behaviors of high-entropy alloy*

*Al$_{0.5}$CoCrCuFeNi.* Journal of Alloys and Compounds, 2009. **486(1)**: p. 427-435.

92. Bracke, L., Verbeken, K., Kestens, L. and Penning, J., *Microstructure and texture evolution during cold rolling and annealing of a high Mn TWIP steel.* Acta Materialia, 2009. **57(5)**: p. 1512-1524.

93. Fullman, R.L. and Fisher, J.C., *Formation of Annealing Twins During Grain Growth.* Journal of Applied Physics, 1951. **22(11)**: p. 1350-1355.

94. Donadille, C., Valle, R., Dervin, P. and Penelle, R., *Development of Texture and Microstructure during Cold-Rolling and Annealing of Fcc Alloys - Example of an Austenitic Stainless Steel.* Acta Metallurgica, 1989. **37(6)**: p. 1547-1571.

95. Saleh, A.A., Pereloma, E.V. and Gazder, A.A., *Texture evolution of cold rolled and annealed Fe-24Mn-3Al-2Si-1Ni-0.06C TWIP steel.* Materials Science and Engineering A, 2011. **528(13-14)**: p. 4537-4549.

96. Bracke, L., Verbeken, K. and Kestens, L.A.I., *Texture generation and implications in TWIP steels.* Scripta Materialia, 2012. **66(12)**: p. 1007-1011.

97. Barrales-Mora, L.A., Lu, Y. and Molodov, D.A., *Experimental Determination and Simulation of Annealing Textures in Cold Rolled TWIP and TRIP Steels.* Steel Research International, 2011. **82(2)**: p. 119-126.

98. Lü, Y., Molodov, D.A. and Gottstein, G., *Recrystallization kinetics and texture evolution during annealing of Fe-23.2Mn-0.57C alloy.* Materials Science Forum 2012. **702-703**: p. 443-448.

99. Lu, Y.P., Molodov, D.A. and Gottstein, G., *Correlation Between Microstructure and Texture Development in a Cold-rolled TWIP Steel.* ISIJ International, 2011. **51(5)**: p. 812-817.

100. Chowdhury, S.G., Datta, S., Ravikumar, B., De, P.K. and Ghosh, R.N., *Randomization of texture during recrystallization of austenite in a cold rolled metastable austenitic stainless steel.* Materials Science and Engineering A - Structural Materials Properties Microstructure and Processing, 2007. **443(1-2)**: p. 114-119.

101. Haase, C., Barrales-Mora, L.A., Molodov, D.A. and Gottstein, G., *Texture evolution of a cold-rolled Fe-28Mn-0.28 C TWIP steel during recrystallization.* Materials Science Forum. 2013. **753**: p. 213-216.

102. Chowdhury, S.G., Das, S., Ravikumar, B. and De, P.K., *Twinning-induced sluggish evolution of texture during recrystallization in AISI 316L stainless steel after cold rolling.* Metallurgical and Materials Transactions A, 2006. **37(8)**: p. 2349-2359.

103. Salimon, A.I., Korsunsky, A.M. and Ivanov, A.N., *The character of dislocation structure evolution in nanocrystalline FCC Ni-Co alloys prepared by high-energy mechanical milling.* Materials Science and Engineering: A, 1999. **271(1–2)**: p. 196-205.

104. Loretto, M.H., Clarebrough, L.M. and Segall, R.L., *Stacking-fault tetrahedra in deformed face-centred cubic metals.* Philosophical Magazine, 1965. **11(111)**: p. 459-465.

105. Howie, A. and Swann, P.R., *Direct measurements of stacking-fault energies from observations of dislocation nodes.* Philosophical Magazine, 1961. **6(70)**: p. 1215-1226.

106. Million, B. and Kučera, J., *Concentration dependence of nickel diffusion in nickel-cobalt alloys.* Czechoslovak Journal of Physics B, 1971. **21(2)**: p. 161-171.

107. Million, B. and J. Kučera, *Concentration dependence of diffusion of cobalt in nickel-cobalt alloys.* Acta Metallurgica, 1969. **17(3)**: p. 339-344.

108. Schmidt, U. and Lucke, K., *Recrystallization textures of silver, copper and alpha -brasses with different zinc-contents as a function of the rolling temperature.* Texture of crystalline solids, 1979. **3(2)**: p. 85-112.

109. Paul, H., Morawiec, A., Piątkowski, A., Bouzy, E. and Fundenberger, J.J., *Brass-type shear bands and their influence on texture formation.* Metallurgical and Materials Transactions A, 2004. **35(12)**: p. 3775-3786.

110. Jia, N., Roters, F., Eisenlohr, P., Kords, C. and Raabe, D., *Non-crystallographic shear banding in crystal plasticity FEM simulations: Example of texture evolution in α-brass.* Acta Materialia, 2012. **60(3)**: p. 1099-1115.

111. Jia, N., Eisenlohr, P., Roters, F., Raabe, D. and Zhao, X., *Orientation dependence of shear banding in face-centered-cubic single crystals.* Acta Materialia, 2012. **60(8)**: p. 3415-3434.

112. Duggan, B. and Lee, W., *Annealing Texture Transitions in Cold-Rolled alpha-Brass Caused by Different Strains, Temperatures and Grain Sizes.* in ICOTOM: Eighth International Conference on Textures of Materials. 1987.

113. Lü, Y., Molodov, D.A. and Gottstein, G., *Recrystallization kinetics and microstructure evolution during annealing of a cold-rolled Fe–Mn–C alloy.* Acta Materialia, 2011. **59(8)**: p. 3229-3243.

114. Weiss, M., Taylor, A.S., Hodgson, P.D. and Stanford, N., *Strength and biaxial formability of cryo-rolled 2024 aluminium subject to concurrent recovery and precipitation.* Acta Materialia, 2013. **61(14)**: p. 5278-5289.

115. Panigrahi, S.K. and Jayaganthan, R., *Influence of solutes and second phase particles on work hardening behavior of Al 6063 alloy processed by cryorolling.* Materials Science and Engineering: A, 2011. **528(7)**: p. 3147-3160.

116. Yu, H.I., Tieu, A.K., Lu, C., Liu, X.H., Godbole, A. and Kong, C., *Mechanical properties of Al–Mg–Si alloy sheets produced using asymmetric cryorolling and ageing treatment.* Materials Science and Engineering: A, 2013. **568**: p. 212-218.

117. Zherebtsov, S., Dyakonov, G.S., Salem, A.A., Sokolenko, V.I., Salishchev, G.A. and Semiatin, S.L., *Formation of nanostructures in commercial-purity titanium via cryorolling.* Acta Materialia, 2013. **61(4)**: p. 1167-1178.

118. Dasgupta, A., Murugesan, S., Saroja, S., Vijayalakshmi, M., Luysberg, M., Veron, M., Rauch, E. and Jeyakumar, T., *Structure of grains and grain boundaries in cryo-mechanically processed Ti alloy.* Journal of Materials Science, 2013. **48(13)**: p. 4592-4598.

119. Kumar, R., Dasharath, S.M., Kang, P.C., Koch, C.C. and Mula, S., *Enhancement of mechanical properties of low stacking fault energy brass processed by cryorolling followed by short-annealing.* Materials & Design, 2015. **67**: p. 637-643.

120. Bahmanpour, H., Kauffmann, A., Khoshkhoo, M.S., Youssef, K.M., Mula, S., Freudenberger, J., Eckert, J., Scattergood, R.O. and Koch, C.C., *Effect of stacking fault energy on deformation behavior of cryo-rolled copper and copper alloys.* Materials Science and Engineering: A, 2011. **529**: p. 230-236.

121. Trivedi, P., Goel, S., Das, S., Jayaganthan, R., Lahiri, D. and Roy, P., *Biocompatibility of ultrafine grained zircaloy-2 produced by cryorolling for medical applications.* Materials Science and Engineering: C, 2015. **46**: p. 309-315.

122. Panigrahi, S.K. and Jayaganthan, R., *Effect of Annealing on Thermal Stability, Precipitate Evolution, and Mechanical Properties of Cryorolled Al 7075 Alloy.* Metallurgical and Materials Transactions A, 2011. **42(10)**: p. 3208-3217.

123. Smallman, R. and Green, D., *The dependence of rolling texture on stacking fault energy.* Acta Metallurgica, 1964. **12(2)**: p. 145-154.

124. Zhang, H., He, Y.Z., Pan, Y. and Guo, S., *Thermally stable laser cladded CoCrCuFeNi high-entropy alloy coating with low stacking fault energy.* Journal of Alloys and Compounds, 2014. **600**: p. 210-214.

125. Wang, Y.B., Liao, X.Z., Zhao, Y.H., Lavernia, E.J., Ringer, S.P., Horita, Z., Langdon, T.G. and Zhu, Y.T., *The role of stacking faults and twin boundaries in grain refinement of a Cu-Zn alloy processed by high-pressure torsion.* Materials Science and Engineering: A. **527(18-19)**: p. 4959-4966.

# List of Publications

**International journals**

1. P.P. Bhattacharjee, **G.D. Sathiaraj**, M. Zaid, J.R. Gatti, C. Lee, C.W. Tsai, J.W. Yeh, Microstructure and texture evolution during annealing of equiatomic CoCrFeMnNi high-entropy alloy, *Journal of Alloys and Compounds*, 587 (2014) 544–552. (DOI:10.1016/j.jallcom.2013.10.237) (I.F:3, Cited 37 times)

2. **G.D. Sathiaraj**, P.P. Bhattacharjee, Analysis of microstructure and microtexture during grain growth in low stacking fault energy equiatomic CoCrFeMnNi high entropy and Ni-60 wt.%Co alloys, *Journal of Alloys and Compounds*, 637 (2015) 267–276. (DOI:10.1016/j.jallcom.2015.02.184) (I.F:3, Cited 7 times)

3. **G.D. Sathiaraj**, P.P. Bhattacharjee, Effect of starting grain size on the evolution of microstructure and texture during thermo-mechanical processing of CoCrFeMnNi high entropy alloy, *Journal of Alloys and Compounds*, 647 (2015) 82-96. (DOI:10.1016/j.jallcom.2015.06.009) (I.F:3, Cited 1 time)

4. **G.D. Sathiaraj**, P.P. Bhattacharjee, C.W. Tsai, J.W. Yeh, Effect of heavy cryo-rolling on the evolution of microstructure and texture during annealing of equiatomic CoCrFeMnNi high entropy alloy, *Intermetallics*, 69 (2016) 1-9. (DOI:10.1016/j.intermet.2015.10.005)

5. **G.D. Sathiaraj**, P.P. Bhattacharjee, Effect of cold-rolling strain on the evolution of annealing texture of equiatomic CoCrFeMnNi high entropy alloy, *Materials Characterization*, 109 (2015) 189-197. (DOI:10.1016/j.matchar.2015.09.027)

6. **G.D. Sathiaraj**, P.P. Bhattacharjee, Microstructure and texture of heavily cold-rolled and annealed fcc equiatomic medium to high entropy alloys, *Journal of Alloys and Compounds* (under review)

**International Conference Proceedings/Periodicals**

7. **G.D. Sathiaraj**, C. Lee, C.W. Tsai, J.W. Yeh, P.P. Bhattacharjee, Evolution of microstructure and crystallographic texture in severely cold rolled high entropy equiatomic CoCrFeMnNi alloy during annealing. *IOP conf. Materials Science and Engineering*, 82 (2015) 012068. (DOI:10.1088/1757-899X/82/1/012068)